TECHNICAL REPORT RD-76-23

AERODYNAMIC PERFORMANCE OF MISSILE
CONFIGURATIONS AT TRANSONIC SPEEDS
INCLUDING THE EFFECTS OF A JET PLUME

J. M. Wu, T. H. Moulden and N. Uchiyama
The University of Tennessee
Space Institute
Tullahoma, Tennessee 37388

Prepared For

MARCH 1976

U.S. ARMY MISSILE COMMAND
Redstone Arsenal, Alabama 35809

Technical Report RD-76-23
UTSI

REPORT DOCUMENTATION PAGE		READ INSTRUCTIONS BEFORE COMPLETING FORM
1. REPORT NUMBER TR-RD-76-23	2. GOVT ACCESSION NO.	3. RECIPIENT'S CATALOG NUMBER
4. TITLE (and Subtitle) AERODYNAMIC PERFORMANCE OF MISSILE CONFIGURATIONS AT TRANSONIC SPEEDS INCLUDING THE EFFECTS OF A JET PLUME		5. TYPE OF REPORT & PERIOD COVERED Technical Report
		6. PERFORMING ORG. REPORT NUMBER TR-RD-76-23
7. AUTHOR(s) J. M. Wu, T. H. Moulden and N. Uchiyama		8. CONTRACT OR GRANT NUMBER(s)
9. PERFORMING ORGANIZATION NAME AND ADDRESS University of Tennessee Space Institute, Tullahoma, Tennessee 37388		10. PROGRAM ELEMENT, PROJECT, TASK AREA & WORK UNIT NUMBERS (DA) 1W362303A214 AMCMS Code 632303.11.21400
11. CONTROLLING OFFICE NAME AND ADDRESS Commander US Army Missile Command Attn: DRSMI-RPR Redstone Arsenal, Alabama 35809		12. REPORT DATE 18 February 1976
		13. NUMBER OF PAGES 219
14. MONITORING AGENCY NAME & ADDRESS(If different from Controlling Office)		15. SECURITY CLASS. (of this report) UNCLASSIFIED
		15a. DECLASSIFICATION/DOWNGRADING SCHEDULE

16. DISTRIBUTION STATEMENT (of this Report)

Approved for public release; distribution unlimited.

17. DISTRIBUTION STATEMENT (of the abstract entered in Block 20, if different from Report)

18. SUPPLEMENTARY NOTES

19. KEY WORDS (Continue on reverse side if necessary and identify by block number)

Missile configurations
Slender bodies
Small incidence
Rear-end geometries

20. ABSTRACT (Continue on reverse side if necessary and identify by block number)

This report discusses the flow over various missile configurations with and without fins. Attention has been restricted to transonic flight conditions and to slender bodies at small incidence. Various rear-end geometries are treated, including boattail and flare configurations.

The effect of plume induced separation is also included so that realistic estimates of the forces on the body can be made. It is shown that the agreement between theory and experiment is adequate for engineering calculations.

DD FORM 1473 EDITION OF 1 NOV 65 IS OBSOLETE
1 JAN 73

CONTENTS

FORWARD

This report summarizes the results obtained to date of an analysis conducted by The University of Tennessee Space Institute under US Army Contract No. DAAH01-74-C-0183. This contract was initiated under DA Project No. IM 26230A 214 and AMC Management Structure Code No. 632303.11.21505.01. The technical effort was performed between May 1971 and September 1975, under the direction of the Aerodynamics Group, Aeroballistics Directorate, US Army Missile Command, Redstone Arsenal, Alabama. The Army technical representative was Dr. D. J. Spring.

I. INTRODUCTION

Since our last summary report was prepared [1], significant progress has been made both in the areas of inviscid flow analysis on various missile configurations and in understanding the viscous flow field interaction with an exhaust jet plume. Several publications have resulted from the studies and these are listed as References 2 through 25. The objective of the present report is to summarize the results of our continued effort to develop an understanding of the flow over missile configurations at transonic speeds.

The goal of the entire research project is to develop calculation techniques that allow the aerodynamic characteristics of missile configurations to be estimated. Particular interest centers around the effects a jet exhaust plume may have on the flow field over the body when the free-stream conditions are transonic. A strong interaction flow has to be treated and the basic flow configuration is shown in Figure 1.

The theory has developed within the spirit of the component approach wherein individual flow items are treated separately and the results matched together to cover the entire flow field. The major of these divisions lies between the potential and viscous elements of the flow, with each being further broken down to suit specific flow situations. Sections II and III treat the potential and viscous elements of the flow respectively. Section IV presents some calculated results for plume induced separation under various conditions.

The potential flow theories described in Section II are based upon the slender body approximation and are restricted to small incidence. This same restriction carries over to the viscous flow analysis, treated in Section III, where the cross-flow component in the boundary layer is neglected.

Figure 2 is a summary statement of the geometric configurations that are considered in the potential flow analysis. Each of these items is described in greater detail in Section II and their calculation in the computer program is indicated in Appendix A. The range of applicability of the theories associated with each of these items is expressed in Table 1 as a function of the pertinent parameters. Table 2 presents similar information for the viscous flow calculations. When building up a configuration from the various components, it is the most stringent of the parameter limitations which control the region of validity of the final result. It should be noted that most of the computer program components will yield numbers when used outside the recommended limits of Tables 1 and 2 but the results should then be treated with caution.

Part II of this report will present the details of the computer program and its utilization.

TABLE 1.   PARAMETER LIMITATIONS FOR INVISCID FLOW

Component	M Limits	α Limits (deg)	Other
Fore-body			
Ogive	0.8 - 1.2	0 to 5	Very low M may have convergence problem
Conical	0 - 1.5*	0 to 15	Applicable till shock attaches which depends on apex angle*
Polynomial	0.7 - 1.5	0 to 10	
Arbitrary Smooth	0.7 - 1.5	0 to 10	
Rear-end geometry			
Conical boattail	1.0 - 1.5	0 to 10	
Conical flare	0 - 1.5*	0 to 10	Same limitation as conical nose*
Smooth boattail	0.8 - 1.5	0 to 10	
Fin configurations			
Slender fin	0 - 1.5	0 to 10	Applicable to cruciform
Nonslender fin	0 - 1.0	0 to 10	Applicable to cruciform
Control surface (flap or Elevon)	Same as fin	0 to 30	Applicable to cruciform

*Can be determined by the graphs given in NACA - 1134:
Shock attachment angle and Mach number relationship.

II.   ANALYSIS OF INVISCID FLOW

In order to calculate the aerodynamic performance of missile configurations, it is essential that accurate knowledge of the inviscid flow over the body is available. This is necessary as a starting point in the determination of the viscous flow over the body and also for the

TABLE 2. LIMITATIONS FOR VISCOUS FLOW ANALYSIS

Component	M Limits	α Limits*	Other
Laminar boundary layer	0 - 2.0	0	Unit Prandtl number
Turbulent boundary layer	0 ~ 2.0	0	
Flow at slope Discontinuity	-	0	Small angle change
Separation	> 0.5	0	
Free-shear layer	0 ~ 2.0	0	
Confluence	> 1.0		

* Approximate results can be obtained for small incidence
  by appeal to a strip theory.

significant interaction which may take place between the viscous and
potential flow components. The analysis starts with a discussion of the
inviscid flow over a variety of missile configurations. The basic theore-
tical work has been properly documented in References 2-9, 11, 12, 15-18,
and 23 and will be briefly described below. Greater emphasis will be
placed upon a discussion of the flow over fin-body combinations.

A. Basic Potential Flow Theories For Noses and Tails

The inviscid, transonic flow small perturbation equation has
been employed to solve most of the axisymmetric nose and tail flows.
Various techniques were developed for solving the different geometries.
All theories developed so far have been carefully compared with data and
shown to possess very satisfactory agreement with experimental data within
their regions of validity. Thus, all theories developed can be employed
with confidence for performance predictions (for example, the Navy has
accepted some of our theories in their standard program [26]).

1. Flow Field Around Ogive-Cylindrical Bodies. The nonlinear,
inviscid, transonic flow small perturbation equation has been used to
solve the problem of flow over an ogive-cylindrical body with small angle
of incidence. Hosokawa's nonlinear correction theory [27 and 28] known
as a parabolic method with a stretching procedure [2, 4, 8, 16] has been
applied to such geometries. The agreement with experiment, in general, is excel-
lent. This theory was summarized in our last summary report [1] and a further
check with experiment was made by Spring [29]. A typical comparison of

theory with MICOM's data is given in Figure 3. In these comparisons, the effect due to the boundary layer build up are also considered. From this comparison, it is concluded that the Reynolds number effect on the surface pressure calculation is negligibly small for the flow over a body of revolution at small angles of incidence [6] in the absence of a propulsive jet. This is drastically different from the situation that can occur with two-dimensional geometries [30].

2. Flow Field Around Various Smooth Nose-Cylindrical Bodies. The previously mentioned method has been extended to cover general smooth shaped nose-cylindrical bodies. Various examples have been treated [16 or 17] which range from an arbitrary smooth frontbody, given in tabular form, to bodies described by various order polynomials.

The inviscid transonic flow small perturbation equation for a body of revolution states that:

$$\left(1 - M_\infty^2\right)\Phi_{XX} + \frac{1}{r}\frac{\partial}{\partial r}\left(r\Phi_r\right) + \frac{1}{r^2}\frac{\partial^2 \Phi}{\partial \theta^2} = (\gamma + 1)M_\infty^2 \; \Phi_X\Phi_{XX} \quad . \tag{1}$$

When linearized in the parabolic sense, the above equation can be written in the form:

$$\left(1 - M_\infty^2\right)\phi_{XX} + \frac{1}{r}\frac{\partial}{\partial r}\left(r\phi_r\right) + \frac{1}{r^2}\frac{\partial^2 \phi}{\partial \theta^2} = K \; \phi_X \quad . \tag{2}$$

The Hosokawa's nonlinear correction method assumes that the solution of Equation 1 can be obtained by considering the solution of Equation 2 with an addition of a correction function g, so that,

$$\Phi(x,r,\theta) = \phi(x,r,\theta) + g(x,r,\theta) \tag{3}$$

where g represents the local correction. The governing equation for the correction term g, as well as the method of relaxation after passing through the acceleration phase of the flow is given in detail in References 1, 2, and 8.

The necessary derivatives of the radius and the cross-sectional area of the front body are determined by a finite difference scheme. The m-th derivative of a tabulated function is:

$$D^m \{f(a)\} = \sum_{n=m}^{\infty} \frac{m!}{n!} \frac{\Delta^n f(a)}{h^m} S_n^m \tag{4}$$

Where D is the derivative operator, h the stepsize between two known values of the function, Δ the difference operator, and S_n^m the Sterling number. The difference operator and the Sterling number are respectively:

$$\underset{h}{\triangle} f(x) = f(x + h) - f(x) \tag{5}$$

and

$$S_n^m = \left[\frac{1}{m!} D^m \left(x\right)_n\right] x = 0 \tag{6}$$

The basic notation used in the development is shown schematically in Figure 4. The forebodies studied are expressed by the equations:

$$R(x) = D \left\{\left[\left(\frac{\overline{R}}{D}\right)^2 - \left(\frac{x}{D} - \frac{\ell}{D}\right)^2\right]^{1/2} - \left(\frac{\overline{R}}{D} - 1/2\right)\right\} \tag{7}$$

for a secant body, and

$$R(x) = (-1)^{n+1} R_o \left(\frac{x}{\ell} - 1\right)^n + R_o \tag{8}$$

for polynomial bodies when n takes the values 3, 4, or 5. In addition to these configurations, an artificially generated forebody, based upon a tabulated radius distribution, was used in the computations [17].

It is found that the sonic point (indicated as the parabolic point in Figure 4) as well as the shock wave, shifted location considerably as the forebody configuration is changed (Figure 5). The local Mach number distributions for the various bodies are shown in Figure 6 when the free stream Mach number is sonic. The effect of free stream Mach number on surface pressure distribution for the fifth order polynomial body and for an ogive body are compared in Figure 7.

   3.   Conical Nose Cylindrical Bodies. An excellent inviscid flow solution has been obtained for a conically shaped forebody which can be applied within the subsonic, sonic to supersonic flow regions. The originally proposed theory [1 and 8] has been modified [15] to incorporate better iteration and integration techniques. The detailed analysis as well as the calculative procedures are given in Reference 15.

The inviscid transonic flow small perturbation equation, as given in Equation (1), is transformed by placing:

$$f^2(x) = \left(1 - M_\infty^2\right) - (\gamma + 1)M_\infty^2 \phi_X \tag{9}$$

Then it follows that:

$$f^2(x)\phi_{xx} + \phi_{rr} + \frac{1}{r}\phi_r + \frac{1}{r^2}\phi_{\theta\theta} = 0 \tag{10}$$

7

where Equation (10) is a linear partial differential equation with a variable coefficient. This equation is then solved to first order approximation [15] with the complete boundary conditions. Some typical comparisons of theory and experimental data are given in Figures 8 and 9. Note that a blunting of the nose, as shown in Figure 9, only influences the surface pressure distribution near the apex. The influence due to the angle of attack has also been included in the theory (see Figures 10 and 11). The theory allows the pressure distribution to be computed over a rather wide Mach number range. The comparison with data shows excellent agreement (Figure 12). A comparison of the changes in pressure drag with Mach number is given in Figure 13.

4.   Flow Over a Conical Flare. It has been found that the conical flare configuration can go some way toward controlling the undesirable flow separation characteristics generated by a high thrust jet. For this reason there is interest in calculating the flow over this type body geometry. The nose cone solution described in the previous subsection has been extended [16 or 18]. The agreement between the theory and experimental data is found to be excellent.

The treatment of the governing equation is practically the same for the nose-cone case. Two assumptions are basic to the development. First, it is assumed that the flow experiences a stagnation point at the beginning of the flared body and, second, that the flow accelerates to sonic velocity conditions at the end of the flare. The latter boundary condition is somewhat verified by experiment [31], while the first one is only true for inviscid flow. In reality, the viscous flow will modify the pressure field at the flare root and this is discussed later.

The conical flare geometry may be described by the equation

$$R(x) = (\tan \delta) \, x + R_o \tag{11}$$

where δ is the flare angle, R_o is the radius of the cylindrical body ahead of the flare, and the origin for the streamwise coordinate, x, is taken at the flare root. The nomenclature is shown in Figure 14 together with a computed local Mach number distribution for a fixed flare angle. Comparisons with experiment are given in Figure 15 and 16, and the variation of pressure coefficient with flare angle is given in Figure 17.

5.   Solution On a Cylindrical Body Behind a Sharp Shoulder. The problem here is to calculate the flow along a cylindrical body just downstream of the junction with a conical nose. Due to the slope discontinuity at such a point on the body, it is necessary to employ different methods. The technique developed is to combine the local two-dimensional approximation analysis proposed by Tani [32] with the transonic similarity transformation. The detailed analysis as well as the calculative procedure are given in Reference 5, 8, or 11.

The basic nonlinear small perturbation equation for the transonic flow over a body of revolution, Equation (1), is first transformed by placing

$$y = r - R \text{ with } y \ll R$$

$$\Phi = (1 + ay + by^2 + \ldots) \tilde{\varphi}(x,z) \tag{12}$$

$$z = y + ky^2 + my^3 + \ldots$$

where $\tilde{\varphi}$ is the transformed perturbation velocity potential and a, b, c, . . ., k, m, n, . . . are constants. These constants can be chosen so that Equation (1) can be transformed into the corresponding two-dimensional form

$$\left(1 - M_\infty^2\right) \tilde{\varphi}_{xx} + \tilde{\varphi}_{zz} = (1 + \gamma)M_\infty^2 \tilde{\varphi}_x \tilde{\varphi}_{xx} \quad . \tag{13}$$

The body boundary condition takes the form

$$-\frac{2}{5} \tilde{\varphi}(x,0) + \tilde{\varphi}_z(x,0) = \frac{dR}{dx} \quad . \tag{14}$$

Equation (13) is now solved for the case of a sonic flow, and a wider transonic flow range obtained by applying Spreiter's similarity transformation [33]. A typical comparison of this theory with experimental data is given in Figure 18. The agreement is very good in the upper transonic flow regime. In the lower transonic flow regime it is found that a shock wave and a local flow separation are usually present. The location of the shock wave may be estimated, therefore, by employing a turbulent boundary layer separation criterion to recover the free stream pressure [5 and 34]. The result of employing such a scheme is compared with the experiment on Figure 19.

6. Flow Over a Conical Boattail. The above analysis is also applicable to a conical boattail geometry as long as the approaching Mach number is close to unity. To develop the solution for a conical bottail, the body geometry is expressed in the form

$$R(x) = 1 - \lambda x \tag{15}$$

where λ denotes the boattail angle in radians.

Now the analysis for a body with discontinuous curvature can be applied directly. It is necessary, however, to assume that the body is sufficiently long for the flow ahead of the boattail junction to be considered as a uniform free stream. The detailed analysis is referred to in References 5 and 8. The calculation terminates when the free-stream Mach number is recovered if this condition is satisfied before the end of the body is reached.

9

A typical comparison with MICOM's data is shown in Figure 20 where it is seen that the agreement is good.

7. <u>Flow Over a Smoothly Contoured Boattail</u>. The above analysis has been extended to a smooth boattail by simply assuming that the boattail may be segmented into a series of conical boattails each at the local slope. This analysis was carried out by Whitfield [35] and a typical calculation is shown in Figure 21.

B. Fin-Body Interaction By Slender Body Theory

1. <u>Slender Body Theory and Flow Model</u>. The research into fin-body interaction problems has assumed increased importance. In response to this need, an analysis of the aerodynamic performance of a slender fin-body combination has been developed. This permits us to estimate the pressure coefficient on slender, delta-cruciform fins and on cylindrical bodies in inviscid flow. The analysis has been extended to include the case with small angle of attack and with sideslip (due to yaw) as well as the case of a canted fin. The analysis is mainly based on the slender body theory of Spreiter [36 and 37] and the source and sink method of Adams and Dugan [38].

In the light of slender-body theory, the current analysis (for the details, see [23]) is valid not only for subsonic flow but also for moderately supersonic flow over a fin-body combination; provided that the fin has a subsonic leading edge. Furthermore, the analysis is valid even at free-stream speeds, very close to sonic, provided that no shock waves appear on the fin-body combination. The analysis developed here checks well with experimental data over the Mach number range mentioned and details will be given later. The analysis is outlined below.

Much previous research on fin-body combination problems has centered around finding the "load" distribution and little work is available concerning the surface pressure distribution. Spreiter [36 and 37] developed a method based upon slender body theory for calculating the aerodynamic loading on slender delta fin-body combinations with small angles of attack and sideslip (due to yaw). Adams and Dugan [38] have treated the load distribution on a slender canted fin by means of the source and sink method. Nielsen [39] summarized previous work and considered the aerodynamic loading in a more general case. He treated slender fin-body combinations with small angles of attack and sideslip (due to yaw) in addition to fins with small cant angles. Recently, Spreiter and Stahara [40, 41] investigated in detail the pressure coefficient distribution on slender fin-body combinations at transonic speed. However, for the case of the flow over a slender, zero thickness fin mounted on a cylindrical body reduces to Spreiter's earlier works [36, 37] and to that of Lawrence and Flax [42].

10

Figure 22 shows three different body-fixed Cartesian coordinate systems used in the present analysis. The Cartesian coordinate system with the axes x, y, and z is taken such that the x-axis is positive rearward and coincides with the longitudinal fin-body combination axis, the y-axis is positive to the right, facing forward, and can rotate about the x-axis lying in a pair of horizontal fins of symmetry, and the z-axis is positive vertically upward and can rotate about the x-axis lying in a pair of vertical fins of symmetry. The $\bar{x}$, $\bar{y}$, $\bar{z}$ coordinate system is taken where the $\bar{x}$-axis aligns parallel to the free stream velocity, the $\bar{z}$-axis is in the plane containing the $\bar{x}$-axis and the fin-body longitudinal axis. The Cartesian x', y', z' coordinate system is taken where the x'-axis is positive rearward of the body and coincides with the fin-body longitudinal axis, and the x'-axis is positive upward normal to the body.

The angle α_c is the angle between the x'-axis and the x-axis. The angle φ is the angle of bank and can rotate about the x'-axis. For small α_c, the angle of attack, α, and sideslip (due to yaw) β, can be defined as follows:

$$\left.\begin{array}{l} \alpha = \alpha_c \cos \varphi \\[2mm] \beta = \alpha_c \sin \varphi \end{array}\right\} \tag{16}$$

The free stream velocity, V_o, can be decomposed into two components for small α_c; the axial flow with the velocity V_o and the cross flow, $V_o \alpha_c$. Furthermore, the cross flow, $V_o \alpha_c$, can be decomposed into two components with velocities $V_o \alpha$ and $V_o \beta$, respectively. In the case of a fin-body combination where the fin has a small cant angle about the hinge axis at the mid point of the root chord length, the cant angle will be designated by δ as shown in Figure 23.

A positive rolling moment contributed to a left fin with its trailing edge inclinded downwards will be designated as positive "cant" in this analysis.

Figures 24 and 25 show the computational flow models and coordinate systems used in Sections 2 and 3 respectively. In these figures, "a" is the body radius and "s" the fin semispanwise length. Figure 26 shows the computational model with a fin having different ratios of semispan to body radius used in Section 4.

The perturbation velocity potential equation, which governs the flow around the slender fin-body combination, can be written as

$$\emptyset_{yy} + \emptyset_{zz} = 0 \tag{17}$$

11

in the x, y, z coordinate system [39], where ϕ is the small perturbation velocity potential, and the subscripts indicate partial derivatives with respect to the corresponding coordinate axes. This means that the equation which governs a flow around a slender body remains invariant for a slight rotation of the coordinate system. The boundary conditions for ϕ in the fin-body combination can be written as

$$\phi\,(\infty) = 0 \quad ; \tag{18a}$$

in the far field, and

$$n_2 \left(-V_o\beta + \phi_y\right) + n_3 \left(V_o\alpha + \phi_z\right) = 0 \quad , \tag{18b}$$

on the body. Here n_2 and n_3 are the directional cosines of the unit vector normal to the body surface in the y and z directions, respectively

$$\phi_z = -V_o\alpha \pm V_o\delta \tag{18c}$$

on the horizontal fins, where the upper sign is for the right horizontal fin and the lower sign is for the left horizontal fin, and

$$\phi_y = V_o\beta \mp V_o\delta \tag{18d}$$

on the vertical fin where the upper sign is for the upper vertical fin and lower sign is for the lower vertical fin, respectively.

The perturbation potential for a unit velocity can be decomposed as

$$\phi = \alpha\phi_\alpha + \beta\phi_\beta - \delta\phi_\delta \tag{19}$$

where ϕ_α, ϕ_β, and ϕ_δ are the perturbation potentials for unit angle. The expression for ϕ_α and ϕ_β can be written as

$$
\phi_\alpha = \pm \frac{1}{\sqrt{2}} \left\{ \left[-\left(1 + \frac{a^4}{r^4}\right) r^2 \cos 2\theta + s^2 \left(1 + \frac{a^4}{s^4}\right) \right] \right.
$$
$$
+ \left[r^4 \left(1 - \frac{a^4}{r^4}\right)^2 + 4a^4 \cos^2 2\theta + s^4 \left(1 + \frac{a^4}{s^4}\right)^2 \right.
$$
$$
\left. \left. - 2s^2 \left(1 + \frac{a^4}{r^4}\right) \left(1 + \frac{a^4}{s^4}\right) r^2 \cos 2\theta \right]^{1/2} \right\}^{1/2} - z \tag{20}
$$

where the upper sign is for the upper half of a fin-body combination as shown in Figure 27 (i.e., $0 \leq \theta \leq \pi$), and the lower sign is for the lower half (i.e., $\pi \leq \theta \leq 2\pi$). For $\emptyset_\beta$ the expression is

$$\emptyset_\beta = \pm \frac{1}{\sqrt{2}} \left\{ \left[\left(1 + \frac{a^4}{r^4} \right) r^2 \cos 2\theta + s^2 \left(1 + \frac{a^4}{s^4} \right) \right] \right.$$

$$+ \left[r^4 \left(1 - \frac{a^4}{r^4} \right)^2 + 4a^4 \cos^2 2\theta + s^4 \left(1 + \frac{a^4}{s^4} \right)^2 \right.$$

$$\left. \left. + 2s^2 \left(1 + \frac{a^4}{s^4} \right) \left(1 + \frac{a^4}{r^4} \right) r^2 \cos 2\theta \right]^{1/2} \right\}^{1/2} + y \qquad (21)$$

where the upper sign is for the right half of a fin-body combination (i.e., $-\frac{\pi}{2} \leq \theta \leq \frac{\pi}{2}$), and the lower sign is for the left half (i.e., $\frac{\pi}{2} \leq \theta \leq \frac{3}{2}\pi$).

By a conformal transformation, the flow in the physical plane (termed the x-plane) is mapped into a flow in the mapping plane (termed the σ-plane) (Figure 28) by using a source and sink method [38], the perturbation velocity potential $\emptyset_\delta$ for unit velocity and unit cant angle, can be written as

$$\emptyset_\delta = \frac{a}{\pi} \ell n \left| \frac{\sin 2 (\gamma - \mu)}{\sin 2 (\gamma + \mu)} \right| - \frac{2R}{\pi} (I_1 + I_2 + I_3 + I_4) \sin 2\mu \qquad (22)$$

for all values of μ, $(-\pi \leq \mu \leq \pi)$. In this equation I_1 and I_3 are the complete elliptical integrals of the third kind, while I_2 and I_4 are the incomplete elliptical integrals of the third kind. (For details of the theory, see [23]).

The pressure coefficient C_p, including quadratic terms but neglecting the higher order terms in the perturbation velocity components, can be written for a unit free stream velocity in the form:

$$C_p = -2 (u - v\beta + w\alpha) - (v^2 + w^2) \qquad (23)$$

where u, v, and w are the perturbation velocity components parallel to the x, y, and z axes, respectively.

13

The load distribution on the fin-body combination in this analysis is defined as follows:

$$\Delta p/q = \left(C_p\right)_{lower} - \left(C_p\right)_{upper}$$

$$= \left(C_p\right)_{left} - \left(C_p\right)_{right} \tag{24}$$

where q is the dynamic pressure (equal to $\rho_0 V_0^2/2$), and the subscripts "lower" and "upper" are the lower (negative z) and upper (positive z) part of the fin-body combination. The subscripts "left" and "right" are the left (negative y) and right (positive y) part of the fin-body combination, respectively, when facing forward (see Figure 24a). By considering the symmetric properties of the perturbation velocity components on the upper and lower surfaces, it is found that the load distribution on the horizontal fin is given as

$$\Delta p/q = -4\alpha \, u_\alpha^+ + 4\delta \, u_\delta^+ + 4\alpha \, \beta v_\alpha^+ \left(1 - v_\beta^+\right) - 4\beta\delta \left(1 - v_\beta^+\right) v_\delta^+ \tag{25}$$

where the "+" superscript on the perturbation velocity components refers to the lower panels of the horizontal fins.

The load distribution on the vertical fins is given as

$$\Delta p/q = -4\beta \, u_\beta^+ + 4\delta \, u_\delta^+ - 4\alpha \, w_\beta^+ \left(1 + w_\alpha^+\right) + 4\alpha\delta \, w_\delta^+ \left(1 + w_\alpha^+\right) \tag{26}$$

where the "+" superscript on the perturbation velocity components refer to the right-hand panels of the vertical fins.

The load distribution on the body (positive when upward) is expressed in the form

$$\Delta p/q = -4\alpha \, u_\alpha^+ + 4\delta \, u_\delta^+ - 4\alpha\beta \left[w_\beta^+ \left(1 + w_\alpha^+\right) - v_\alpha^+ \left(1 - v_\beta^+\right)\right]$$
$$- 4\beta\delta \left[v_\delta^+ \left(1 - v_\beta^+\right) - w\delta^+ \, w_\beta^+\right]. \tag{27}$$

where now the "+" superscript on the perturbation velocity components refer to the lower part of the body.

2. <u>Surface Pressure Distributions On Fin Body Combinations With Angles of Attack and Yaw.</u>

(a) Effects of Angles of Attack (with an example for $\alpha = 3°$, $\beta = -\delta = 0°$).

14

An example of the computation of the surface pressure and the load distribution was carried out on a fin-body combination at angle of attack with zero fin cant angle. The flow model used is shown in Figure 24a. Figure 29 presents the calculated C_p distribution corresponding to each side of the fin panel.

The C_p distribution pattern is symmetric which respect to the z-axis which aligns in the cross flow direction. The expected reason why the positive C_p (i.e., the pressure side) close to the horizontal fin edge decreases is that the second order term v^2 in Equation (23) is getting larger when compared to the first order velocity components near the fin edge. The C_p distribution on the vertical fins is the same and will become zero as z becomes $\pm \infty$. Figure 30 shows the body C_p distribution which is also symmetric with respect to the z-axis. It shows the greatest change at the junction of the horizontal fins with the body. The schematic load distribution on the entire fin-body combination is shown in Figure 31. The body has an ogive nose in this example. It should be noted that no attempt was made to calculate the load distribution for the vertical fins in this particular case. Thus, the load distribution on the cruciform fin is exactly the same as that for the planar fin case.

(b) The Effects of Angles of Yaw (with an example of $\beta = 3°$, $\alpha = -\delta = 0°$):

Again, as a demonstration of the calculation procedure, the sideslip angle was taken to be $\beta = 3°$, while $\alpha = -\delta = 0°$. In this case, the C_p distribution and the load distribution will have exactly the same pattern as would be obtained by rotating the C_p and the load distribution patterns of the above example (see Figures 29, 30, and 31) 90° counterclockwise.

(c) The Combined Effects of Angles of Attack and Sideslip (with an example, $\alpha = \beta = 3°$, $-\delta = 0°$):

As a sample calculation, the values $\alpha = \beta = 3°$ were assumed. In this simple combined case, it is expected that the C_p distribution and load distribution will have approximately the same pattern as the resultant pattern of the above cases for $V_0 \alpha$ and $V_0 \beta$.

Figures 32 and 33 show the C_p distributions on the surfaces of the fins and the body, respectively. The flow model for this case is shown in Figure 24b.

The C_p distribution is symmetric with respect to the z'-axis which has the same direction as the resultant cross flow $V_0 \alpha_c$ with bank angles of 45°, because $\alpha = \beta$. The reason that the C_p distribution on the surface

15

has a larger negative value (i.e., on the suction side) and larger positive C_p (i.e., on the pressure side) in the second quadrant and the fourth quadrant, respectively, as shown in Figure 32 and 33, is because the pressure caused by the cross flows $V_0\alpha$ and $V_0\beta$ intensify each other in these quadrants.

By examining the C_p distribution on the body, an interesting characteristic is found (Figure 33). The value of C_p at one point on the first or the third quadrant of the body becomes "zero". This means that the pressure at these points recovers to that of the free stream and is a consequence of the co-existence of both compression and suction regions in the same quadrant. Figure 33 presents the quantitative surface pressure distributions around the circumference of the body.

3. Effect of Canted Fin.

(a) C_p and Load Distribution on Cruciform Canted Fin-Body Combination (with an example for $-\delta = 3°$, $\alpha = \beta = 0°$):

As a sample calculation, the pressure and load distribution were calculated for cruciform fins at a cant angle of "3°" (in a negative sense, see Figure 25) on a circular cylinder with its longitudinal axis aligned to the free stream direction. The geometry is shown in Figure 25a. The computed C_p distribution on the fins is shown in Figure 34. The C_p distribution on the corresponding panel of each fin has exactly the same pattern and has a symmetric pattern with respect to the origin of the coordinate.

The C_p distribution on each quadrant of the body also has the same pattern which is again symmetric with respect to the origin of the coordinates. The C_p distribution appearing in Figure 35 is regarded as the perturbation disturbance created by the fins since the body alone would not generate a disturbance The reason why the C_p distribution on each quadrant has a zero point is a consequence of the pressure differential across the fins (see Figure 34).

(b) Comparison with the Case When Only the Horizontal Fins are Canted (with an example for $-\delta = 3°$, $\alpha = \beta = 0°$):

Figure 36 shows the computed C_p distribution on the fins. The C_p distribution shows nearly the same values as those in Figure 29 of subsection (a).

16

Figure 37 shows the C_p distribution on the body which results from the pressure disturbance transmitted by the horizontal fins. The C_p distribution on each quadrant (Figures 30 and 37) yields a similar pattern. The approximate C_p distribution on both the fins and the body, in the case where all four fins are canted, can be obtained by superimposing the C_p distribution for the cases when only the vertical and horizontal fins are canted (Figures 36 and 37).

(c) Comparison of C_p and Load Distribution on Fin Body Combinations in Various Cases:

The C_p and load distributions for various cases have been compared. For one of these examples, Figure 38 shows the C_p distribution on the right horizontal fin and body while Figure 39 shows the load distribution on the fin-body combinations. The load distribution on the body is computed for a unit projected spanwise length. The reason why $\Delta p/q$ on the body, for the case of all fins canted, is equal to zero at $y/a \approx 0.7$ is the C_p distribution in this case becomes the same for both the upper and lower parts of the body (see Figures 35 and 38) at the midpoint of a half body ($y/a = \cos 45° \approx 0.71$).

4. Comparisons Of Various Configurations Of Fin-Body Combinations.

2(a) Surface Pressure Distributions:

As a sample calculation, the case when $\alpha = \beta = -\delta = 3°$ has been considered. It can be surmised that the C_p and $\Delta p/q$ distribution in this case will yield approximately the same pattern as those obtained from the results of the combined cases of $\alpha = \beta = 3°$ (Section c) and $-\delta = 3°$ (Section a). In fact, the computed C_p distribution as shown in Figures 40 through 42 is nearly the same as that of the combined C_p distribution for the case $\alpha = \beta = 3°$ (Figures 32 or 33), and for the case $-\delta = 3°$ (Figures 34 or 35). The C_p distributions on each surface are more similar than those of the corresponding case for $\alpha = \beta = 3°$ due to the small influence of the $-\delta = 3°$ cant angle in such cases. A larger value of positive C_p is found in the fourth quadrant while the negative C_p is larger in the second.

2(c) Mutual Effects of α, β, and δ — Discussion on Coupling Terms:

There will be a "mutual interaction" between the effects of angle of attack α, the angle of yaw β, and the cant angle δ. The magnitude of this

17

interaction flow field has been estimated. Figures 43 and 44 show the load distribution caused by each perturbation angle for one particular configuration at s/a = 2.5. These figures also show the interaction between the three effects of incidence, yaw and cant angle. From these figures, it is observed that the major contribution to $\Delta p/q$ on each fin is made by $\Delta p/q$ on the right and left horizontal fins from the incidence effect, and on the upper and lower vertical fins from the yaw effect. This is mainly due to the first term on the right-hand side of Equations (25) and (26), respectively. In general, the effect of cant angle on $\Delta p/q$ is small, and is due to the second term on the right-hand side of Equations (25) or (26). Pertaining to the load distribution, the interaction between incidence and yaw affects all fins, but the mutual interaction between incidence and cant angle appears only on the vertical fins. The mutual interaction between yaw and cant angle appears on the horizontal fins only, as can be realized by examining Equations (25) or (26). It is clear that the coupling terms mentioned above do not contribute significantly to the load distribution over the fins.

C. Fin-Body Interaction By Singularity Distribution

1. Basic Considerations. The aerodynamic performance of various kinds of fin-body combinations in inviscid flow can be analyzed by the "singularity method" [43 and 44]. Körner's approach [43] is followed in this analysis. In general the singularity method has advantages over the slender body theory since there is less restriction on admissible fin shapes. The pressure coefficient can also be calculated rather simply.

The surface pressure distribution on rectangular, sweptback, and tapered sweptback fin-body combinations have been obtained. The analysis has also been extended to include slender, cruciform and canted delta fin-body combinations as discussed earlier, and also to include the case of slender, cruciform, clipped delta fin-body combinations with a deflected small control fin. The results have been compared with slender body theory and with other singularity methods [44].

The present method, with slight modification, can also be applied to a fin-body combination when the fin is twisted, cambered, of finite thickness and of arbitrary plan form.

For simplicity, the following assumptions were made in the present analysis, i.e.,:

(i)   The free-stream flow is subsonic, steady, inviscid and uniform.

(ii)   The fin is of zero thickness and has straight leading and trailing edges and a streamwise tip.

18

(iii)   The fins are attached to a cylindrical body.

(iv)   The angle of attack is small.

Based on the singularity method concepts, constant strength vortex singularities on a horizontal plane are used to replace the lifting fin. Image vortices are placed inside the body in order to compensate the body displacement effect. To obtain a good aerodynamic interaction for a fin-body geometry, source — sink singularities are distributed along the body surface and doublet singularities are distributed along the body axis. The doublet distribution gives the effect of the body being inclined to the free stream. An interaction scheme is used so that all the simulated lifting surfaces can eventually satisfy the flow boundary conditions everywhere on the surface of the fin-body combination.

Figure 45 shows a schematic model of a basic fin-body combination for this analysis. A fin (or wing) has been divided into many panels and each one has been replaced by a horseshoe-type vortex which consists of three vortices (i.e., one bound vortex and two free vortices). The body has also been divided into many panels, each consisting of a correct part of the body, and it has been replaced by a source or sink on its surface.

2.   Basic Equations and Coordinates. Figure 46 shows the coordinates used on the fin. Each fin is divided into a number of trapezoidal panels having their sides parallel to the free stream. Each panel has three vortices of constant strength, i.e., one bound vortex, which is located at the one quarter local panel chord length, and two free trailing vortices which are located at the local panel edges and are parallel to the free stream. The control point location, at which the boundary condition is to be satisfied, is assumed to be the three quarter point of the local panel chord length and on its center line, shown in Figure 47. In addition to this, the Goethert compressible similarity rule has been employed in the present analysis, i.e., the coordinates normal to the free stream have been multiplied by the Prandtl-Glauert parameter β. The following five steps are essential to the analysis and were established in [43]:

(i) Determining the circulation distribution (γ_i) on the fin:

The normalized perturbation velocity components at any control point on panel "i" induced by any panel "j" (that is four discrete horseshoe vortices, two from a pair of fins themselves, and two from their body images) can be written as,

$$\frac{u_i}{U_\infty} = \sum_{j=1}^{n} P_{ij} \gamma_j$$

$$\frac{v_i}{U_\infty} = \sum_{j=1}^{n} Q_{ij} \gamma_j \qquad\qquad (28)$$

$$\frac{w_i}{U_\infty} = \sum_{j=1}^{n} R_{ij} \gamma_j \qquad i = 1, n$$

where: u_i, v_i, w_i are the perturbation velocity components and P_{ij}, Q_{ij} and R_{ij} are the aerodynamic matrices.

The third equation as stated above is used for satisfying the boundary conditions on any panel, i.e.,

$$-\beta \omega_i = \frac{w_i}{U_\infty} = \sum_{j=1}^{n} R_{ij}\gamma_j \qquad i = 1, n \qquad\qquad (29)$$

where $\omega_i = \alpha_{fi}$. Equation (29) consists of n simultaneous linear equations with n x n constant coefficients. The γ_j can be solved by a Gaussian elimination technique.

(ii) Determining the source distribution (q_ν) on the body

The induced velocity components at any point on panel "ν" on the body surface due to the fin and its image vortices associated with the control point of panel "j" is expressible as,

$$\vec{W}_\nu = \begin{bmatrix} u_{b\nu} \\ v_{b\nu} \\ w_{b\nu} \end{bmatrix} = \sum_{j=1}^{n} R_{\nu j} \gamma_j; \quad \nu = 1, 2M \qquad\qquad (30)$$

In cylindrical coordinates there exist the transformation:

$$v_{n1} = v_b \cos\theta + w_b \sin\theta$$

$$\qquad\qquad (31)$$

$$v_t = -v_b \sin\theta + w_b \cos\theta$$

where the geometrical relationships are illustrated in Figures 48 and 49.

20

The m-th approximation of the source strength q_ν at a point ν on the body surface, which cancels the induced normal velocity v_{nl} in Equation (31), can be written as

$$q_{m\mu} = -2\left(v_{nl}\right)_{m\mu} - \sum_{\substack{\nu=1 \\ \nu \neq \mu}}^{2M} \frac{q_{(m-1)\nu}}{2\pi} \times$$

$$\frac{[1 - \cos(\theta_\mu - \theta_\nu)]\,\beta\,a\,\Delta S_\nu}{\left\{\left(x_\mu - x_\nu\right)^2 + \beta^2\,[1 - \cos(\theta_\mu - \theta_\nu)]\,a^2\right\}^{3/2}} \tag{32}$$

and

$$\Delta S_\nu = \beta\,a\,\Delta\theta\,\Delta x_\nu \tag{33}$$

(iii) Determining the downwash $(w_{b\mu})$ on a fin due to sources distributed on the body surface

The downwash on panel "μ" due to source on panel "ν" can be written as

$$w_{b\mu} = \sum_{\substack{\nu=1 \\ \nu \neq \mu}}^{2M} \frac{q_\nu}{4\pi} \frac{\beta(z_0 - z_\nu)\,\Delta S_\nu}{\left[\left(x_\mu - x_\nu\right)^2 + \beta^2\left\{\left(y_\mu - y_\nu\right)^2 + \left(z_0 - z_\nu\right)^2\right\}\right]^{3/2}} \tag{34}$$

(iv) Determining the circulation distribution (γ_i) for the second iteration

As a result of the downwash obtained in Equation (34), the corresponding angle of attack induced on a fin can be written as w_{bi}/U_∞. This term should be added to the geometrical angle of attack in Equation (29) so that ω_i is written as

$$-\omega_i = -\alpha_{fi} + \frac{w_{bi}}{U_\infty} \quad ; \quad i = 1, n \tag{35}$$

After these ω_i values have been obtained on the fin panels, the procedure is repeated until the values of γ_i do not change greatly.

(v) Extension to the case of a body with angle of attack.

Downwash on a fin due to the doublet distribution along the body axis (as shown in Figure 50) can be written as

$$\frac{w_f}{U_\infty} = \alpha_b a^2 \frac{y^2 - z_o^2}{\left(y^2 + z_o^2\right)^2} \quad . \tag{36}$$

This downwash has been assumed constant at any spanwise location, where it causes an apparent change in the angle of attack (ω_i) as mentioned above. Thus, in this case, ω_i should be replaced by,

$$-\omega_i = -\alpha_{fi} + \frac{w_{bi}}{U_\infty} + \frac{w_{fi}}{U_\infty} \quad . \tag{37}$$

The aerodynamic performance coefficient can be computed in the usual manner for the pressure coefficient, C_p on the panel,

$$C_{pj} = \pm \frac{\Delta C_{pj}}{2} \quad \text{for fin}$$

$$= - \frac{2u_{bj}}{U_\infty} \quad \text{for body} \tag{38}$$

where "+" denotes the upper surface of the fin and "-" the lower surface.

For load distribution, ΔC_p, there results

$$\Delta C_{pj} = \frac{b \, \gamma_i}{\beta^2 \left(x_{dj} - x_{vj}\right)} \quad \text{for fin}$$

$$= \left(C_{pj}\right) \begin{matrix} \text{lower} \\ \text{surface} \end{matrix} - \left(C_{pj}\right) \begin{matrix} \text{upper} \\ \text{surface} \end{matrix} \quad \text{for body} \tag{39}$$

The spanwise lift distribution, $C_L(y)$ is given as

$$C_L(y) = \frac{2b}{\beta^2 l(y)} \sum_{i=1}^{n'} \gamma_i \tag{40}$$

where n' is the total number of panels along the chord $l(y)$ at a fixed y station.

For the lift coefficient, C_L, the final result is

$$C_L = \frac{\sum\limits_{j=1}^{P} C_{pj} \Delta S_j}{\sum\limits_{j=1}^{P} \Delta S_j} \tag{41}$$

where $\Delta S_j = 4\beta h_j \left(x_{dj} - x_{vj} \right)$ for the fin

$$= \beta a \Delta\theta \Delta x_j \sin(\theta_j) \quad\quad \text{for the body} \tag{42}$$

and represents the projected area on the horizontal plane.

3.   <u>Results and Discussion on Various Fin-Body Combinations.</u>

(a)   Rectangular Fin-Body Combination:

The spanwise lift distributions have been calculated for a rectangular fin alone and for a fin-body combination configuration at $M_\infty = 0$. They agree well with the original calculations of Körner [43] as is shown in Figure 51. The discussion of the compressibility effect will be given later. The body treated in this example has zero angle of incidence, and the fins are canted by 1° (clearly, results for a larger cant angle can be obtained by a simple linear multiplication of the amplitude). The computed results for the fin-body interaction agreed well with the limited experimental data shown in Figure 51, except in the region very close to the fin root. Körner pointed out that this disagreement resulted from the presence of the boundary layer in the real flow over the fin and body [43]. This suggests that a study of viscous effects is necessary in order to obtain a more accurate result in this region. As can be seen from Figure 51, when comparing cases with and without body, the mutual interaction between the body and the fin is rather strong.

The chordwise load distributions on the body, for the same fin-body geometry as shown in Figure 51, were computed at three different azimuthal positions. The results are shown in Figure 52. It can be seen that the influence of the fin on the body becomes stronger near the fin root. It affects both the upstream and downstream flow beyond the fin location. The calculated chordwise lift distribution on the fin very close to the fin root is also included in Figure 52 for a comparison.

(b)   Constant Chord Sweptback Fin-Body Combination:

Figure 53 shows a calculated chordwise load distribution on the fin of a 45° sweptback fin-body combination. The variation of the load distribution, which is rather small along the spanwise direction, can be seen from this figure.

(c) Tapered, Sweptback Fin-Body Combination:

The sweptback fin-body combination, with two different taper ratio fins, as used by Körner [43], has been investigated. Figure 54 shows the computed spanwise lift distribution on this type of geometry when the taper ratio λ = la/li is 0 and one-third (where 'li' is the maximum chord length through the body, and 'la' is the fin tip chord length). The sweptback angle for both cases was taken as 30° at one-quarter of the local chord length. The angle of incidence of the body was assumed to be 1° (again, for larger angles, a linear multiplication of the amplitude is sufficient) and the fin was assumed to have a zero cant angle. The lift distribution for λ = 0 agrees well with the characteristics of the delta fin-body combination, in spite of the fact that it is not quite a delta fin. (For example, compare it with the result shown in Figure 39 computed by slender body theory).

All the above results closely agree with those given in Reference 43, on which the present calculation is mainly based.

(d) Cruciform Slender Delta Fin-Body Combination:

Figure 55 shows the calculated longitudinal pressure distribution on the body. A pair of horizontal fins are canted by 3° so as to cause a negative rotation about the body axis (i.e., x-axis) in the sense of the commonly accepted sign convention. It should be noted that the rate of perturbation pressure change is very sharp at the leading and trailing edges and the magnitude of the pressure is lower when compared with the case of a large aspect ratio fin (see Figure 52). This is expected because the fin is slender so that the influence of the fin on the body should be small. This result agrees with the concept of slender-body theory which suggests that the aerodynamic disturbance is restricted to the cross plane.

4. <u>Discussions on the Compressibility Effect</u>. The effect of compressibility on the lift coefficient of a cruciform slender delta fin-body combination is shown in Figure 56. (Only the angle of attack influence is considered here for the sake of discussion). The fin area was extended through the body, as shown by the dotted line, in order to specify a reference area for the lift coefficient computation. In general, the Prandtl-Glauert rule results in an over-correction for this type small aspect ratio fin configuration (see Figure 56) and, [45].

It is more appropriate to use Goethert's rule to calculate the compressibility effect on fin-body combinations. For a slender fin-body combination, after using the Goethert rule correction, the result (see Figure 56) agreed very well with the result computed by the slender body theory. In view of a wider range of Mach number applicability of the slender body theory, such an agreement is not totally surprising. In the same figure, a result due to Nielsen [39] is also included for comparison. For a non-slender fin case, the result obtained by using a Goethert's rule correction is shown in Figures 57 and 58.

5. Körner's Approach Compared with Other Methods and with
Data.

(a) Comparison with Slender-Body Theory:

A comparison of the results obtained from the results obtained from
the singularity method and from slender-body theory has previously been
briefly discussed. A surprisingly good agreement between the two methods
was obtained for the lift coefficient of a cruciform slender delta fin-
body combination.

The pressure and load distribution on the same fin-body combination
as used in the slender body theory example (see Figure 25) was calculated.
The results are shown in Figures 59 to 61. Figure 59 shows the pressure
distribution on one horizontal fin. It is worthwile to note that the
linearized C_p expression was used in the present analysis while the C_p
expression used for the slender-body theory was of second order. The
pressure coefficient was computed azimuthally, at six positions on the
one-half body, and is shown in Figure 60. Note that the difference in the C_p
expression is more sensitive on the fin than on the body. This means that
the second order expression for the C_p is more important for such slender
fin-body combinations even though its absolute value is small. Figure 61
shows the load distribution on both a horizontal and a vertical fin. It
can be seen from Figures 59 to 61 that the results of the present analysis
and of slender-body theory agree satisfactorily with each other. From
these comparisons, it can be concluded that both methods will yield a
similar result for a small aspect ratio fin-body combination. This
merely proves that the singularity method can be applied for fins with a
wide range of aspect ratios and, therefore, is more versatile.

(b) Comparisons with the "Flexstab" Singularity Distribution Method and with Data:

The "Flexstab" method [46] has been applied to an aircraft wing-body
combination for flight at high subsonic, transonic and supersonic speeds
[44 and 46]. A comparison of computations based on Körner's scheme, as
adapted in this analysis, was made for those configurations calculated
by the "Flexstab" technique.

The paneling scheme employed for the present calculations, as well
as those by the "Flexstab" method, are given in Figure 62. The main
difference between the "Flexstab" method and Körner's technique is in
the treatment of the "body". The "Flexstab" method treats the body by
a number of discrete vortices distributed on the mean body surface. The
mean body surface is approximated by a number of rectangular strips with
streamwise surfaces [44]. In addition, the "Flexstab" method is more

25

complicated and takes into account thickness, camber and twist effects on the wing by means of an additional source-sink and vortex singularity distribution.

The calculated chordwise pressure distribution on the wing is shown in Figure 63. The angle of incidence of the body was taken to be, 2°, and the free-stream Mach number was 0.85. The computation was made near the spanwise mid-point. The agreement with "Flexstab" results was surprisingly good. The agreement with the experimental data were also satisfactory, except in the region very close to the wing leading edge, where a sudden pressure drop, due to local flow separation, is found in the data. The case for an angle of incidence of 8° is shown in Figure 64. The agreement with the "Flexstab" method was very good in this case also; however, the agreement with data was not too good from the leading edge to the mid-chord. The reason for this disagreement with data may be attributed to flow separation from the sharp leading edge because of the high angle of incidence. A further study for such a situation is needed.

A further comparison with the "Flexstab" method was made for the effect of a wing flap. The calculated chordwise pressure distribution, based on both methods, is given in Figure 65. In this case, it is assumed that the wing has 0° angle of attack and that the flap angle is 8.3°. The agreement between the methods is good; however, the inviscid flow theory predicts a larger pressure difference than is indicated by the data over the flap surface. Again, the disagreement is probably attributed to flow separation on the upper wing resulting from the high flap angle. Finally, the normal force coefficient has been compared as shown in Figure 66. The agreement with the experiment is very good. The compressibility effect based on the Goethert's similarity rule is again proven to be very satisfactory.

D.   Comparisons of Potential Flow Theories with Data on Slender
       Clipped Delta Fin-Body with Elevon Deflection

The computational model employed for a cruciform slender clipped delta fin-body combination is given in Figure 67. Each fin has a small control fin, called an "elevon", and it is assumed that its hinge line is located near the trailing edge of the main fin.

The angle of incidence of the body is taken to be 8.54° with an elevon deflection angle of ± 30°, so that the body generates a counter-clockwise rolling moment then facing the upstream direction. The free-stream Mach number is 1.62. With proper sweptback, as in this example calculation, the leading edge of the fin is submerged in a subsonic stream. Because of the slenderness of the fin and its subsonic leading edge, one expects that a better agreement would result by employing slender body theory than from use of the singularity distribution method. A comparison with the data, indicates that this is indeed true.

26

Figures 68 to 73 show the chordwise pressure distributions, computed by the singularity distribution and by the slender body theory, at different spanwise positions, together with experimental measurements [45]. The agreement of the singularity distribution method of Körner with the data was adequate in general over the fin surface, even though the flow is supersonic. The pressure distribution on the elevon surface could not be compared due to a lack of data.

As was expected, the computed result from slender-body theory showed better agreement with the fin data. This is especially so on the lower surface of the fin. However this method cannot calculate the effect of the elevon deflection or the clipped tip effect. 'Karmans' method estimated a rather large pressure distribution on the fin close to the hinge line of the elevon as a result of the very large elevon deflection angle. The large pressure increase is again attributed to flow separation. This can be seen more clearly on the upper surface of the fin near the hinge line. The tip effect caused by the leading point P of the tip Mach cone may cause the pressure to increase. However no correction has been made for this in the present analysis.

The longitudinal C_p distribution at a fixed azimuth angle on the body has been computed and is shown in Figure 74. The fin-body combination in this example has angle of incidence of $7.4°$ and a bank angle of $2.8°$. The C_p distribution was computed from a linear summation of the C_p resulting from separate calculations for angle of attack and for yaw angle. The results are as shown in Figure 74. (Also, see Figure 27 for results for the individual flows). The trends of the C_p distribution in this case is very similar to the one discussed previously in Figure 55.

Various compressibility corrections for the pressure coefficient at a sample point on the fin are shown in Figure 75. An angle of attack of $8.5°$ was assumed in this case. Computed results using the Prandtl-Glauert and the Kármán-Tsien rules showed the over-correction discussed earlier. The total lift coefficient in this particular fin-body combination with zero elevon angle is shown in Figure 76. The maximum body cross-section area was taken as the reference area for the lift coefficient calculation. The contribution of the body to the total lift coefficient is very small, and may be neglected.

III.   ANALYSIS OF VISCOUS FLOW AND INTERACTION WITH PLUME

The basic theoretical statements associated with the determination of the viscous flow are made in the following section. Two basic flow areas need treatment. In the first is included the boundary layer development, both laminar and turbulent, over the body, while the second relates to the strong interaction in the base flow region.

So far the development has been restricted to a body of revolution when the cross-flow component in the boundary layer is not a feature. For small incidences, when it is reasonable to expect only minimal cross flow, then it is possible to adopt a strip theory approach to obtain an approximate solution.

The strong interaction, as calculated here, is essentially a first order result since no attempt has been made to correct the flow over the body (ahead of the interaction) for the large disturbance created by the plume interaction. It was shown earlier [6] that in the absence of the plume interaction at the rear of the body, there was very little influence of the viscous flow on the potential flow structure. While with a large plume interaction present, it is likely that the adjustment to the fore-body flow would be more significant, this has been neglected in the present study. The numerical calculations of South [47] for bodies of revolution show the expected magnitude of this correction. In a two-dimensional flow where the pressure gradients are more severe and the boundary layer growth more rapid, it is shown that the viscous effect is of great importance [48].

Figure 77 shows the overall flow field for the type of situation under discussion and identifies the principle segments of the flow. A boundary layer develops over the forward part of the body (laminar initially followed by a turbulent portion) under essentially the potential flow pressure distribution. This boundary-layer may pass under a shock interaction and may negotiate discontinuities in slope at a cylinder boat-tail junction for instance. Near the rear of the body, the boundary layer development is influenced by the strong interaction with the plume and sufferes both a separation process and a wake confluence before issuing into the far field.

The basic concept of the methods adopted for the solution of the strong interaction shows a close connection with the classical component approach [49], but there have been certain developments and modifications to suit the situation in hand. The adoption of the component concepts in no way suggests its superiority over an integral technique, but rather, was chosen on the basis of available experience. The comments made later will indicate that, in the present writers' opinion, both these approaches have been developed to their limit and are still not completely adequate in all situations. There is a strong urge to develop numerical methods for the entire flow field.

Another theme runs through the viscous flow development as presented here. No attempt has been made to include thermal effects in the analysis, which implies that any modification of the strong interaction flow due to non-isoenergetic considerations is neglected. Base heating rates cannot be determined. Consistent with this overall approach, it was felt that chemical reactions and other non-equilibrium effects could be neglected in the plume calculations. The whole theory must be considered within this restriction.

A.   The Viscous Flow

The equations of motion for the viscous flow over a body of revolution can be stated:

$$\frac{\partial}{\partial x} (R\rho u) + \frac{\partial}{\partial r} (R\rho v) = 0 \tag{43}$$

$$u\frac{\partial u}{\partial x} + v\frac{\partial u}{\partial r} + \frac{1}{\rho}\frac{\partial p}{\partial x} = \nu\frac{\partial^2 u}{\partial r^2} + T \tag{44}$$

Over the leading edge of the body, the flow is laminar and then the contribution 'T' from the Reynolds shear stress vanishes identically. R denotes the local body radius.

The viscous flow calculation over the body is to serve two major purposes: determination of the body drag and evaluation of initial conditions at the start of the plume induced separation. For both these activities, it is only necessary to determine the integral characteristics of the boundary layer (the momentum thickness and skin friction being the most significant quantities in this connection).

With this in mind, it was considered unnecessary to solve the boundary layer equations in great detail and large numerical expense. Hence the Thwaites' method was adopted for the laminar flow (in conjunction with Stewartson/Illingworth and the Mangler transformations) and Nash's technique was used for the turbulent part of the boundary layer.

Certain limitations implicit in this approach should be clearly recognized at the outset. Integral methods cannot treat flows containing discontinuities without some additional empiricism. Hence the boundary layer development over such configurations as a cone or boattail/cylinder junction cannot be treated without special attention. The same is true for the interaction of a shock-wave with the boundary layer and the individual treatments reserved for these flows will be dealt with in subsequent sections.

Throughout the boundary layer calculation, the external pressure has been determined from the potential flow solution that was discussed in Section II for various body configurations. As yet there has been no attempt to calculate the boundary layer development over the fin or at the fin-body junction. In cases where plume-induced separation has been calculated for finned bodies [24], this has been done on a strip theory basis with those segments close to the fin root being neglected. The wake issuing from the fin, and its interaction with the plume, has also been disregarded. It is felt that, provided the fin incidence is sufficiently low to assure attached flow over the fin, then the modification to the viscous layer-plume surface mixing will be minimal.

29

1. The Laminar Boundary Layer Development. The theoretical treatment of the laminar boundary layer development rests upon the application of two transformations to the calculation procedure of Thwaites [50]. First, there is the Mangler transformation [51, 52] which relates the flow past a body of revolution to that past an equivalent two-dimensional body, then the Stewartson/Illingworth transform [53, 54] converts the result to a compressible flow. The limitations implicit in the use of these transformations (for example, the boundary layer must be thin compared to the body diameter, the fluid has unit Prandtl number, etc.) has been reviewed elsewhere [1 and 7] and need not be restated here. In the present application, these restrictions should not represent too severe a limitation.

As in Reference 7, we can state the final result for the laminar boundary layer momentum thickness development in the form:

$$\frac{\theta}{L} = \left[\frac{0.45}{R_e (R/L)^2} \left(\frac{U_e}{U_\infty}\right)^{-6} \left(\frac{T_e}{T_o}\right)^{\frac{2\gamma-4}{\gamma-1}} \int_o^{x/L} \left(\frac{U_e}{U_\infty}\right)^5 \left(\frac{T_e}{T_\infty}\right)^{\frac{2-\gamma}{\gamma-1}} \times \left(\frac{R}{L}\right)^2 d(x/L) \right]^{1/2} \quad (45)$$

Here, L is the characteristic length of the problem (taken to be the body length in this case) and R(x) is the local body radius. The local velocities U_e and the local temperature T_e are simply related to the local Mach number when the external flow is isentropic. T_o is the local total temperature. The Reynolds number R_e used in this equation is based upon the characteristic length L.

The solution is completed by employing the empirical data of Thwaites [50] to determine the form factor H, (and hence the displacement thickness) and the local friction coefficient, C_f.

In particular:

$$C_f = \frac{10^{-6} C_{f_o}}{2 R_e \theta} \left(1 + \frac{\gamma-1}{2} M^2\right)^{1.5} \left(1 + \frac{\gamma-1}{2} M_\infty^2\right)^{2.5} \quad (46)$$

$$H = H_o/\theta \quad (47)$$

The following equations were fitted to Thwaites' data:

$$C_{f_o} = \begin{cases} 0.222 - 1.557\,P - 1.781\,P^2 & P < 0 \\ 0.222 & P = 0 \\ 0.222 - 0.466\,P - 2.222\,P^2 & P > 0 \end{cases}$$

$$\bar{H} = \begin{cases} 2.61 + 3.851\,P + 5.7682\,P^2 + 0.4409\,P^3 & P < 0 \\ 2.61 & P = 0 \\ 2.5728 + 14.2214\,P - 432.396\,P^2 + 5132.96P^3 & P > 0 \end{cases}$$

$$H_o = \frac{1}{R}\left(1 + \frac{\gamma-1}{2}M^2\right)^3 \left\{ \bar{H} + 0.2\,M^2\left[\bar{H} + \frac{\theta R}{\left(1 + \frac{\gamma-1}{2}M^2\right)^3}\right]\right\}$$

and the pressure gradient parameter P is given as:

$$P = -\frac{R_e\,\theta^2}{M_\infty}\left[\frac{\left(1 + \frac{\gamma-1}{2}M_\infty^2\right)^{1.5}}{\left(1 + \frac{\gamma-1}{2}M^2\right)^2}\right]\frac{dM}{dx}$$

A typical calculation of the laminar boundary-layer over an ogive forebody is shown in Figure 78. Here the skin friction and momentum thickness variations for several Reynolds numbers are presented for the flow over an ogive forebody. The free-stream Mach number is 1.1.

2. <u>Transition</u>. No attempt has been made to predict a transition point in the present study. Two courses are open in the execution of the calculation procedure. First, a transition point can be inserted as an arbitrary parameter in the calculation and the laminar boundary layer development is determined up to that point. If the separation condition ($C_f = 0$) is reached during the progress through this laminar flow calculation, then the calculation is stopped and transition is assumed to occur at this point. The remainder of the boundary layer is determined from the turbulent boundary layer calculation procedure. In either case, the final value of momentum thickness at the termination of the laminar flow calculation is used as an initial condition at the start of the turbulent flow.

3. <u>The Turbulent Boundary Layer Development</u>. The boundary layer equations 43 and 44 are solved by first integrating across the boundary layer to give:

$$\frac{1}{R} \frac{d}{dx} \left(\rho_e U_e^2 R\theta \right) = \tau_w - \rho_e U_e \frac{dU_e}{dx} \delta^* \qquad (48)$$

which is the momentum integral equation for a turbulent boundary layer. This equation can then be solved numerically provided that sufficient additional information concerning the physical nature of the turbulence is included. Nash [55] selected various empirical data to close the system of equations for a compressible turbulent boundary layer.

In addition to Equation 48, it is required that the kinetic energy integral equation,

$$\frac{1}{2R} \frac{d}{dx} \left(\rho_e U_e^3 R\theta^* \right) = \int_0^\infty \tau \frac{\partial u}{\partial y} \, dy - \rho_e U_e^2 \frac{dU_e}{dx} \delta^{**} \qquad (49)$$

is also solved.

The variable G is introduced to determine the variation of the turbulence production integral. Let

$$G = 1/2 \ C_f + \frac{2}{\rho_e U_e^2} \int_0^\infty \tau \frac{\partial u}{\partial y} \, dy$$

and assume that the function G is determined from the differential equation.

$$\frac{dG}{dx} = \frac{\lambda}{\delta} G \left[\sqrt{\overline{G}} - \sqrt{G} \right] \qquad (50)$$

where the 'constant' $\overline{G}$ is given as

$$\overline{G} = -0.00883 + 0.02781 \ H_u - 0.03488 \ H_u^2$$

$$+ 0.01950 \ H_u^3 - 0.00359 \ H_u^4 \qquad (51)$$

and, the "shape factor" H_u, relates to a flow with no density changes (i.e., is identical to H when the flow is incompressible).

The various integral quantities can be related if the velocity profile relations

$$\frac{U}{U_e} = \frac{u_\tau}{U_e K} \log\left(\frac{y}{\delta}\right) + 1 - \frac{U_\beta}{U_e}\left[1 + \cos\left(\frac{\pi y}{\delta}\right)\right]$$

(52)

$$\frac{\rho_e}{\rho} = 1 + 0.178\, M_e^2 \left[1 - \left(\frac{U}{U_e}\right)^2\right]$$

are adopted.

Nash [55] showed that the following empiricism is adequate for the present purposes:

$$H = H_u\left(1 + 0.135\, M_e^2\right) + 0.228\, M_e^2$$

$$H_u = 1 + 1.33\,\triangle + 12\,\triangle^4$$

$$\triangle = (2 - \overline{H})\left(1 + 0.0135\, M_e^2\right)$$

$$H* = \left(\frac{0.0655}{H_u - 0.5} + 0.238\right) M_e^2$$

$$c_f = \frac{\dfrac{T_e}{T_w}\left(\dfrac{1}{H_u} - 0.4\right)}{\left[3.18 \log_{10}\left(\dfrac{T_e}{T_w}\dfrac{U_e \theta}{\nu_e}\right) - 1.0\right]^2}$$

(53)

This completes the solution, except for the boundary layer thickness, δ, which can be determined from

$$\frac{\theta}{\delta} = \frac{0.17\left\{1 - \exp\left[-3.5\left(H_u - 1\right)\right]\right\}}{1 + 0.1\, M_e^2}$$

(54)

The differential relation expressed by Equation 50 goes some way towards modeling the behavior of the turbulence structure. Different values of the constant λ are taken as

$$\lambda = 4 \qquad dG/dx > 0$$

$$\lambda = 10 \qquad dG/dx < 0$$

so that different boundary layer responses are incorporated depending upon the nature of the flow's departure from equilibrium.

33

In simple physical terms, this differential equation just assesses the rate at which the turbulent boundary layer would return to the equilibrium condition after suffering some perturbation. While this is clearly superior to a simple algebraic relation for departure from equilibrium, it still does not incorporate very much detail about the physical structure of the Reynolds stress tensor and its response to an external distrubance. In consistency with the basic premise that only an indication of the integral properties of the boundary layer are required in the present application, it was considered that such a simple representation of the turbulent stresses would be adequate.

The turbulent boundary layer calculation is started at the transition point with an initial value of momentum thickness, θ, equal to that at the termination of the laminar flow calculations. The initial value of H was taken to be

$$H = 1.6 + 0.417\, M_{et}^2$$

where M_{et} is the local Mach number at the transition point.

Calculated skin friction distributions are displayed on Figure 79 for three different Reynolds numbers. The curves show the change in skin friction at the transition point and also at the boattail shoulder. Details of the calculation procedure at the boattail slope discontinuity are discussed in Subsection 4 of the current section.

4. Change in Integral Parameters Across Discontinuities. Several flow situations of interest require knowledge of the turbulent boundary layer development across some form of discontinuity. Particularly, this involves the interaction of a weak shock wave with a boundary layer under conditions that do not involve separation, and the flow over a slope discontinuity. The latter situation develops at the junction of a boattail or flare or at the shoulder of a conical nose.

In the current development, it is considered that only a very approximate analysis is appropriate since the entire boundary layer calculation is attempted within the context of the integral theory. Not even the more sophisticated approaches to such flows [56] are adopted, although they could be with little effort.

Basic to the approach adopted is the idea that, if the pressure change is sufficiently rapid, then any changes that it may produce in the turbulence structure can be neglected to the first order and changes in the integral parameters determined from an inviscid model. The experimental work of Rose and Johnson [57] for the interaction of an oblique shock-wave with a turbulent boundary layer tends to confirm this flow model: in the outer (wake) region of the boundary-layer the turbulence structure remains more or less frozen. As is often observed in such

34

interactions in turbulent flow [58], however, the wall region quickly returns to equilibrium. This is to be expected when the pressure gradient across the viscous region is small the wall boundary conditions must be imposed.

Consistent with the basic model (and the further requirement that the total change be small), Nash [59] developed the relation:

$$\rho_e U_e M_e \theta = \text{constant} \tag{55}$$

as the first-order change in momentum thickness across a discontinuity. In the present work, this relationship is adopted in the treatment of both expansive and compressive pressure discontinuities.

The form factor, H, of the boundary layer was also allowed to change discontinuously. The magnitude of the change being given by:

$$\frac{H_2}{H} = 1 + \frac{\gamma-1}{2} \left[\left(\frac{M}{M_2}\right)^3 \sqrt{\frac{1 + \frac{\gamma-1}{2} M_2^2}{1 + \frac{\gamma-1}{2} M^2}} - 1 \right] \tag{56}$$

where the suffix 2 denotes downstream conditions at the boundary layer edge.

New values of θ and H thus allow the turbulent boundary layer calculation to continue and other quantities (friction coefficient say) are returned. The complete boundary-layer development up to the start of the plume interaction is now available.

In some situations, particularly where the flow downstream of the discontinuity is subject to an adverse pressure gradient, the subsequent flow development can be sensitive to initial values as calculated from the above relations. Figure 80 shows this effect for the boundary layer calculated on a conical boattail. The potential flow theory (Section II) for this geometry yields a discontinuous decrease in pressure at the boattail junction. In reality there would be a smooth, but rapid, change. The calculations reported on Figure 80 were for different estimates of this smoothing of the pressure change across the surface slope discontinuity.

Based on this result it appeared that a further study of the problem was desirable and an experimental program was set up to study the flow development over slope discontinuities. A typical two-dimensional model is shown mounted in the wind tunnel in Figure 81. More details of the wind tunnel are given in Reference 60. The slope discontinuity afforded by this model configuration was 6.5° and its length was 8.8 inches.

Surface static pressures were measured over the entire model length and boundary layer velocity profiles were obtained at specific locations. Figure 82 shows a measured surface static pressure distribution at a free-stream Mach number of 0.9. As expected, the flow suffers a strong expansion at the corner followed by a recompression. Due to the boundary layer development over the configuration, the flow does not recompress to a stagnation condition. Far downstream it is found that the flow returns to the free-stream pressure.

Typical mean velocity profiles are presented on Figure 83. It is shown that, as the flow approaches the expansion corner from the undisturbed upstream (flat plate) boundary layer, there is a marked thinning of the boundary layer with a consequent increase in wall shear. After the flow has negotiated the rapid expansion at the corner, the boundary layer thickens and the wall shear is reduced.

The integral techniques for calculating the turbulent boundary layer development do not include details of this type when applied to flow over slope discontinuities. Neither the calculation techniques, nor the experimental study considered here, discussed the change in turbulence structure that is associated with the flow. This subject must receive greater attention in the future.

A somewhat different problem exists at the junction of a flared rear end with the cylindrical forebody. The potential flow theory discussed in Section II would place a stagnation point at this junction and does not in any way reflect the real flow development. If this potential flow pressure distribution were adopted as the starting point for a boundary layer calculation, then it is evident that a separation would be predicted and the calculation terminated. The experimental data of Reference 61. was evaluated to determine an empirical relation for this junction pressure so that the boundary layer calculation could continue uninterrupted to the end of the body. With the notation

$$\left. \begin{array}{l} \tilde{P} = P_f/P_\infty - 1.0 + 0.047\,\theta_f - 0.004\,\theta_f^2 \\[2em] \tilde{M} = \left[0.076\,\theta_f - 0.005\,\theta_f^2 \right] M_\infty \end{array} \right\} \tag{57}$$

where P_f/P_∞ is the static pressure ratio at the flare junction and θ_f the flare angle, the correlation is as shown in Figure 84, and is included in the computer program. Details of the body geometries used in the studies are summarized in Appendix B.

5. <u>Calculation of the Free-Shear Layer</u>. Several restrictions from complete generality are contained in the free-shear layer calculation. First, it is assumed that the flow is turbulent so that :

no comparison between laminar and turbulent base flow is possible. It is also assumed that the shear layers evolve along a conical trajectory and that their profile can be approximated by the asymptotic turbulent shear-layer profile. Two major assumptions are involved here. First, it is supposed that the effect of the initial velocity profile (i.e., that associated with the separating boundary layer at the start of the interaction) is insignificant in as far as the distribution of mass flow in the shear layer is concerned. This latter quantity is significant since the solution to the base flow problem is closed by means of a mass balance in the dead air region. An approximate correction for this initial profile effect is included [61] by definition of a coefficient of the form:

$$\left. \begin{array}{ll} \text{Coeff} = 1.21 - 0.004 \; x/\theta & x/\theta \leq 50 \\ \qquad = 1.00 & x/\theta > 50 \end{array} \right\} \tag{58}$$

which changes the location of the median streamline (see Equation 66). The second assumption relates to the neglect of any external influences on the shear layer development. In this connection it is supposed that the external stream is at constant pressure and that the shear layer development is not influenced by its close proximity to the body surface or to the jet plume. It is certainly not true that the external flow is a constant pressure flow, but the relative shift between the streamline dispositions resulting from the pressure gradient and the upstream profile effect is not known.

Although the shear layer velocity profile does not match that of the approaching boundary layer, this is acknowledged to the extent that the momentum thickness of the shear layer is selected to be equal to that of the boundary layer. Two cases must be considered. When the base pressure is lower than the ambient pressure then the boundary layer must negotiate an expansion fan at the base of the body. The equations discussed in Subsection 3 provide the change in boundary layer momentum thickness:

$$\rho_e U_e M_e \theta = \text{Constant} \tag{59}$$

so that the value at the start of the free-shear layer can be estimated. This relation is also used at the nozzle exit to determine the change in boundary layer momentum thickness at the start of the plume shear layer. The other case occurs when the boundary layer leaves the body ahead of the base plane due to the interaction of a shock wave. Now the analysis of Stratford [62] and McDonald [63] shows that

$$\theta_{SL} = \theta_{BL} \left[\frac{1 + \frac{\gamma-1}{2} M_2^2}{1 + \frac{\gamma-1}{2} M_o^2} \right]^3 \quad A \tag{60}$$

37

where

$$A = 1.0 - 0.605 \left(1 - \frac{M_2^2}{M_o^2}\right) + 11.75 \left[1 - \frac{M_2^2}{M_o^2}\right]^2$$

Here, M_o denotes the approach Mach number at the start of the interaction and M_2 denotes the Mach number downstream of the shock wave. This latter value is determined from the theory of Mager [64] and is discussed in Subsection 7.

Finally, it is assumed that the entire shear layer development takes place under isoenergetic conditions and base heating effects and hot exhaust plumes are not treated.

With these assumptions, it is well known that the velocity profile is given in the form:

$$u/U_e = 1/2 \left[1 + \text{erf } (\eta)\right] \tag{61}$$

where the similarity parameter η is $\eta = \sigma y/x$. The coordinate among the shear layer is x and y is perpendicular. The mixing coefficient, σ, will be related to the Mach number at the edge of the shear layer (M_e) by the Korst and Tripp [64] relation

$$\sigma = 12.0 \ (1 + 0.23 \ M_e) \tag{62}$$

As it stands, this error function velocity profile is for a two-dimensional shear layer but can, with restriction, be adopted for the axisymmetric flow situation. Provided that the boundary layer remains thin compared with the diameter of the body and that the confluence point is not located too close to the axis of symmetry then the Mangler-Stepanov transformation could be adopted [51, 52]. It should be cautioned, however, that this transformation is only valid for a laminar flow and its application to the turbulent shear layer is, at best, an approximation [65].

In the present implementation of the transformation it is supposed that the shear layer is essentially conical so that the modified similarity parameter is

$$\eta = \frac{3R_o R_p \ \sigma}{R_o R_p + R_o^2 + R_p^2} \ \frac{y_a}{x_a} \tag{63}$$

where R_o is the shear surface radius at the base plane, R_p is the value at the station of interest and x_a and y_a are the coordinates in the axisymmetric configuration. The value of the mixing coefficient, σ, is left unchanged without justification.

The streamlines within the shear layer are located on the basis of Nash's development [59]. Then it is found that:

$$\Delta \psi = \frac{\sqrt{\pi}}{\sigma} \cdot x \left[G_u - G_m \right] + \theta \left[\frac{G_u - G_1}{G_1 - G_m} \right] \tag{64}$$

where x is the coordinate along the streamline and θ is the value of momentum thickness [from either Equation (59) or Equation (60) and the appropriate boundary layer calculation] at the start of the shear layer. As shown in Reference 61, the function G_α is expressed by the equation:

$$G_\alpha(\eta) = \int_\alpha^{1.0} \frac{\exp(\eta^2) \, (u/U_e)}{1 + \frac{\gamma-1}{2} M_e^2 \left[1 - \frac{u}{U_e} \right]^2} \, d(u/U_e) \tag{65}$$

with the velocity profile being given by Equation 61. The velocity, u_m/U_e, along the median streamline was given [59] to be

$$\frac{u_m}{U_e} = \left[0.348 + 0.018 \, M_e \right]^{1/2}$$

and determine the reference function G_M in terms of the external Mach number M_e. Typical distributions of the function G across the shear layer are shown in Figure 85.

6. Treatment of the Strong Interaction. Free shear layers are placed along the surface of the plume and as a boundary between the external flow and the dead-air region (see Figure 77). The solution is closed at the confluence point which is so selected as to give a net mass entrainment in the dead-air region equal to zero.

Equation (64) provided a relationship between the length of the shear layer and the initial momentum thickness, with the external Mach number (assumed constant along the entire shear layer) acting as a parameter. The two shear layers are matched via the geometric constraints of the problem and a pressure criterion at the confluence point. Now Equation 64 gives,

$$\Delta\psi_s = \frac{\sqrt{\pi\ell}}{\sigma_s} \left[G_{us} - G_{ms} \right] + \theta_s \left[\frac{G_{us} - G_{1s}}{G_{is} - G_{ms}} \right]$$

$$\Delta\psi_p = \frac{\sqrt{\pi S}}{\sigma_p} \left[G_{up} - G_{mp} \right] + \theta_p \left[\frac{G_{up} - G_{1p}}{G_{ip} - G_{mp}} \right]$$

and the condition

$$\Delta\psi \equiv \Delta\psi_s + \Delta\psi_p = 0 \qquad\qquad (67)$$

must be imposed on the solution to satisfy the zero net entrainment require-
ment. In these equations, the suffix "s" refers to the free-shear layer
and "p" refers to the shear layer along the plume boundary. The momentum
thickness at the start of the shear layer is again denoted by θ.

Figure 86 shows that the following geometric constraints must hold:

$$\tan(\theta_s - \theta) = \frac{y_p + R_n - R_s}{1 - x_s + x_n + x_p}$$

and $\ell^2 = (1 - x_s + x_n + x_p)^2 + (y_p + R_n - R_s)^2 \qquad\qquad (68)$

$$S^2 = y_p^2 + x_p^2$$

provided that it is assumed that the plume boundary is conical between
the nozzle exit plane and the confluence point.

The final pressure, P_c, at the end of the confluence process is
unknown. It is supposed that the individual pressure rises for either
the external or the internal flows can be expressed in the form of the
small turning relation modified by an undetermined factor. Thus it is
supposed that:

$$\frac{P_c}{P_s} = 1 + f(M_s) \Gamma\alpha_s \qquad\qquad (69)$$

where the coefficient, Γ, is determined empirically, and relates to the
N factor of Reference 61. The function f(M) has the form:

$$f(M) = \frac{\gamma M^2}{\sqrt{|M^2 - 1|}}$$

40

and is applied for either subsonic or supersonic Mach numbers. The angle α_s (and the corresponding angle α_p) are defined in Figure 87. The local plume slope θ_L is determined from the plume geometry and then α_s and α_p are related by the equation:

$$\alpha_s = \alpha_p + \theta_L - \theta_s + \theta.$$ (70)

The velocity u_m is determined from Equation 66 and hence the function G_m is known. Now the only remaining unknown quantity is the velocity on the reattaching streamline which determines G_u via Equation (65). It is assumed that the flow on the reattaching streamline is reduced to a stagnation condition at the confluence point where the pressure is P_c. The fact that this pressure is unknown accounts for the quantity Γ in the relation between the pressure ratio and turning angle contained in Equation (69).

$$\text{If } c = \left[\frac{\frac{\gamma+1}{2} M^2}{1 + \frac{\gamma-1}{2} M^2} \right]^{1/2} .$$

Then for isentropic compression along the reattachment streamline to a pressure ratio of P_c/P_{ref} demands that:

$$\left(\frac{u}{U_e} \right)^2 = \frac{\left(P_c/P_{ref} \right)^{\frac{\gamma-1}{\gamma}} - 1}{c_{ref}^2 \left(P_c/P_{ref} \right)^{\frac{\gamma-1}{\gamma}}} .$$ (71)

The solution procedure is as follows. An angle θ_s is selected (or when the base pressure is equal to the plateau pressure, the separation point, x_s, is the parameter since then $\theta_s = \theta_m$) and the above equations solved iteratively to determine $\Delta\psi$. The initial conditions (θ_s or x_s) are systematically changed over a range of values until $\Delta\psi$ changes sign. Interpolation then gives the solution, $\Delta\psi = 0$, and all parameters of the base flow are determined. Of particular interest are the base pressure and the length of the separation region.

Comparison of the theoretical calculation with experimental data (a typical variation of base pressure with Γ is shown on Figure 88) indicated that it was appropriate to take

41

$$\Gamma = 1.277739 \times M_s - 0.356621 \times M_s^2 - 0.69188; \quad z > 0.8$$

$$\Gamma = 0.1 \qquad\qquad\qquad\qquad\qquad z \leq 0.8$$

7. *The Separation and Plateau Pressures.* When the base pressure is lower than the ambient pressure it is possible to introduce an expansion fan at the base of the body to determine the conditions along the outer edge of the free-shear layer and complete the calculation using the analysis of the previous section. A different situation exists when the base pressure is greater than the ambient value. Now it becomes necessary to estimate the pressure rise that occurs under the compression in the external flow.

The method adopted is as follows. As the base pressure increases from the free-stream value, it is assumed that the external flow deflects through an angle θ_s such that

$$P_b/P = 1 + \frac{\theta_s \gamma M_o^2}{\sqrt{M_o^2 - 1}} \tag{72}$$

where M is the local Mach number at the start of the interaction (for a parallel sided body this will usually coincide with the free-stream Mach number). This compression process cannot continue when the angle θ_s becomes too large since then the boundary layer will suffer a separation from the body surface. In the present analysis it is assumed that the limit point at which flow separation is initiated can be described by the theory of Mager [34]. Details of this theory were given in Reference 1 and need not be repeated herein. It may be remembered, however, that this theory does not include any reference to the Reynolds number in specification of the separation pressure. For completeness, we note that the separation pressure [34] is given by the relation:

$$P_s/P_o = 1 + \frac{\frac{\gamma-1}{2} M_o^2 K}{1 + \frac{\gamma-1}{2} M_o^2} \tag{73}$$

where the constant K has been given the value 0.45 as the best representation of the available data. Details of the plateau pressure (which provides the maximum value θ_m to the flow separation angle θ_s) are presented along with the discussion of Equation 76. The Mach Number downstream of the interaction, M_2, is related to the approach Mach number M_o by:

$$M_2 = \sqrt{K} M_o$$

and the momentum thickness change (Equation 60) can be determined.

42

As the base pressure increased from the ambient value, it is assumed that the flow still leaves the body at the base plane until the base pressure has risen to the separation pressure level. At this condition the separation point is ready to move forward on the body, but it is still possible for the base pressure to increase. It will continue to do so until the separation has migrated sufficiently far from the base for the entire base area to be influenced by the plateau pressure.

To complete the solution in this phase of the flow development, it is necessary to specify both the plateau pressure and the streamwise length scale for the pressure rise as a whole. It is assumed here that the pressure signature under the interaction is unique and independent of the position of the separation point relative to the base. With this assumption, it is possible to adopt a correlation, somewhat similar to that suggested by Zukoski [66] for the pressure rise through the interaction. The form adopted is shown in Figure 89 and the two length scales x_p and x_o required in this correlation are shown in Figure 90. This latter curve reduces to Zukoski's values when the approach Mach number is greater than 1.5 but contains an elongation of the interaction length at lower Mach numbers roughly in accord with the measured distributions of Rubin [60]. The extended separation length is also used for subsonic approach conditions as will be discussed later.

The pressure signature of Figure 90 is fitted by the relations

$$P_p/P_o = 1.0 + (P_p/P_o - 1.0)\chi \qquad (74)$$

where the function χ is expressed as

$$\left.\begin{array}{ll} \chi = 5\ z^2; & 0 < z < 0.2 \\[2mm] \chi = \text{Sin}[\pi\ (z - 0.1)/1.8]\ ; & 1.0 > z > 0.2 \\[2mm] \chi = 1.0\ ; & z > 1.0 \end{array}\right\} \qquad (75)$$

Here $z = (x - x_s + x_o)/x_p$ and x_o represent the location of the separation point and the length scales x_s and x_p are given in Figure 90.

The above equations specify the entire pressure rise from the approach value P_o to the plateau value P_p. Some experimental data for the plateau pressure are shown in Figure 91 along with the theoretical values of Mager [34] and Zukoski [66]. In the present work the curve labeled (A) given by

$$P_p/P_o = 0.915 + 0.484\ M_o \qquad (76)$$

43

has been adopted for specifying the plateau pressure. The limiting flow turning angle is now determined from Equation 72.

Figure 92 indicates how the separation and plateau conditions are situated in terms of the development of the base pressure signature as a function of jet pressure ratio. The limiting base pressure at large jet thrust is also defined. It should be noted that much of the total pressure rise above the ambient value takes place before the separation point encroaches upon the body.

The correlation shown by Equation (76) is only adequate for two-dimensional flows and for flow over parallel-sided bodies of revolution. When the rear end of the body has a conical configuration then the data of Reference 62 shows that the limiting base pressure can be a strong function of conical angle. Only limited data are available since in most of the cases contained in Reference 62, the jet pressure ratio was not increased sufficiently to reach the limiting base pressure. Some data are presented on Figure 93 and shows the trends exhibited. Similar data for two-dimensional supersonic boattail flow are given in Reference 67.

A simple idea evolves the from consideration of the data shown in Figure 93. It is suggested that the ratio of the limiting base pressure at a given conical angle to that at 0 angle (P_p/P_{po} say) is almost independent of Mach number. This reduction of the data is shown in Figure 94 and substantiates the suggestion for supersonic flow, when the relation

$$P_p/P_{p_o} = 1 - 0.02440 \, \theta + 0.00074 \, \theta^2$$

correlates the data well. All that remains now is to scale the plateau and separation pressure relations contained in Equations 73 and 76 to yield more realistic limiting conditions for conical aft ends.

Finally, it is of interest to compare the predicted pressure rise under the separation (from Equation 74 and the related structure) with experimental data.

The curves on Figure 95 show the theoretical results for jet pressure ratios of 87.7 and 100 compared with the experimental data [62] for a jet pressure ratio of 87.7. The free-stream Mach number is 1.1. It is clear that the theoretical pressure signature is of the correct form and the length scale is more or less of the correct order.

When the approach Mach number is less than sonic then the situation is not so easily predicted. The experimental data shown on Figure 93(b) suggests that the separation pressure is given as,

$$P_s/P_\infty = 0.565M_o + 0.795; \qquad 0.5 < M_o < 1.0$$

The corresponding maximum pressure is given as:

$$P_p/P_\infty = P_s/P_\infty + 0.01$$

and the difference between the separation and "plateau" conditions is very small.

8.　Evaluation of Force Coefficients. Two basic drag integrals are required. One of these produces the form drag while the other generates the skin friction. For the purposes of analysis it was expedient to evaluate the form drag separately for each component of the body.

The expression for the base drag is given as:

$$C_{D_B} = \frac{\left(P_\infty - P_B\right) A_B}{1/2\rho_\infty U_\infty^2 A_{ref}}$$

$$= \frac{2}{\gamma} \left(1 - P_B/P_\infty\right) \frac{R_B^2 - R_N^2}{M_\infty^2 R_{ref}^2}$$

In the present case the reference area for the drag coefficient was taken to be that of the parallel section of the body.

The friction drag is determined from the equation

$$C_{D_F} = \frac{1}{\pi R_{ref}^2} \iint C_f \, dx \, R(x) \, d\theta$$

and the form drag follows from the expression

$$C_{D_P} = \frac{1}{\pi R_{ref}^2} \iint C_p \, \frac{dR}{dx} \, dx \, R(x) \, d\theta$$

In the calculation of the friction drag the approximation that the skin friction is 0 downstream of the separation point has been made and the integration is stopped at the separation point. The form drag has been broken into two parts (in addition to the base drag), and the boattail contribution is displayed separately.

45

The usual expression for a form drag involves an integral with respect to the body radius:

$$\int C_p \, dR$$

In situations where both the body radius and the pressure are varying rapidly, it is more accurate to adopt the following as the appropriate integral:

$$\int C_p \, \frac{dR}{dx} \, dx$$

provided that the body geometry is sufficiently well known.

The normal force and moment coefficient are expressed by the equations:

$$C_N = \frac{1}{\pi R_{ref}^2} \iint C_p \, \cos\theta \, dx \, R(x) \, d\theta$$

$$C_M = \frac{1}{2\pi R_{ref}^3} \iint C_p \, \cos\theta \, x dx \, R(x) \, d\theta$$

where the pitching moment is positive nose up and is taken about the nose of the body. These integrals are evaluated on the basis of a strip theory using 7 asithumal locations.

9. Summary of the Base Flow Calculation. The two principal modes of base flow that have been discussed correspond to base pressures either below or above the ambient pressure. Figures 96 and 97 show these two flow situations and summarize the equations required for their solution. The computer program (see Appendix A) resolves the differences between the two flows without operator intervention.

B. The Plume Calculation

If it is assumed that the jet expands inviscidly, then the plume boundary can be calculated quite accurately by the method of characteristics. A schematic graph of the interaction is given in Figure 98. A short development of the characteristic equations used for the computation of the plume boundary, assuming that the pressure distribution along the plume varies in a given way follows below:

Consider an axisymmetric flow field whose axis of symmetry coincides with the x-axis of a cylindrical coordinate system (x, r, θ) as shown in

46

Figure 99. An axisymmetric, supersonic, and inviscid flow is fully described by the continuity equation:

$$\frac{1}{\rho} \frac{D\rho}{Dt} + \nabla \cdot \vec{q} = 0 \quad , \tag{77}$$

the equation for the conservation of momentum

$$\rho \frac{D\vec{q}}{Dt} = - \nabla p \quad , \tag{78}$$

the rate of change of entropy, s,

$$\frac{Ds}{Dt} = 0 \quad , \tag{79}$$

and the equation of state, which can be expressed as

$$p = p(\rho, s) \quad , \tag{80}$$

where $\vec{q}$ is the velocity vector, p the pressure, and ρ the density. Equation (79) is valid everywhere except for passage through a shock wave.

Equations (77) through (80) are 4 equations for the 4 unknowns $\vec{q}$, ρ, p, and s and can be combined to give:

$$\left(1 - \frac{u^2}{a^2}\right) \frac{\partial u}{\partial x} + \left(1 - \frac{v^2}{a^2}\right) \frac{\partial v}{\partial r} - \frac{uv}{a^2} \left(\frac{\partial u}{\partial r} + \frac{\partial v}{\partial x}\right) + \frac{v}{r} = 0 \quad , \tag{81}$$

written for an axisymmetric system (x,r). Now consider a line in the x,r, plane passing through a point, P, of the flow inclined to the x axis by the angle $\tan^{-1}\lambda$ then the expression for this line, which is usually called a characteristic, is

$$\frac{dr}{dx} = \lambda \tag{82}$$

The variations of the velocity components, u and v, along this line are

$$\frac{du}{dx} = \frac{\partial u}{\partial x} + \frac{\partial u}{\partial r} \lambda \tag{83a}$$

$$\frac{dv}{dx} = \frac{\partial v}{\partial x} + \frac{\partial v}{\partial r} \lambda \tag{83b}$$

Substitution of Equation (83) into Equation (81) and using the expression for irrotational flow,

47

$$\frac{\partial v}{\partial x} - \frac{\partial u}{\partial r} = 0 \qquad , \tag{84}$$

gives

$$H\frac{du}{dx} + (2K-H\lambda)\frac{dv}{dx} + (H\lambda^2 - 2K\lambda+L)\frac{\partial v}{\partial r} + \frac{v}{r} = 0 \qquad , \tag{85}$$

where

$$L = 1 - \frac{v^2}{a^2} \; ; \; H = 1 - \frac{u^2}{a^2} \; ; \; K = -\frac{uv}{a^2} \tag{86}$$

Now consider lines through the point, P, for which the equation

$$H\lambda^2 - 2K\lambda + L = 0 \tag{87}$$

is valid. This quadratic equation for the tangent has 2 solutions given in the form:

$$\lambda_{1,2} = \frac{K \pm \sqrt{K^2 - HL}}{H} \tag{88}$$

and the 2 lines through the point P are defined by

$$\frac{dr}{dx} = \lambda_1 \qquad \frac{dr}{dx} = \lambda_2 \qquad . \tag{89}$$

Equation (85) becomes

$$\frac{du}{dx} + \lambda_2 \frac{dv}{dx} + \frac{1}{H}\frac{v}{r} = 0 \tag{90a}$$

and

$$\frac{du}{dx} + \lambda_1 \frac{dv}{dx} + \frac{1}{H}\frac{v}{r} = 0 \tag{90b}$$

The flow directions defined by Equation (88) are real only if the inequality

$$K^2 - HL = M^2 - 1 > 0 \tag{91}$$

is satisfied and the local velocity is greater than that of sound.

The expressions for the tangents given in Equation 88 can be simplified to read

$$\lambda_{1,2} = \tan(\theta \pm \mu) \qquad , \tag{92}$$

48

where θ is the inclination of the velocity vector and μ is the local Mach angle. Hence, the expressions (90a) and (90b) are valid along the lines whose tangents are inclined at the Mach angle, μ, with respect to the local streamline direction. These are the characteristic lines for the flow. Similar to the treatment of Equation (92), Equations (90a) and (90b) can be simplified by the introduction of the variables μ and θ to give:

$$\cot \mu \ \frac{dq}{q} - d\theta \ - \frac{\sin \mu \ \sin \theta}{\cos(\theta + \mu) r} \ dx = 0 \tag{93a}$$

and

$$\cot \mu \ \frac{dq}{q} + d\theta \ - \frac{\sin \mu \ \sin \theta}{\cos(\theta - \mu) r} \ dx = 0 \quad , \tag{93b}$$

These are the compatibility equations valid along the corresponding characteristic lines. On characteristic lines the normal derivative of the dependent variables, (u,v), may be discontinuous. This fact makes it possible to patch different flows together along these lines. The only restriction is that the velocity itself must be continuous. The situation differs from that for subsonic flow, where all derivatives are continuous, and a change in any part of the flow field affects every other part.

Along each characteristic line the dependent variables have to satisfy the compatibility equations. In the two-dimensional case, there exists an analytical expression for the relation between q and θ but this is not true for the axisymmetric case and the compatibility equations, Equations (93a) and (93b) have to be solved in a step-by-step procedure along the characteristic lines. The details for calculations of the interior and boundary points can be found in Reference 68 and are not given here.

To start the step-by-step procedure, the flow properties p, T, M, and θ have to be known somewhere in the flow field. In the present case they are specified across the exit plane of the nozzle along with the base pressure, P_b, the pressure distribution after the body, and the total temperature, T_c, of the exhaust gas. Twenty-one meshpoints are specified on the initial line. A concentrated Prandtl-Meyer expansion is put at the nozzle lip to match the exit and base pressures and the region near the lip is treated as a two-dimensional flow field. The expansion fan is subdivided into 10 equal intervals. It has been assumed that the plume is axisymmetrical and the calculation need only be carried out for the upper half plane. A consequence of this is that configurations at incidence cannot be treated.

Figure 100 shows the effect of the ambient pressure changes on the plume boundary. In one case, it is assumed that the ambient pressure is constant and equal to the base pressure, P_b, while in the other case the

assumption was made that the pressure recovers linearly from the base pressure to the reattachment pressure, P_r, at the axial location, $x/L = 0.2$. The deviations of the resulting plume boundaries are small close to the nozzle exit plane.

Figure 101 indicates how the plume boundary expands as the jet pressure ratio is increased. When combined with the strong interaction calculation procedure, a new plume boundary is determined at each step in the iteration after new values for the base and reattachment pressures are obtained.

The present calculation is only intended to provide the plume shape close to the body (at least as far downstream as the reattachment point) and no effort was made to develop the internal structure of the plume in any detail. The Mach disc and other shock situations arising inside the jet are not considered. This does not appear to be a limitation in the present application.

C. Concerning the Nature of the Interaction Flow

For a given forebody shape and given nozzle geometry it is clear that the flow in the interaction region will be a function of several parameters. Particular mention should be made of the jet to ambient pressure ratio, the free stream Mach number, the boattail angle and the Reynolds number. The influence of the latter parameter has not been greatly studied for the type of applications of present concern. It is well documented that there is a problem of great significance in wing and airfoil design [48] and some concern has been expressed in relation to aircraft engine nacelle and fuselage rear end design [67, 68]. Possibly for cases where the jet pressure ratio is large there is less interest in a Reynolds number effect and this will not feature in the present discussion; but some theoretical results will be outlined in a later section.

The experimental data obtained by Rubin [60] can be displayed as on Figure 102. Here, contours of constant base pressure are contained on a jet pressure ratio/boattail angle diagram. The nozzle geometry is fixed (exit to base diameter ratio = 0.45; exit angle = 20°). The design Mach number of the nozzle is 2.7.

Several features of this plot should be brought out. It is seen that each boattail configuration reaches a minimum base pressure as the thrust coefficient of the nozzle is varied. In addition, the value of this minimum base pressure increases as the boattail angle is increased but the value of jet pressure at which this condition is found changes very little. Fortunately, this minimum base pressure occurs at very low jet pressure ratio and is not of great concern in the present application. Physically the occurrence of this base pressure minimum implies that

50

when the jet is operating at low pressure ratio its influence on the base flow is similar to that of an ejector and entrains more mass from the dead-air region than does the intrinsic base flow process (jet-off case). The additional mass entrainment causes the free-shear layers to turn through a larger angle and hence reduce the base pressure. The effect of this additional mixing along the outer edge of the plume boundary is counteracted as the jet pressure increases with the consequent plume diameter increase. Futher increase in jet pressure ratio results in a monotonic increase of base pressure as the free-shear angle is reduced. But this process cannot continue indefinitely. At some point, the free-shear layer turns outward, instead of towards the axis of the flow, and the base pressure increases above the ambient value. From this point on, the conditions in the free-stream become more significant to the entire flow development.

Restricting the discussion to a flow with slightly supersonic free-stream conditions, it is clear that the outward turning of the free shear layer will sponsor a shock wave in the external flow. At this point the flow situation holds some analogy with that over a forward facing step with the step height parameter taking the place of the jet pressure ratio. Czarnecki and Jackson [69] have presented experimental results for such a flow and these data demonstrates that the two flows do have sympathetic characteristics.

For very small step heights (corresponding to a base pressure slightly above ambient), it is found that the external flow suffers an isentropic compression. For greater step heights, the external flow compresses under the classical shock-boundary-layer interaction process. In this latter situation the pressure signature ahead of the step shows a rapid rise in pressure followed by an essentially constant plateau pressure.

Returning to the plume flow, it is expected that as the jet pressure ratio increases to very large values then the base pressure would migrate to a limiting value which associates with the plateau pressure for the corresponding shock-induced separation at the given free-stream Mach number [70].

The base pressure contours in Figure 102 do not reveal this limit base pressure too clearly but the locus of points at which the external flow first shows separation is well defined. As may be expected, a lower jet pressure ratio is required to separate the flow from a larger angled boattail body. As was discussed in Reference 19, this trend continues for negative boattail angles (i.e., for flared bodies). Figure 104 shows the entire flow development for a given body as the jet pressure ratio is increased. Here, the free-stream Mach number is 1.1 and the boattail angle is 9.5°. The nozzle configuration is identical to that for the flows discussed in Figure 102. Both the minimum base pressure and the limit base pressure are displayed along with the changes in flow structure that ensue as the jet pressure ratio is increased.

51

The implication made above that the limiting base pressure related directly to the plateau pressure for shock-induced separation at the free-stream Mach number needs some qualification. As the data of Reference 70 indicated, this is a good statement for a parallel sided body. When the rear end is conical, however, the situation is a little more complex. This is due in part to the approach Mach number being different from the free-stream Mach number and in part to the three-dimensional nature of the flow.

Additional features of the flow become evident from consideration of Figure 103. The free-stream Mach number is 1.1 and is close to the local Mach number ahead of the boattail. At low jet pressure ratio, the Mach number approaching the base region will be supersonic and the confluence between the free-shear layer and the jet is enacted under a shock wave. The classical reattachment analysis adopted in the above theoretical development is essentially applicable. As the jet pressure ratio increases, however, the reattachment (or wake) shock bifurcates with the forward limb moving onto the body surface to play the role of the separation shock. The rearward limb passes on downstream. At these higher jet pressure ratio conditions, it is evident that the confluence is no longer taking place under an oblique wake shock with supersonic downstream conditions. Most probably the entire confluence interaction is subsonic in nature. On this basis, it is expected that the theoretical results for the flow at high jet pressure ratio and low supersonic free-stream Mach number will be less satisfactory.

Certain pertinent pressures are a strong function of Mach number, as has been demonstrated by the experimental work of Nash et al. [71] for the transonic flow over a rearward facing step. Figure 104 shows the variation of both the base pressure and the reattachment pressure with Mach number. The peak pressure occurring in the flow is also included. Very large changes in the pressure levels of these quantities are evident as the Mach number passes through the sonic condition.

The three basic types of interaction are shown diagramatically on Figure 105. For high subsonic Mach number flow there is a slow increase of pressure towards the separation point with the entire interaction length being quite large. The same is true when the approach Mach number is at a low supersonic value and the compression is isentropic. These two flows differ sharply from that which occurs when the interaction takes place under a shock wave. Typical experimental data for flow over a forward facing step is shown in Figure 106. Here it is found that the separation point is very close to the maximum pressure when the approach conditions are subsonic but moves forward to adopt a position close to the inflexion point in the pressure signature at supersonic conditions. The maximum pressure then takes over as a plateau value. Similar results are found for the surface pressures on a parallel sided body of revolution which is suffering plume induced separation (Figure 107). These data are again taken from Reference 60.

A correlation of the separation and plateau pressures was shown in Figure 93 and presents data for both subsonic and supersonic approach conditions. As seen from the preceeding, the subsonic separation condition passes over into the plateau condition for supersonic flow. The supersonic separation then takes place at a relatively lower level. Also included on that figure was some data for the limiting base pressure for various boattail configurations. The influence of the conical nature of the flow is very evident here for the way in which it dominates the level of the limiting base pressure. All the boattail data presented on Figure 93 was for the same nozzle configuration, but it should be recognized that the nozzle geometry does play a role in the detailed development of the entire interaction. A typical comparison for a parallel sided body is shown on Figure 108. These data shown in this figures does not extend to a sufficiently high jet pressure ratio to determine the effect of nozzle geometry on the limiting base pressure.

Some of the flow features discussed in this section have considerable impact on the development of a flow model; the component model discussed above in particular. The most pertinent of these relate to conditions in the separation and confluence regions of the interaction.

Models for flow separation under a small pressure gradient are not well established. This implies that the calculation procedure for the entire interaction may not be completely adequate in those situations where the flow compresses isentropically to the separation point. Typically this will occur in that region of the base pressure curve (Figure 103), where the base pressure is just a little above the ambient level. At this stage in the flow development, the compression waves are coalescing to form the forward limb of the wake shock. With further increase of jet pressure ratio, which causes a strengthening of the forward shock as it moves ahead onto the body, this condition will disappear.

At the same time as conditions near the separation point become less uncertain in their prediction, the confluence region deteriorates to a subsonic-like behavior. This difficulty is more acute for bodies with a large boattail angle. In principle, the subsonic reattachment process is no more difficult to discuss than is the supersonic one. The problem is more a practical one since appeal to oblique shock theory is then no longer valid. It is possible that the use of the 'small turning' approximation adopted herein is adequate for the flows under discussion provided the wake geometry is such that the small disturbance approximations make sense. Iteration between a numerical solution of the outer potential flow and an inner viscous flow may go some way towards improving these flow situations but a solution of the full Navier-Stokes equations is the long-term solution. What to do with the Reynolds stress tensor is then the question for discussion.

IV. CALCULATED RESULTS

Results from the calculation procedure for plume induced
separation as outlined above have been published in several places [13,
14, 19, 20, 21, 22, 24] and the significant features of the calculated
flow development will be outlined below.

A. Results for Bodies in the Absence of Fins

The predicted variation of base pressure with pertinent
parameters (jet pressure ratio, nozzle geometry, etc.) is a ready means
of assessing the validity of the calculation procedures.

As was reported in Reference 21, the nozzle geometry is an important
feature in the configuration design. These data shown in Figure 109
indicate the extent to which the nozzle geometry influences the varia-
tion of base pressure with jet pressure ratio (or equivalently, the thrust
coefficient). In this comparison the nozzle exit diameter ratio and the
nozzle exit angle are both varied. The nozzle exit Mach number was
within the range 2.7 - 3.0 and should not constitute a major variable in
the comparisons.

The effect of a single variable, the nozzle exit diameter ratio,
can be isolated as shown by the calculated results in Figure 110. For
a jet pressure ratio of 20, it is seen that the base pressure is less
than ambient for diameter ratios less than 0.9. The most interesting
feature of the curve is the existence of a minimum base pressure when
the nozzle exit diameter ratio is close to 0.2. This would appear to be
another manifestation of the ejector effect that was discussed in con-
nection with the base pressure minimum in Figure 102. The agreement
shown between theory and experiment in this situation is satisfactory.
In both Figures 109 and 110 the data shown are for a parallel sided
afterbody.

The large changes in base pressure that result from changes in
nozzle exit diameter ratio are reflected in the drag of the body. The
theoretical drag prediction is shown in Figure 111 where the minimum
base pressure is returned as a maximum in the drag cofficent variation.
The total drag is also a strong and complex function of the Reynolds
number and this subject will be taken up later. In cases where the rear
end is conical, the drag changes are also more complex due to the surface
pressure changes that are reflected as a boattail drag. Again, details
of the drag breakdown will be discussed later.

The variation of base pressure with increased jet pressure ratio is
well predicted for a parallel sided body, as is shown in Figure 112,
except in the intermediate thrust range where the base pressure is just
a little greater than the free-stream value. This relates to the problems

discussed earlier of predicting the flow separation under a mild pressure gradient and the difficulties that present themselves when the reattachment process reduces to that of a subsonic flow.

Figure 113 shows a comparison between the predicted and measured base pressures for a body with a 6.5 degree boattail. This result is somewhat disappointing at the higher jet pressure ratios since the theory shows a far greater rate of attainment of the limiting base pressure than is found experimentally. Further work is needed in this area.

B.   Concerning the Forces on the Body

1.   The Body Drag. The drag of a body with a given geometric configuration and free-stream Mach is a function of two parameters; the Reynolds number and the jet pressure ratio. The Reynolds number affects the flow in two ways. First, there is the expected reduction in skin friction coefficient as the Reynolds number increases, and second, there is a complex interaction with the base flow due to the changed initial conditions at the start of the interaction. In this connection there is a strong cross-influence with the second parameter-the jet pressure ratio.

The total drag is composed of several components each of which is a function of both Reynolds number and jet pressure ratio. In the present theoretical development, where there is no second-order iteration between the inviscid flow and the strong interaction, the form drag of the forebody is not influenced by changes in either of these parameters at 0 incidence. The other form drag components are influenced by variations in both parameters. The skin friction is also a function of the jet pressure ratio when this is sufficiently large to move the separation point onto the body.

Typical drag characteristics are presented on Figure 114 which shows the variation of total drag with Reynolds number for several values of jet pressure ratio. For low values of this parameter, it is seen that the total drag behavior is very reminiscent of that resulting from the variation of skin friction with Reynolds number. At high thrust coefficient, however, the situation is significantly different with the total drag coefficient exhibiting a maximum at a Reynolds number of about one million. As will be seen, this drag reduction at low Reynolds number is a consequence of plume induced separation moving onto the body, as the initial conditions due to the different boundary layer development with Reynolds number takes place. In all of these calculations the location of the transition point has been held constant at the shoulder of the ogive forebody. In a practical situation, it is expected that the transition point would also be dependent upon the Reynolds number, but probably not too greatly due to the favorable pressure gradient along the nose of the body.

In a practical situation it is not likely that the transition point would change its location significantly. It should be noted, however,

that the base pressure can be strongly influenced by changes in boundary layer conditions at the start of the interaction. The data presented in Figure 115 shows the calculated base pressure for an axisymmetric back step as a function of the ratio of boundary layer momentum thickness to step height. The free-stream Mach number is again 1.1.

The total drag distributions shown in Figure 114 are broken down into their several components in Figures 116 and 117. Figure 117 for a jet pressure ratio of only 20 is not of great interest and merely shows that the total drag change is mainly a consequence of the skin friction variation with Reynolds number under these conditions.

Figure 117 shows the breakdown of the total drag between its various components when the jet pressure ratio is 100. The situation is now more complex and the discussion will present the flow development as the Reynolds number is decreased. At this value of jet pressure ratio the base pressure is already close to the separation value (being greater than the ambient value, it generates a thrust on the base) and increases slowly as the Reynolds number decreases. Then, as the Reynolds number reduces below 1 million, there is a rapid increase in base pressure to the plateau value as the separation point moves forward onto the body. The extent of the separation, when present at these lower Reynolds numbers, is shown in Figure 118. The presence of the separated flow region also has an influece on the skin friction drag (Figure 117). For values of Reynolds number above 10^6 there is the expected increase of friction coefficient as the Reynolds number decreases. Once separation occurs on the body, however, the forward movement of the separation point is sufficiently rapid to cause a reduction of the friction drag component.

The combined effect of the forward movement of the separation point and the increased base pressure causes an increase in the pressure level over the boattail. This has the effect of reducing the boattail drag. If the Reynolds number were reduced further so that the whole boattail was at the plateau pressure, then there would be no further decrease of boattail drag.

These data shown in Figure 118 is important in its practical implications: once the separation point leaves the base of the body, it moves forward very rapidly. This fact will have severe consequences in relation to the stability and controllability of the body. An additional point should also be made concerning the Reynolds number variation. Provided the flow is not too close to the separation critical conditions, then it is not too sensitive to Reynolds number (other than the readily predictable change due to skin friction) and no scaling problems between test and flight should be evident. However, if the flow is in the separation critical region, then only a very small Reynolds number change can be responsible for a vast change in the flow configuration. Then it is imperative that testing be carried out at the correct Reynolds number for a realistic estimate of stability and controllability characteristics. It can be noted that a factor of 2 in Reynolds number can cause a forward movement in the separation point of about 15% of the body length; the same order as the chord length of the control fins.

56

An additional comment concerning the drag of a body is also of interest. Figures 119 and 120 plot the drag components against boattail angle for a constant jet pressure ratio. In general terms it is found that the total drag is reduced as the boattail angle is increased. This is mainly due to the reduced pressure drag caused by the boattailing. At very small boattail angles, it is the influence of the boattailing on the base drag that causes the total drag reduction while at higher angles it is the boattail pressure itself that is responsible for the drag reduction. The base drag changes for two reasons, one a consequence of the changing base pressure with boattail angle and the other due to the reduced base area.

2. The Normal Force and Pitching Moment. Figures 121 and 122 show the normal force and pitching moment calculated for the MCDAC body (see Appendix B) at a Mach number of 1.0. These calculations are for a body alone without either fins or propulsive jet.

As can be expected, the agreement betwen theory and experiment is quite good for both the lift and pitching moment under these conditions. A more revealing test of the method is when a large jet pressure ratio plume is present.

No comparisons have been made for the drag of the configuration in the present instance since the test model was sting mounted and the computer program is not complete for the discussion of such flow situations. This work will be completed in the near future.

C. Other Considerations

Besides such quantities as the base pressure and forces on the body, there is also interest in the length of the interaction and the size of the plume. A detailed study of these has not been made, mainly due to the lack of experimental data. The only available data are in the form of Schlieren photographs of which Figure 123 is an example. It is also clear that the interaction geometry is not too well defined from such evidence. For comparison, however, the theoretical estimate of the flow shown in the Schlieren photograph is also included on this figure. The disposition of the wake shock does not feature in the theoretical solution and a comparison of this item is not possible.

The geometry of the flow in the confluence region is shown in Figure 124 for the 6.3° boattail body and 2 values of jet pressure ratio. The free-stream Mach number is 1.1. When the jet pressure ratio is only 50 then no separation occurs on the body and the confluence takes place within one base radius distance downstream of the nozzle exit plane. For the higher jet pressure ratio where separation is present, then the confluence point has passed further downstream. The length scale of the interaction in the streamwise sense is considerably greater than that across the flow. This is both in conformity with the usual concept of

57

the small turning approximation that was adopted in the confluence region.

A locus showing the movement of the confluence point as the jet pressure ratio is increased is shown in Figure 125. In this case the body has a 3.2° boattail. Of interest here is the fact that for small jet pressure ratios, there is very little downstream movement of the confluence point. The jet expands almost to the base diameter before the confluence point shows any marked movement in the downstream direction.

From the interaction geometries shown on these figures, it is clear that under most situations the two shear layers are in quite close proximity along most of the "dead air" region. This somewhat reduces the validity of the asymptotic free shear layer concept used in the estimation of the shear layer development. Another feature has been absent in the discussion of the base flow and this concerns the effect of roll on the flow. The work of Reference 74 suggests that rotation of the body can have an effect on the base pressure, due presumably, to the different mixing rates that occur when cross flow is present in the shear layer. The data from Reference 74 are shown in Figure 126 and indicates the effect of rotation. At low rotation speed, it is seen that the base pressure increases, it then reaches a maximum and finally decreases rapidly with further increases in rotation speed.

Similar changes in the mixing rate of the free shear layers could be expected as a result of the wake from the fins, particularly if they have a flow separation. Since the boundary layer on the fin has not been discussed in the present work, no statement can be made about the likely effect of this.

D. Plume Induced Separation of a Finned Body

A few calculations have been carried out to show the effect of fins on the flow in the base region and they were reported in Reference 24. Again, the treatment is not rigorous since the flow was determined along various azimuthal lines with the neglect of a cross flow component.

The procedure is as follows: the surface pressure distribution is calculated on the body with proper allowance for the effect of the fins (within the restrictions of the fin body theory used) and this pressure distribution is used to determine the plume interaction at a given azimuthal location. Thus, the presence of the fin is included only as far as its local effect on the streamwise development of the boundary layer, and any cross flow perturbation is neglected. For small fin loading situations, this may well be an adequate treatment of the problem. It should also be noted that the downstream effect of the fins is neglected; the free shear layer mixing does not acknowledge the presence of the fins in any way. Again for small fin loading this may not be a serious limitation.

Within these limitations, the effect of a fin configuration on base pressure can be assessed from Figures 127 and 128. First, in Figure 127, is the potential flow pressures on the base plane for a 2° angle-of-attack, with and without fins. These base pressures are all very close to the ambient pressure. The effect of the plume interaction is shown on Figure 128 and it is evident that the contribution from the fins is minimal under the conditions of this example.

V. CONCLUSIONS AND RECOMMENDATIONS

This report has outlined the theoretical development of a practical technique for the estimation of the behavior of bodies of revolution in transonic flight. The effects of both fins and a propulsive jet have been considered and results presented. It is felt that as an engineering tool the techniques laid down are an adequate statement of the state-of-the art. Care should be taken, however, not to construe this remark as one of complacency. There is still much to be done in the area of strong interaction aerodynamics.

Thus, in several key areas relating to the separation and reattachment process, appeal has been made to empiricism. This empiricism has been based, in many instances, on a very narrow range of data and could very well be lacking in regard to general applicability. A completely numerical solution to the full Navier-Stokes equations is the only long-term endeavor that is likely to provide satisfaction.

STRONG
VISCOUS
INTERACTION

FIN
CONFIGURATIONS

BOUNDARY LAYER DEVELOPMENT

CYLINDRICAL BODY

REAR—END
GEOMETRY

PLUME FROM
PROPULSIVE JET

FORE—BODY SHAPE
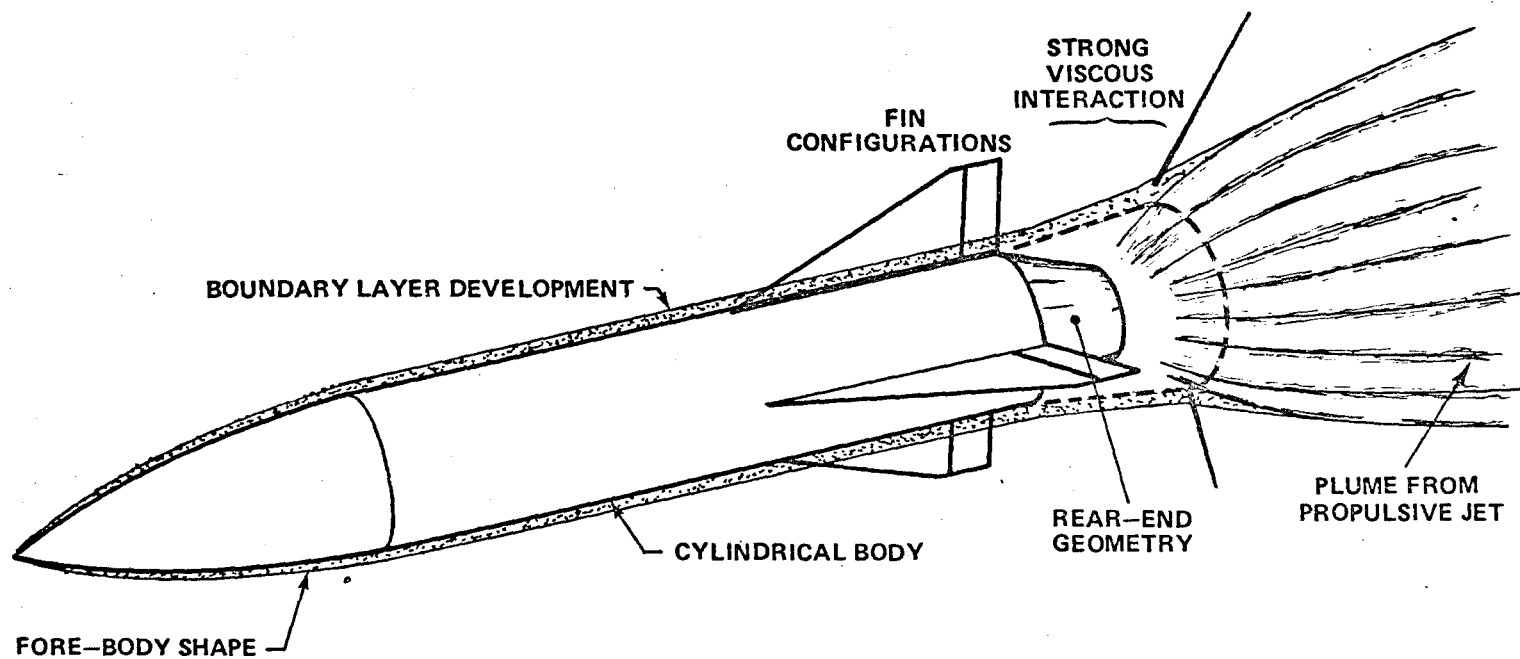
Figure 1.   Outline of flow configurations.
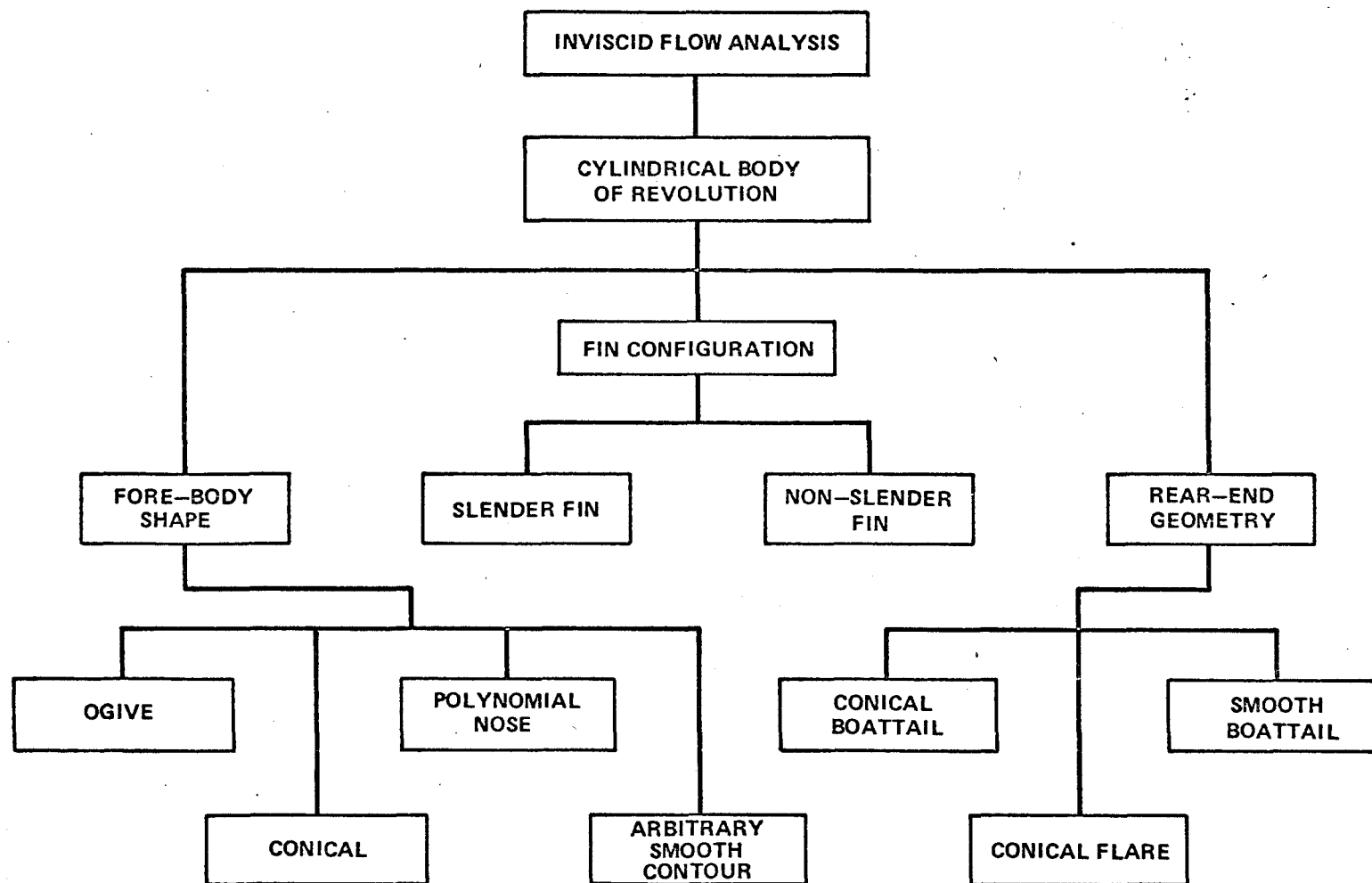
Figure 2. Summary of appendages to the cylindrical body of revolution that are addressed in the inviscid flow analysis.
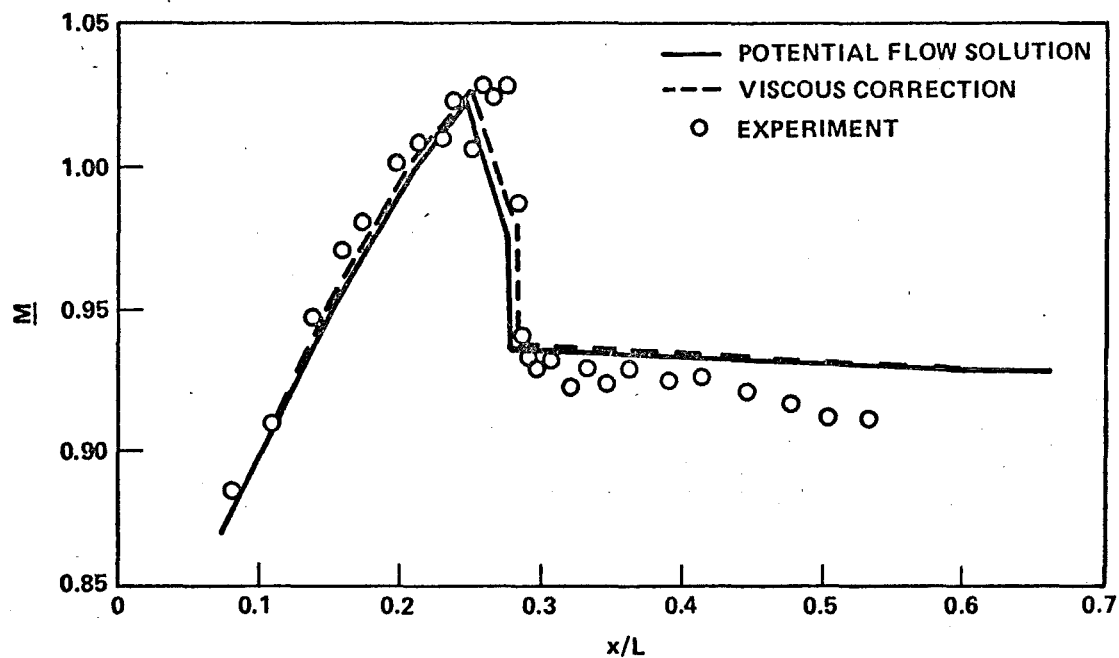
Figure 3. Transonic flow calculation with viscous flow correction for ogive-cylinder compared with MICOM data, $M_\infty = 0.975$, $Re = 1.2 \times 10^6$/ft, total body length = 32.5 in.
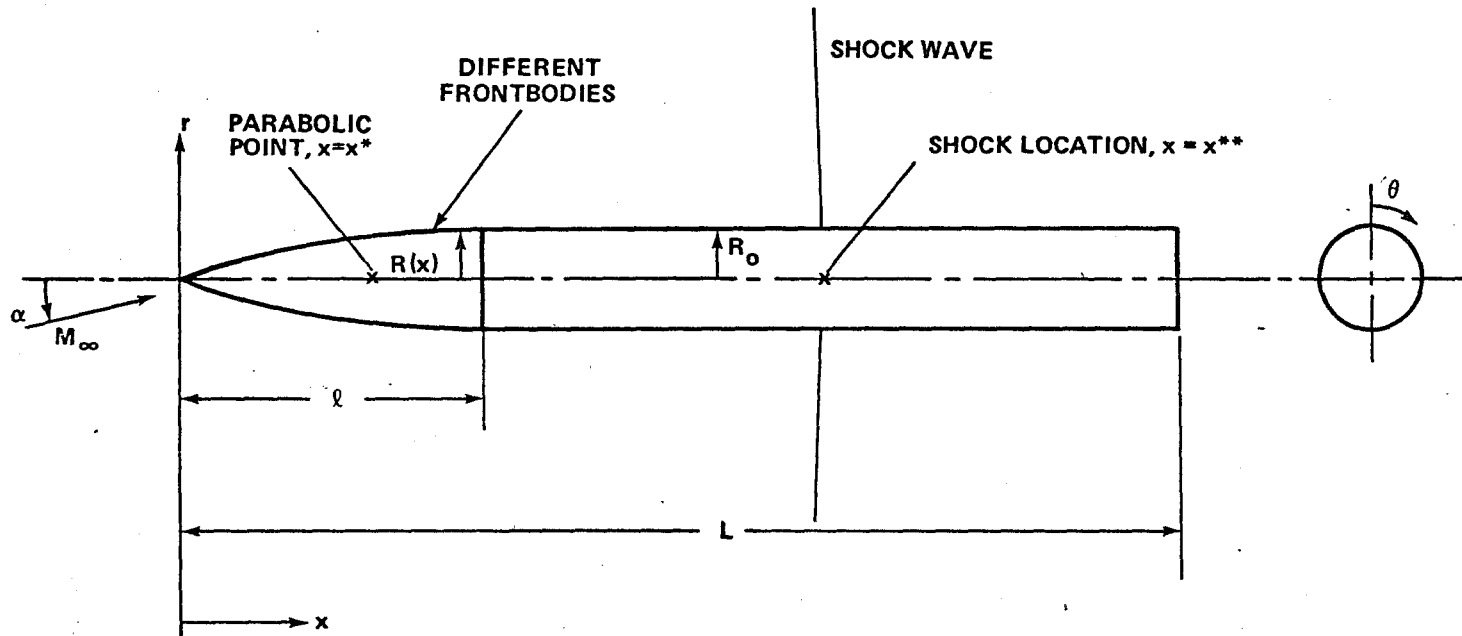
Figure 4. Nomenclature for smooth shaped forebody-cylinder configuration.

Figure 5. Shifting of parabolic point and shock
wave location for various Mach numbers.
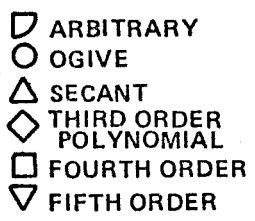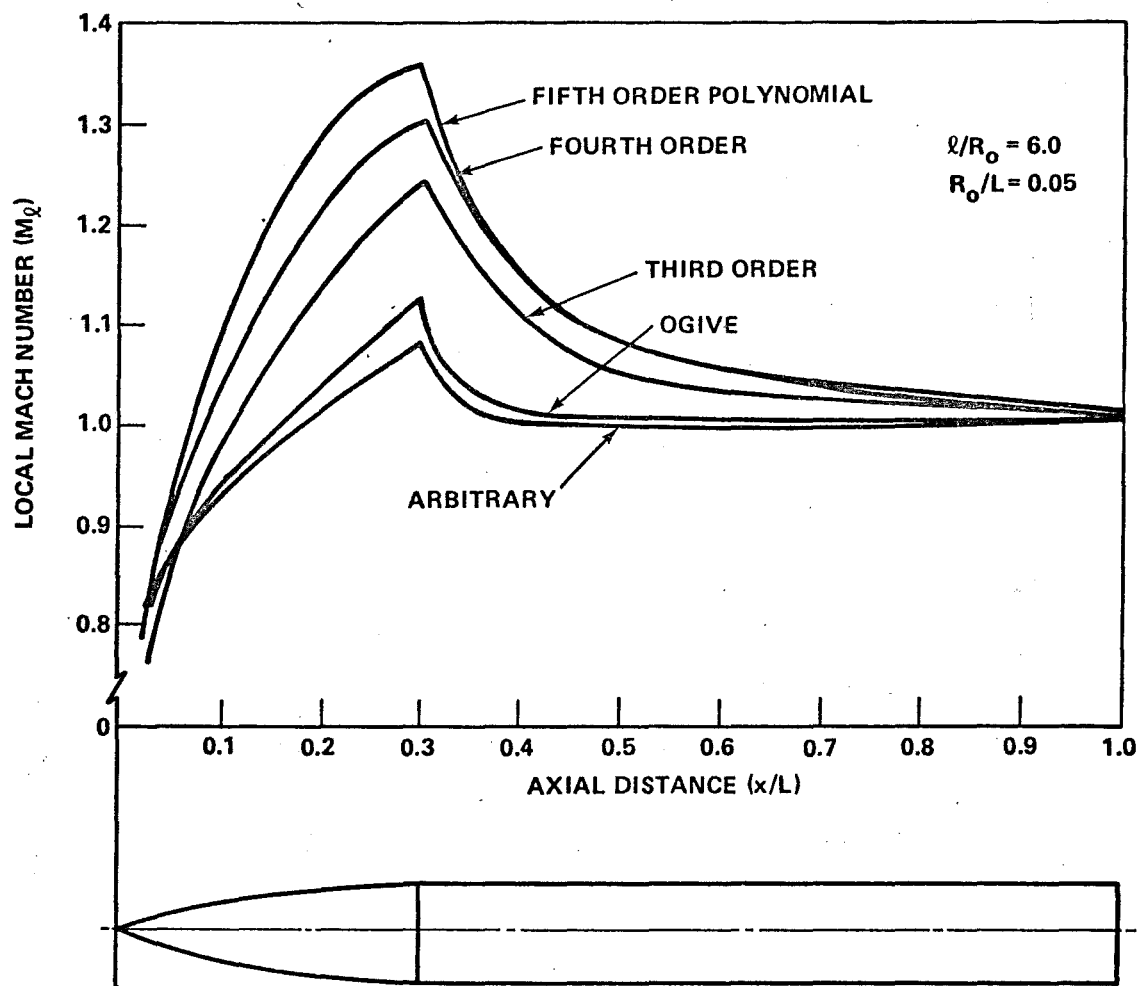
Figure 6. Local Mach number distribution for various
bodies at $M_\infty = 1.0$.
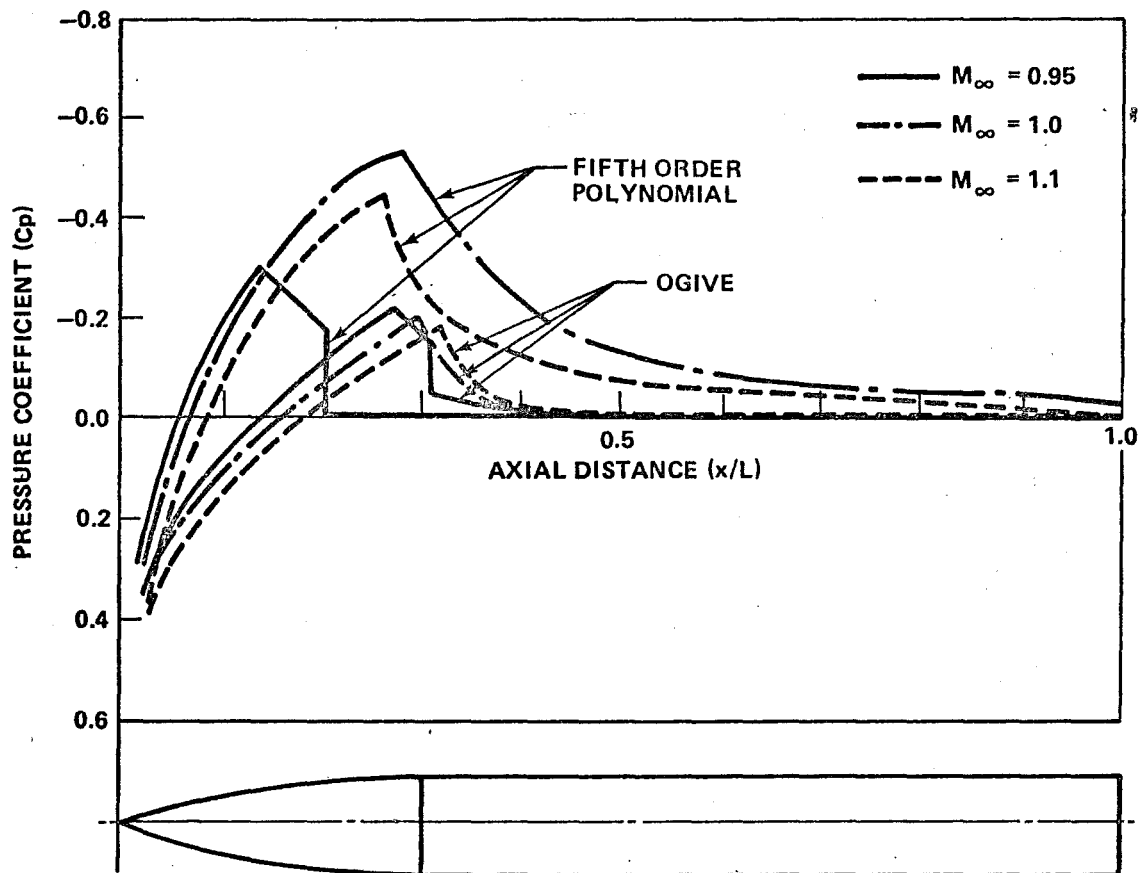
Figure 7.   Effect of free-stream Mach number on the surface
pressure distribution for fifth order polynomial body
and for the ogive-body.
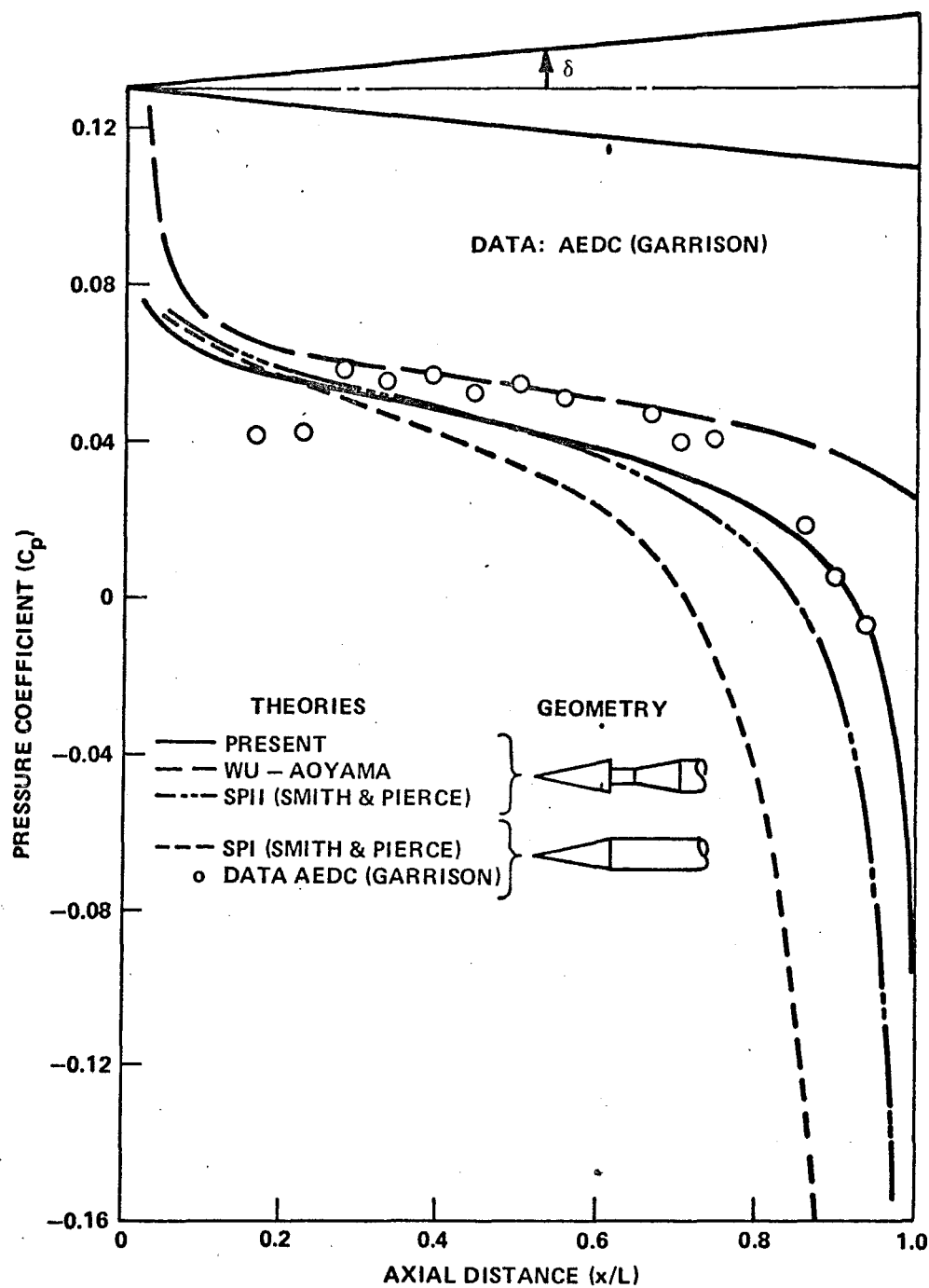
Figure 8. Comparison of present transonic cone solution
with data $\delta = 5°$, $M_\infty = 0.95$.
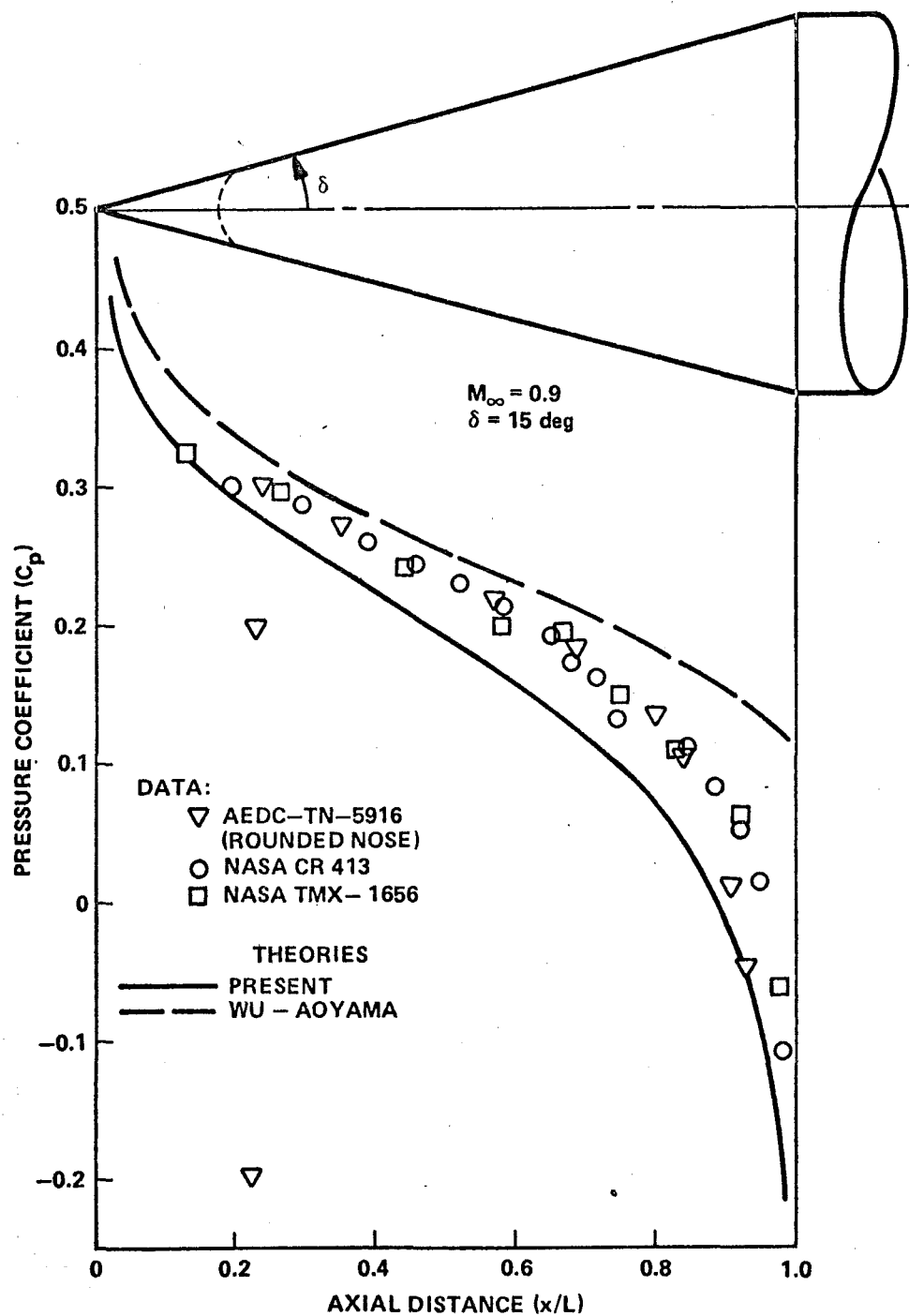
Figure 9. Comparison of present method
with data for a blunted cone.
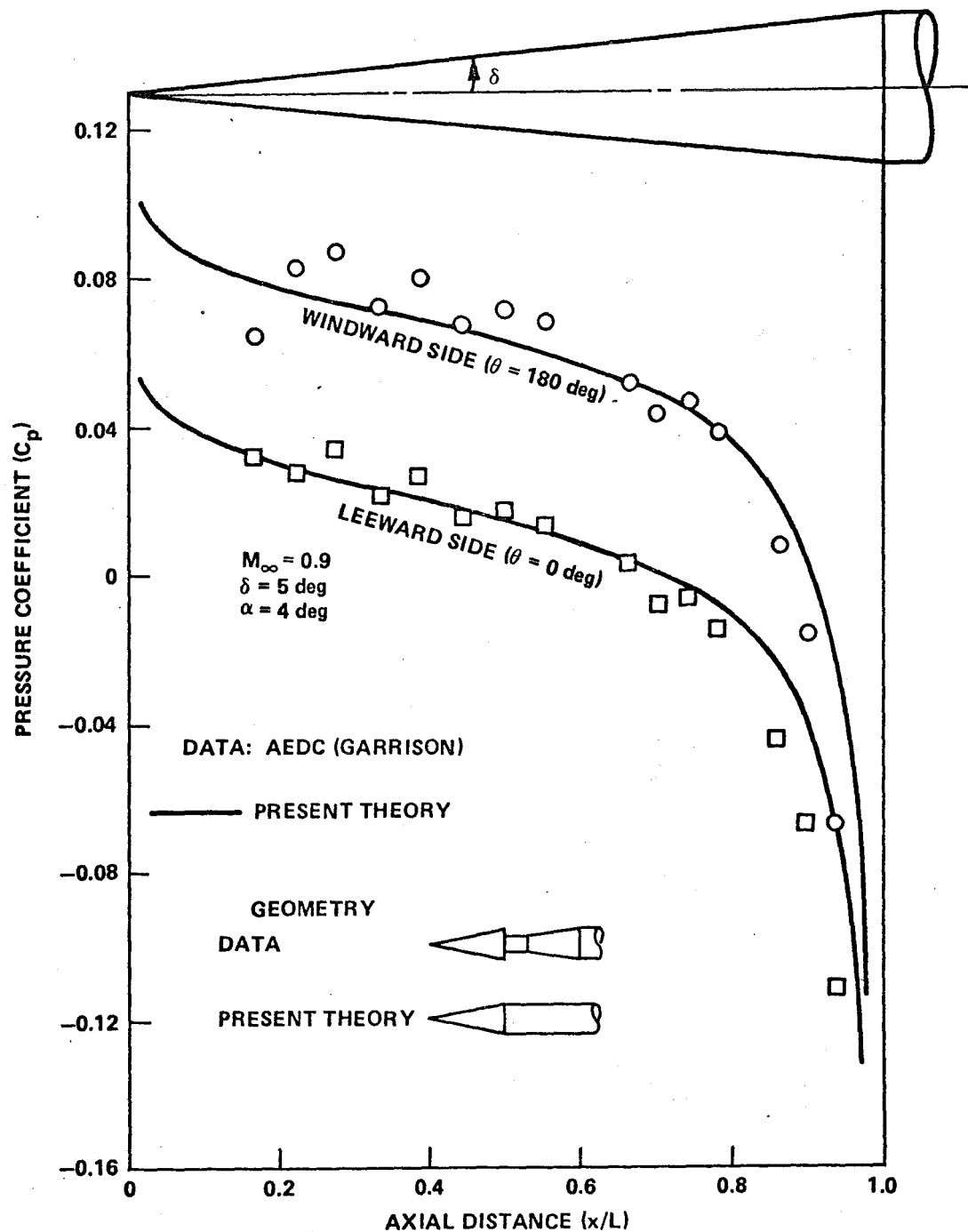
Figure 10. Surface pressure distribution for a sharp cone at a 4° angle-of-attack.
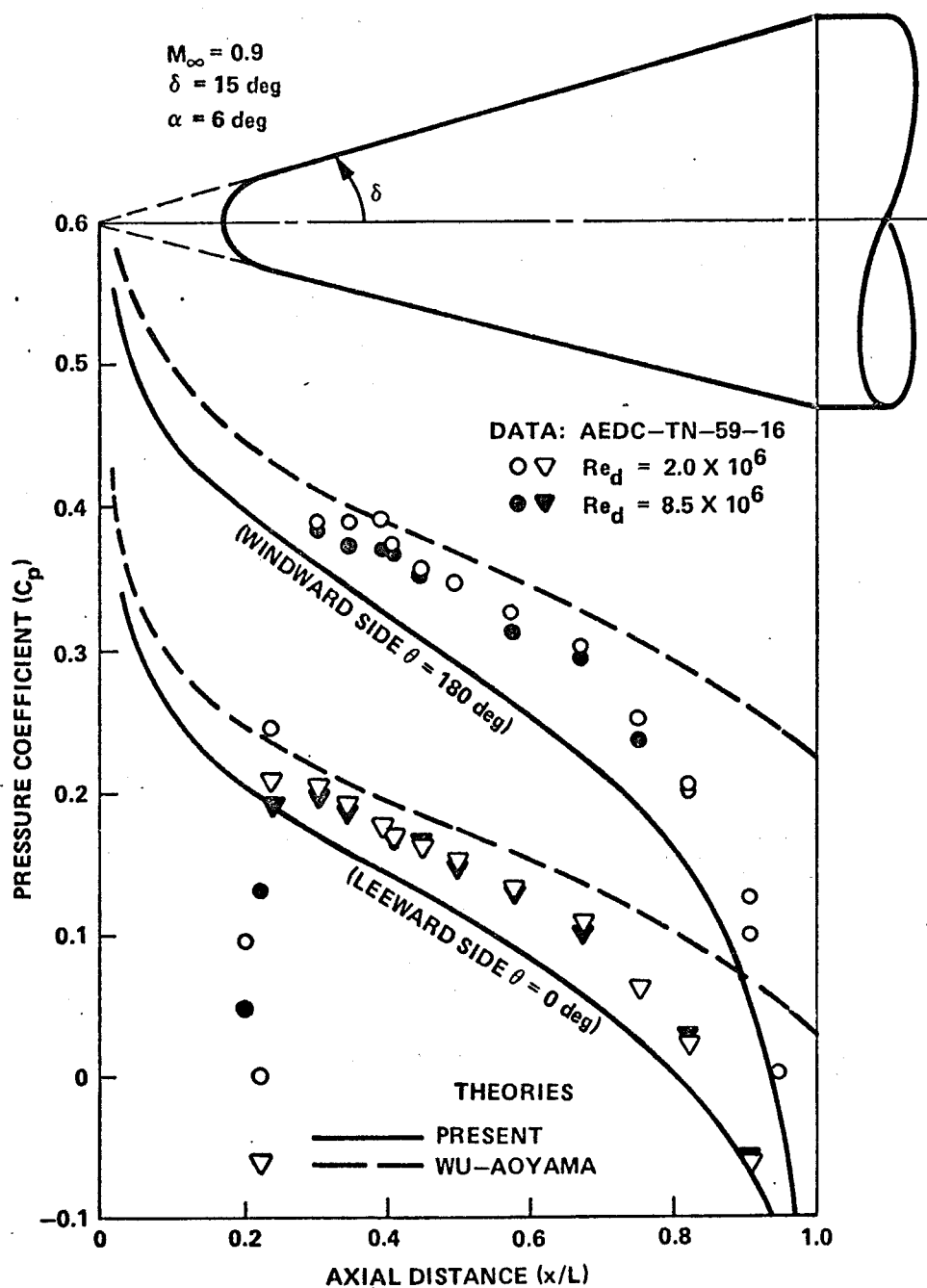
Figure 11. Surface pressure distribution for a blunted
  cone at a 6° angle-of-attack.
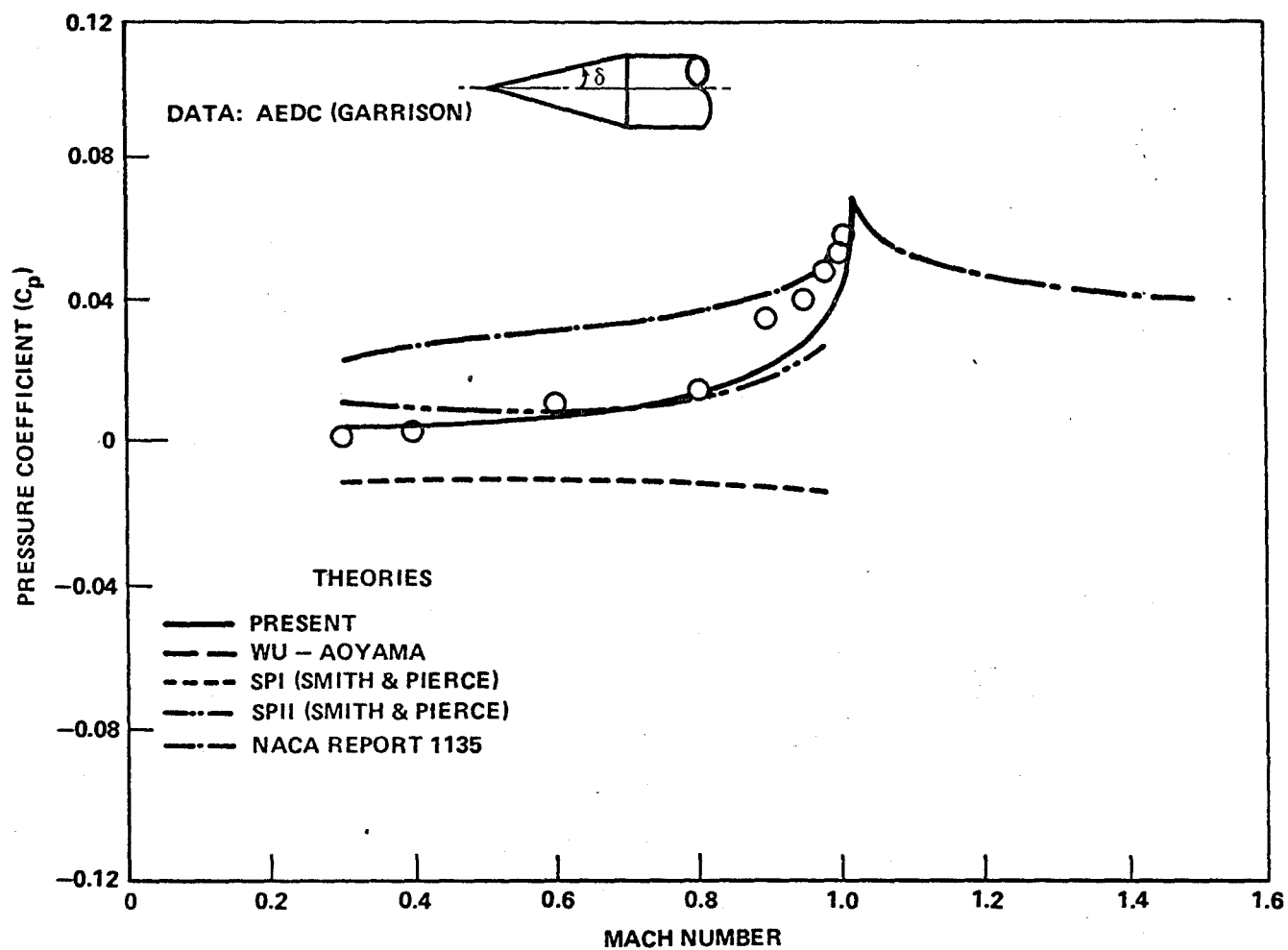
Figure 12. Flow over a conical forebody δ = 5°.
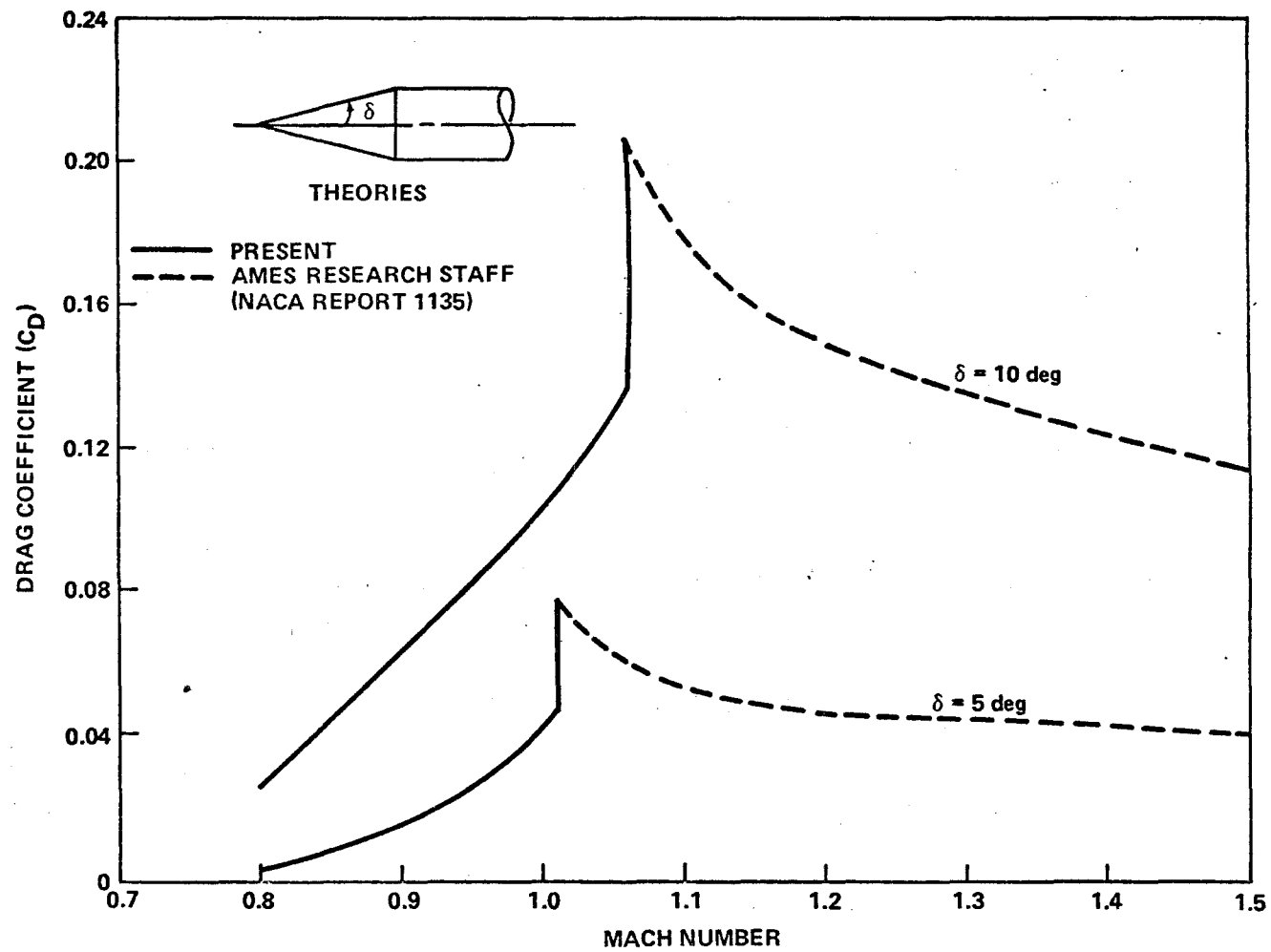
Figure 13. Comparison of pressure drag with Mach number (present method).

δ = 6.541 deg
α = 0 deg
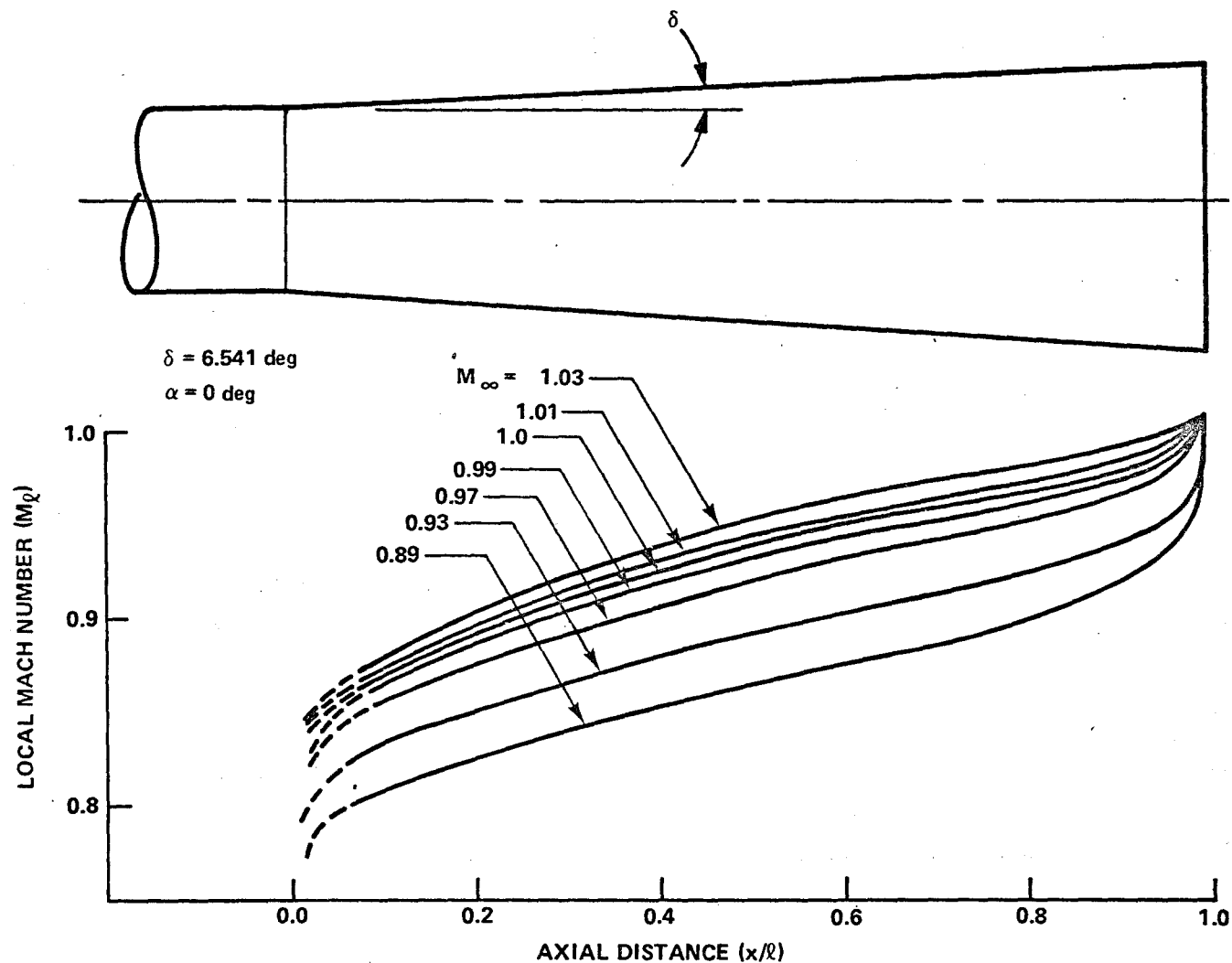
Figure 14.   Local Mach number distribution on the surface of a flare
for various free-stream Mach numbers near M_∞ = 1.0.
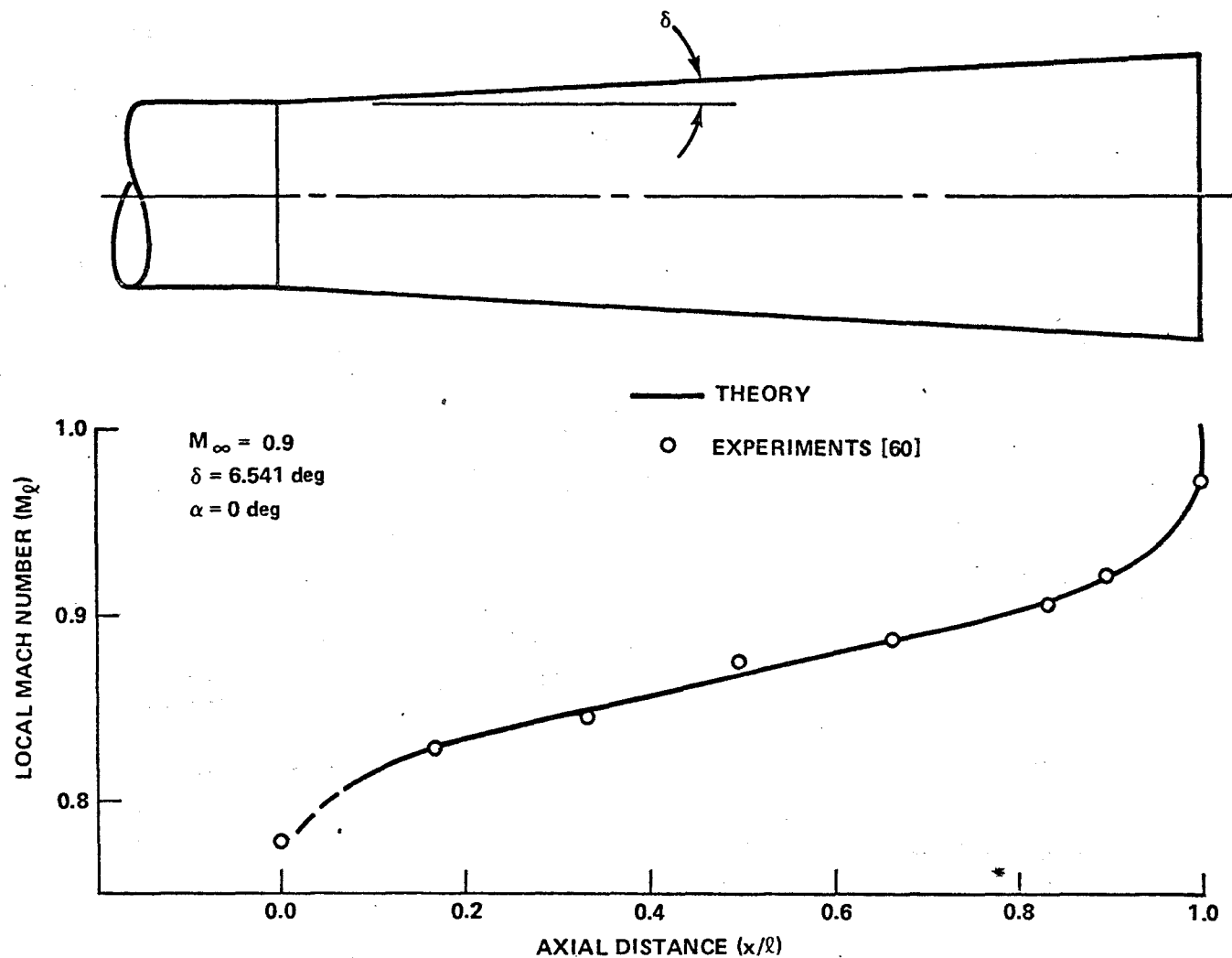
Figure 15. Comparison of theory with data for flared body
with conical angle $\delta = 6.54°$ at $M_\infty = 0.9$.
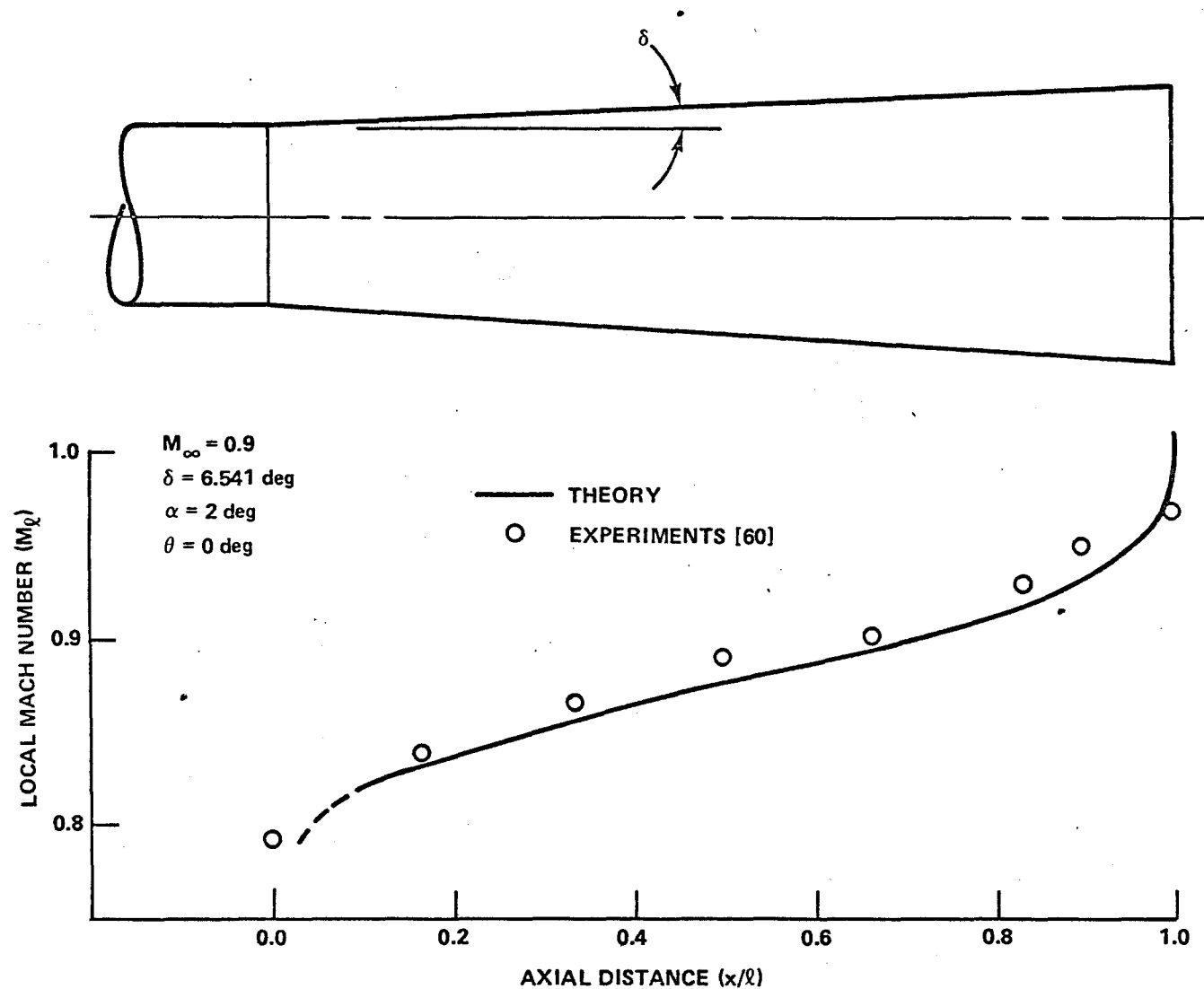
Figure 16. Comparison of theory with data for flared body with angle of attack at α = 2° and M∞ = 0.9.
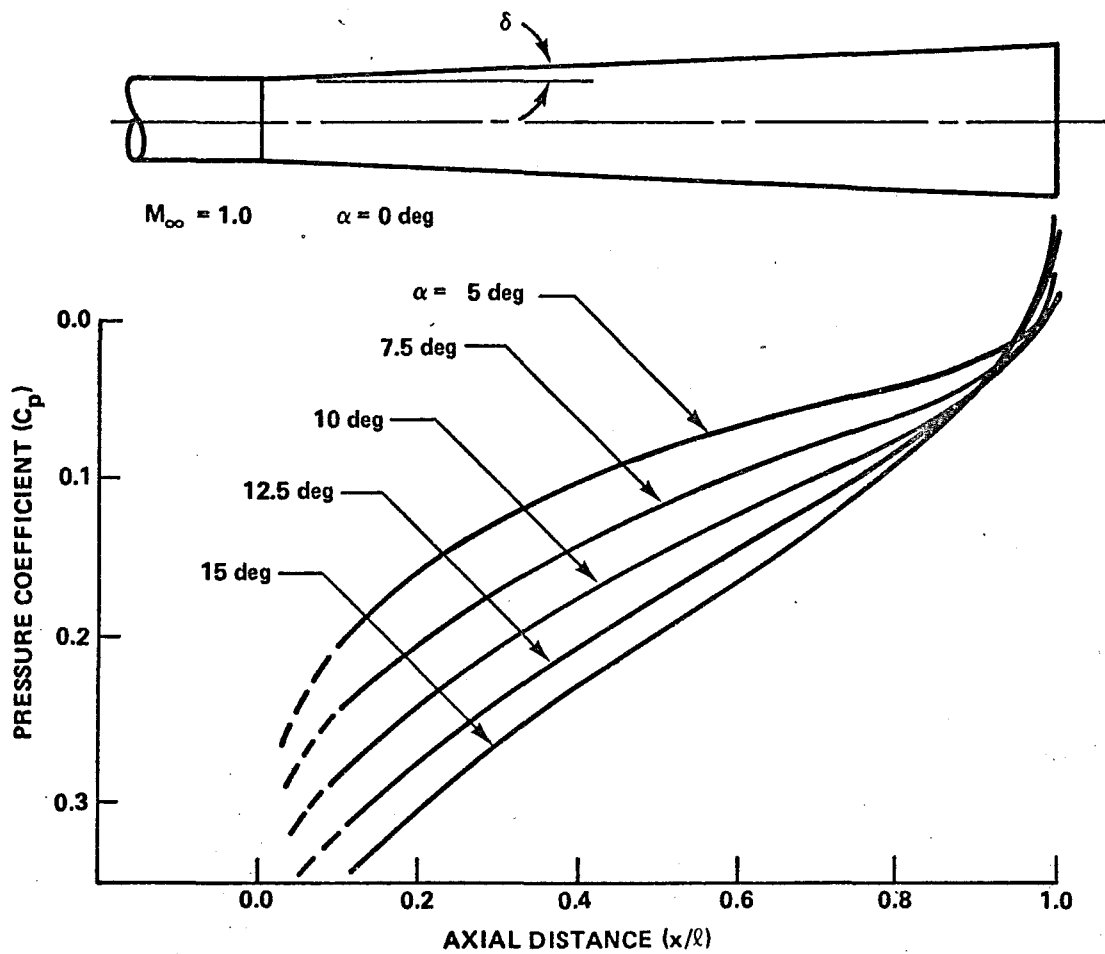
Figure 17. Variation of pressure coefficient for various flare angles δ at M_∞ = 1.0.

76
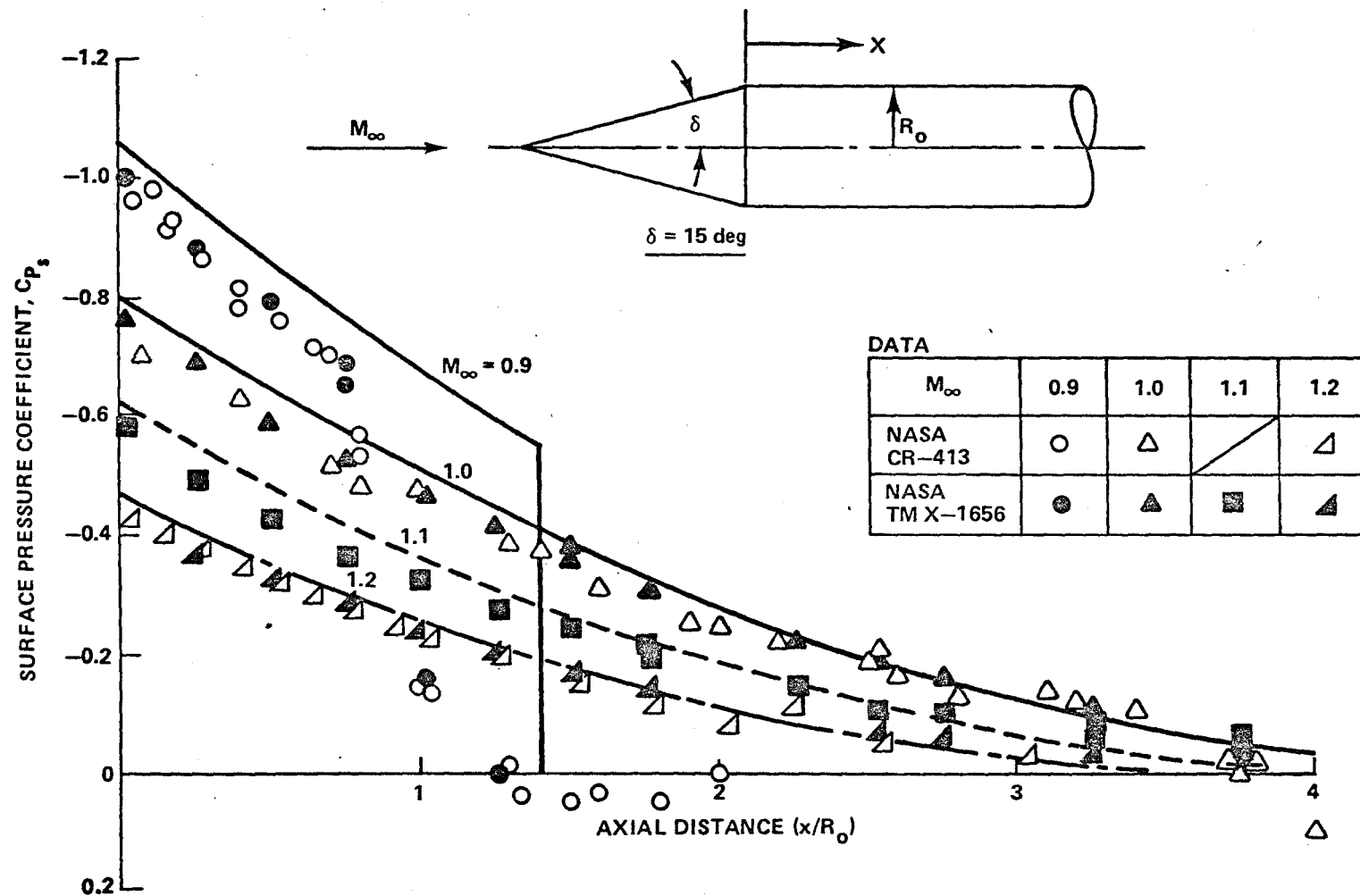
Figure 18.   Comparison of transonic similarity solutions with data
for 15° half-angle conical nose body.
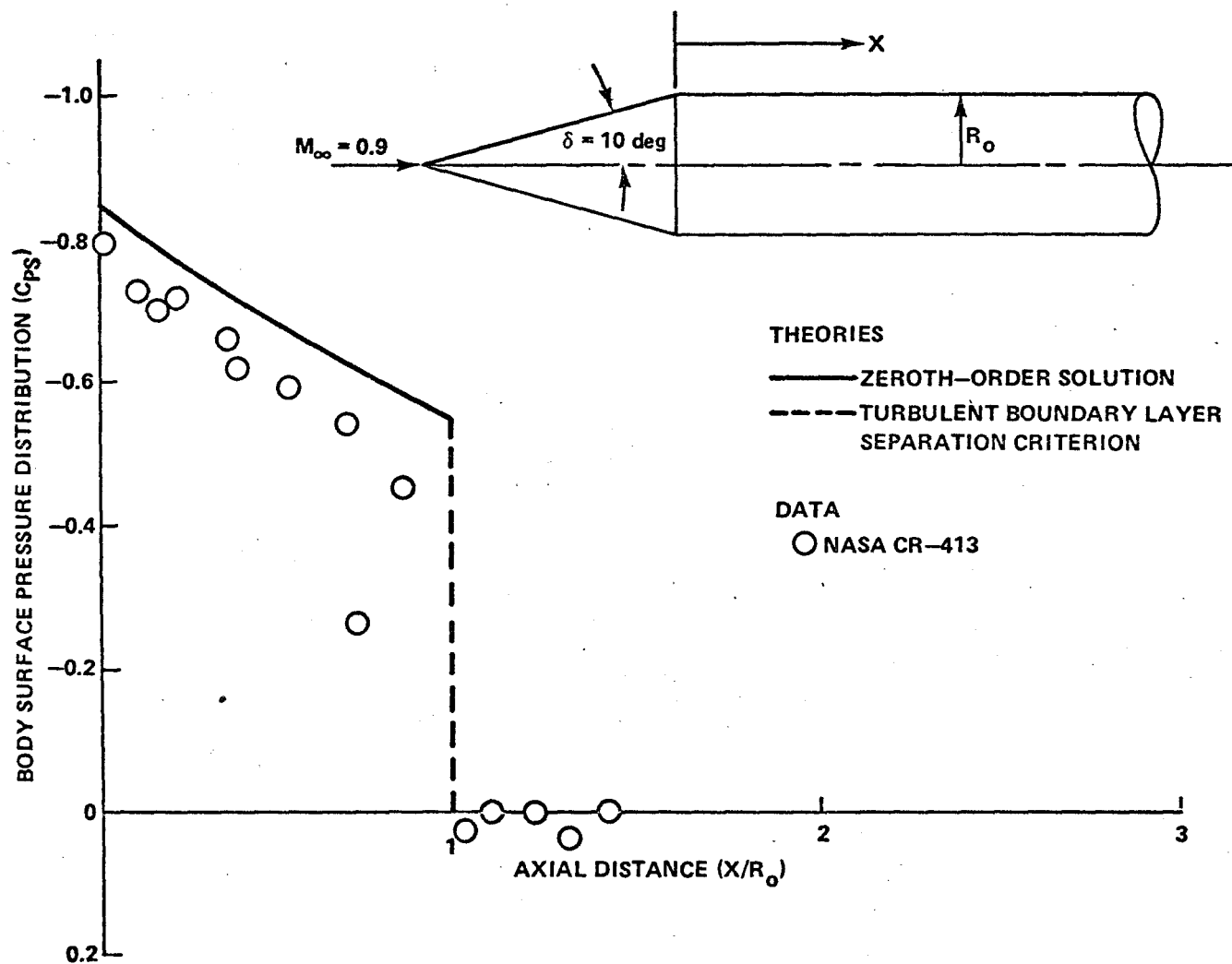
Figure 19. Comparison of zero-order transonic similarity solutions with data for 10° half-angle conical forebody at Mach number 0.90.
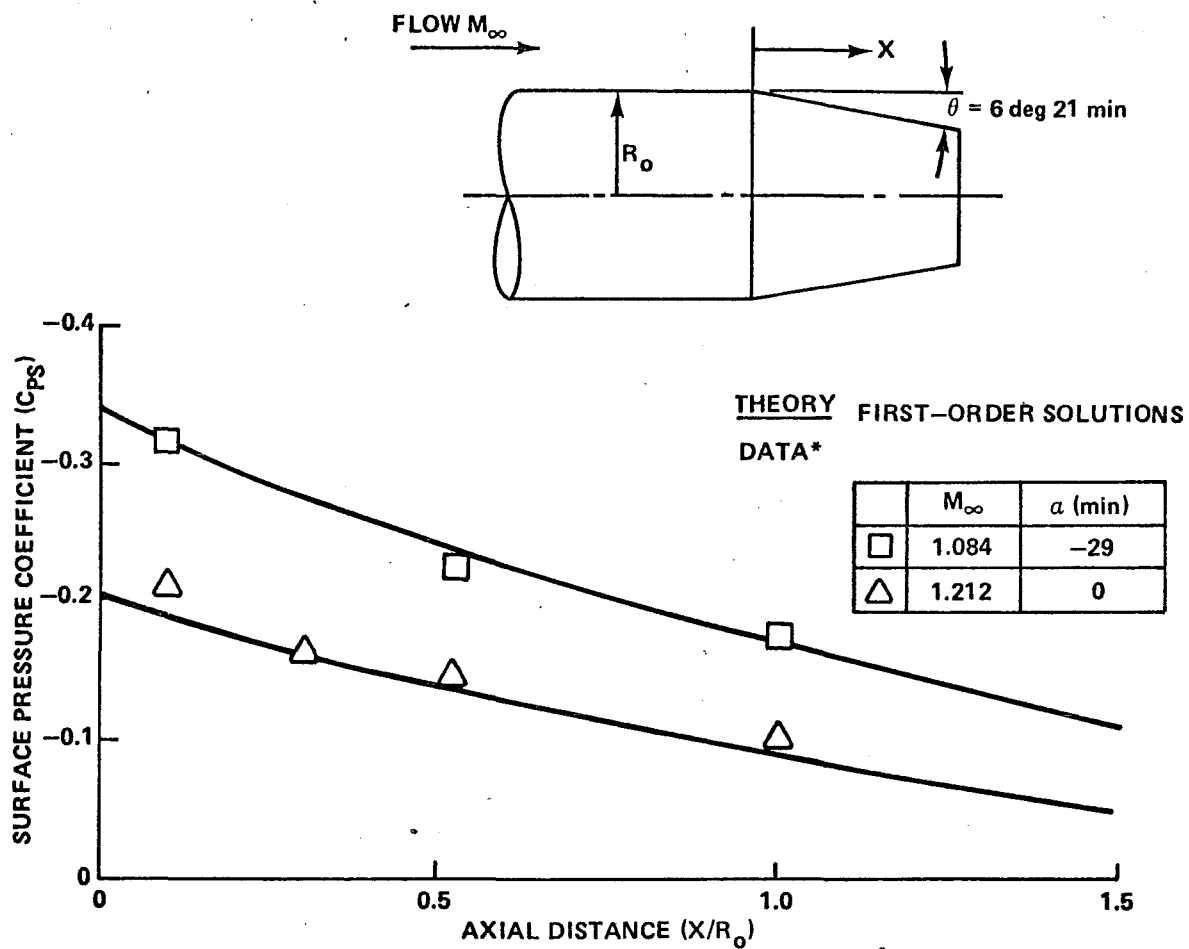
Figure 20. Transonic similarity solutions for boattail with various Mach numbers.
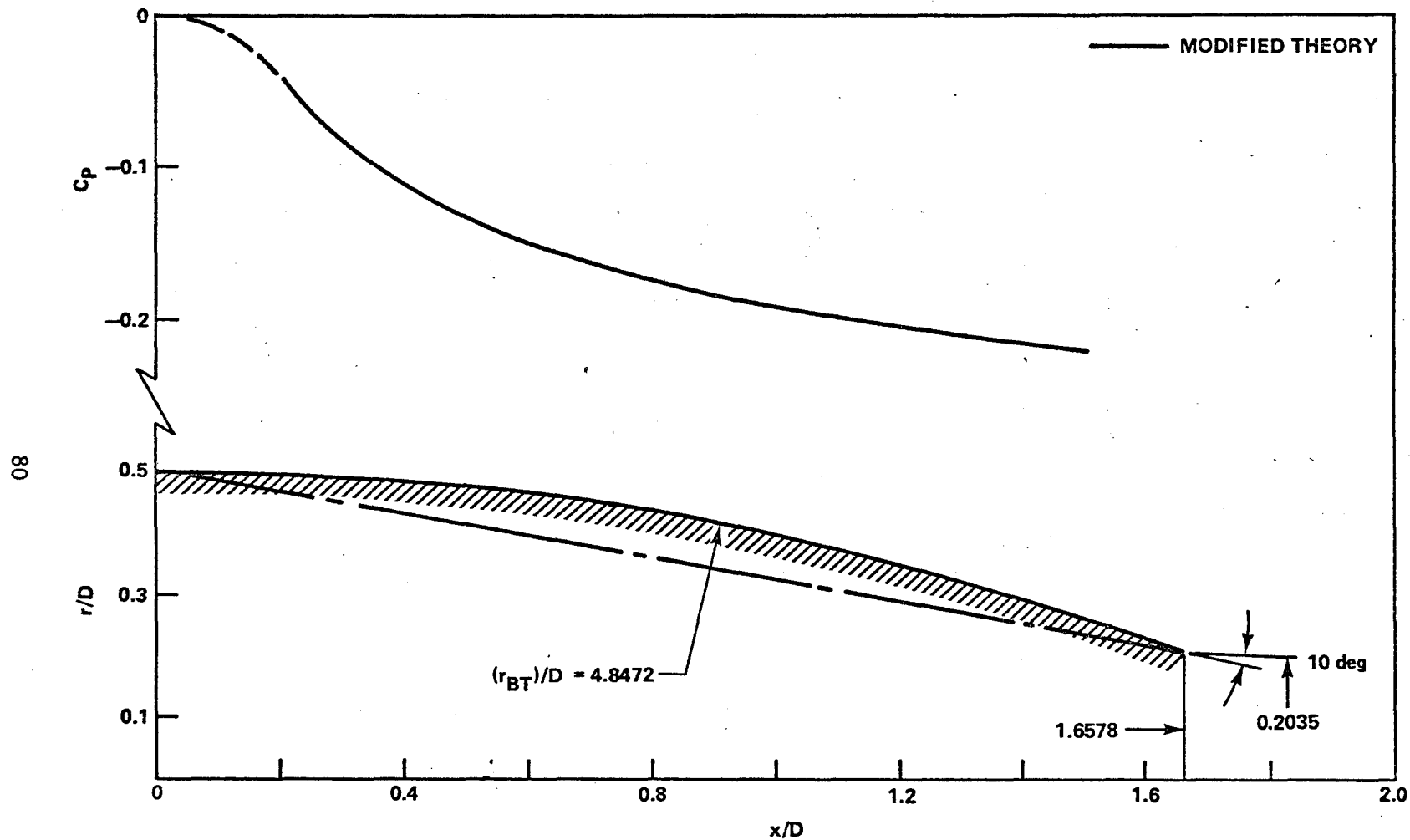
Figure 21. Modified conical boattail program to a smooth-shaped boattail for surface pressure distribution.
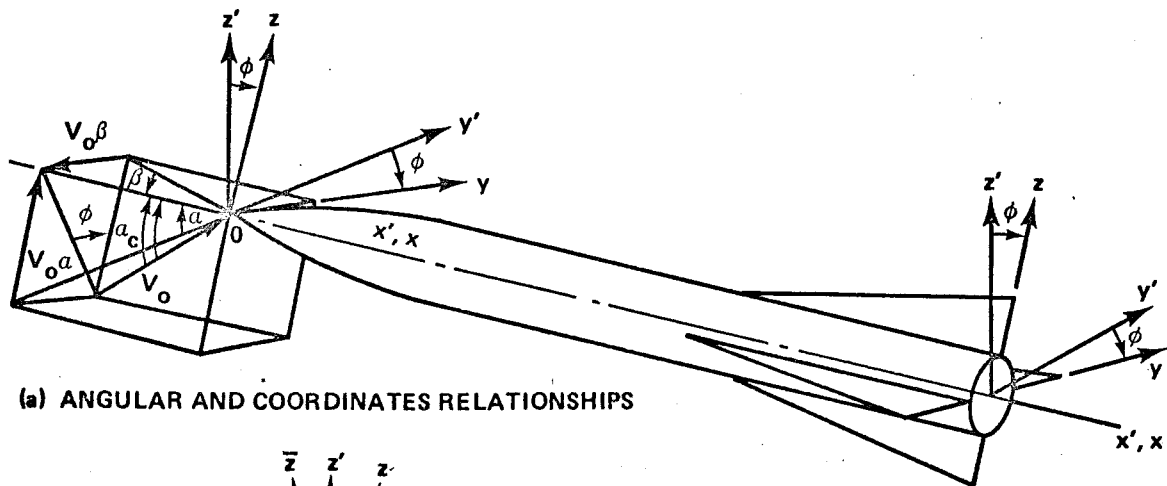
(a) ANGULAR AND COORDINATES RELATIONSHIPS
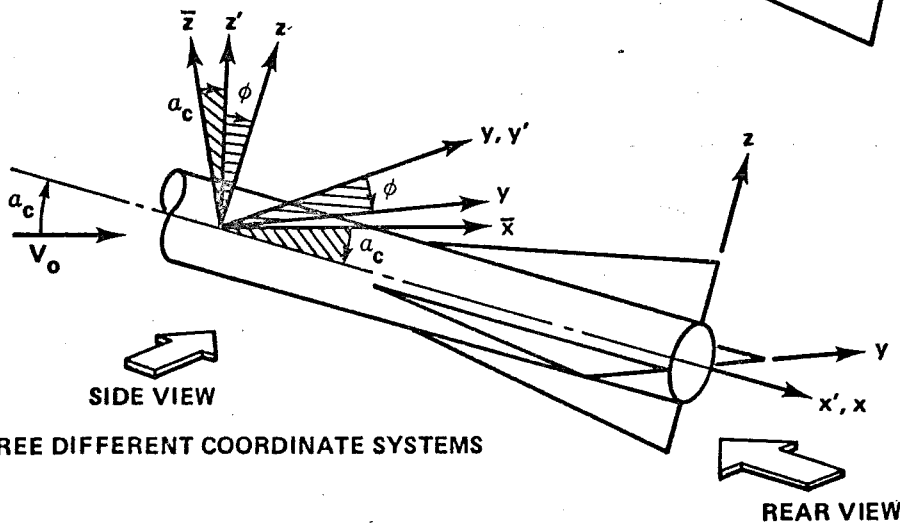
(b) THREE DIFFERENT COORDINATE SYSTEMS

SIDE VIEW

REAR VIEW
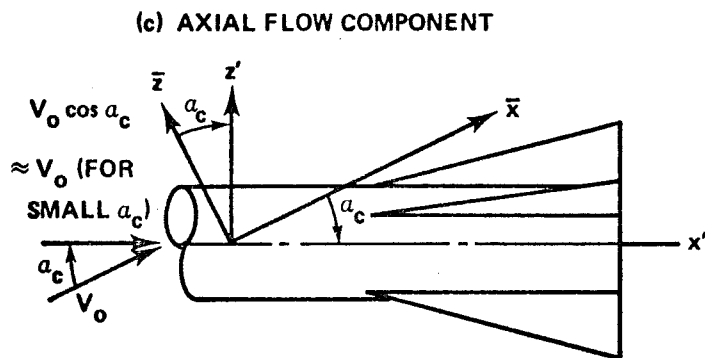
(c) AXIAL FLOW COMPONENT

(d) CROSS FLOW COMPONENT

$V_o \cos a_c \approx V_o$ (FOR SMALL a_c)

$V_o \sin a_c \approx V_o a_c$ (FOR SMALL a_c)
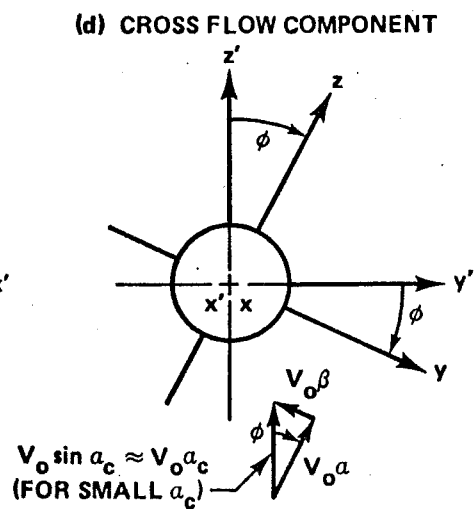
Figure 22.   Uniform flow over fin-body combination and coordinate systems.

81

SIDE VIEW

REAR VIEW
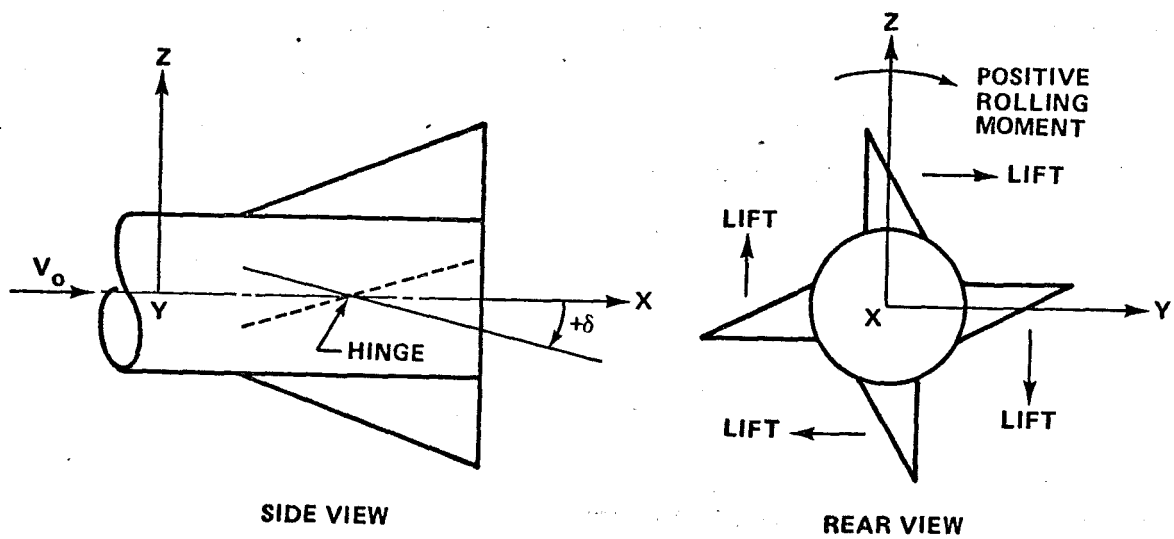
Figure 23. Definition of cant angle.
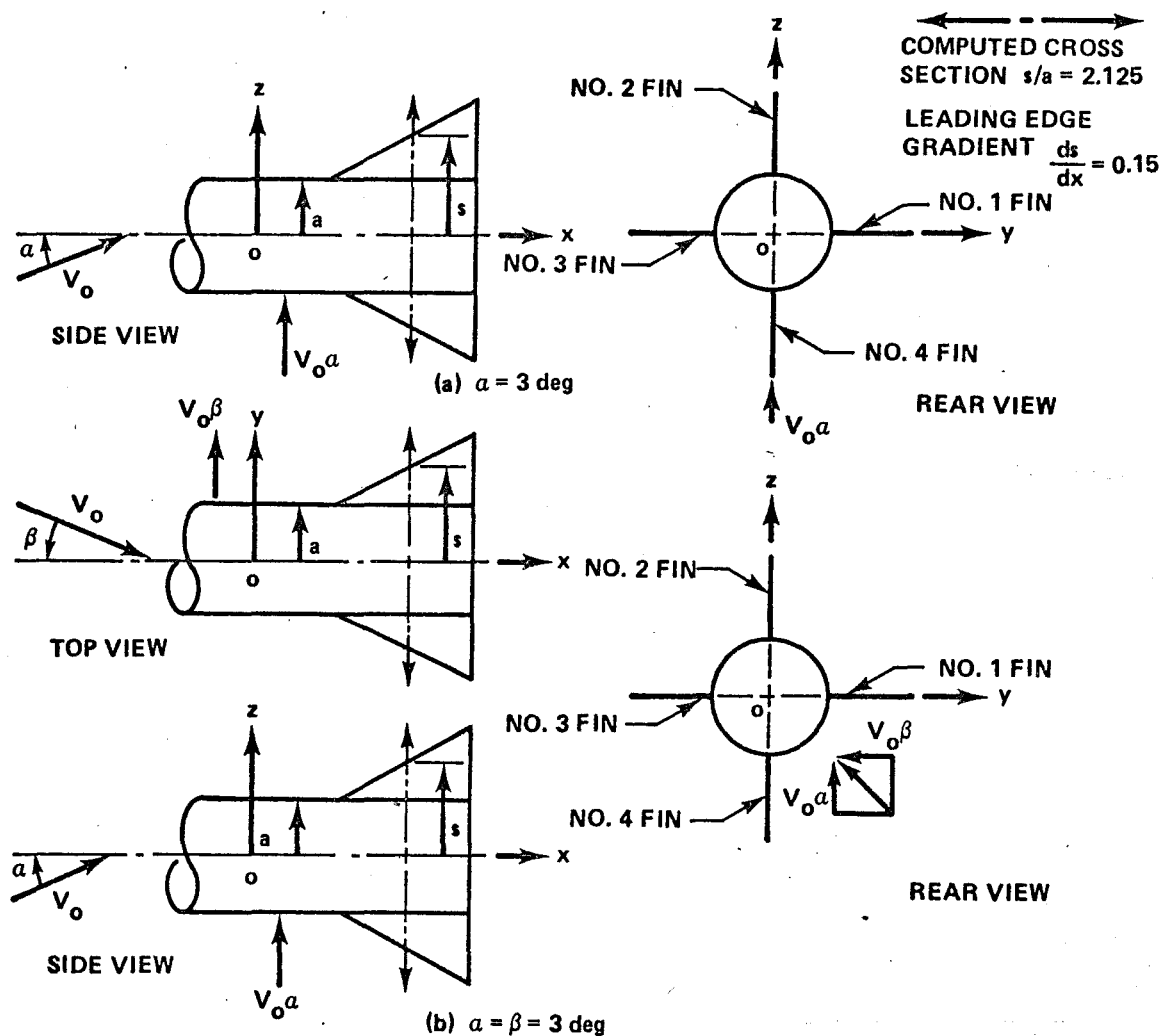
Figure 24. Computational model used in Section II.B

SIDE VIEW

REAR VIEW

TOP VIEW

(a) ALL CANT FINS CASE (−δ = 3 deg)

SIDE VIEW

(b) CANT HORIZONTAL FINS CASE (−δ = 3 deg)

COMPUTED CROSS SECTION
s/a = 2.125
LEADING EDGE GRADIENT
ds/dx = 0.15
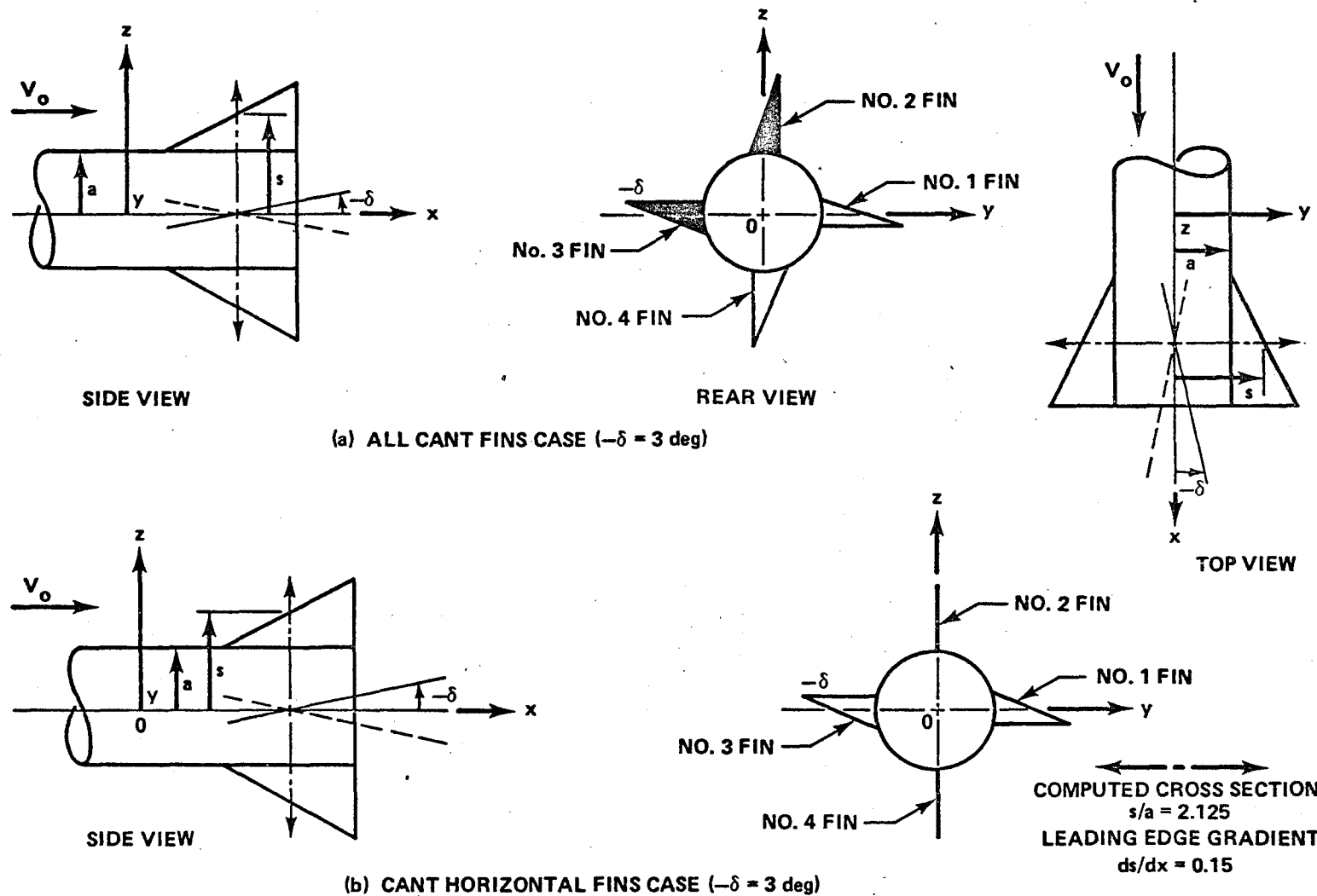
Figure 25.   Computational model used in Section II. C.

84
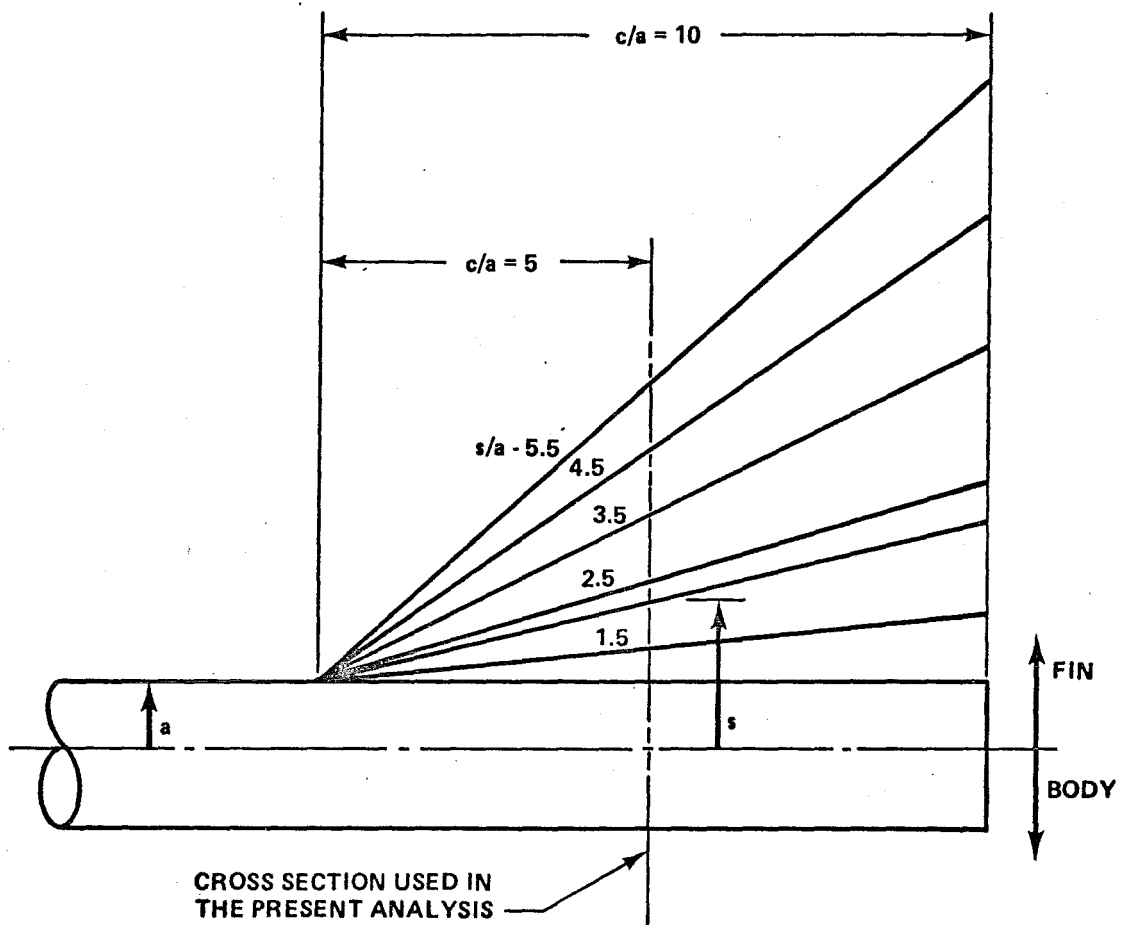
Figure 26.   Computational model used in Section II. D.
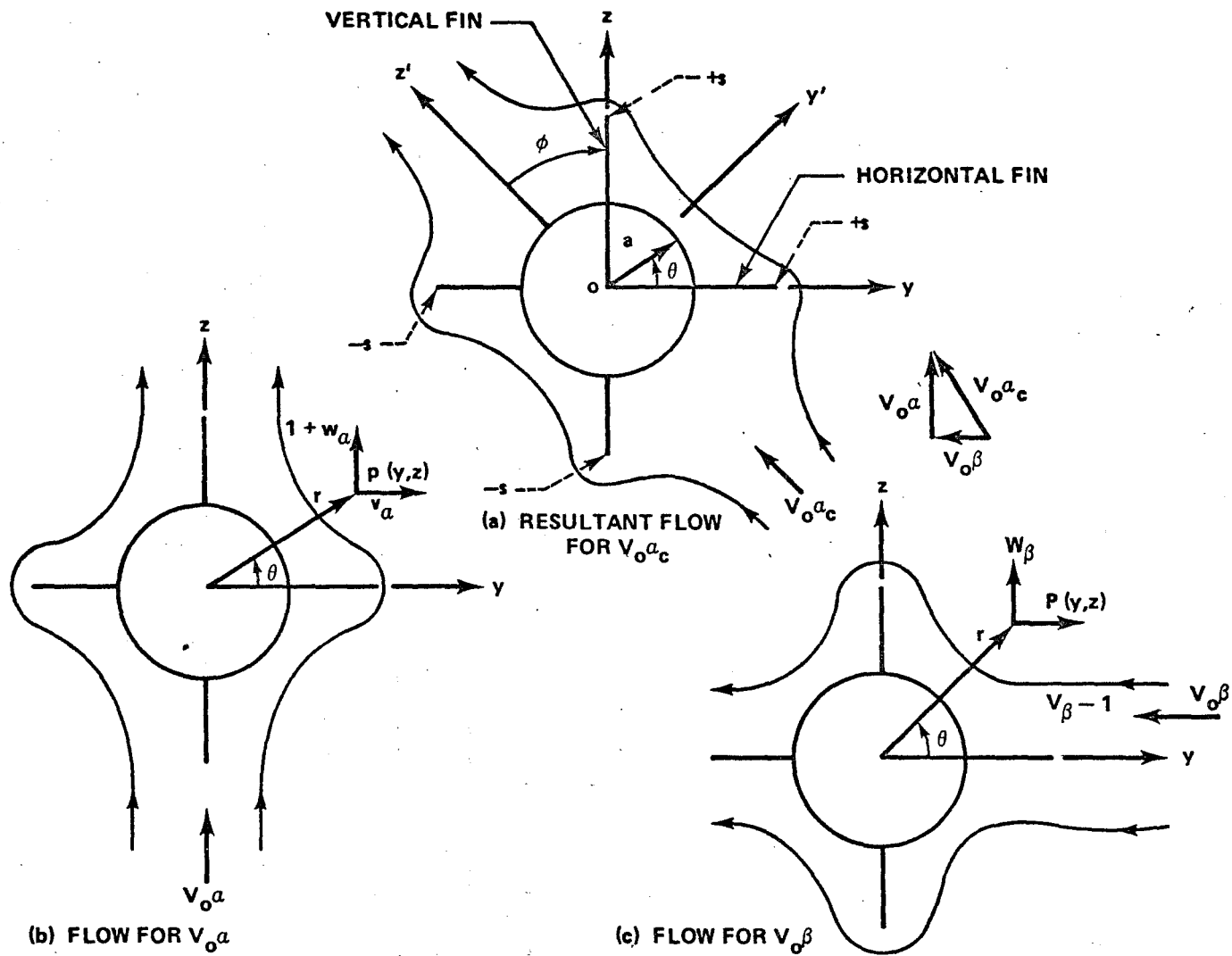
Figure 27. Resultant flow and decomposed flows.

$$x^2 + \frac{a^4}{x^2} = 2\left(\sigma^2 + \frac{R^4}{\sigma^2}\right)$$

$$x = y + iz$$

(a) x - PLANE

(b) σ — PLANE
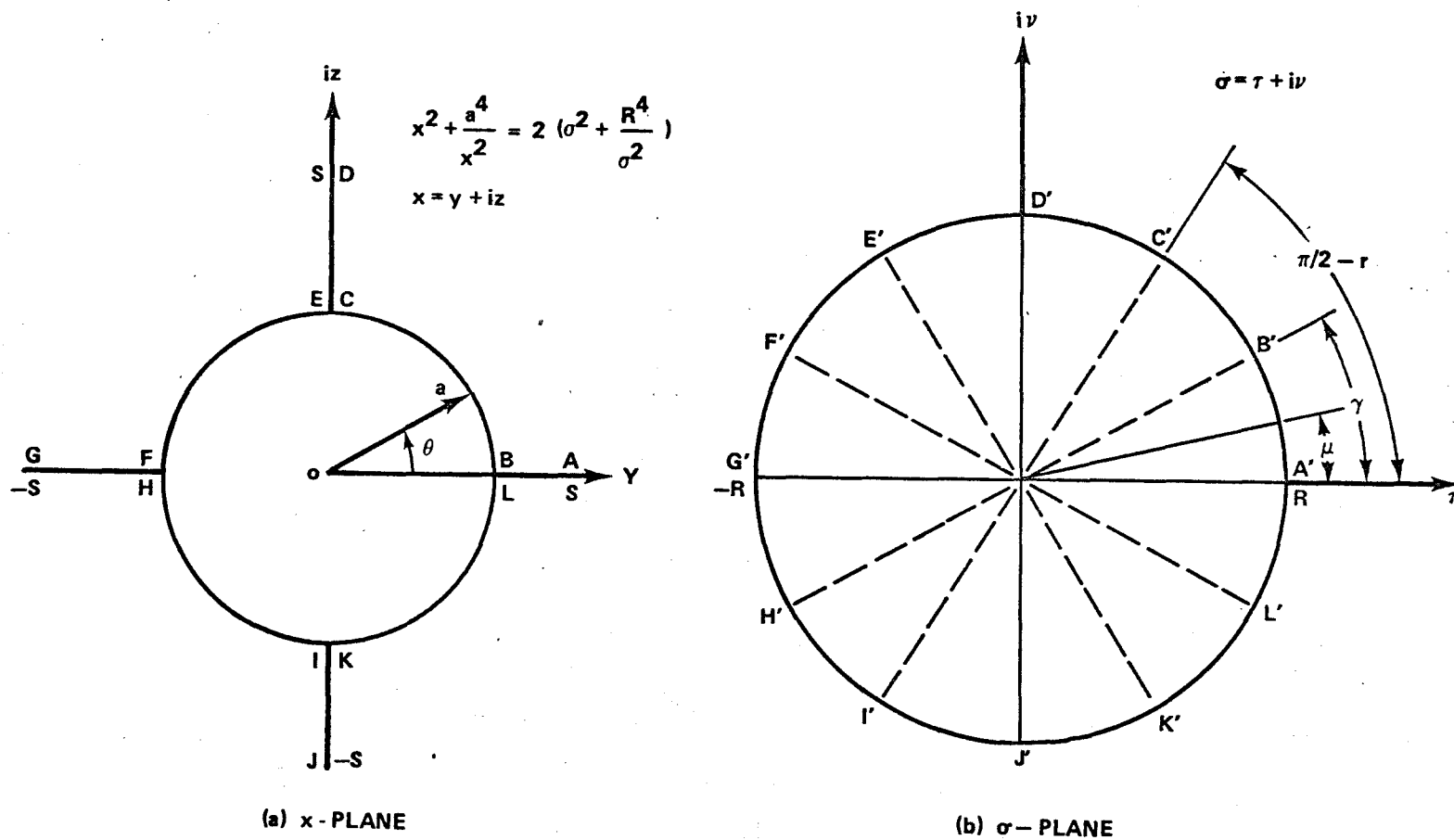
Figure 28. Conformal transformation for cruciform fin-body combination [38].
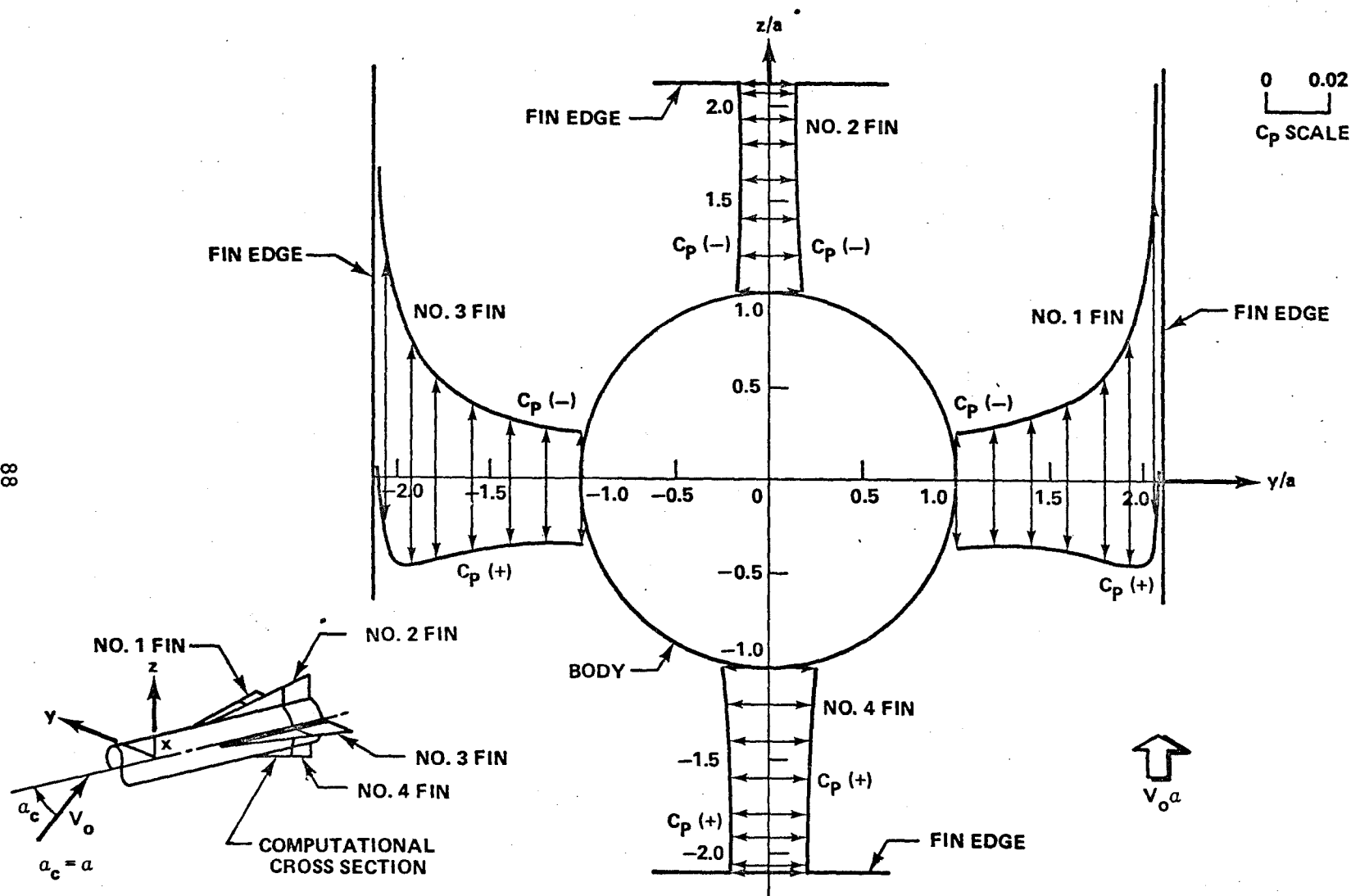
Figure 29. C_p distribution pattern on fins ($\alpha = 3°$).

88
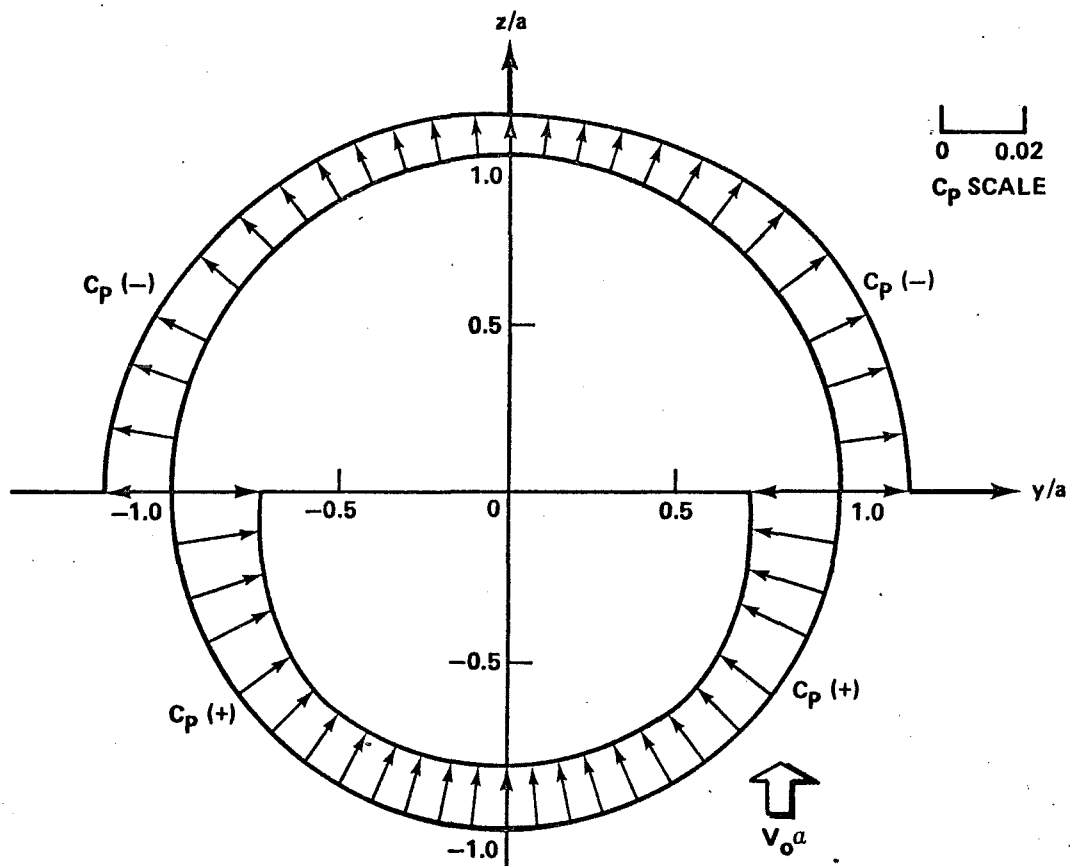
Figure 30. C_p distribution pattern on body ($\alpha = 3°$).
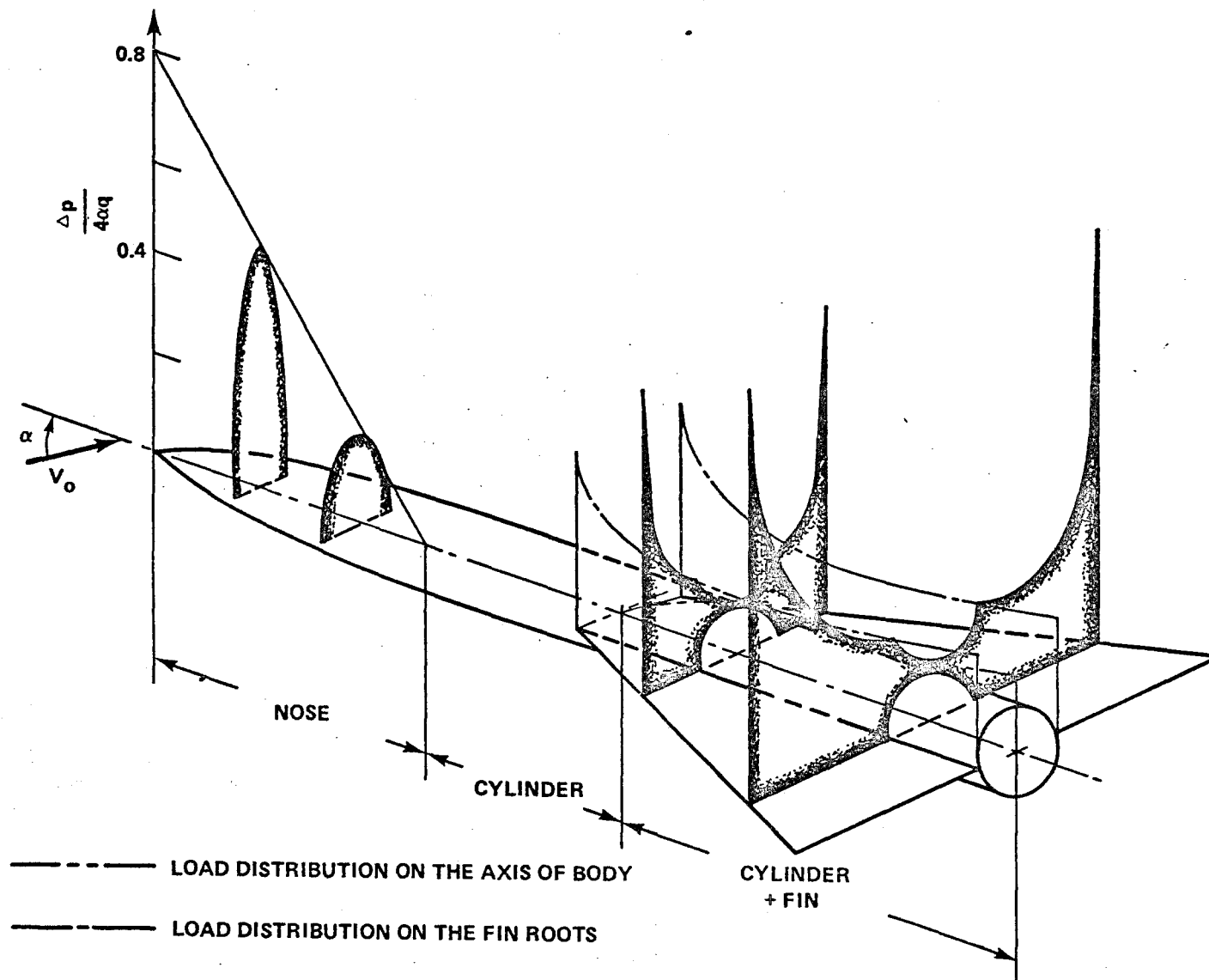
Figure 31. Composite plot of load distribution on the entire configuration.
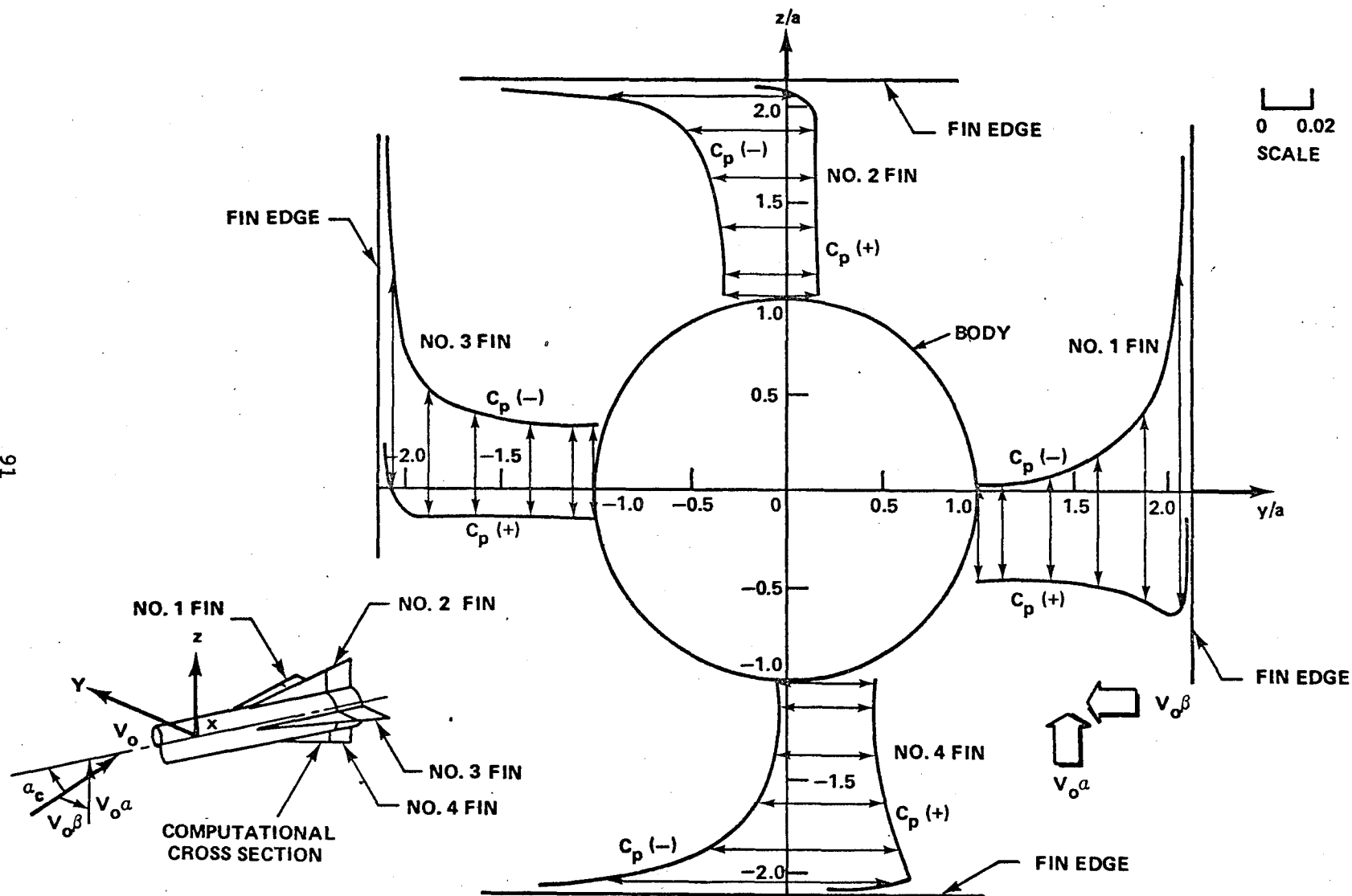
Figure 32. C_p distribution pattern on fins ($\alpha = \beta = 3°$).
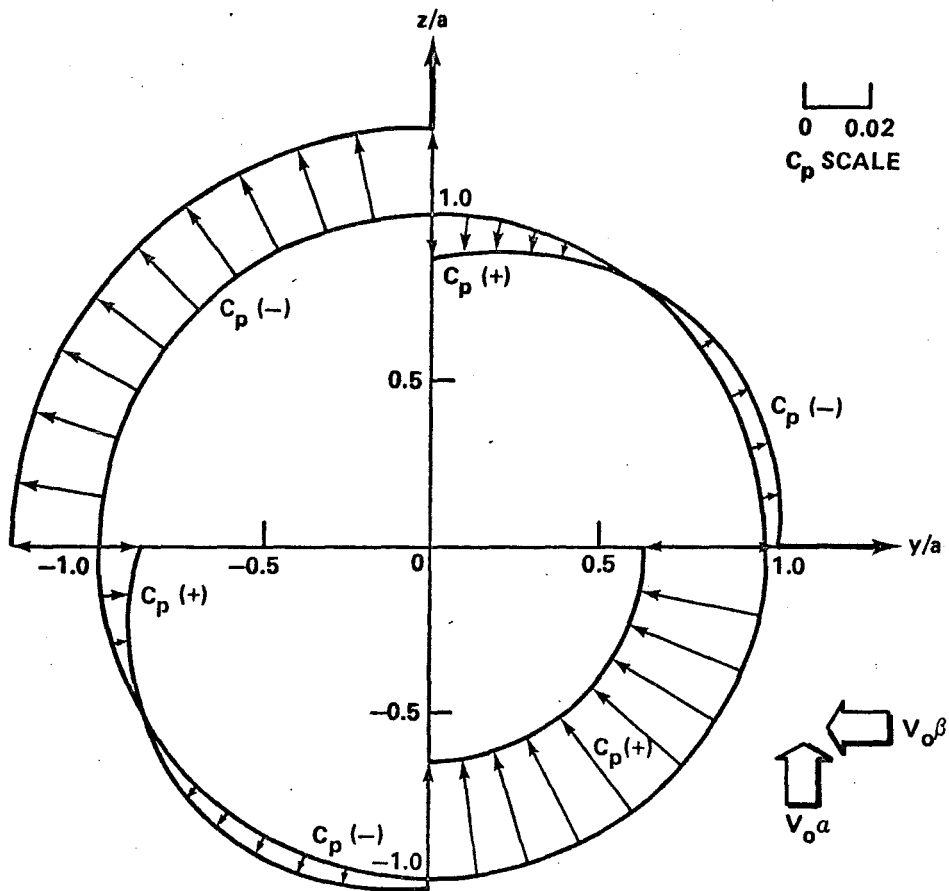
Figure 33. C_p distribution pattern on body ($\alpha = \beta = 3°$).
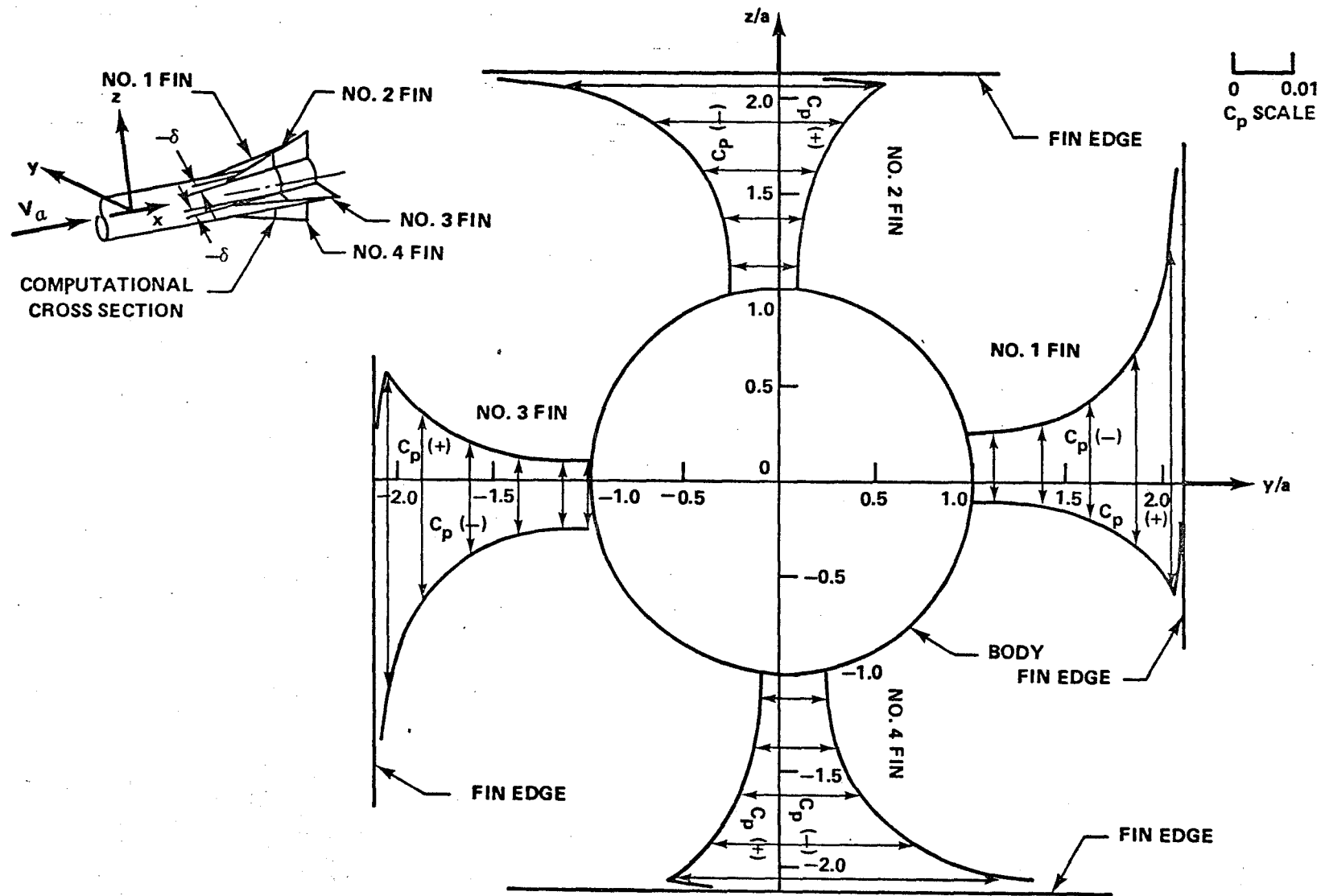
Figure 34. C_p distribution pattern on fins ($-\delta = 3°$, all fins are canted).
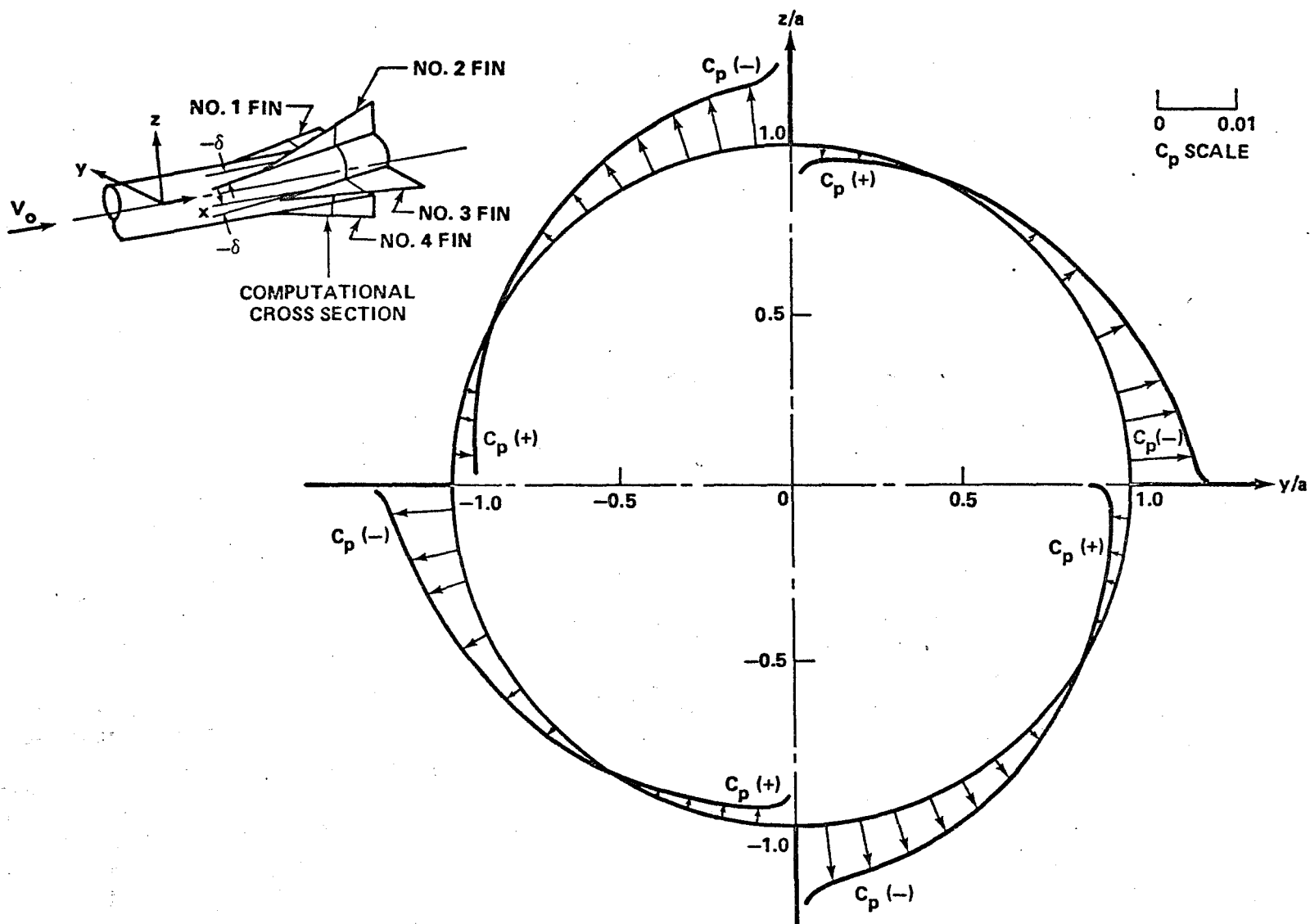
Figure 35. C_p distribution pattern on body ($-\delta = 3°$, all fins are canted).
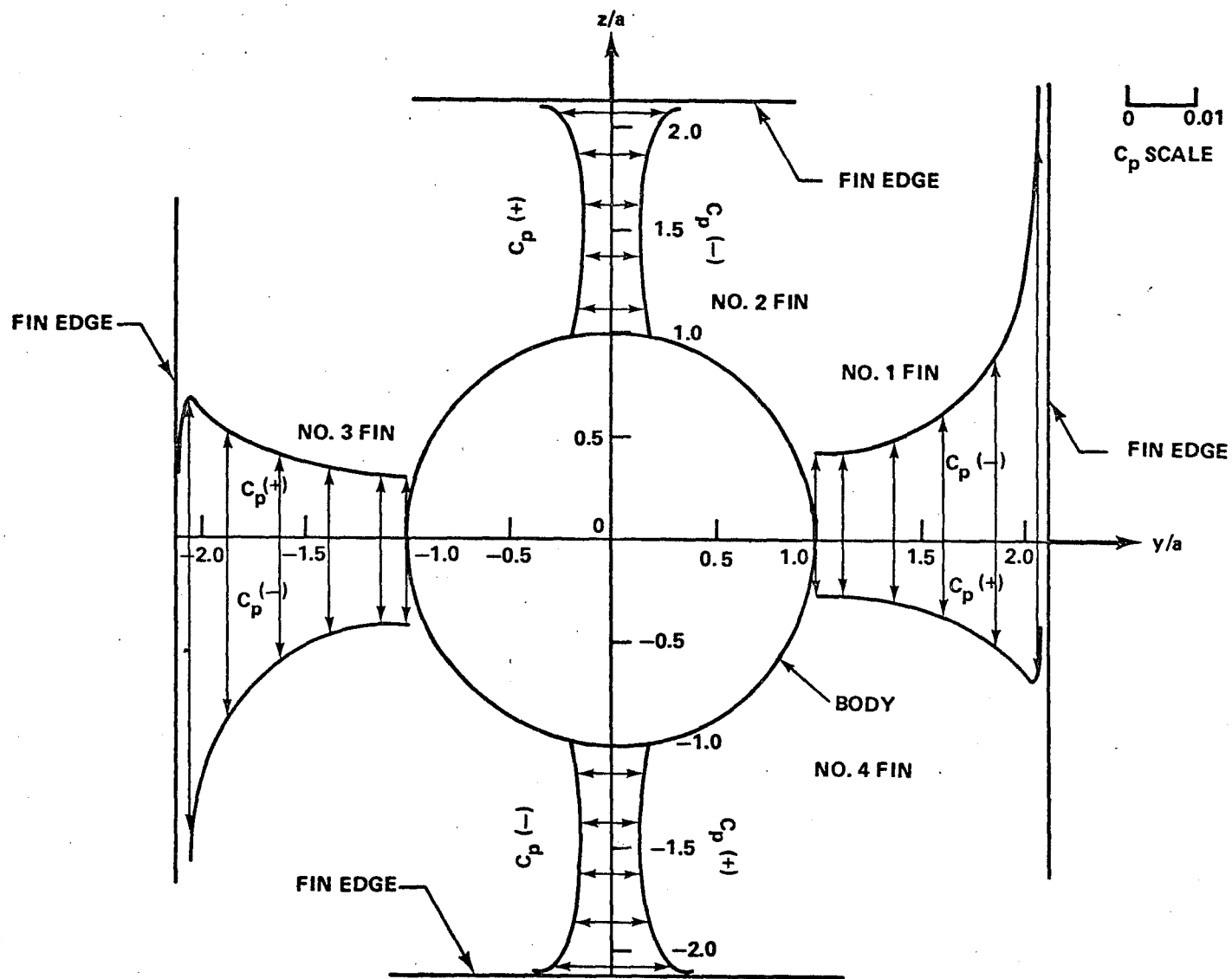
Figure 36. C_p distribution pattern on fins ($-\delta = 3°$, only horizontal fins are canted).
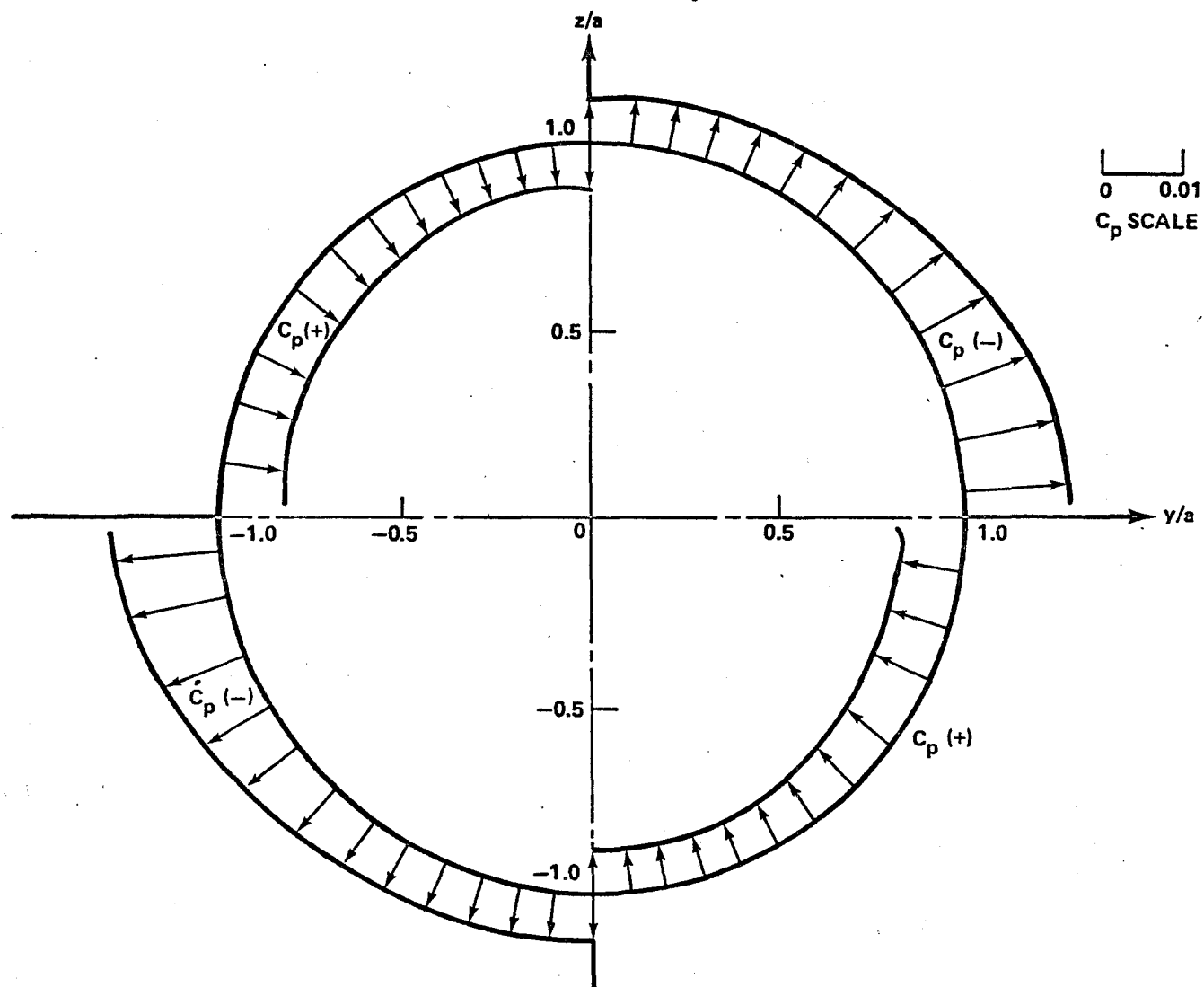
Figure 37. C_p distribution pattern on body ($-\delta = 3°$, only horizontal fins are canted).
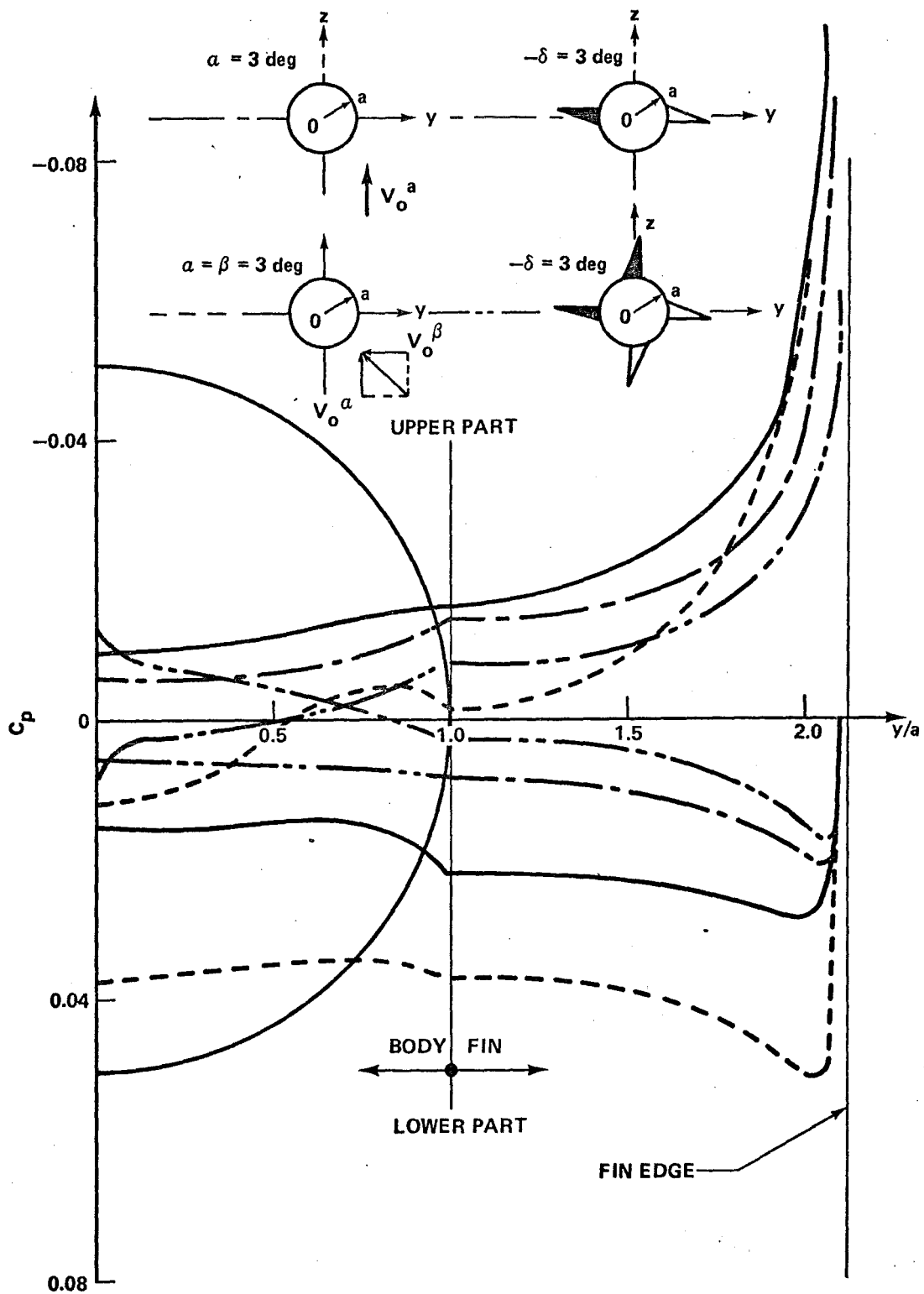
Figure 38. Comparison of C_p distribution on fin-body combinations in various cases.
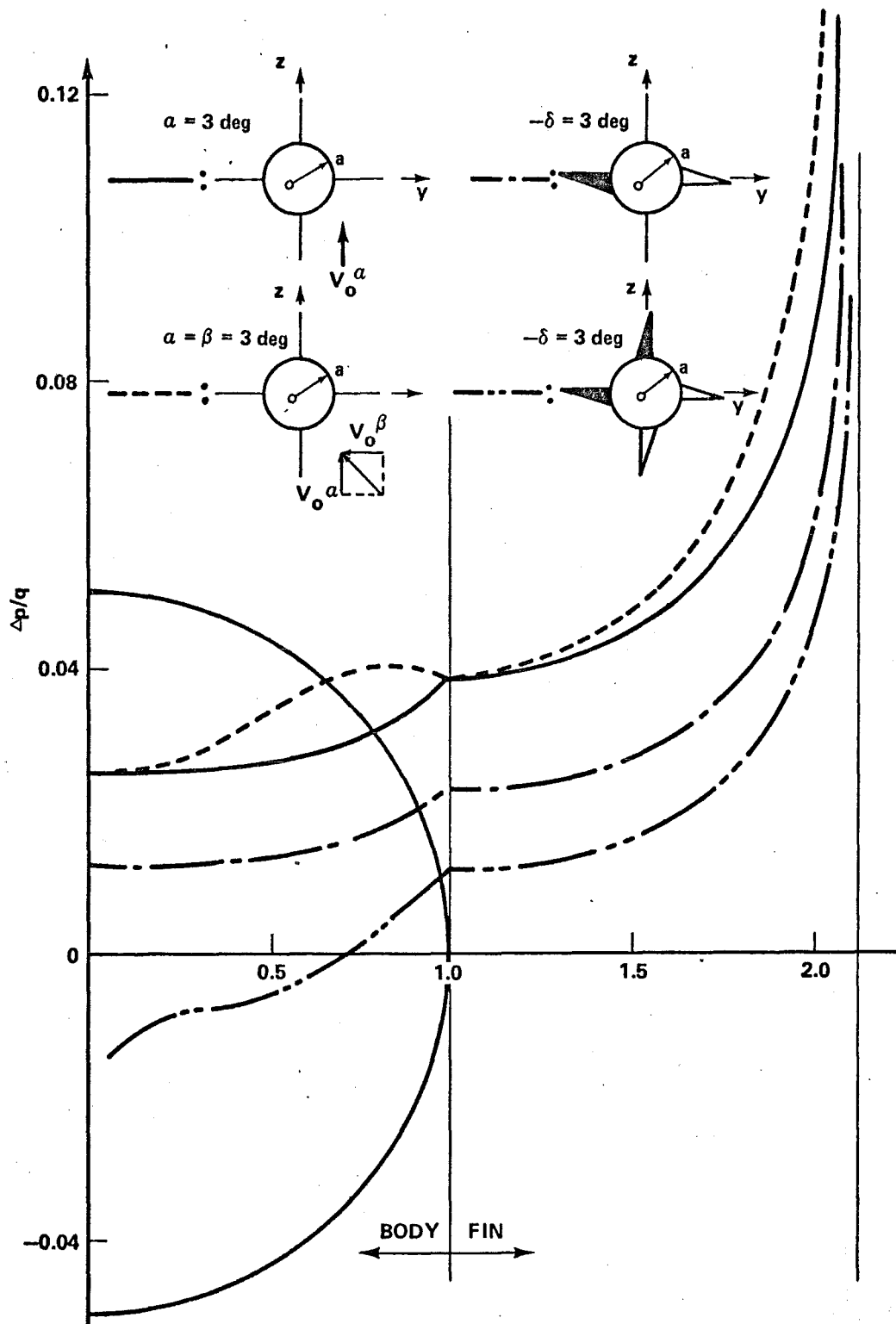
Figure 39. Comparison of load distribution on fin-body
combinations in various cases.
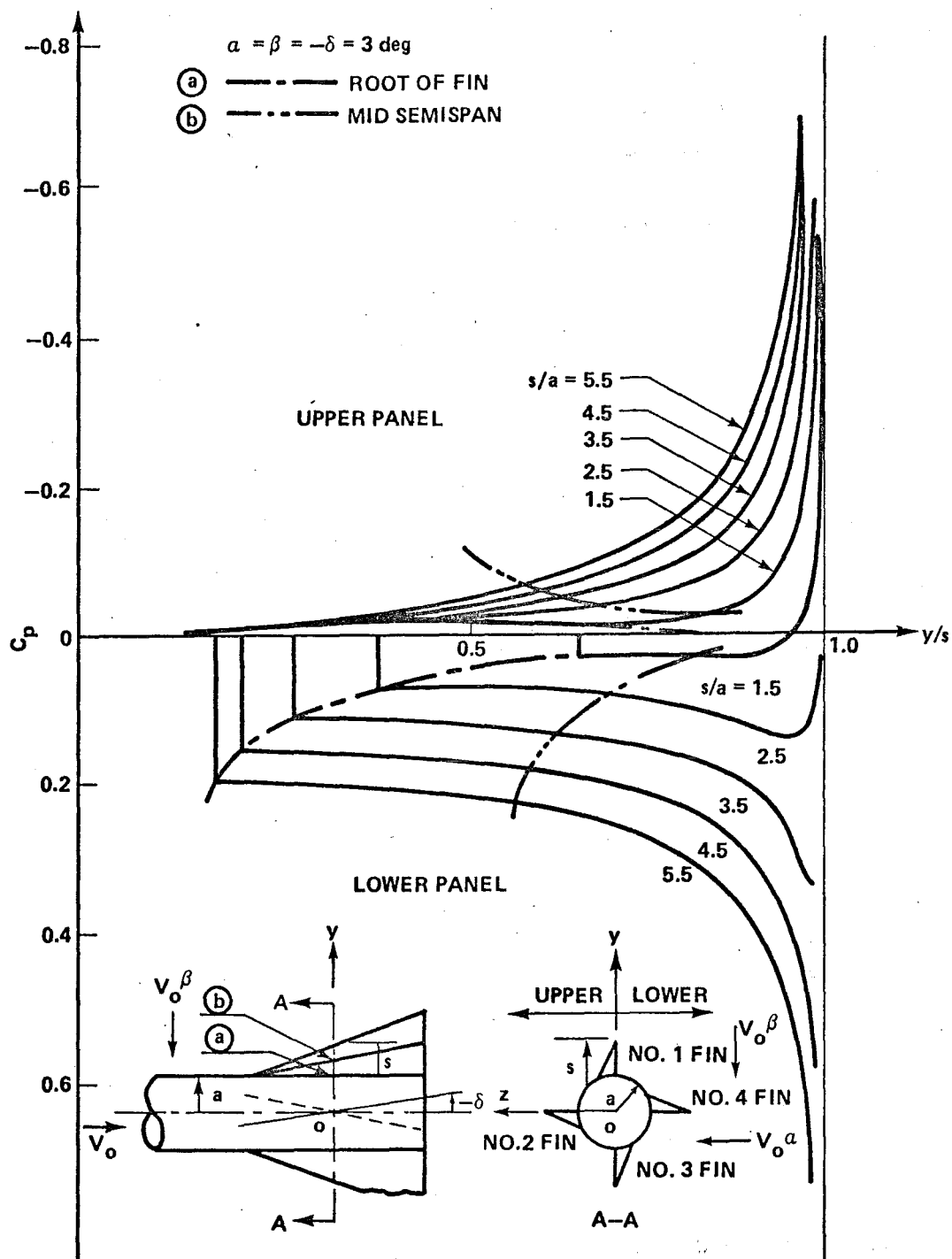
Figure 40. Spanwise C_p distribution on right horizontal fin (No. 1 fin).
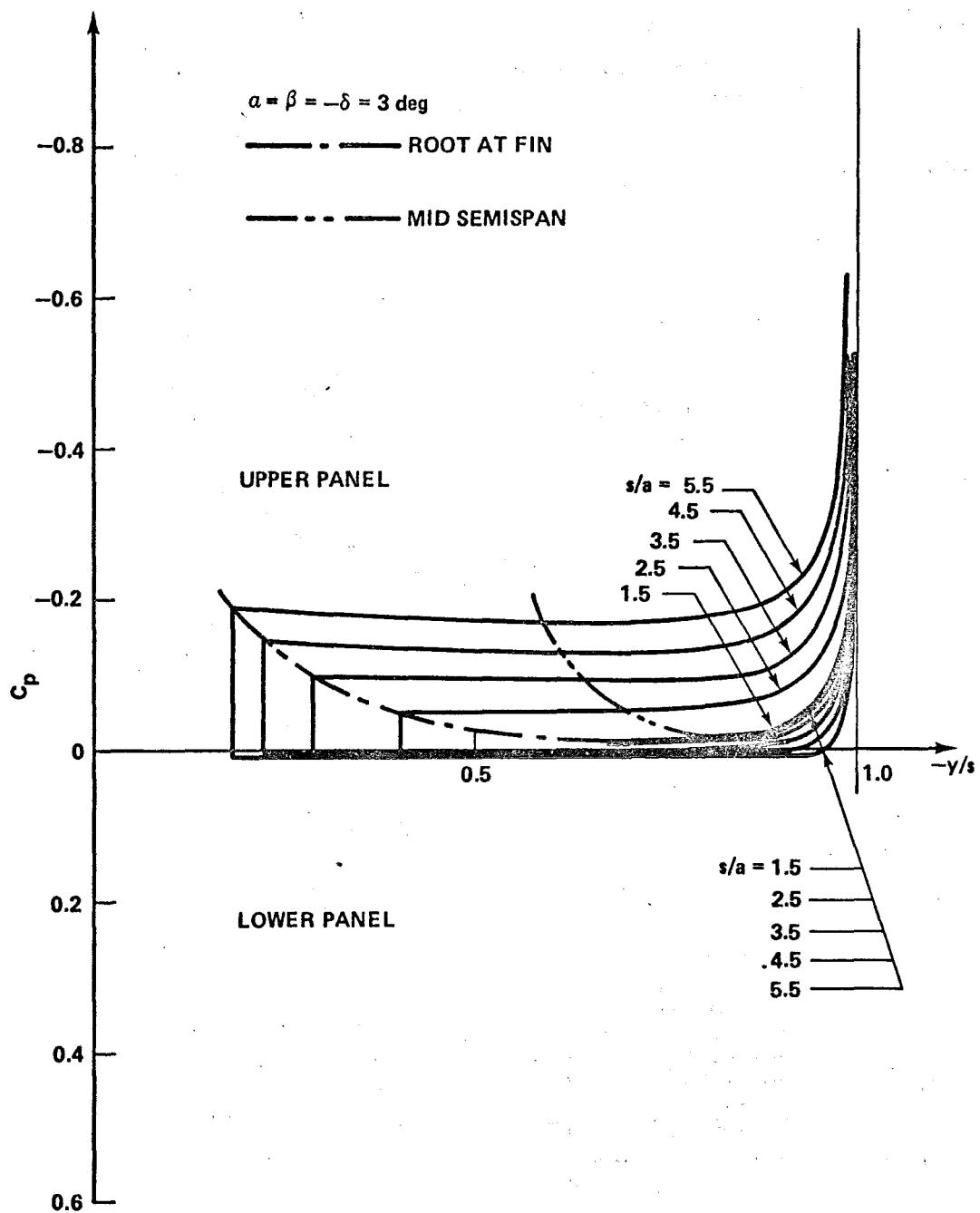
Figure 41. Spanwise C_p distribution on left horizontal fin (No. 3 fin).

100
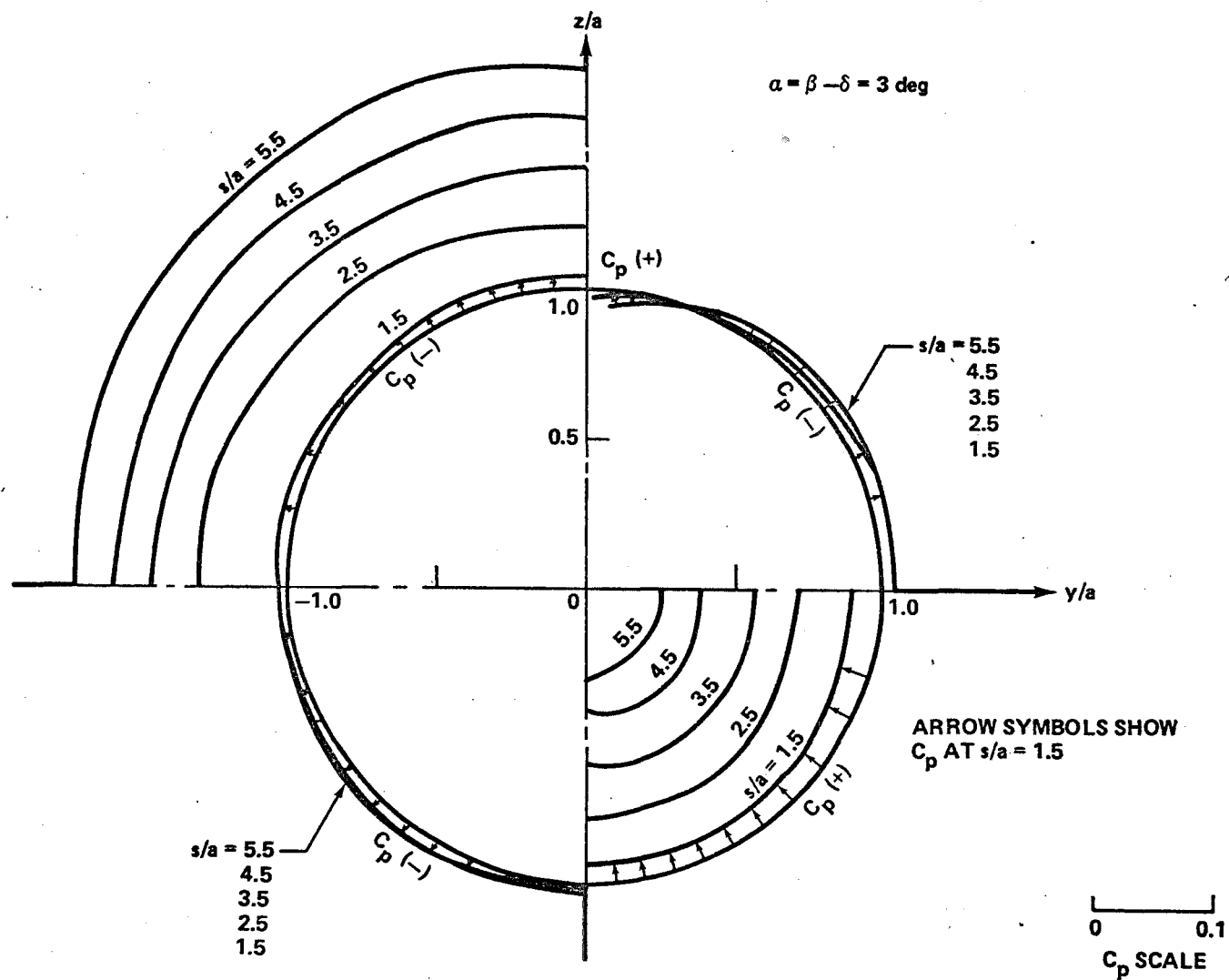
Figure 42. C_p distribution on body.
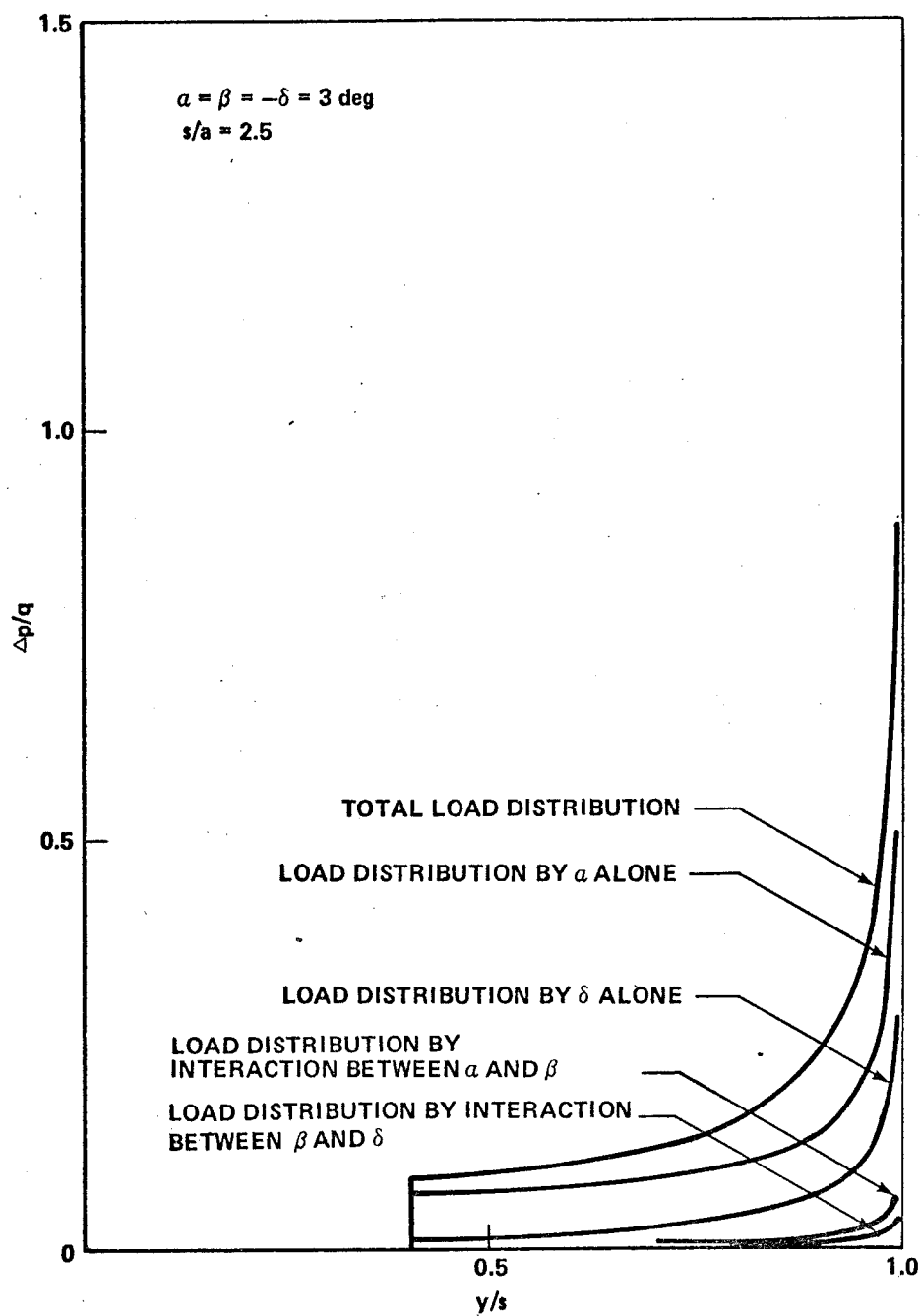
Figure 43. Total load distribution and its elements (No. 1 fin).

102
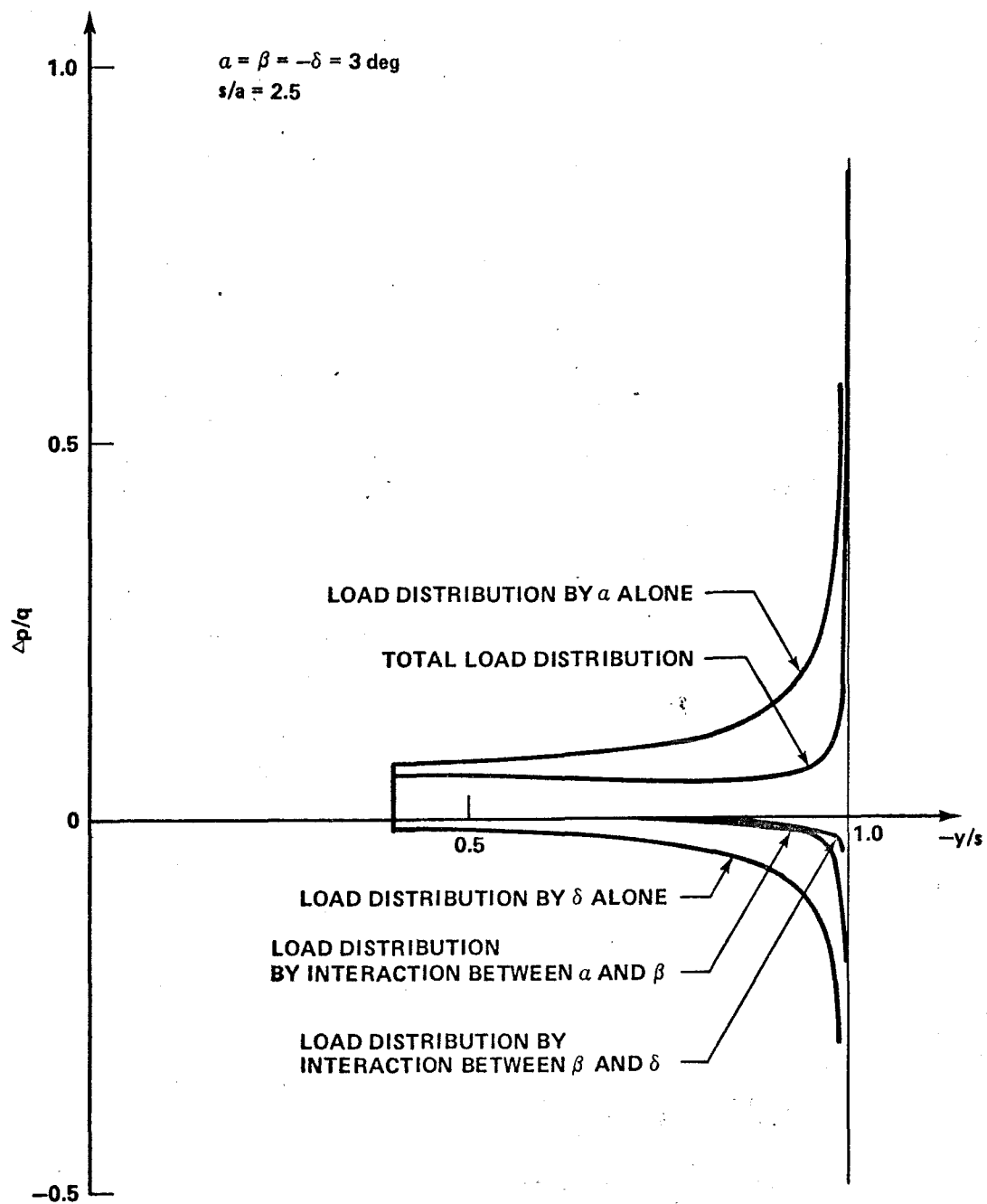
Figure 44. Total load distribution and its elements (No. 3 fin).

103
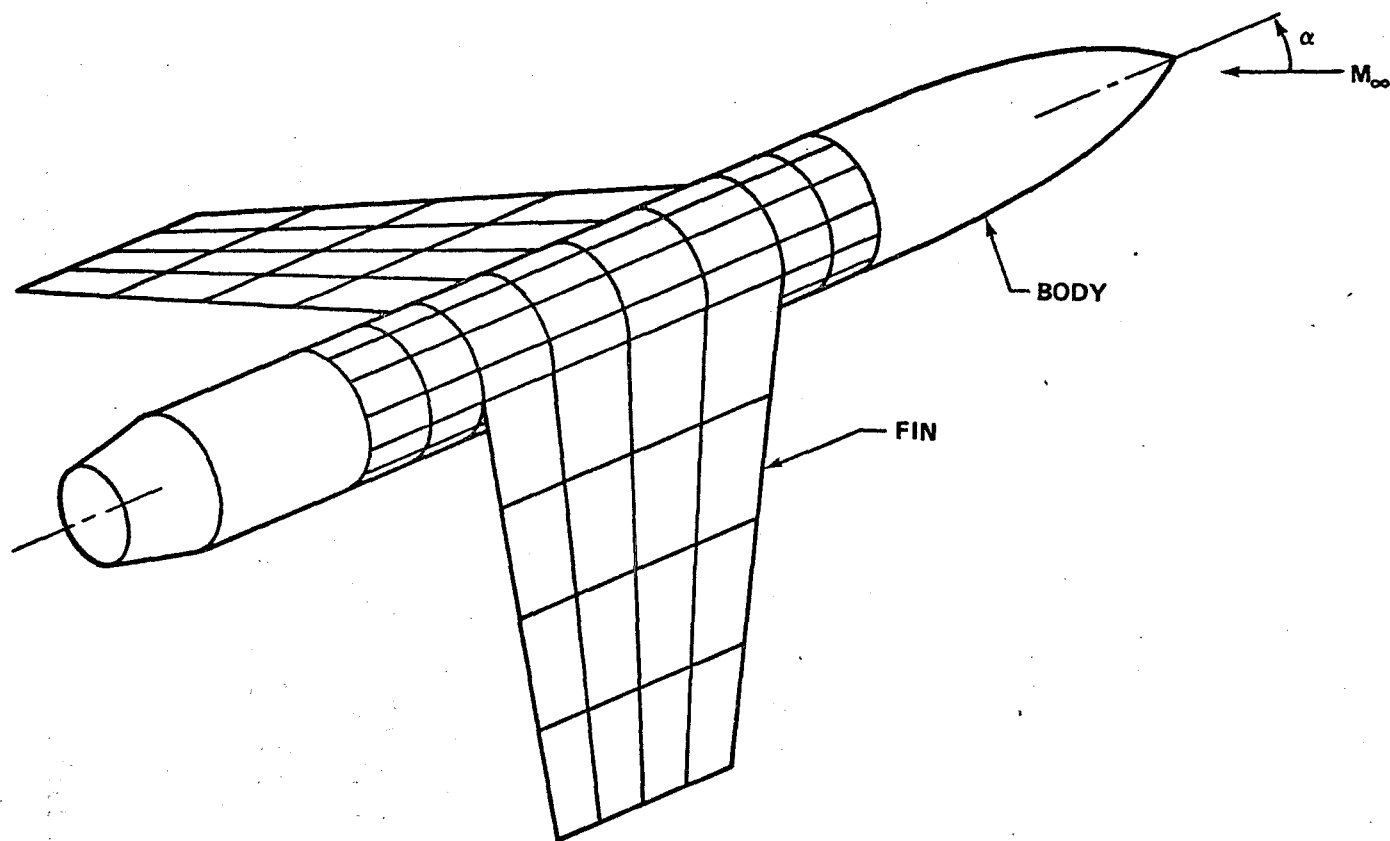
Figure 45. Schematic model of fin-body combinition in present analysis.
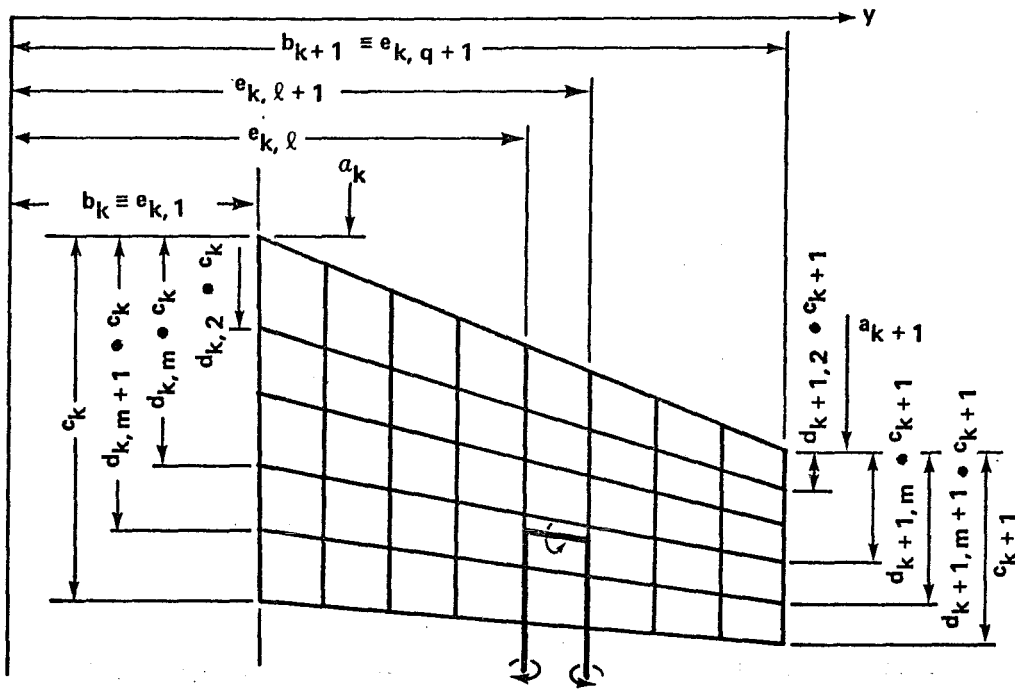
Figure 46. Fin panels.
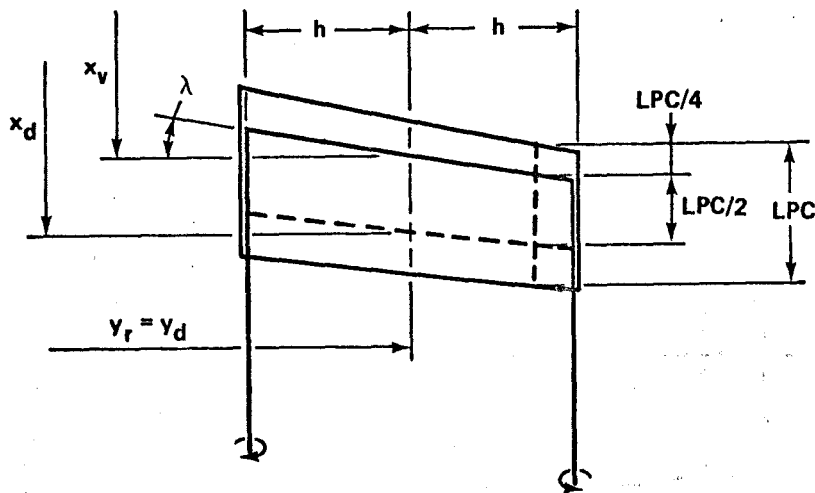
Figure 47. Location of horseshoe vortex and control point on panel.

105
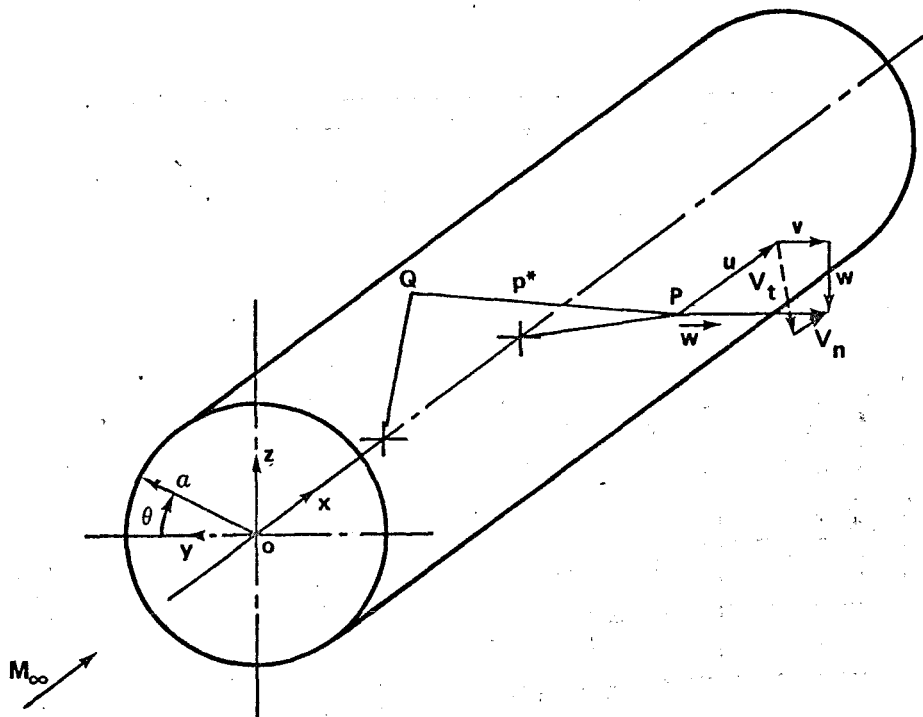
Figure 48. Induced velocity at P by a source Q [43].
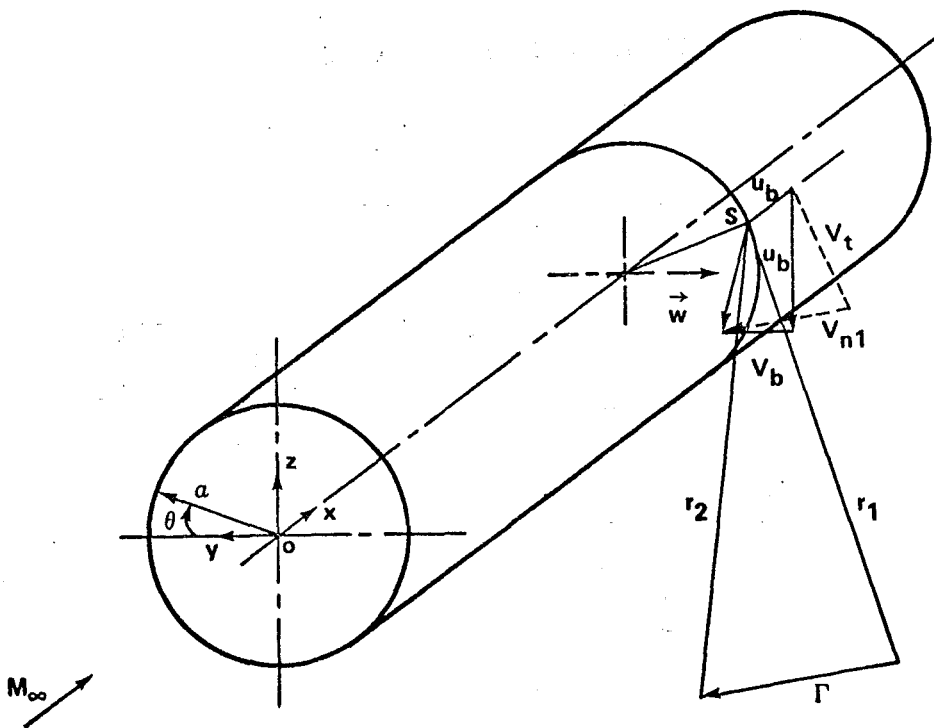
Figure 49. Induced velocity at S by a line vortex element [43].

106
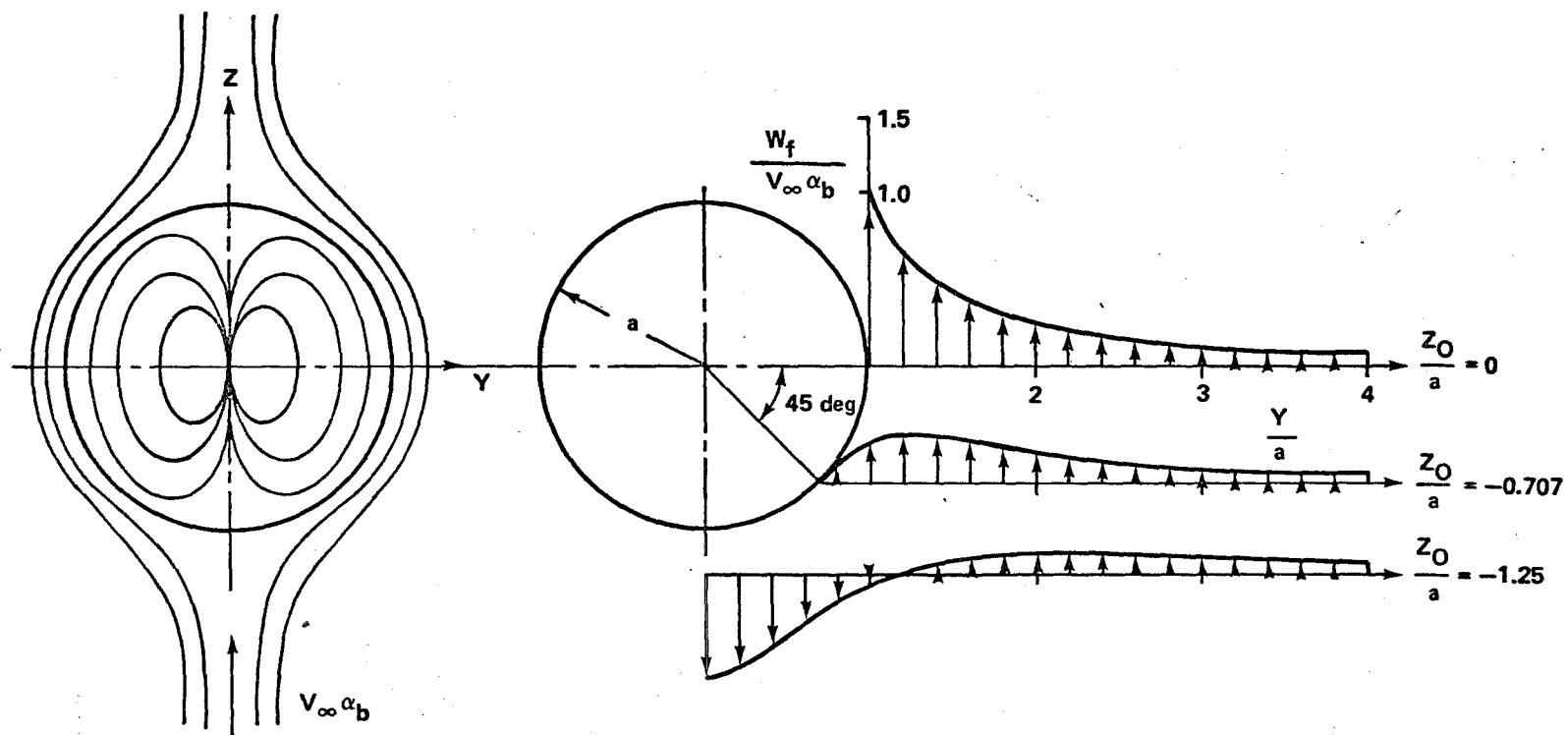
Figure 50. Velocity distribution on fin induced by the body angle of incidence [43].
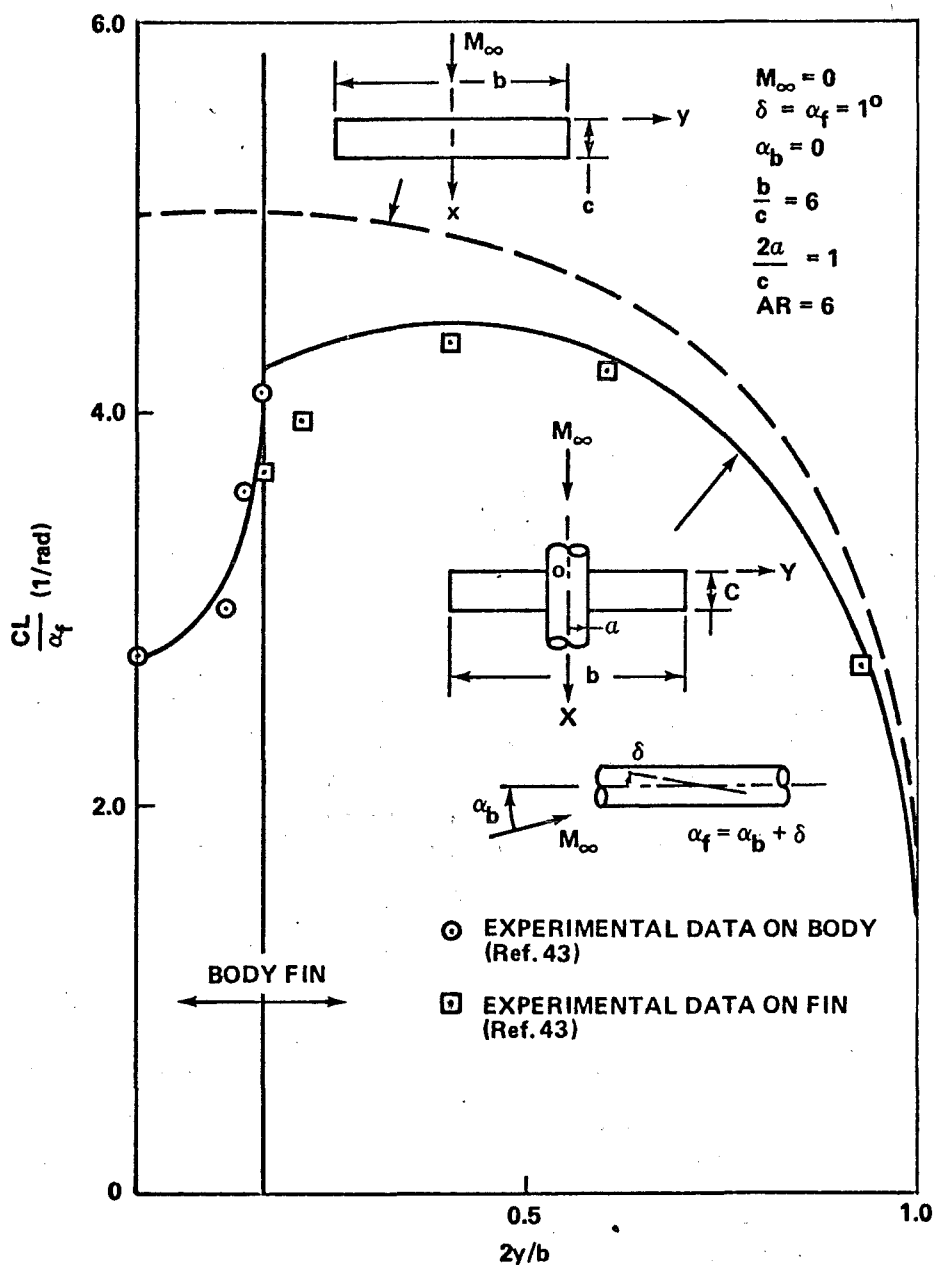
Figure 51. Recalculated spanwise lift distribution of rectangular fin-body combination given by Körner [43].
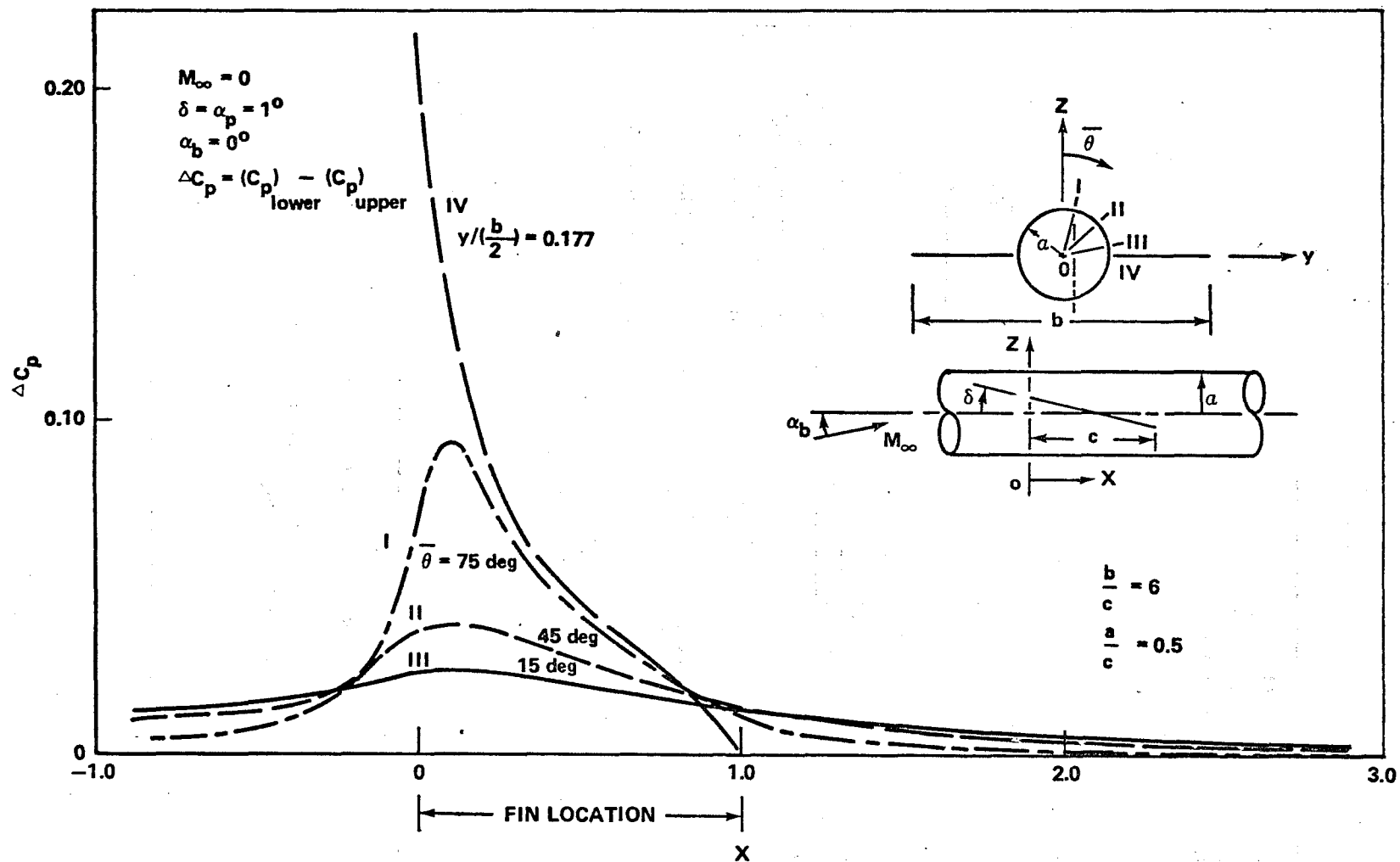
Figure 52. Longitudinal pressure distribution of body with rectangular fin.
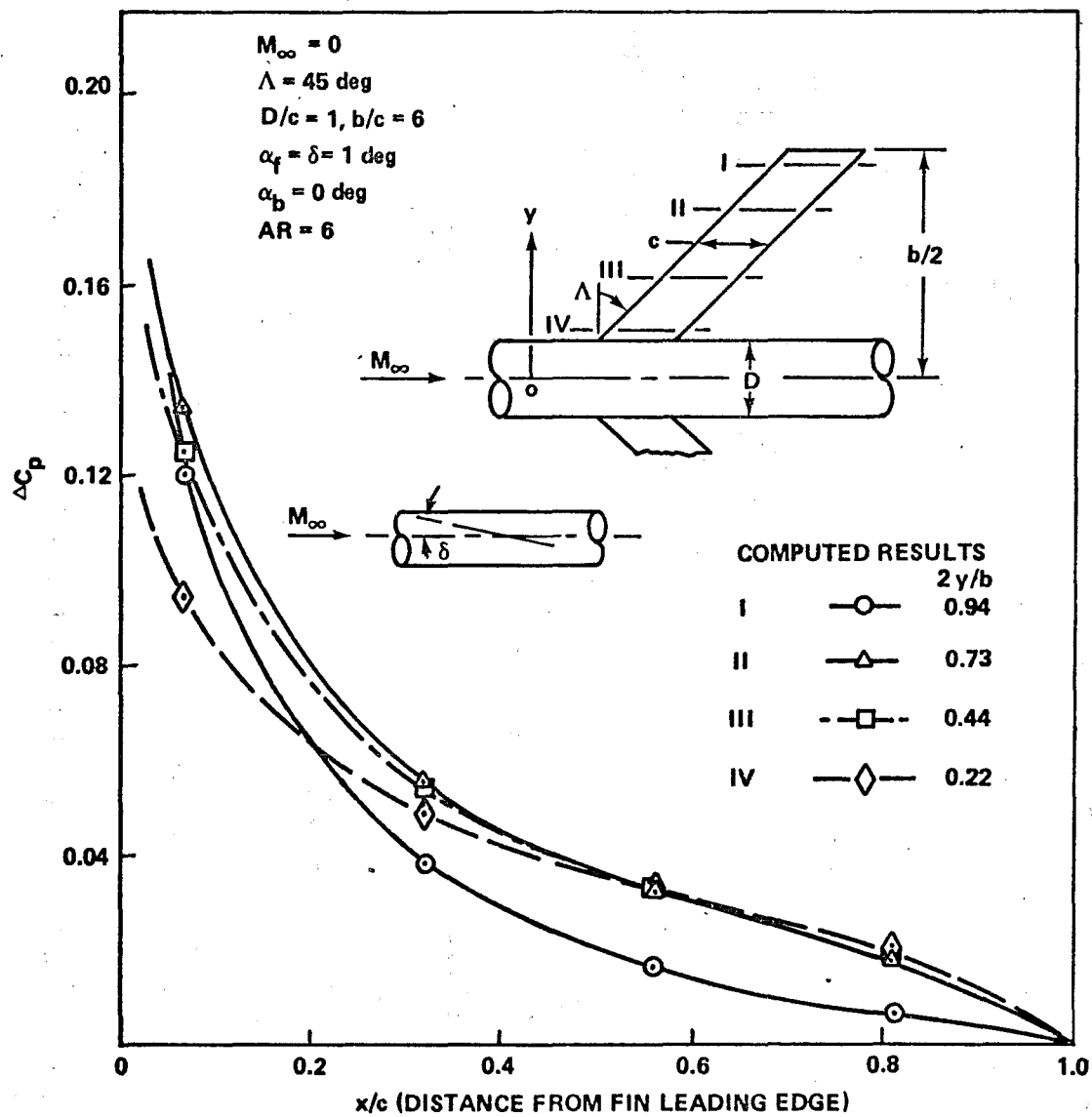
Figure 53. Chordwise pressure distribution on 45° sweptback fin with body.

110
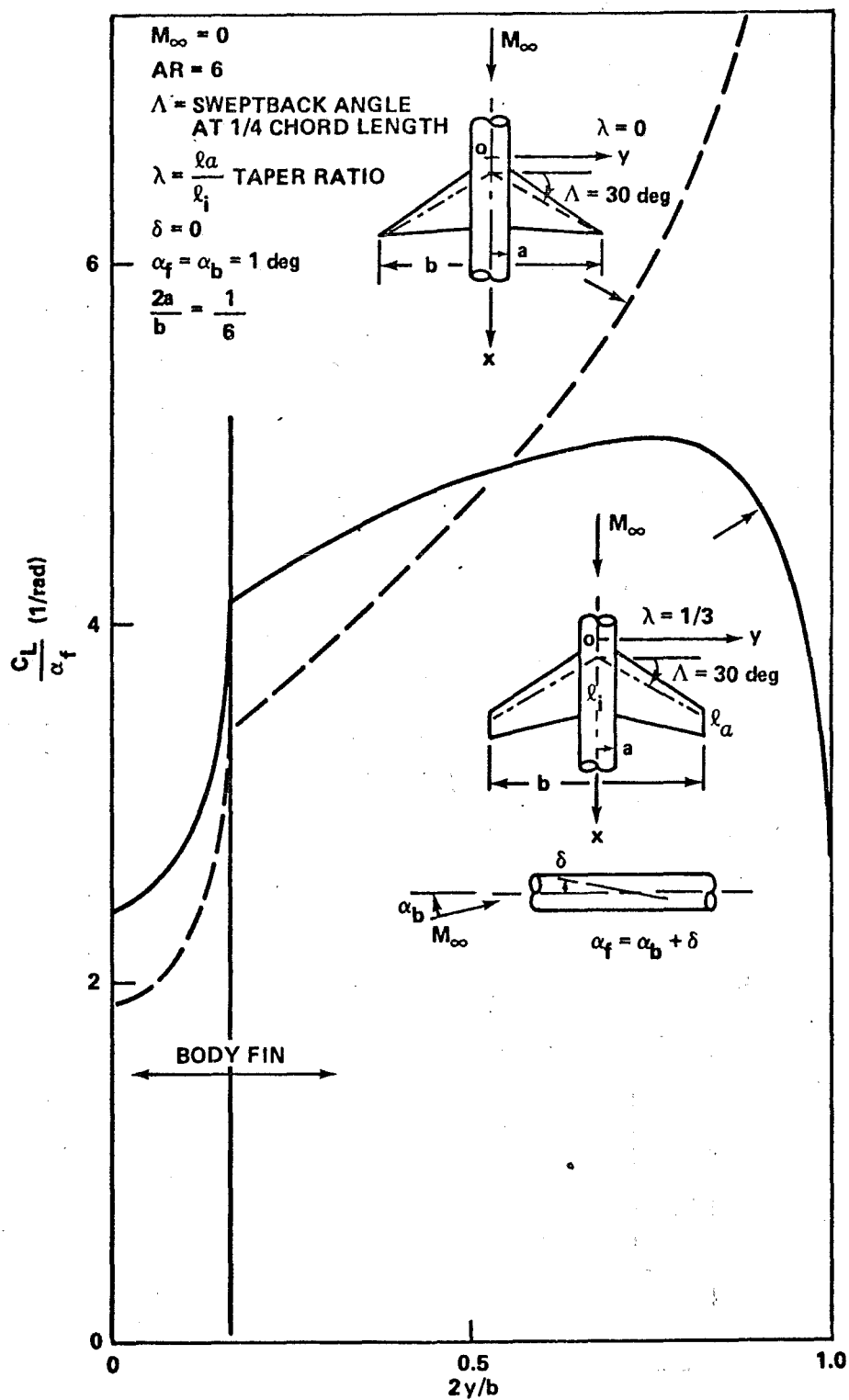
Figure 54. Spanwise lift distribution with different taper ratio fin given by Körner.

111
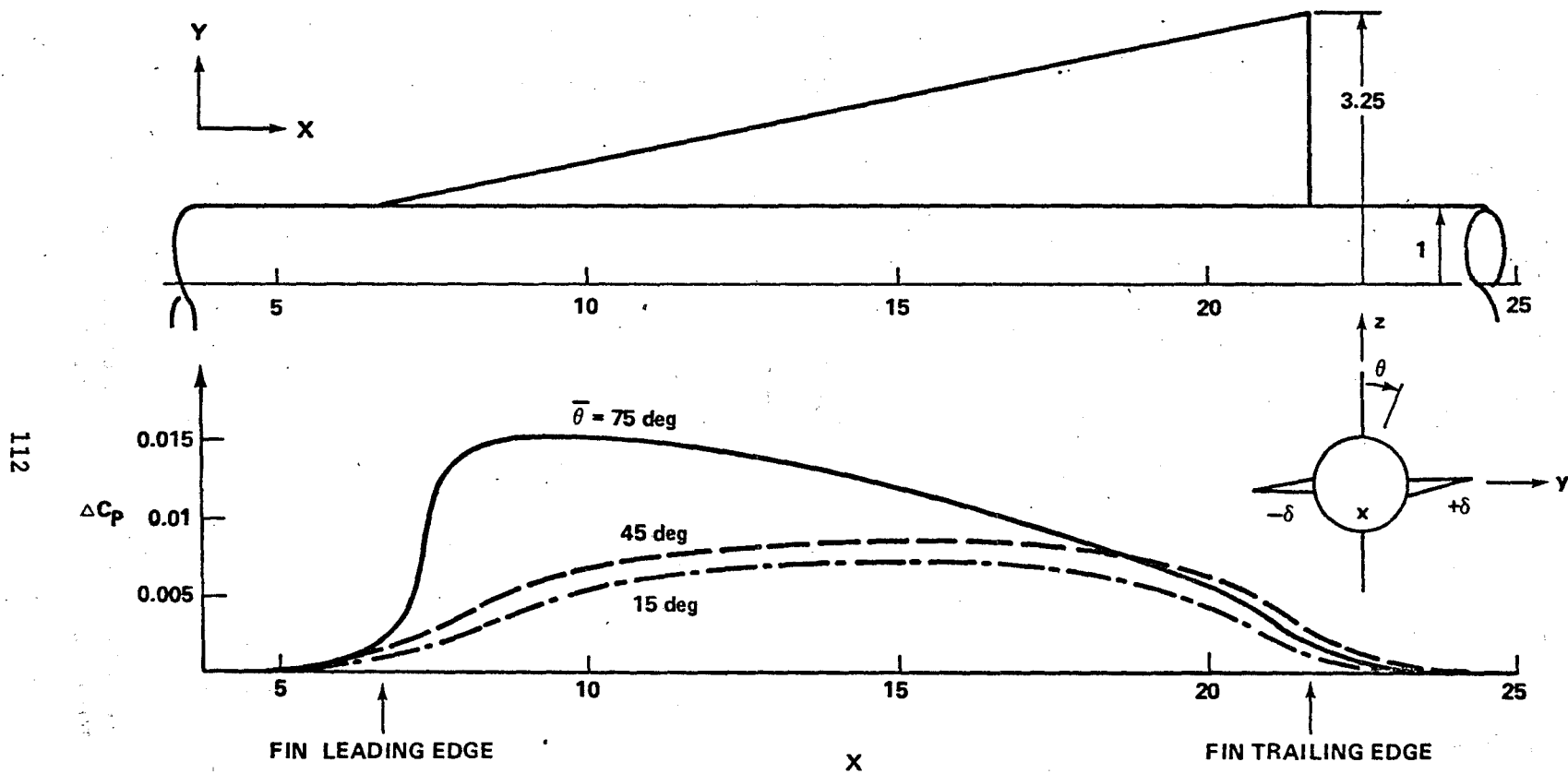
Figure 55.   Longitudinal pressure distribution on body with cruciform
slender delta fin (horizontal fins are canted, $\delta = -3°$).
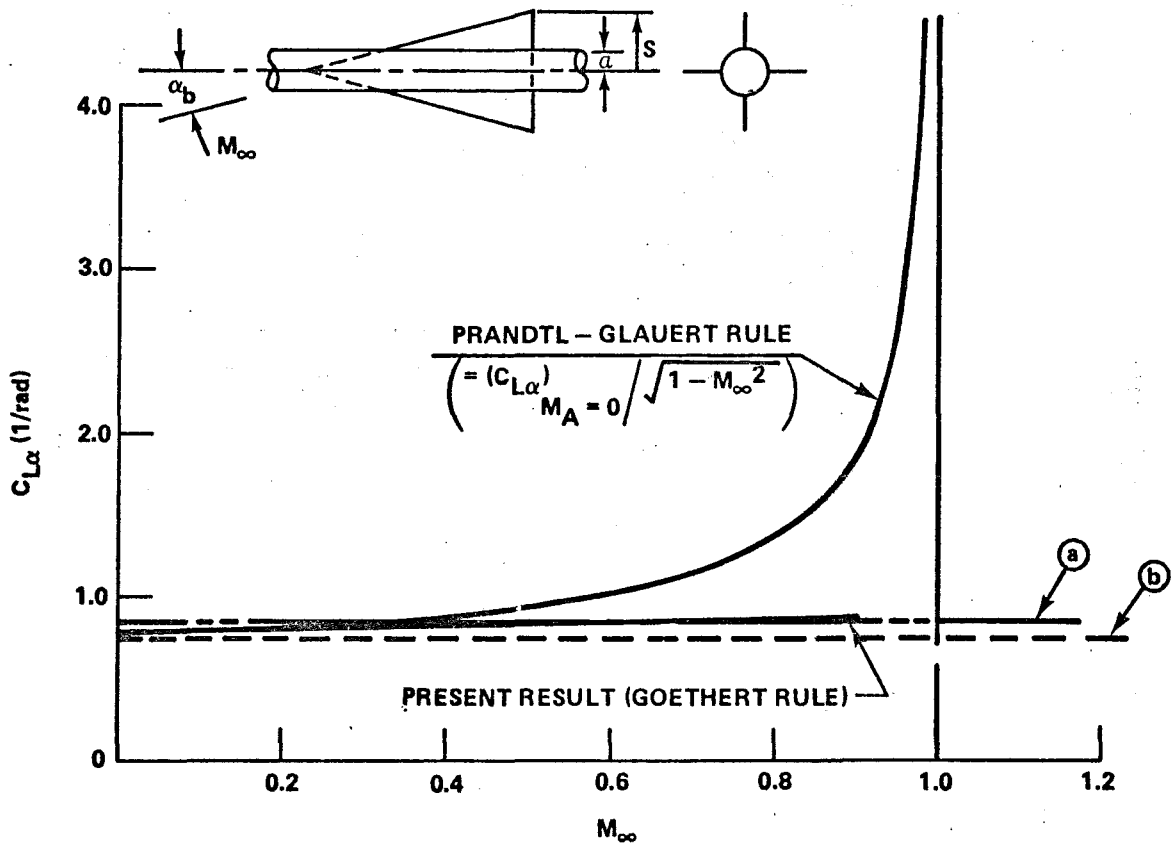
Figure 56. Comparison of subsonic similarity rules for cruciform slender delta fin-body combination at angle of incidence (also includes result from slender body theory).
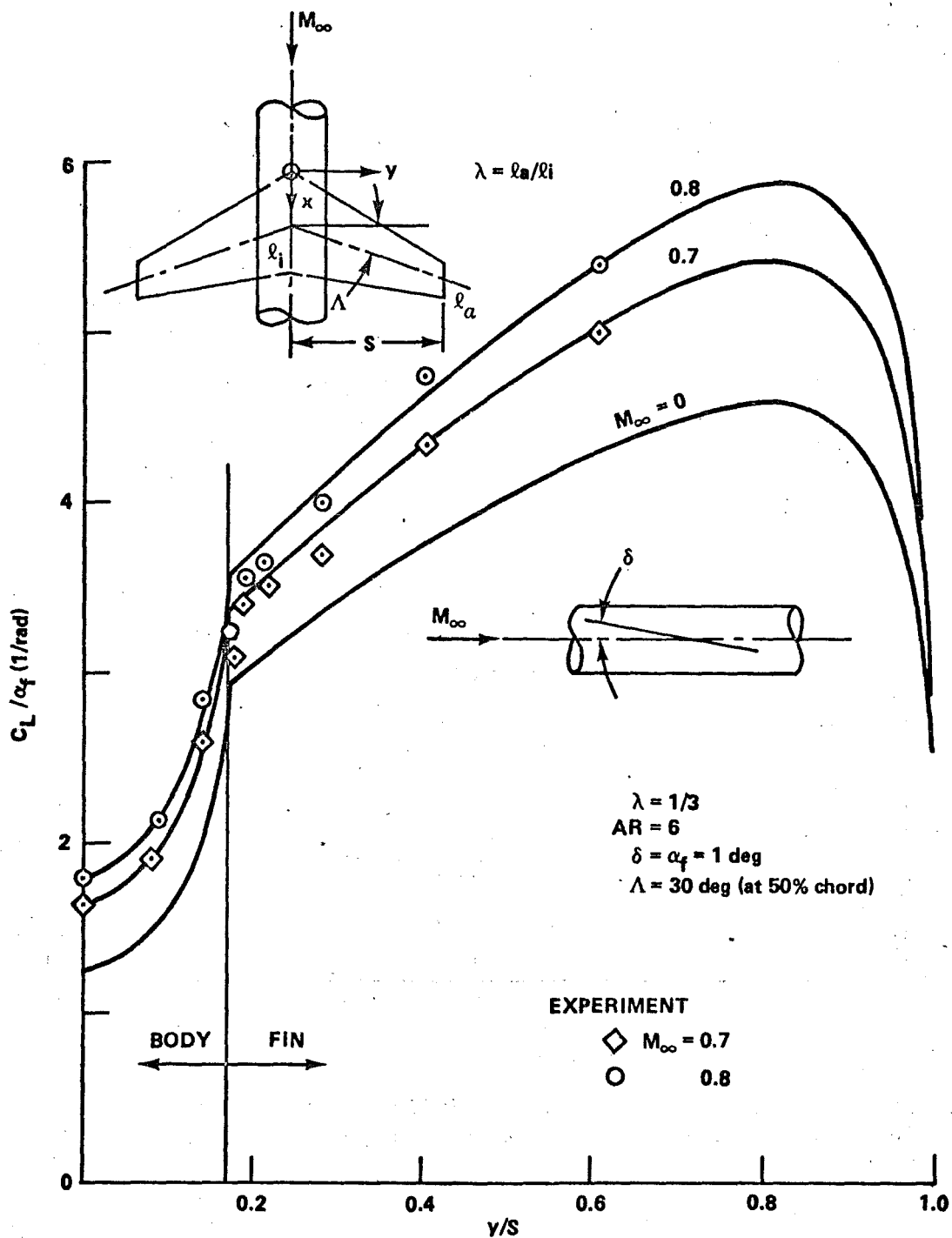
Figure 57. Local lift coefficient on fin body junction
showing effect of Mach number change, -30° swept fin
[43].
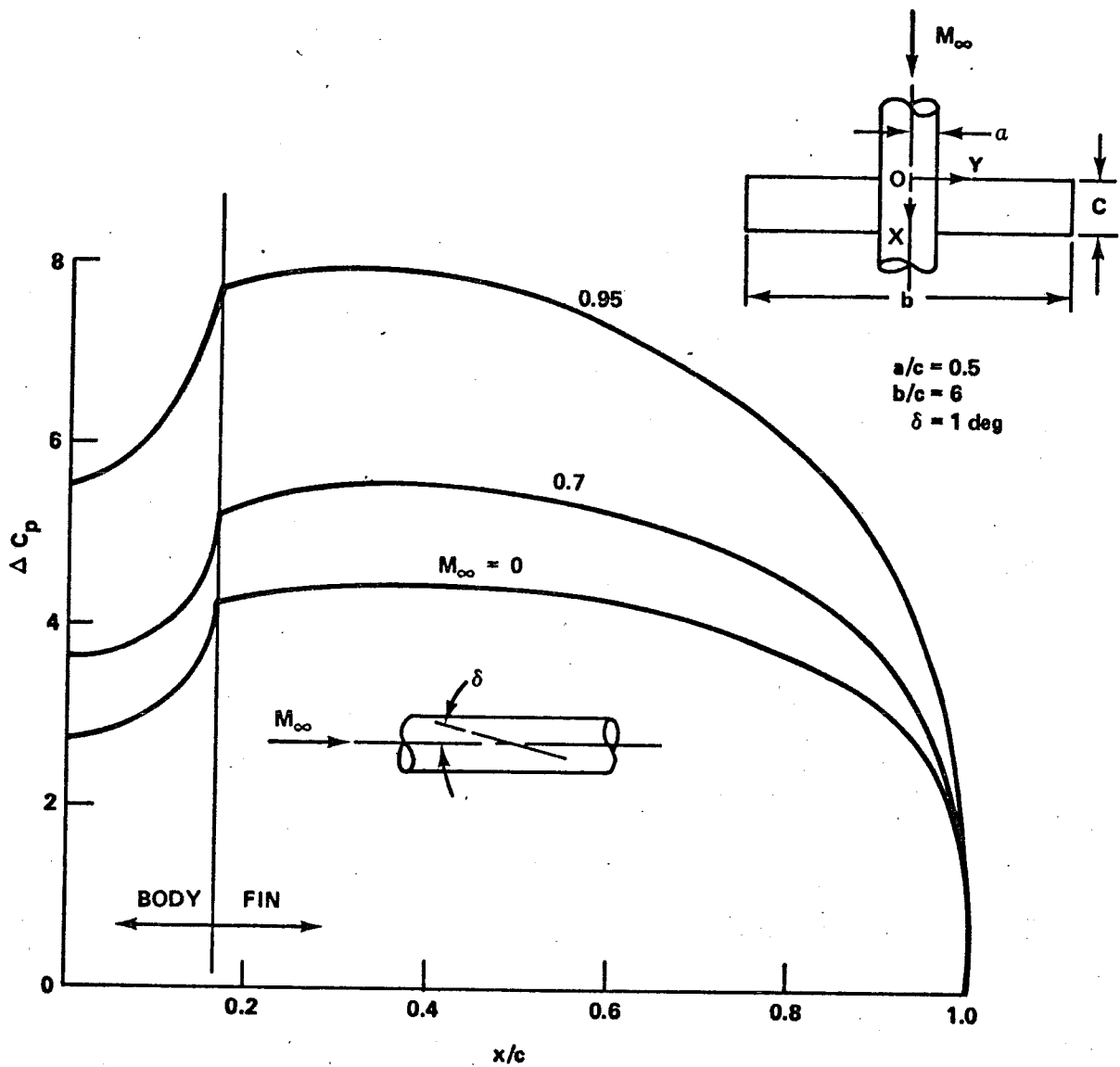
Figure 58. Load distribution on rectangular wing showing the effect of Mach number.
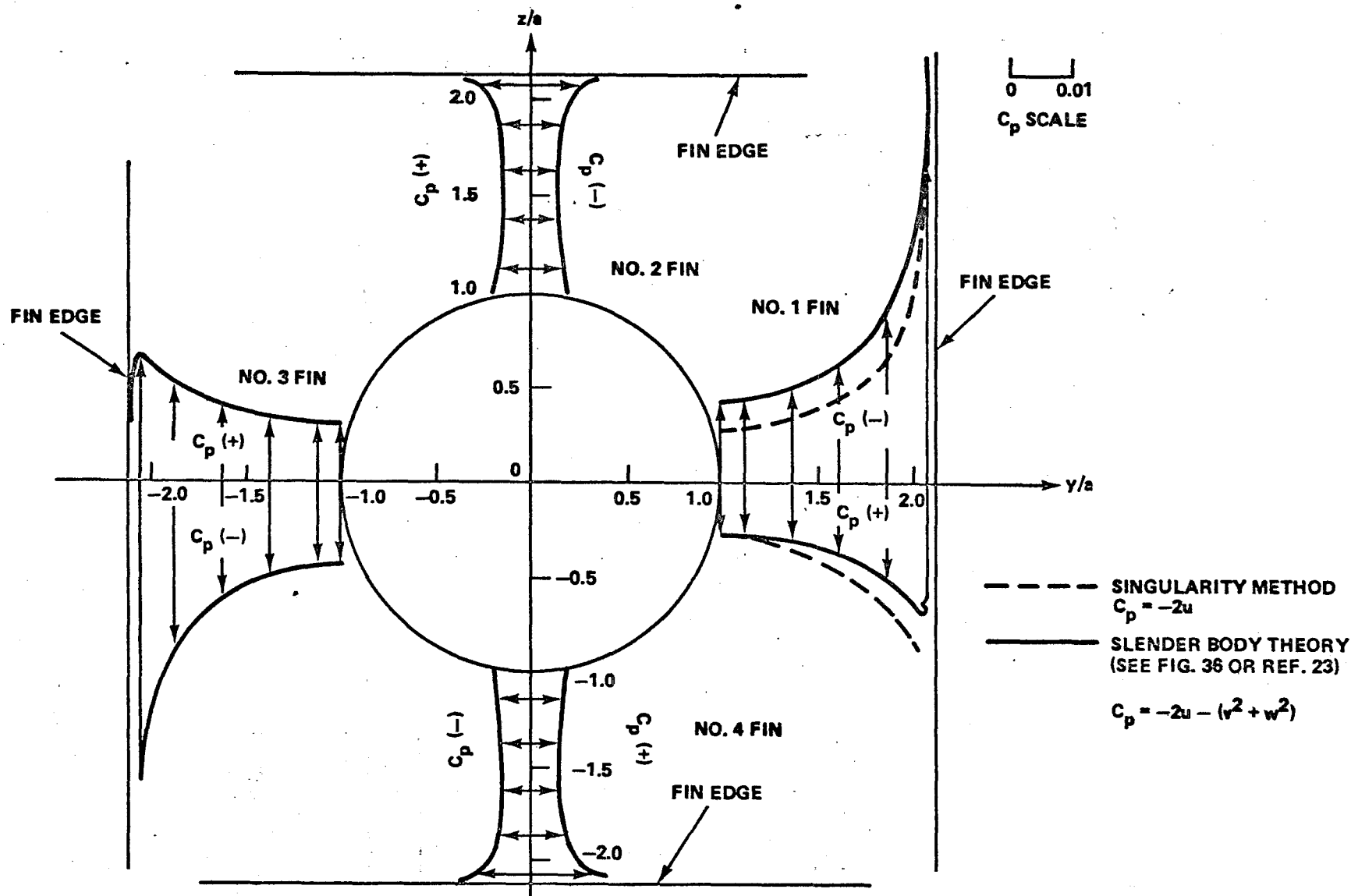
Figure 59. Comparison with slender body theory, C_p distribution pattern. on fins ($-\delta = 3°$, only horizontal fins are canted).
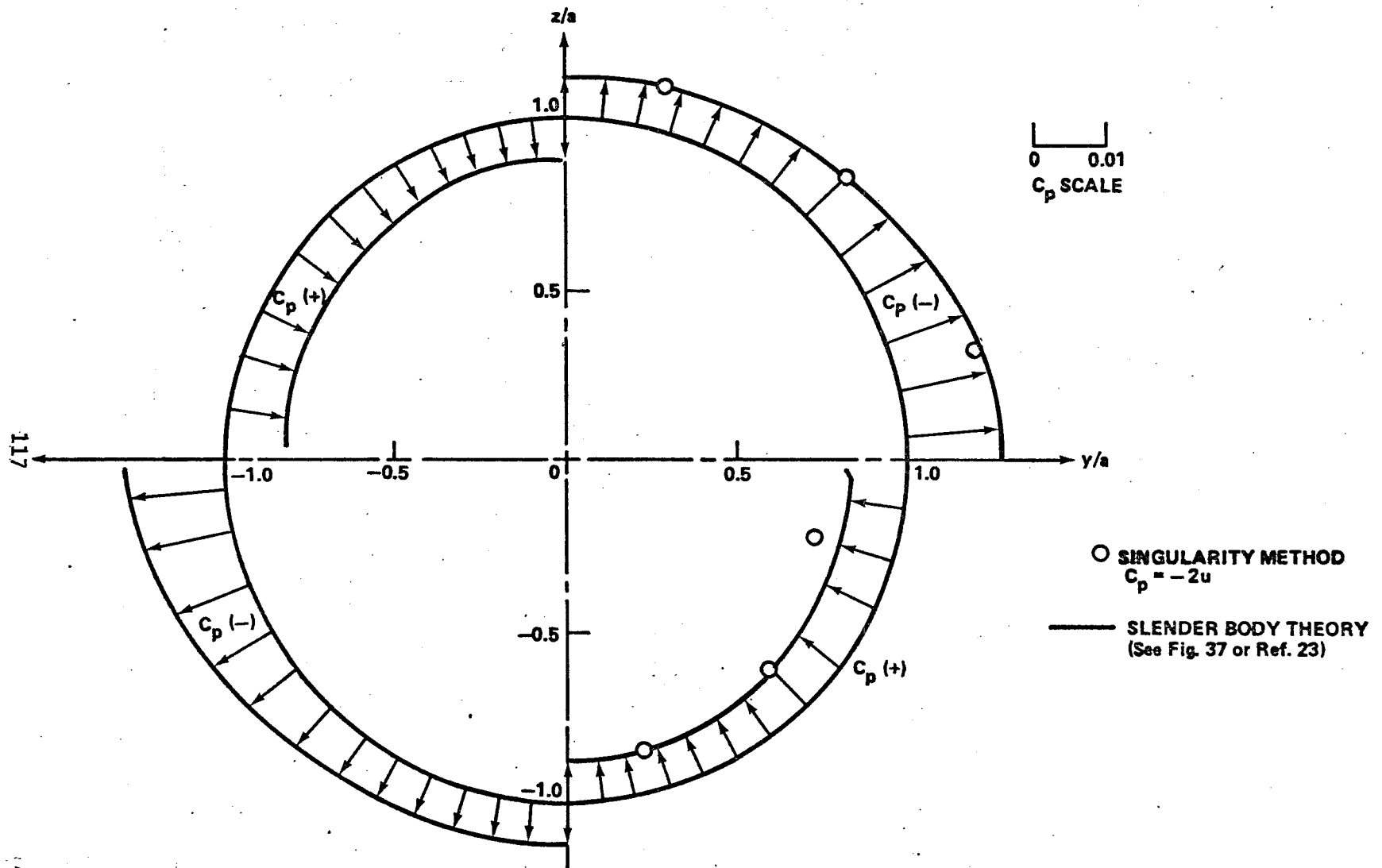
Figure 60.   Comparison with slender body theory on C_p distribution pattern
on body ($-\delta = 3°$, only horizontal fins are canted).
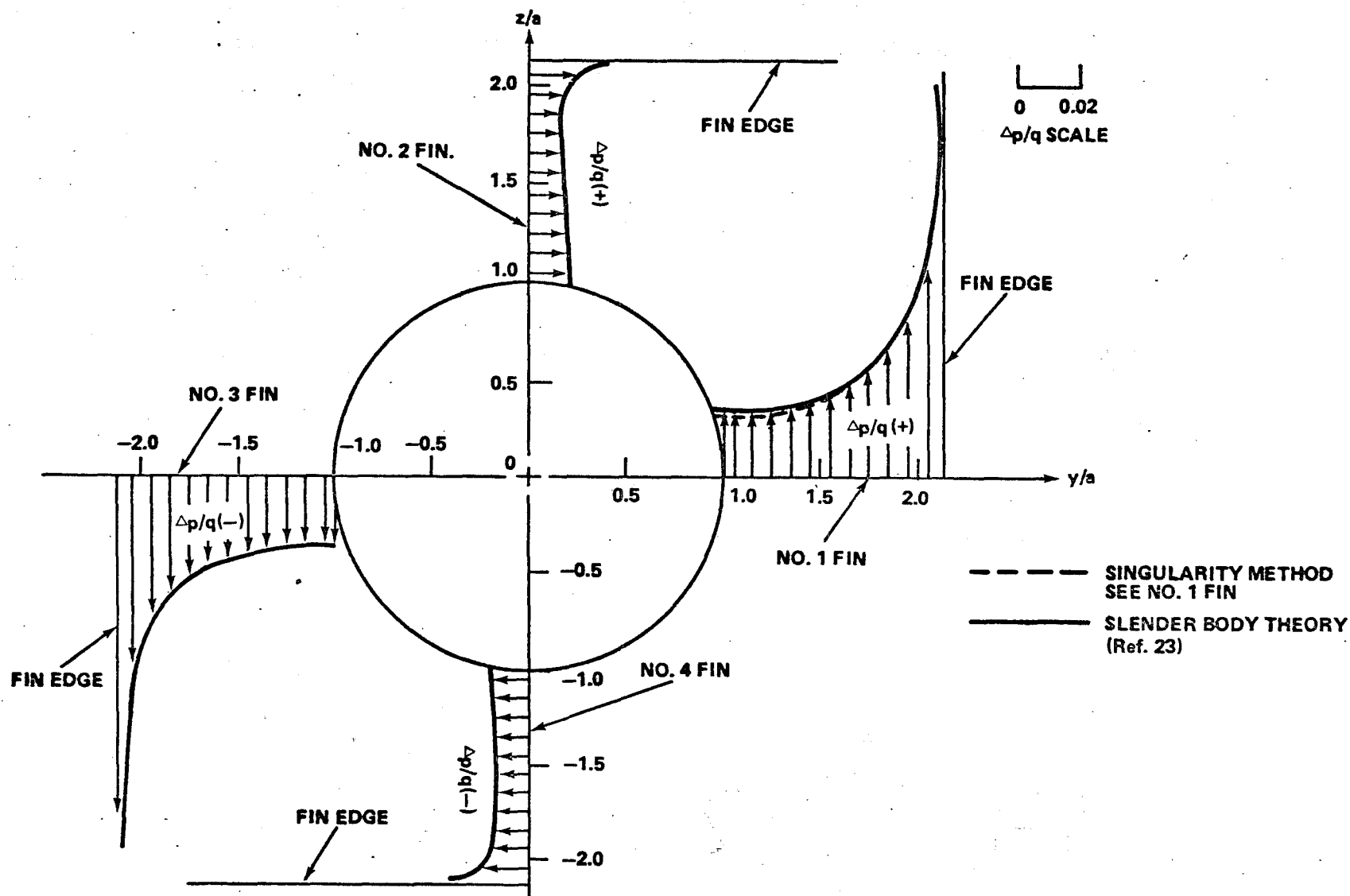
Figure 61. Comparison with slender body theory of load distribution pattern on fins (-δ = 3°, only horizontal fins are canted).

(a) PRESENT PANELING SCHEME (FOR ZERO DEFLECTED FLAP)
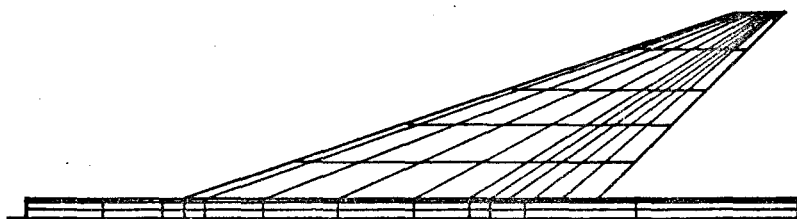
(b) PRESENT PANELING SCHEME (FOR A DEFLECTED FLAP)
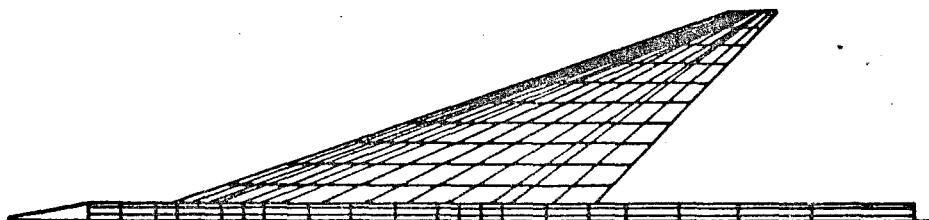
(c) FLEXSTAB PANELING SCHEME. (Ref. 46)

Figure 62.   Paneling schemes.
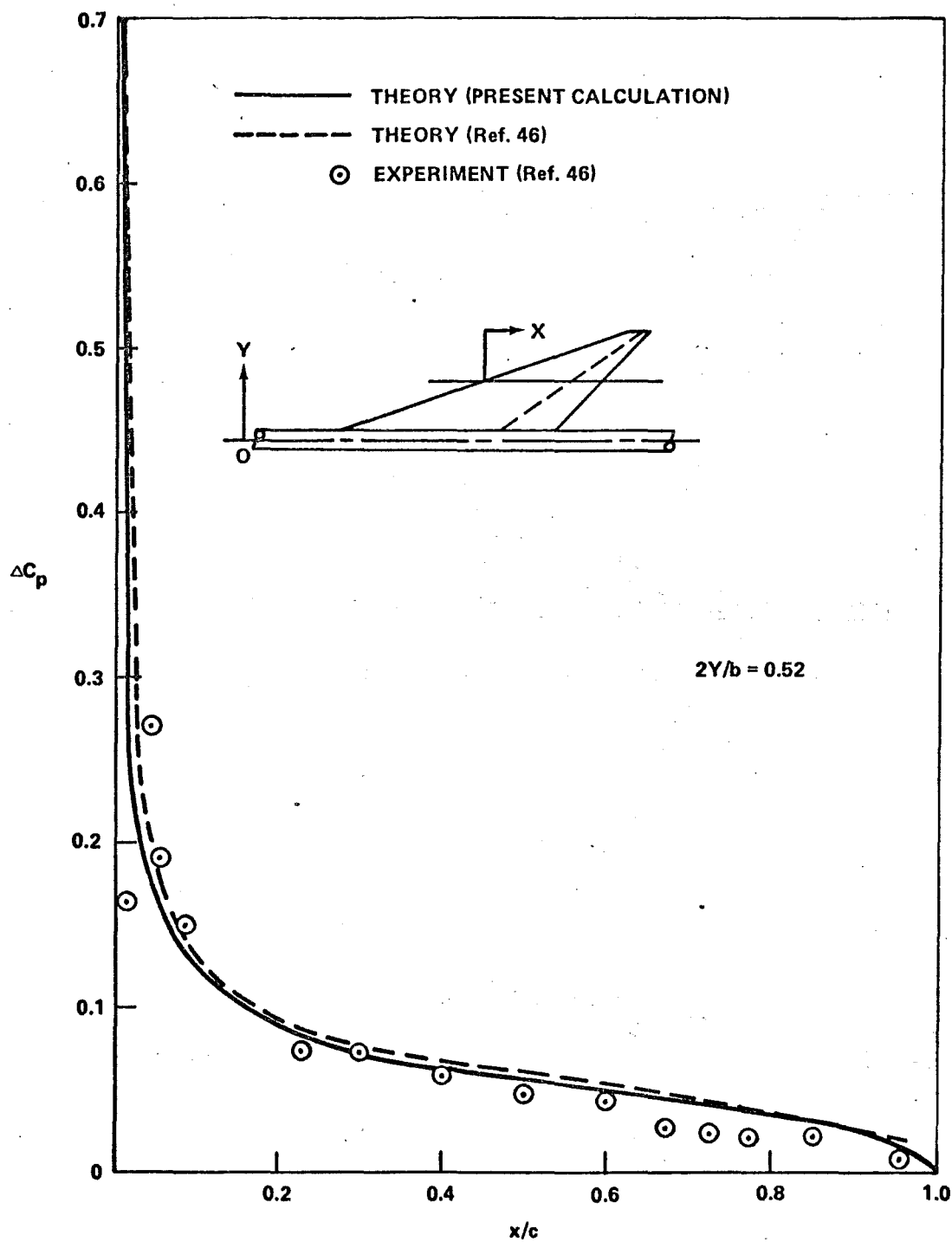
Figure 63.   Flat wing ($\alpha = 2°$, $M_\infty = 0.85$).
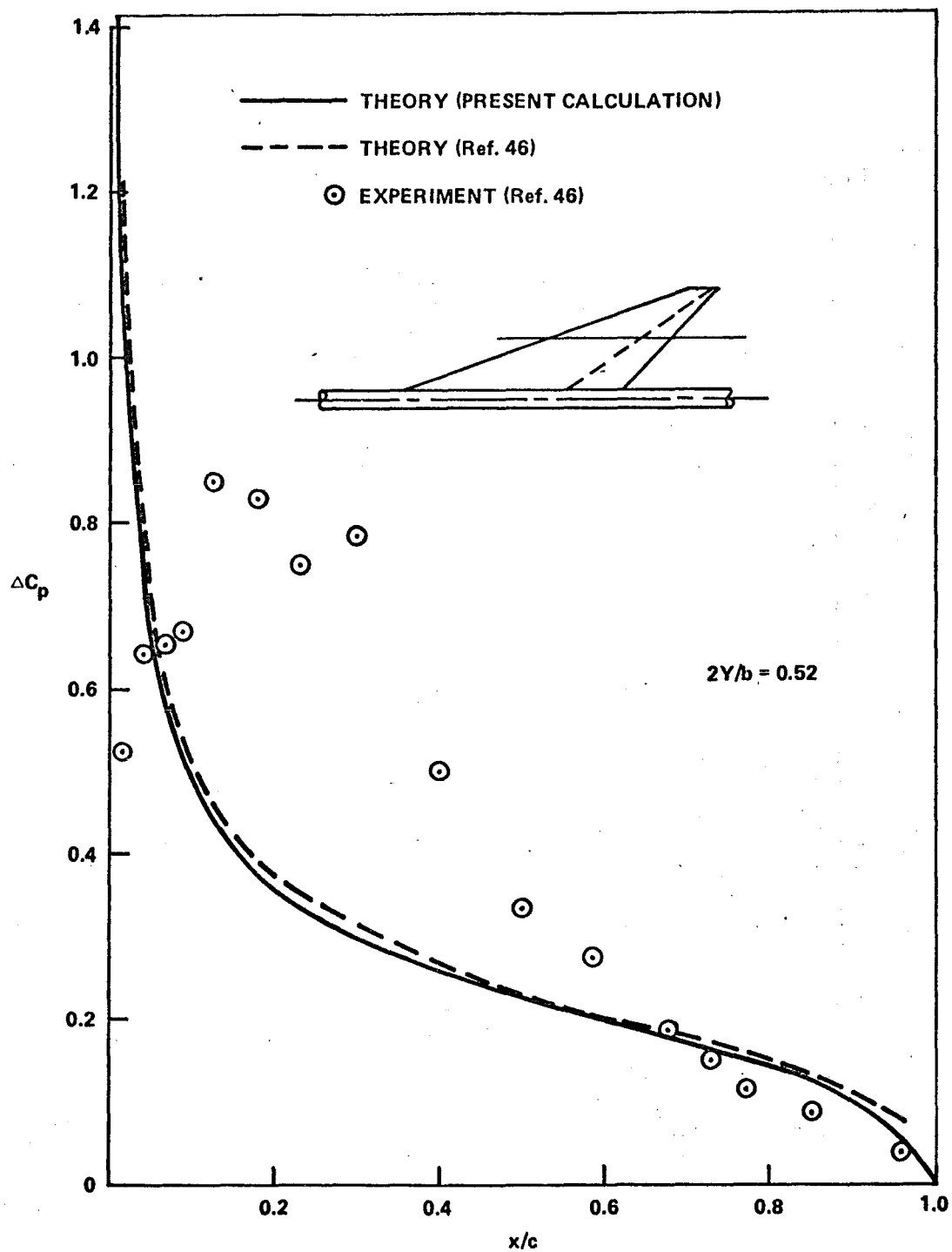
Figure 64.   Flat wing ($\alpha = 8°$, $M_\infty = 0.85$).

121
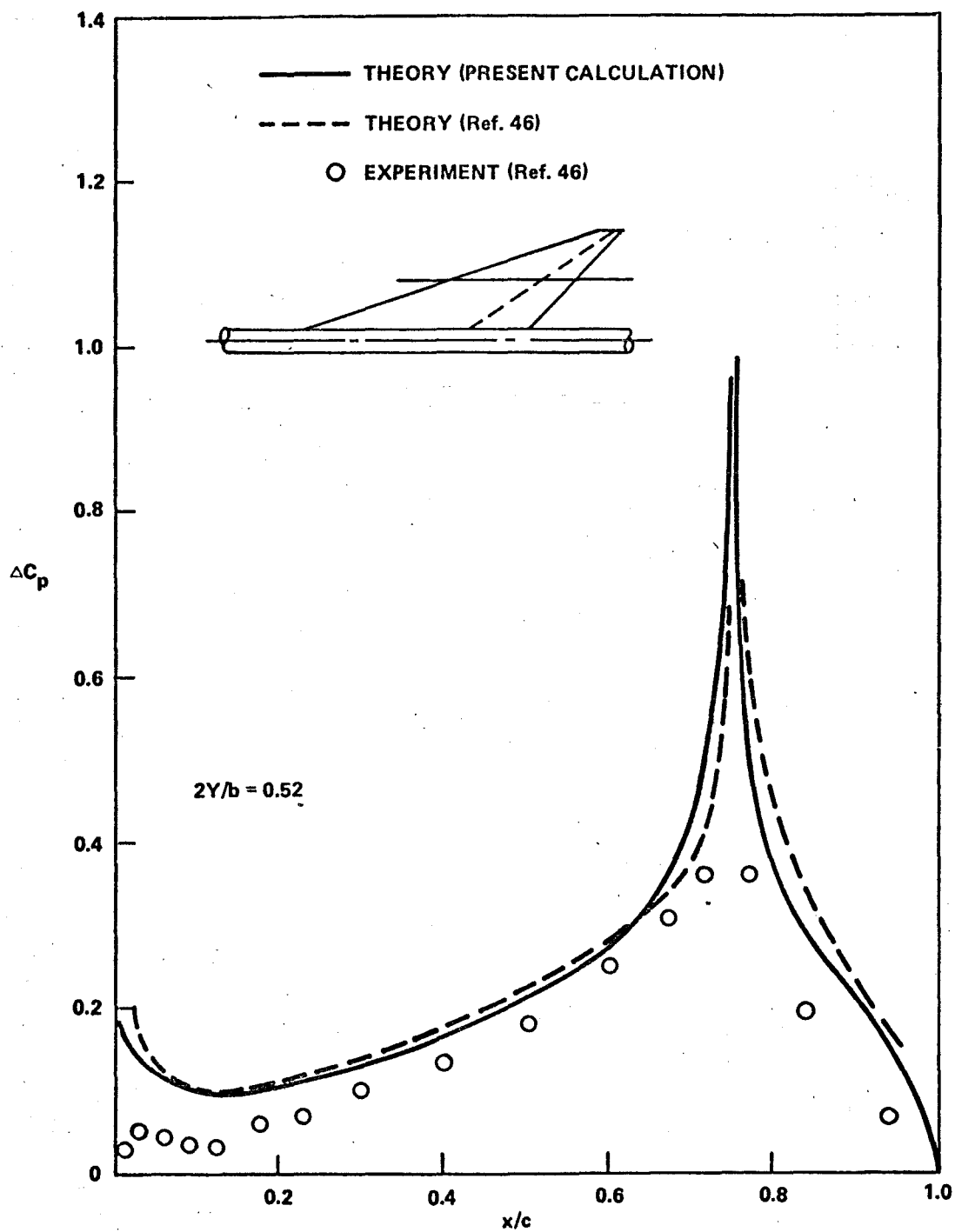
Figure 65. Flat wing with deflected flap (trailing edge δ_F = 8.3°, α = 0°, M_∞ = 0.85).
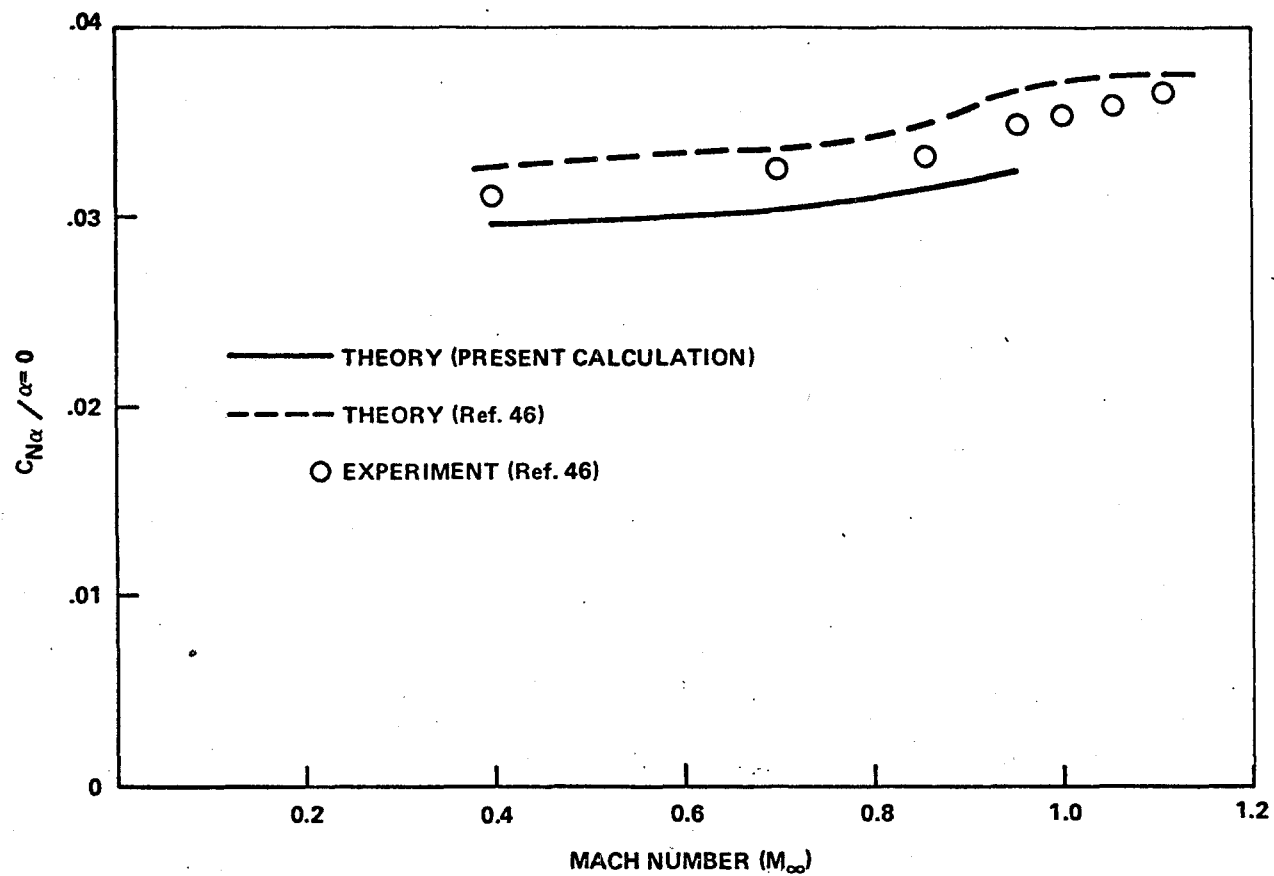
Figure 66. Normal force coefficient.

Figure 67.   Fin-body geometry.
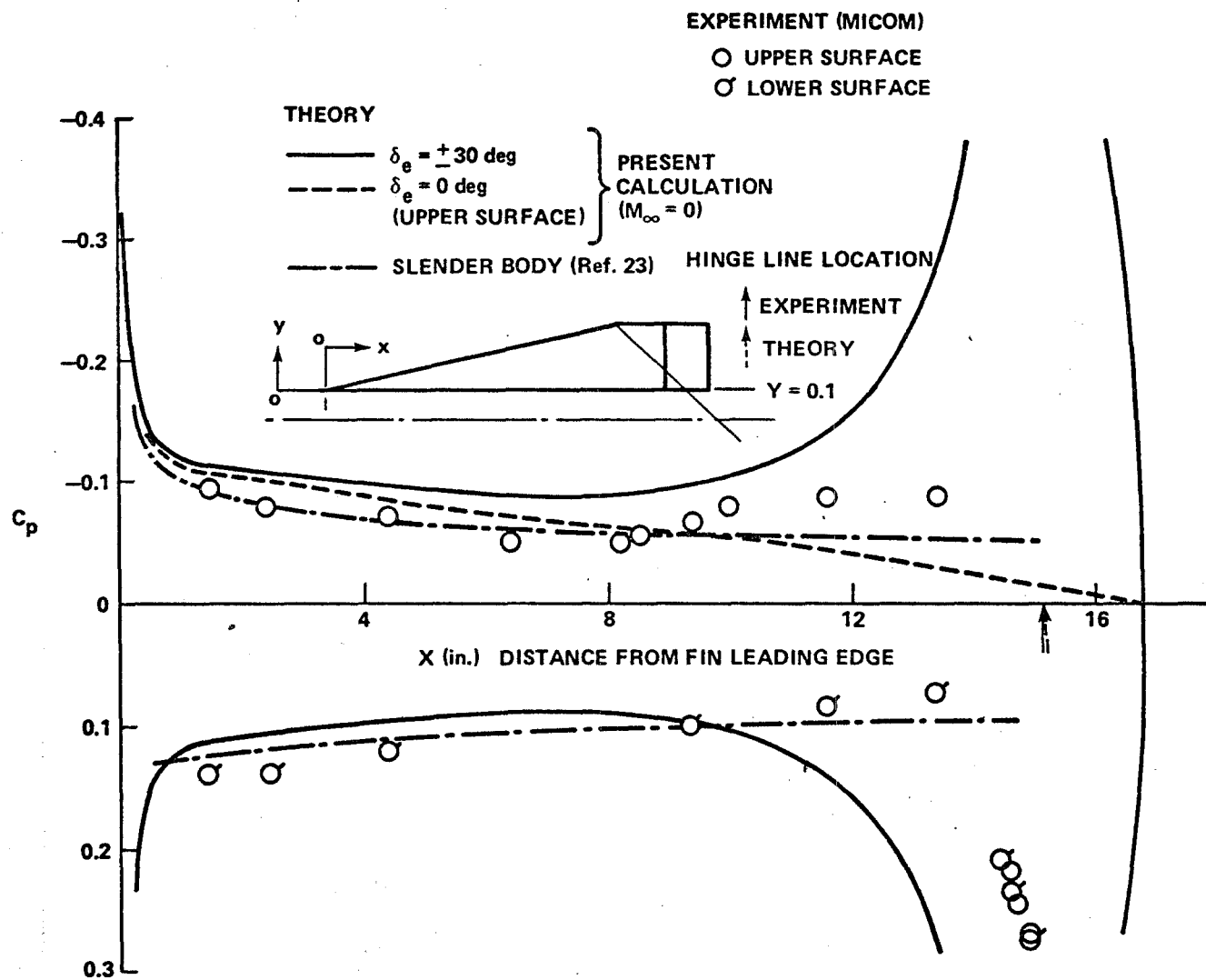
Figure 68. Chordwise C_p distribution on fin: $M_\infty = 1.62$, $\alpha = 8.54°$, $\delta_e = \pm 30°$.
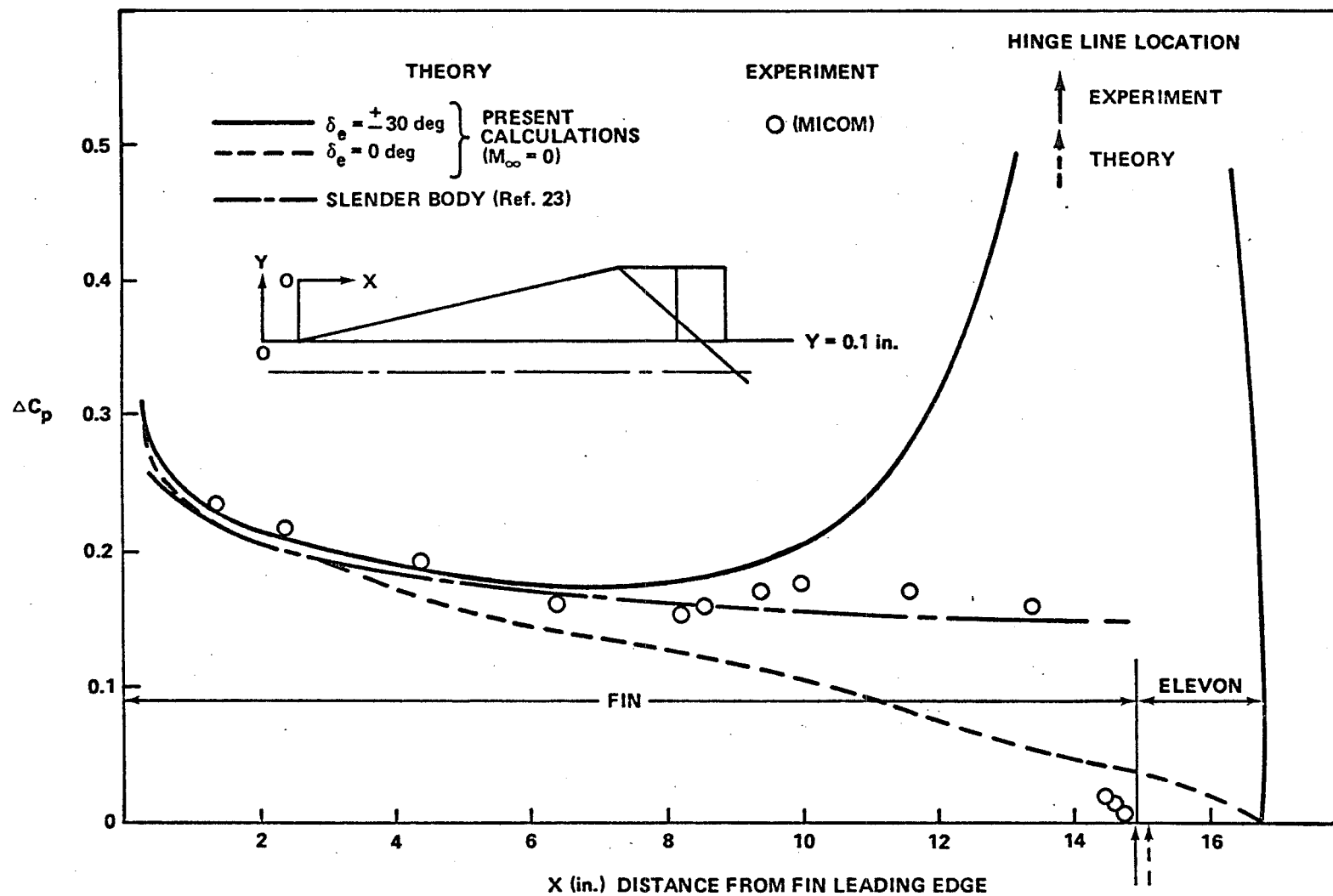
Figure 69. Chordwise load distribution on fin ($M_\infty = 1.62$, $\alpha = 8.54°$, $\delta_e = \pm 30°$): Y = 0.1 in.
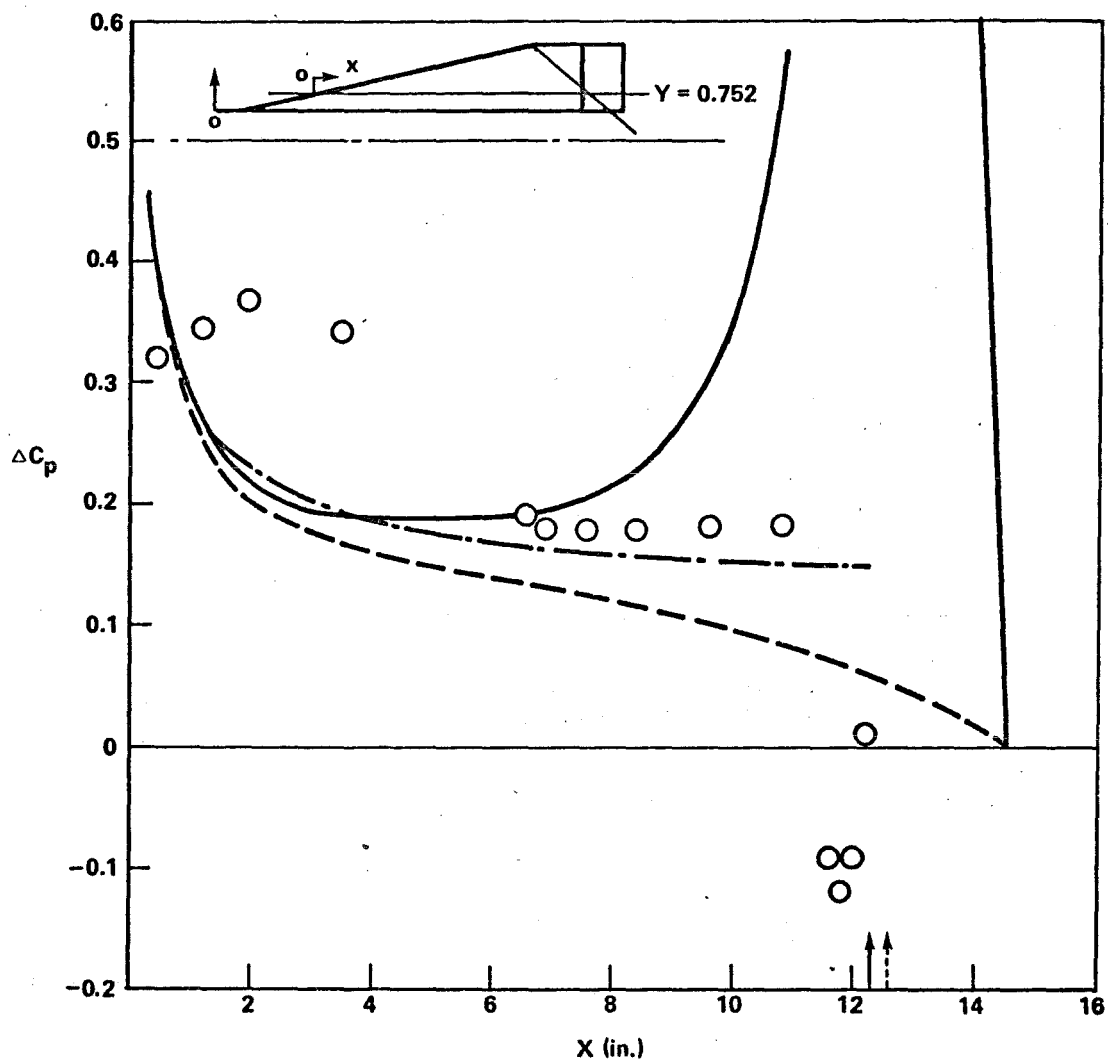
Figure 70. Chordwise load distribution on fin for same conditions
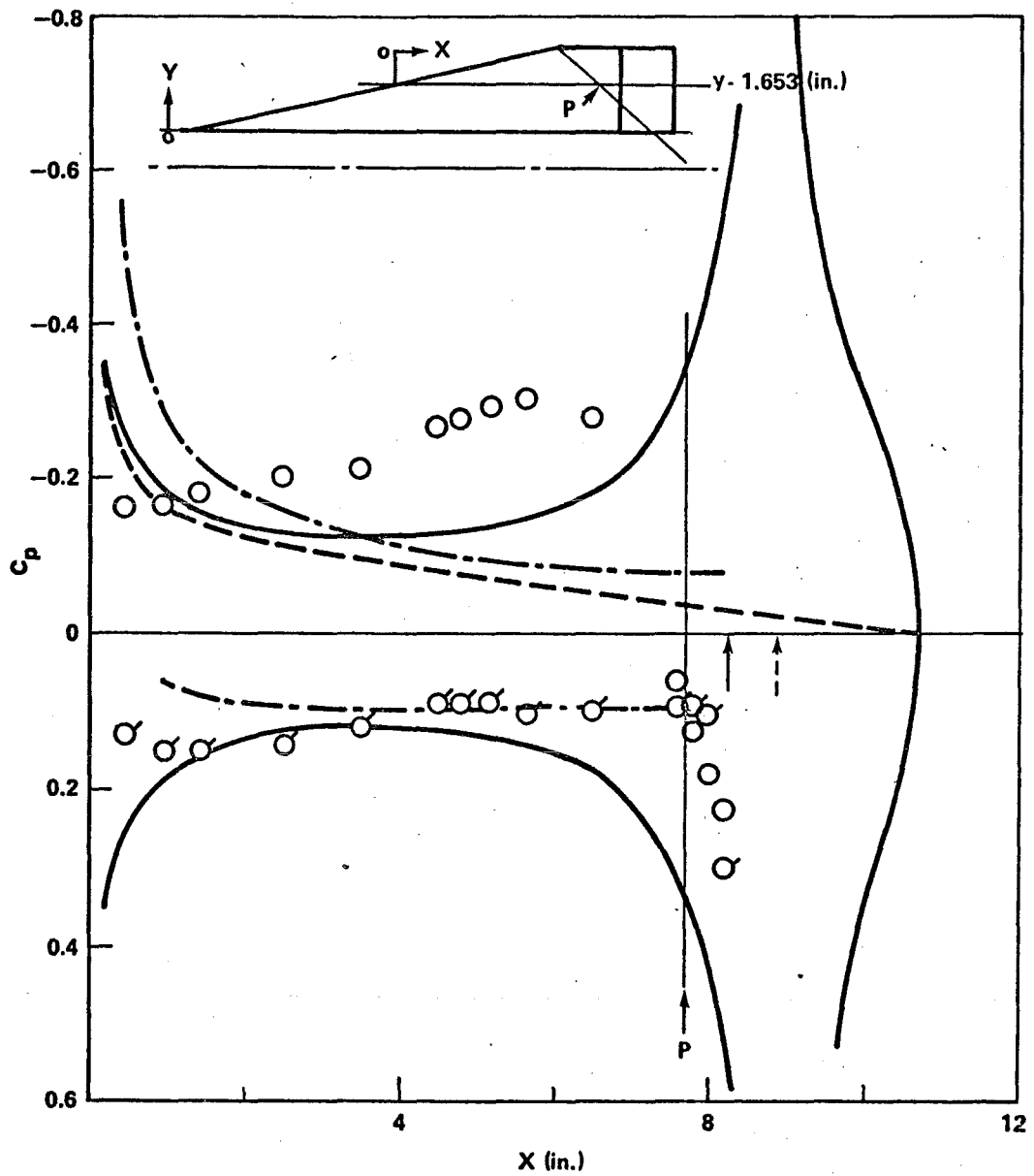as Figure 69. Y = 0.752 in.

Figure 71. Chordwise pressure distribution on fin for same
conditions as Figure 69: Y = 1.653 in.

128
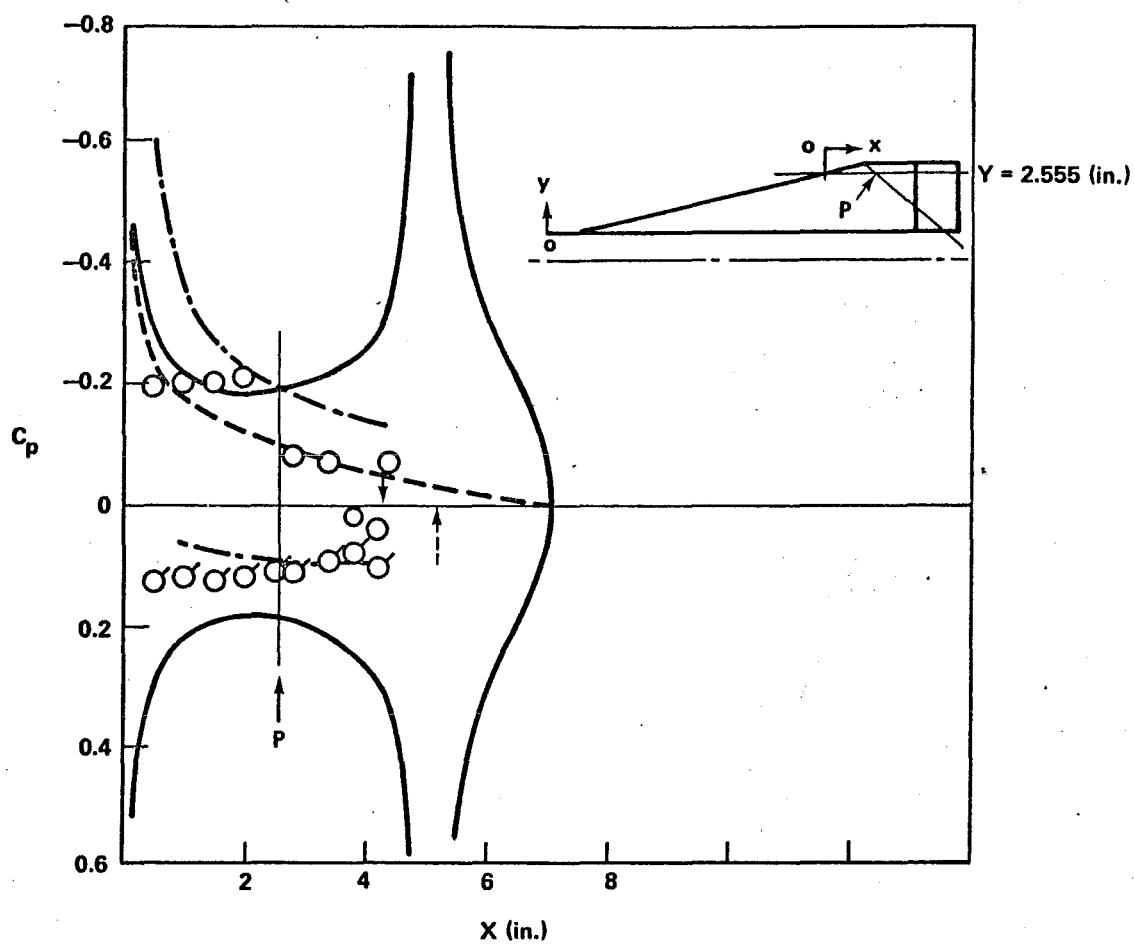
Figure 72. Chordwise pressure distribution on fin for same
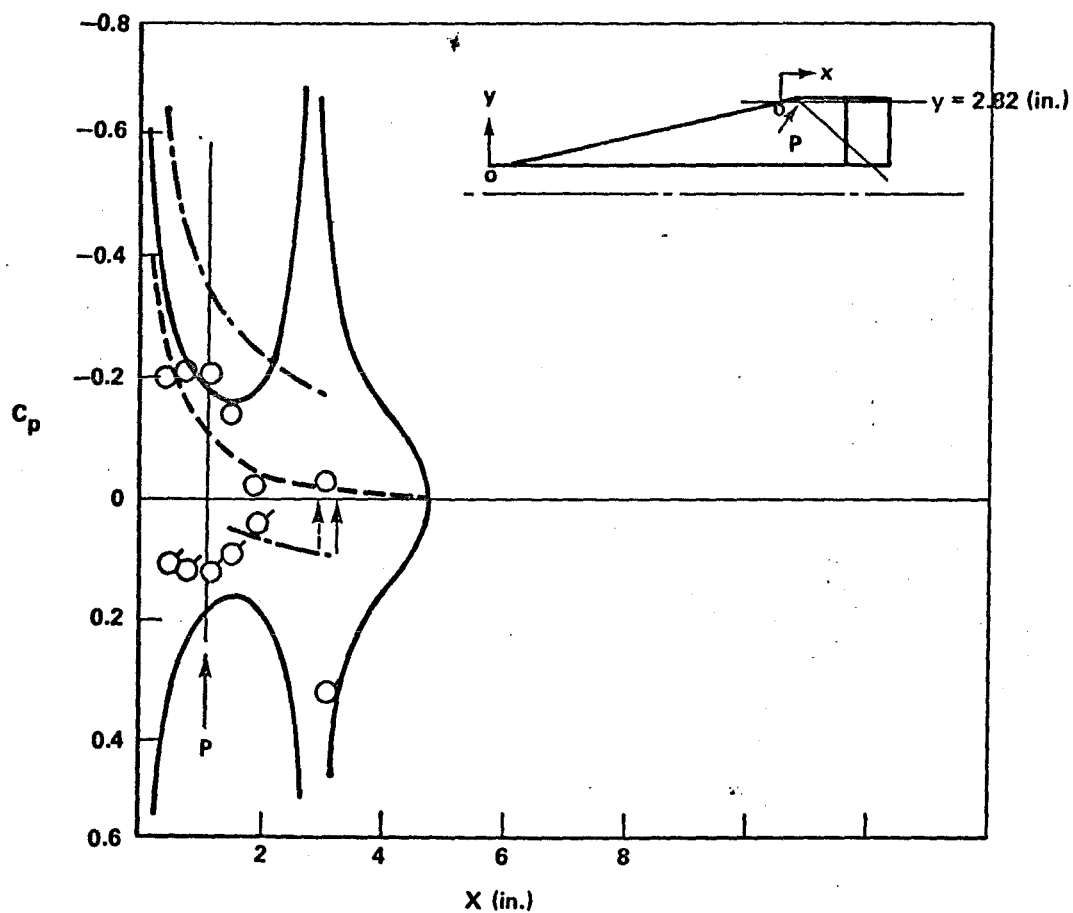conditions as Figure 69: Y = 2.555 in.

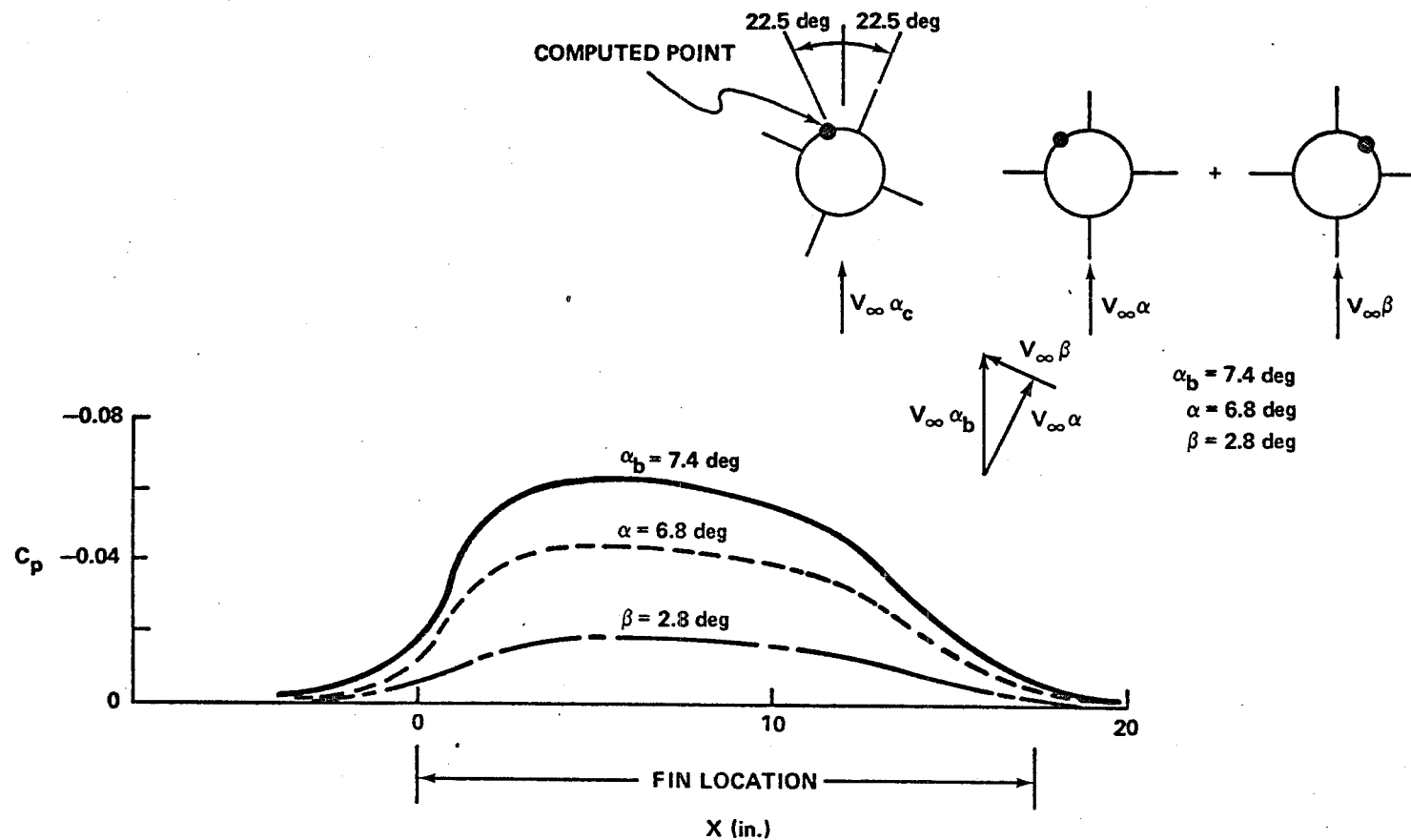Figure 73. Chordwise pressure distribution on fin for same conditions as Figure 69: Y = 2.82 in.

Figure 74. Longitudinal pressure distribution on body with angle
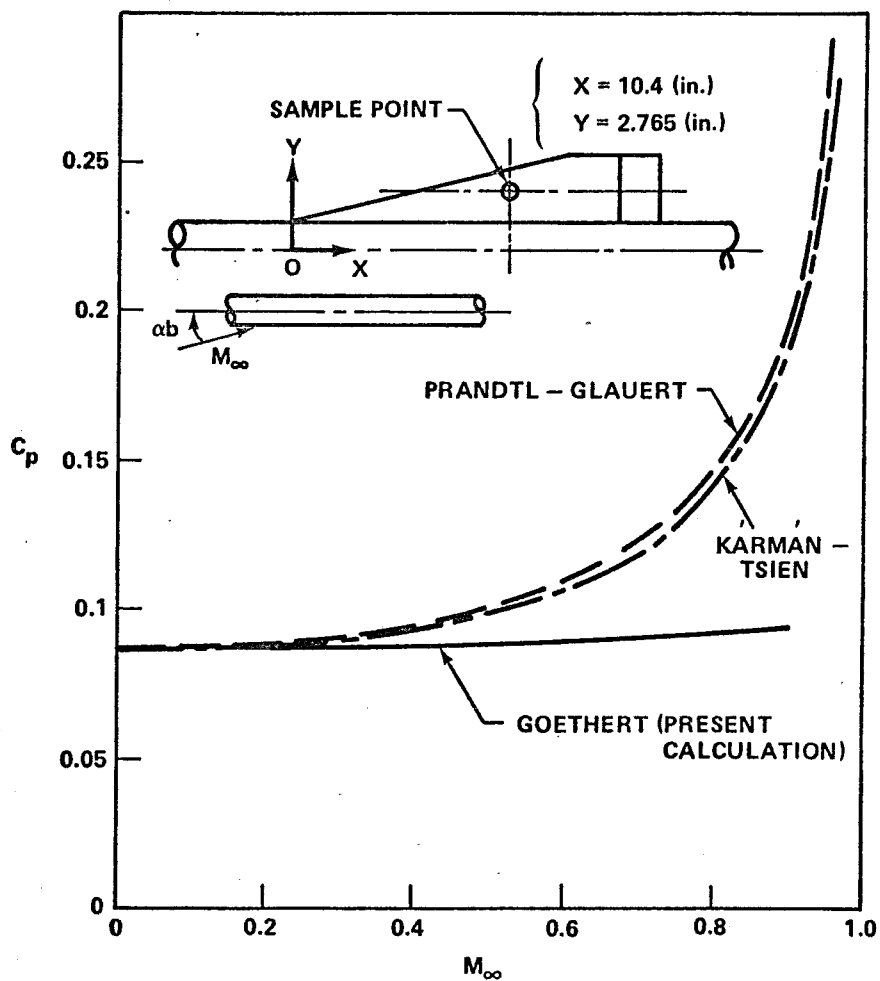of attack and yaw (0° elevon deflection angle).

Figure 75. Comparison of compressibility effect of present result with other similarity rules ($\alpha_b = 8.5°$).
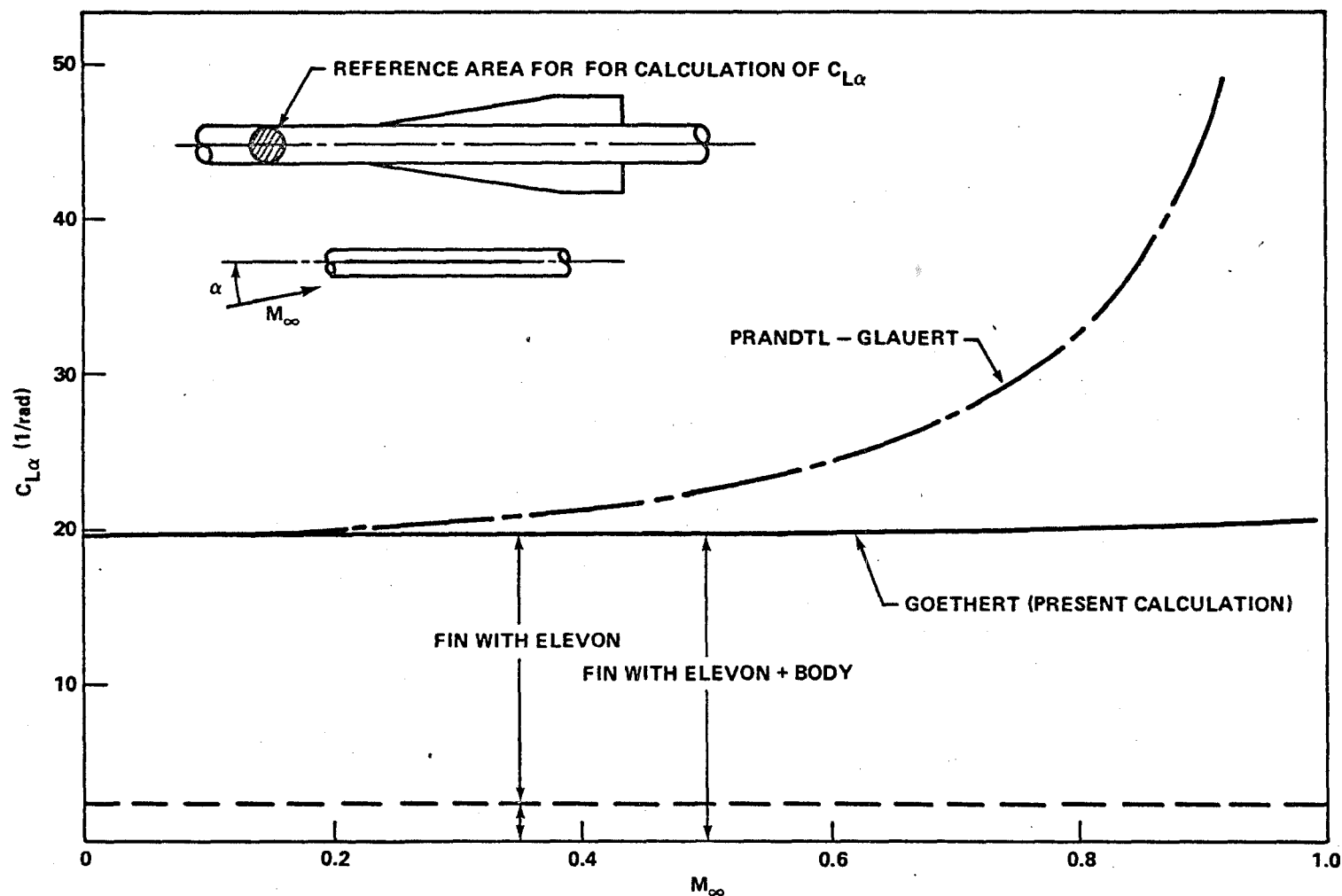
Figure 76. Variation of lift coefficient of fin-body combination with changing free-stream Mach number.
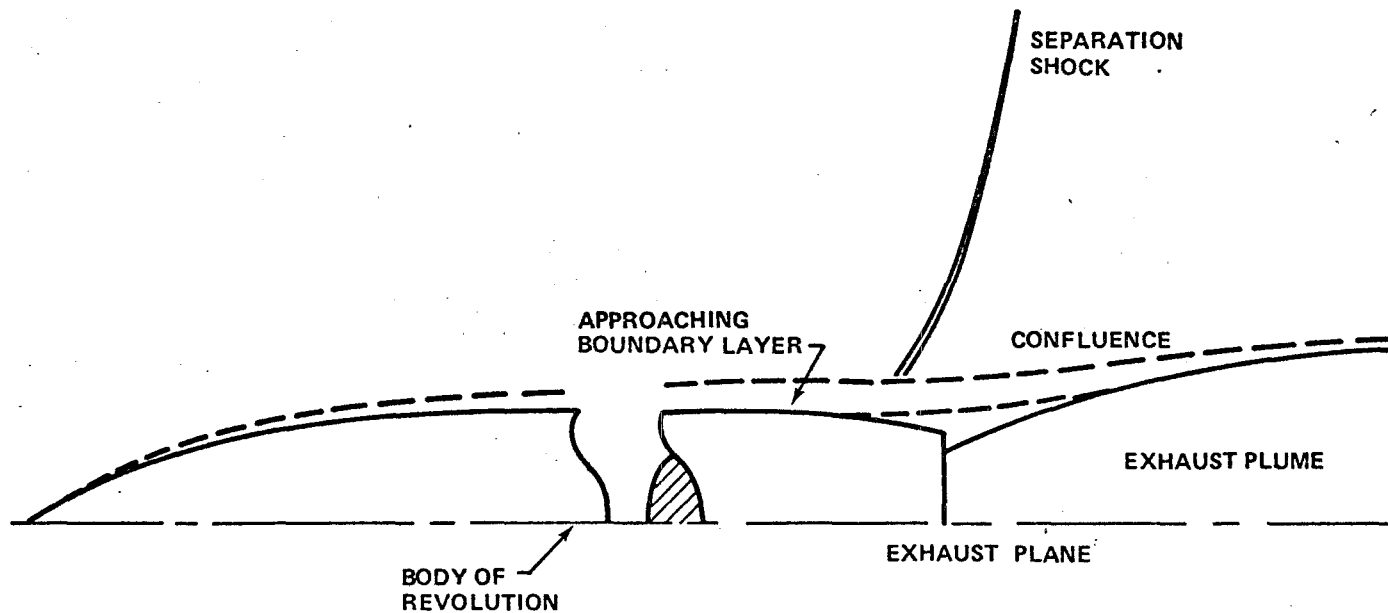
Figure 77. Diagram showing the major features of the viscous flow interaction.
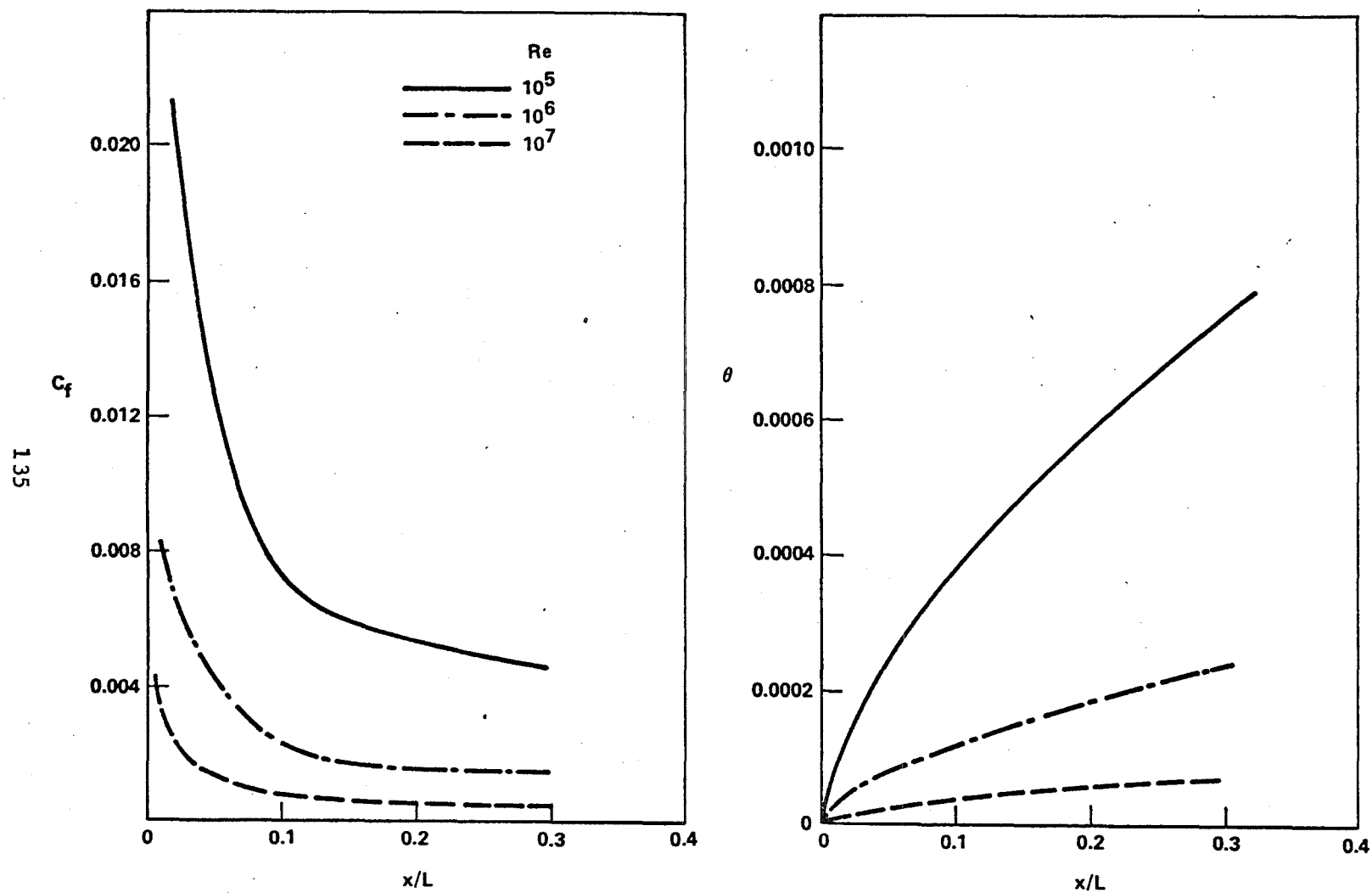
Figure 78.   Laminar boundary layer development on ogive forebody at $M_\infty = 1.1$.
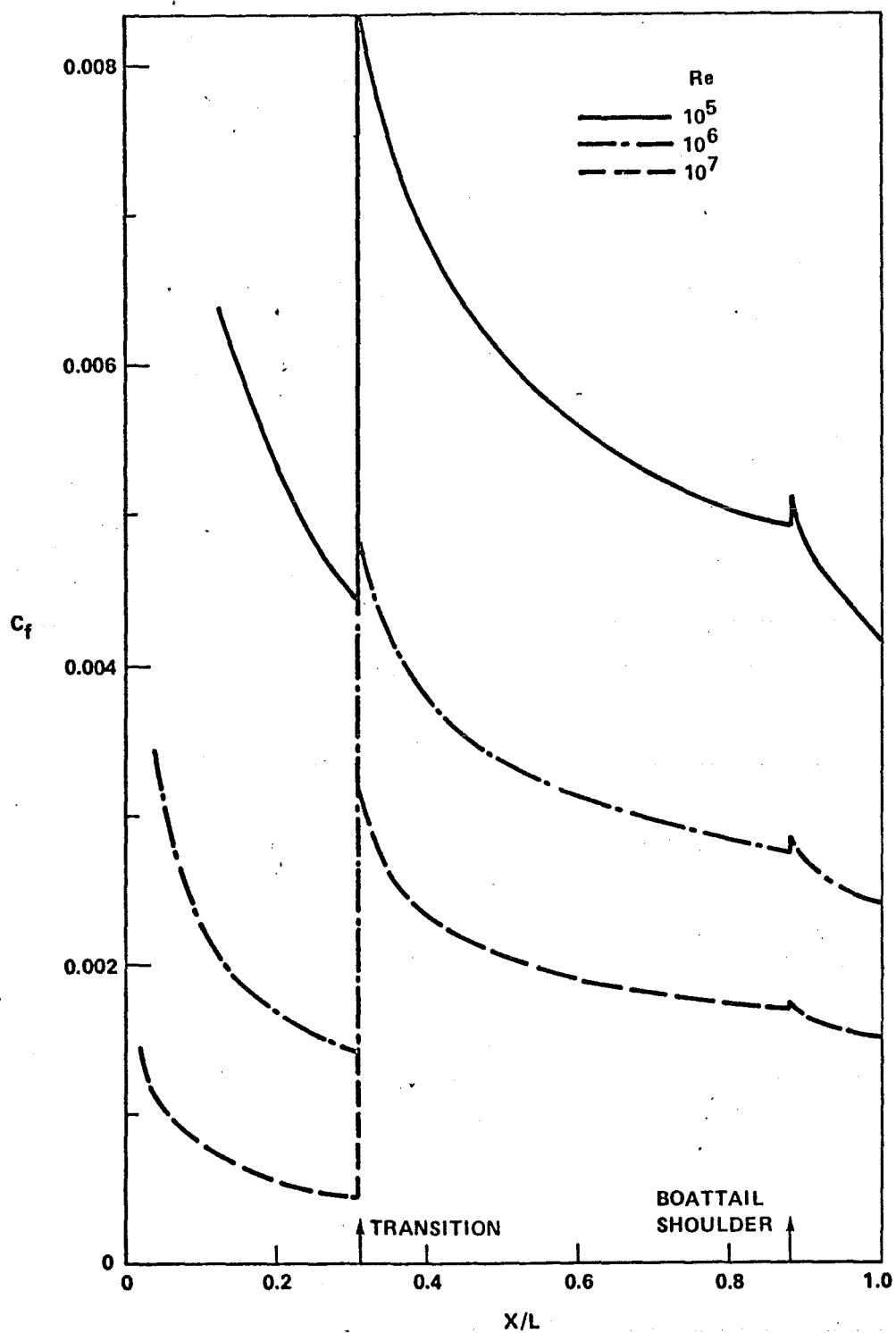
Figure 79. Calculated skin friction on a body of revolution
with a boattail: free-stream mach number = 1.1, body B1.
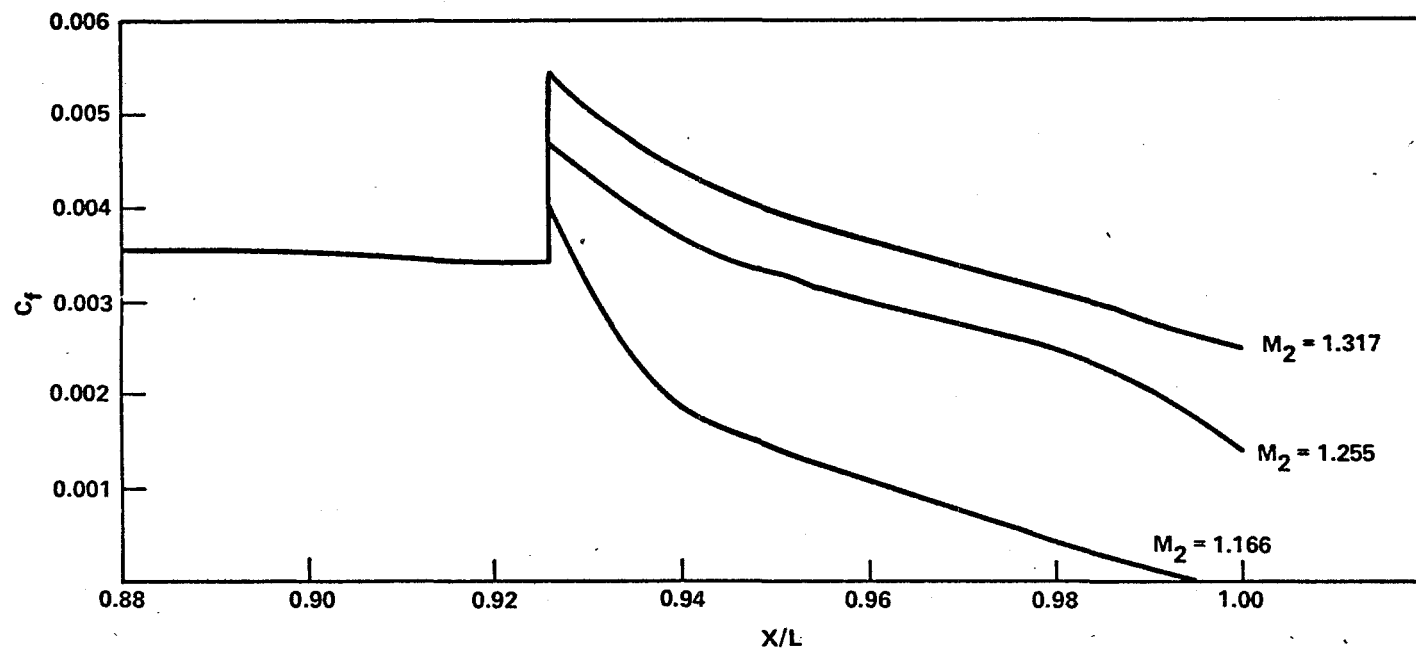
Figure 80. Calculated skin friction distribution of a conical boattail for different assumed Mach numbers (M_2) at the end of the boattail shoulder expansion: body B4.
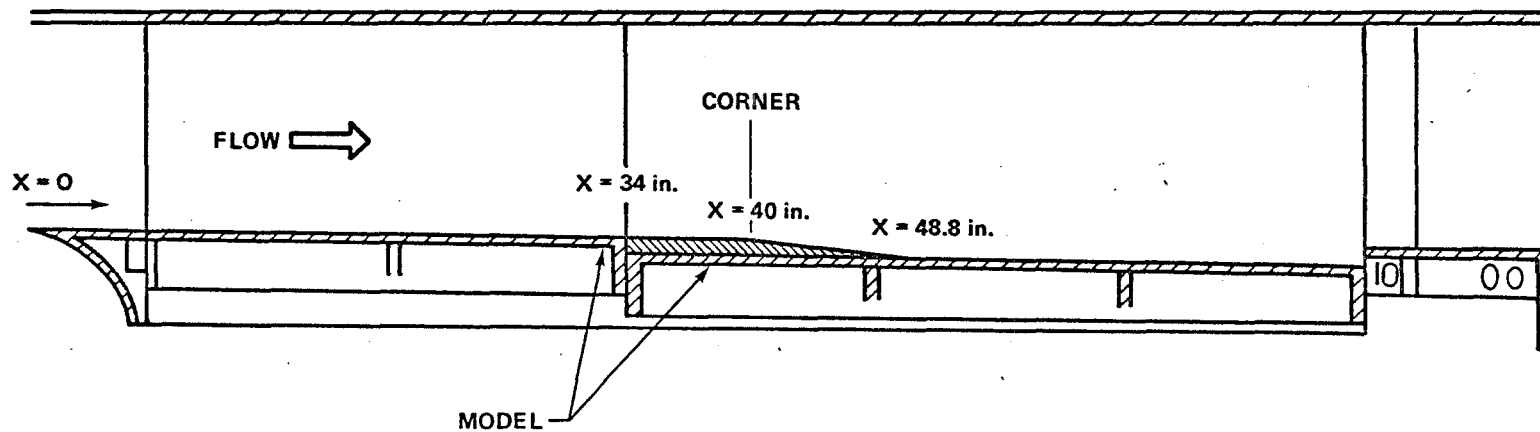
Figure 81. Diagram showing expansion corner model mounted
in the UTSI transonic flow facility.
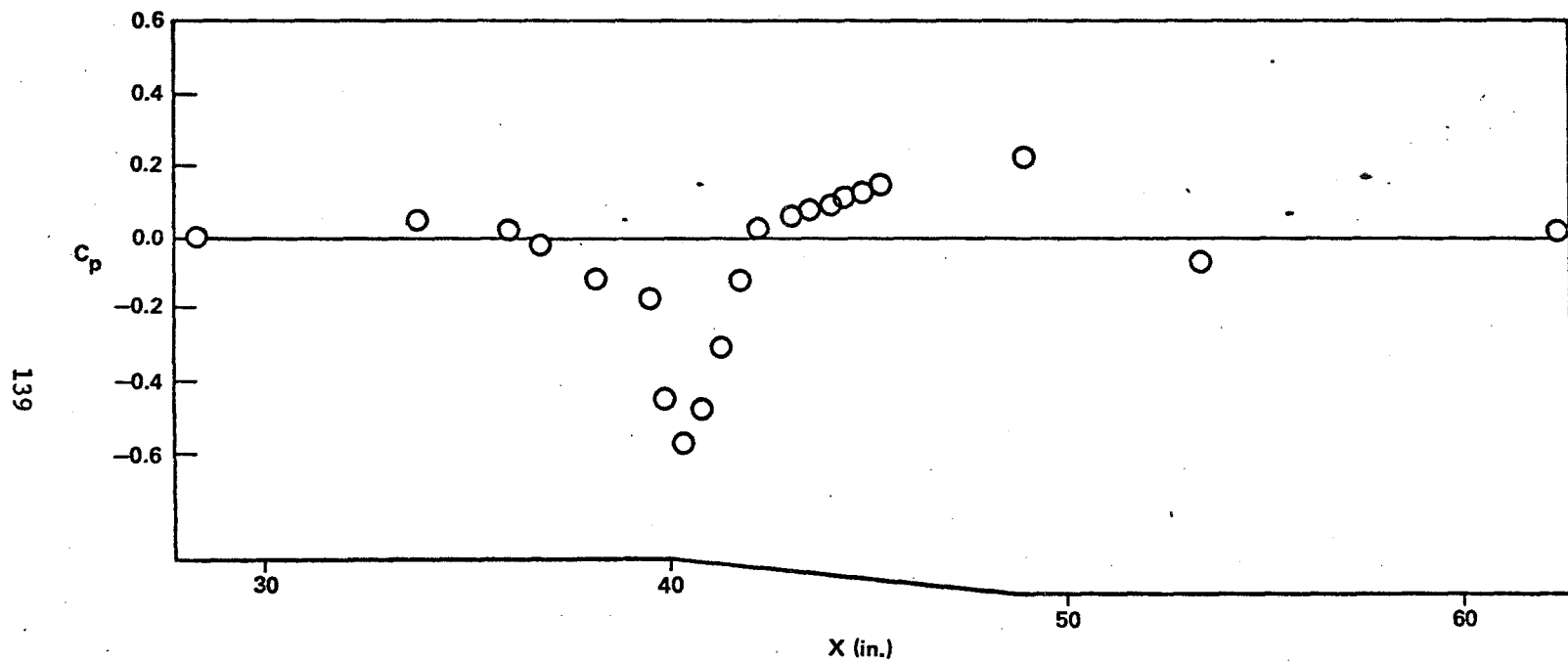
Figure 82. Measured surface pressure distribution over 6.5° expansion corner at a free-stream Mach number of 0.9.
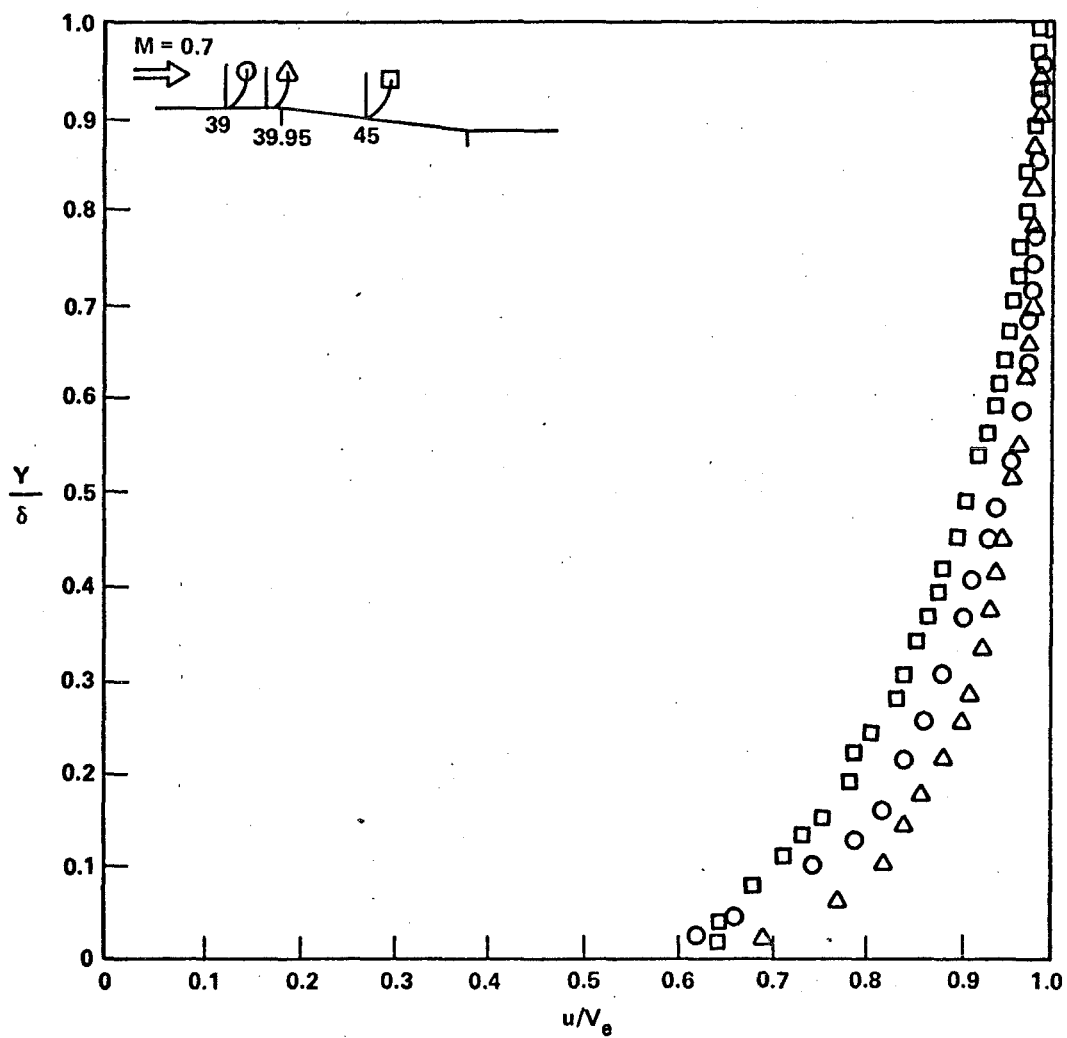
Figure 83. Measured velocity profiles over a 6.5° expansion corner when the approach Mach number is 0.7: corner is located at 40 in.
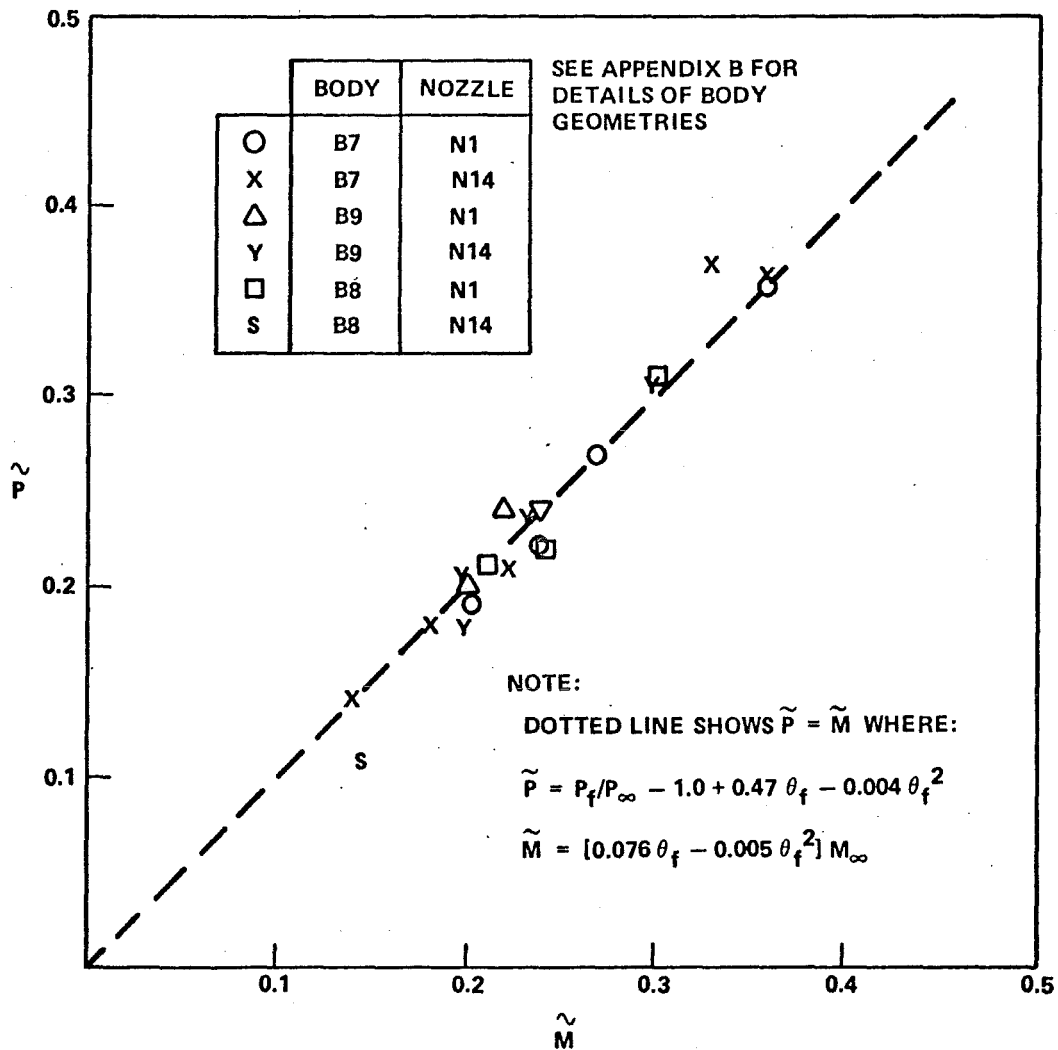
Figure 84. Flare junction pressure correlation from the data of Reference 60.

$$\psi\,(\eta)\;=\;\psi_{ref} + \frac{\rho_e\,u_e}{\sigma}\;\;(G_{ref} - G\,(\eta))\;\sqrt{\pi}$$
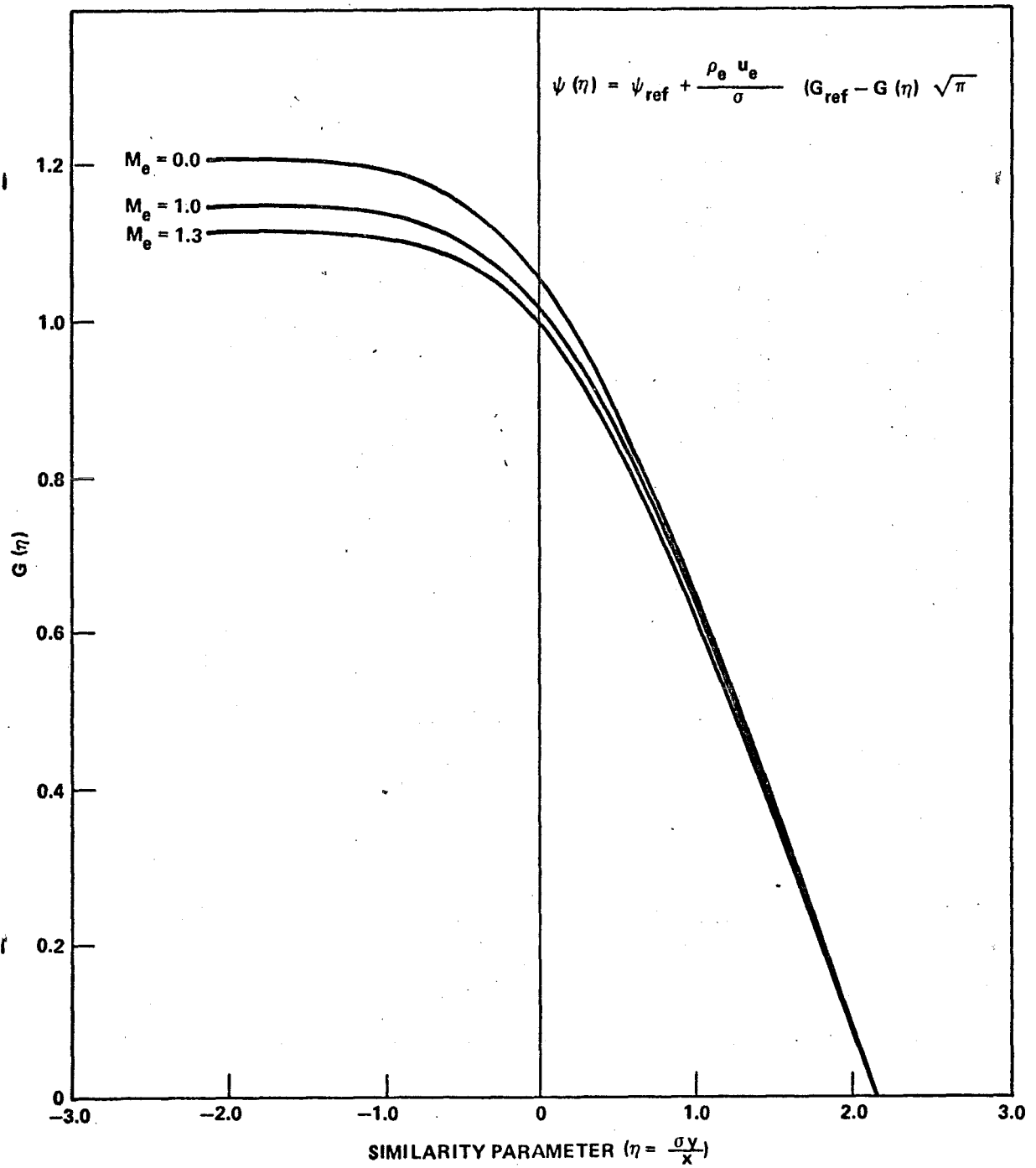
Figure 85. Distribution of streamlines in shear layer for various external Mach numbers.

142
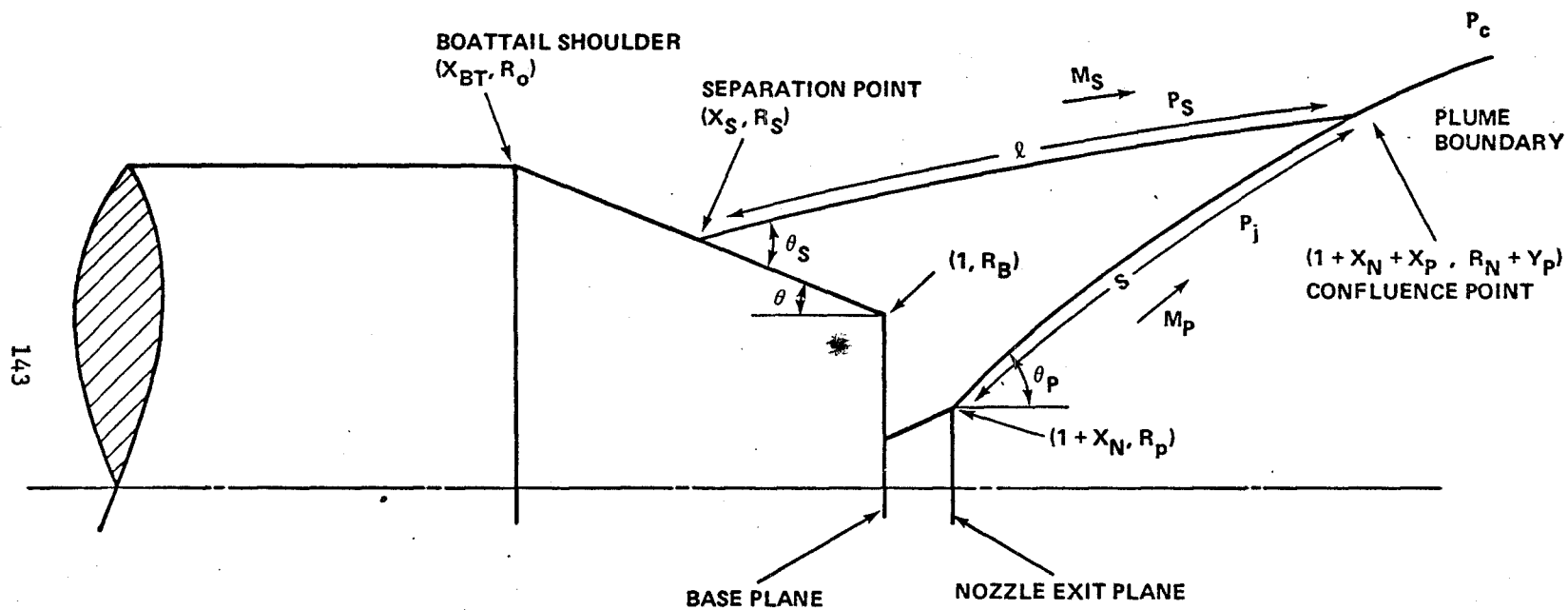
Figure 86. Some geometry of the interaction region.
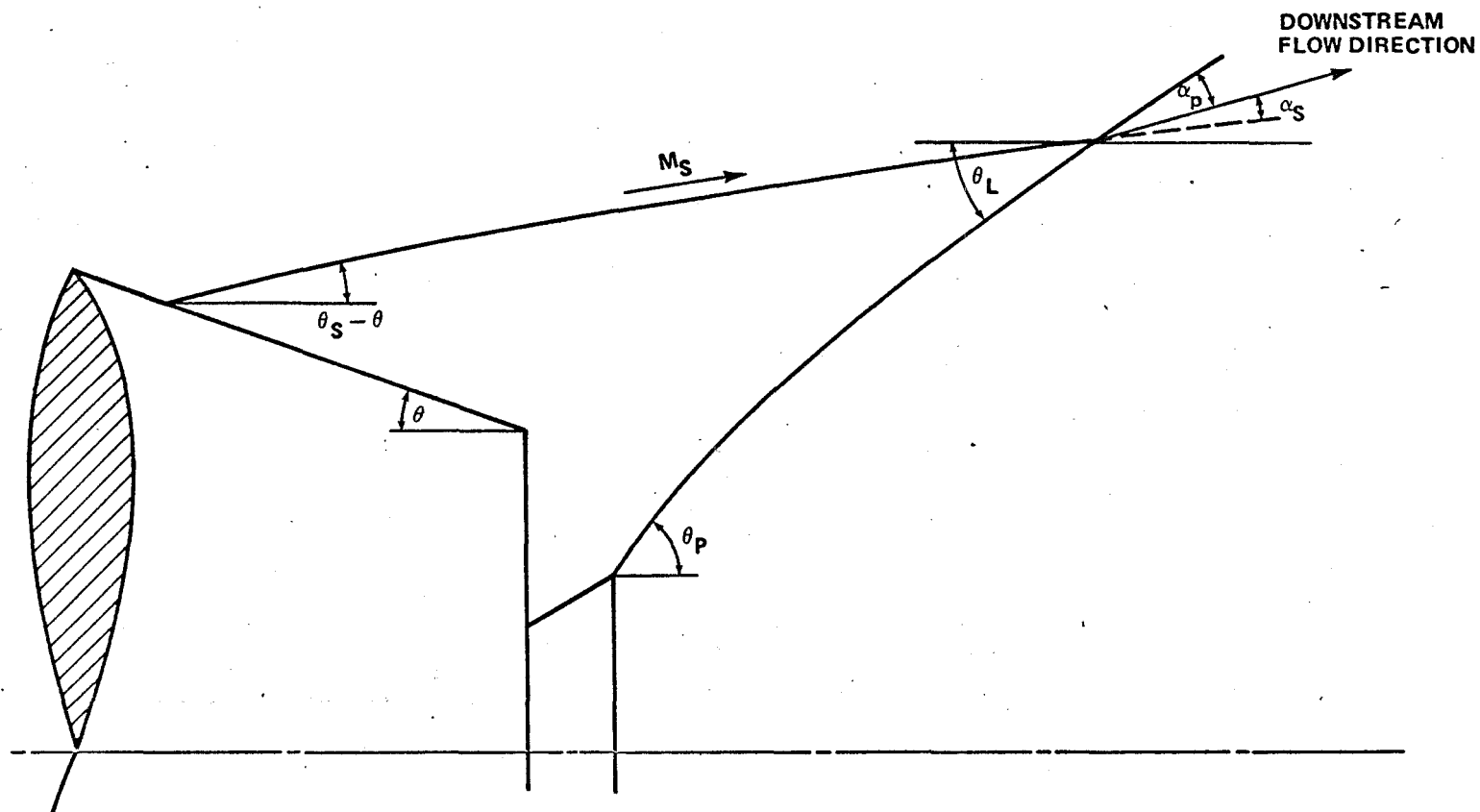
Figure 87. Definition of certain angles in the interaction.
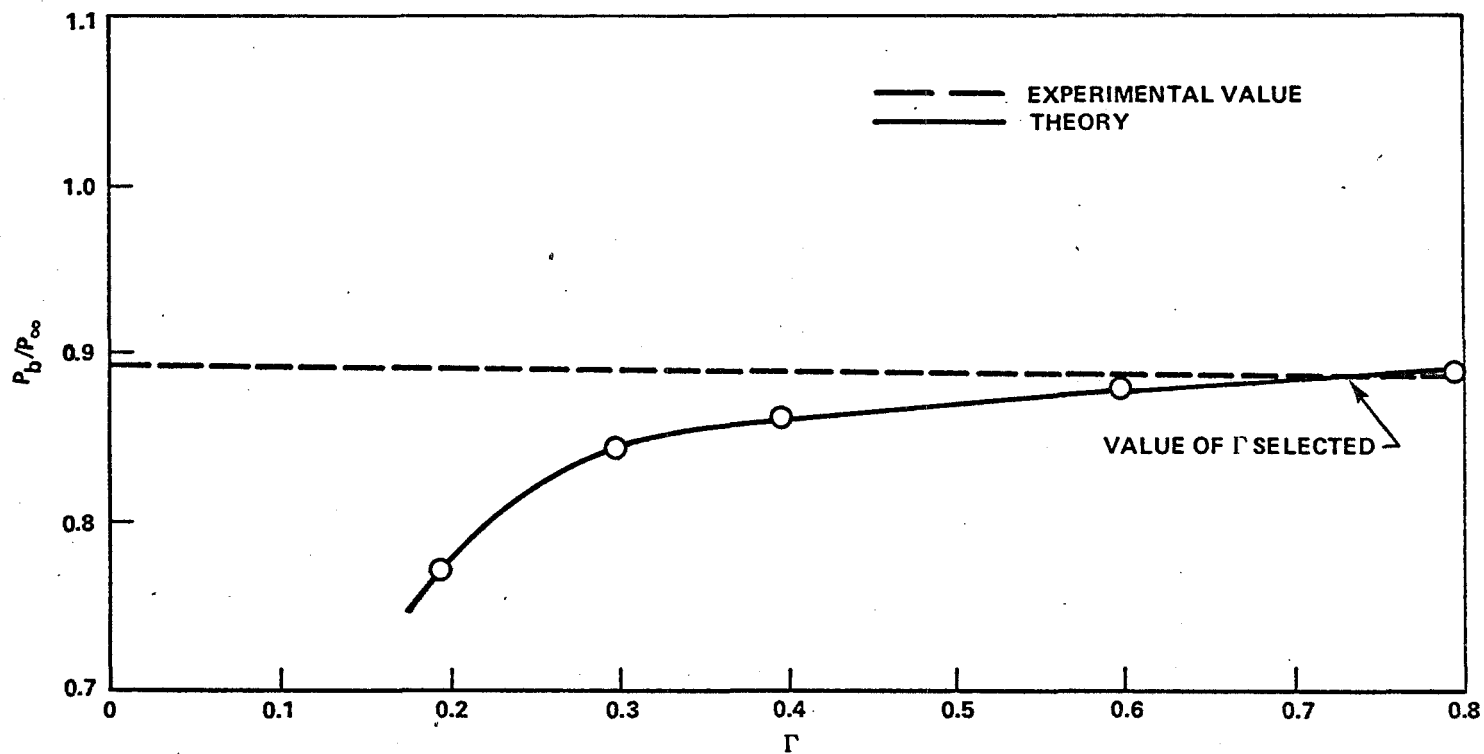
Figure 88. Typical curve showing the variation of base pressure with the coefficient Γ, and the selection of the empirical value: body B1 with nozzle N1, jet pressure ratio = 24.5.
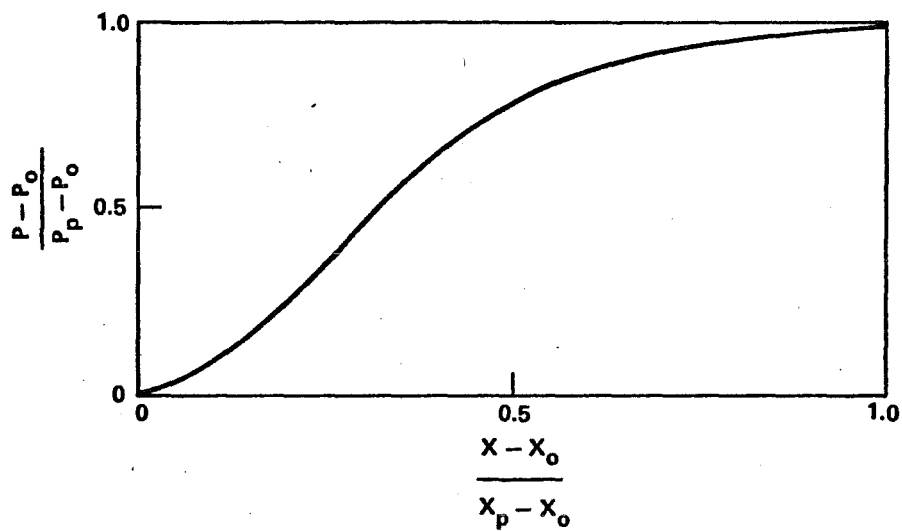
Figure 89. Correlation of pressure rise to separation.
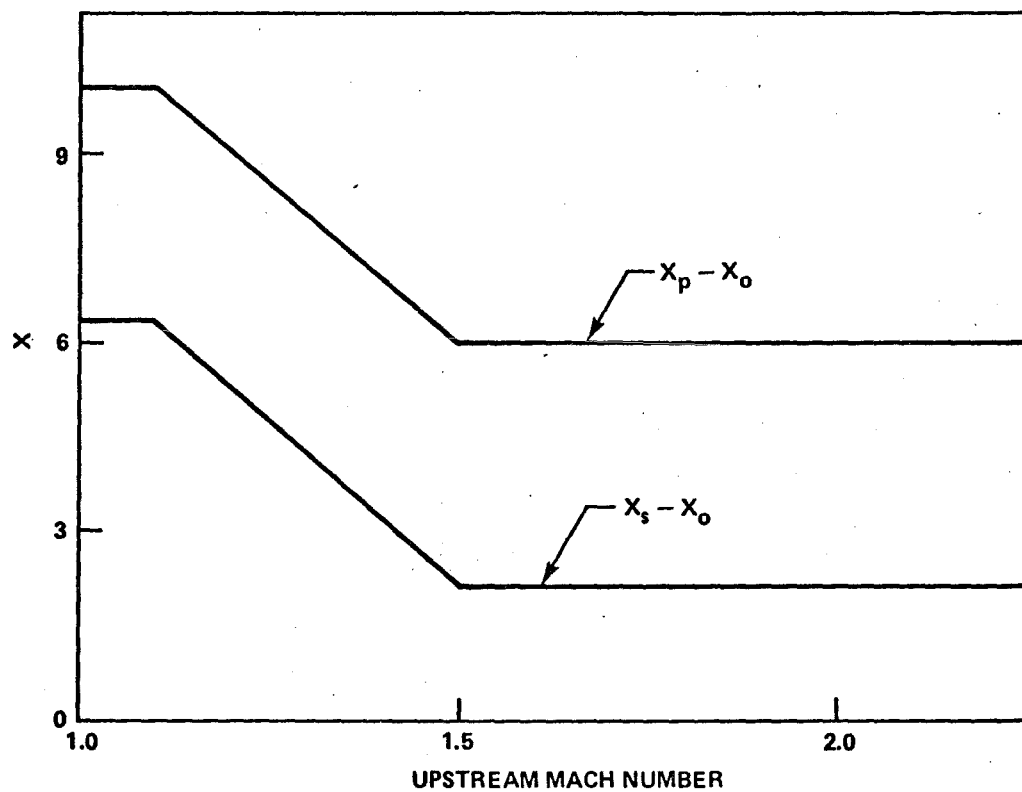
Figure 90.   Specification of the interaction
lengths for transonic flow.
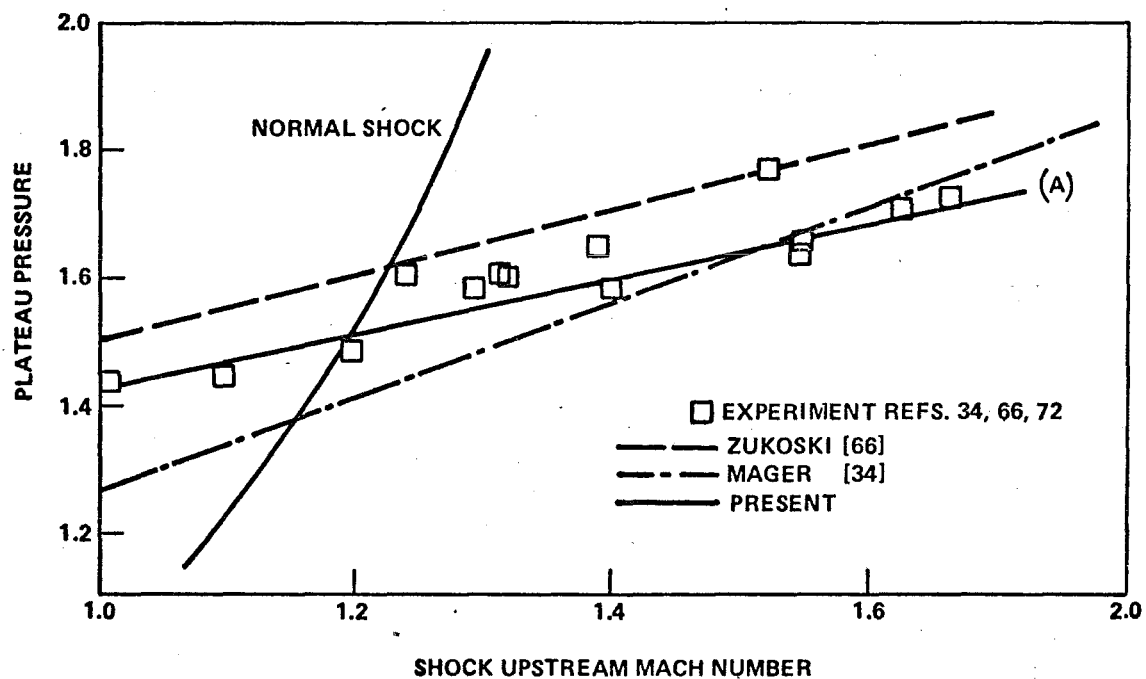
Figure 91.   Estimates of the plateau pressure
for transonic flow.

148
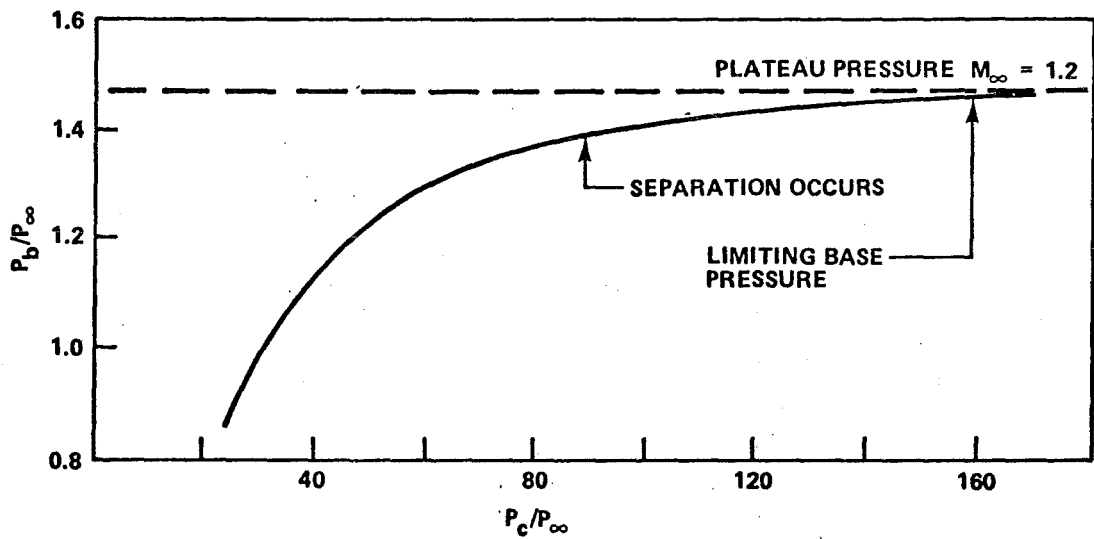
Figure 92. A typical variation of base pressure with jet
pressure ratio showing the onset of separation and the
limiting value of base pressure: body B1 with nozzle N1.
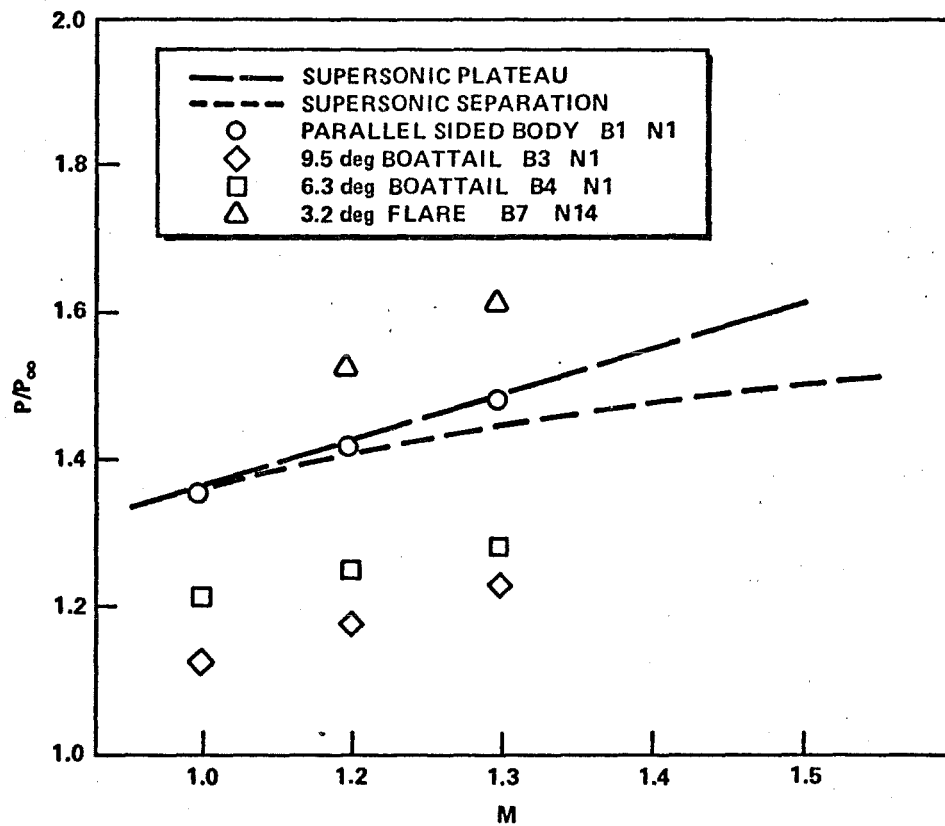
Figure 93(a). Separation and plateau pressure ratios for supersonic flow over various bodies of revolution [60].

$$Ps/P_\infty = 0.795 + 0.565M_0$$
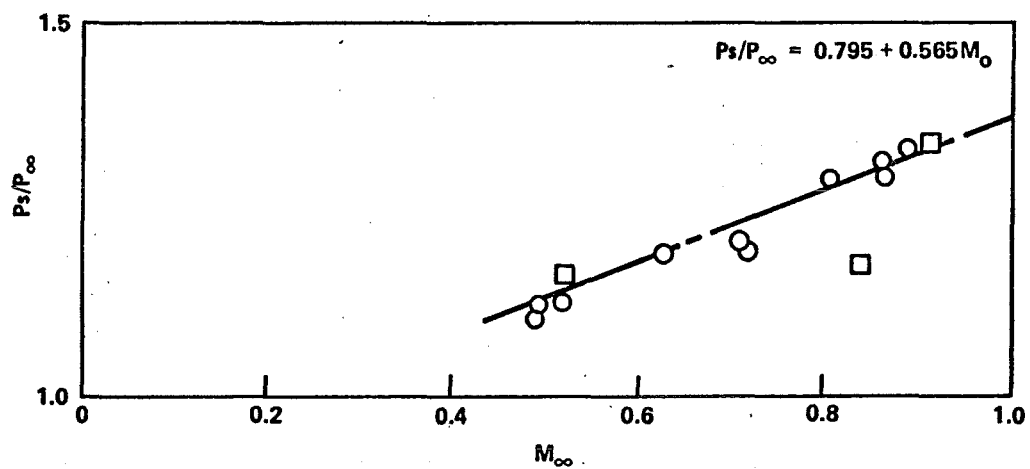
Figure 93(b). Correlation of separation pressure
for subsonic Mach numbers – UTSI data.

$$P_p/P_p)_o = 1 - 0.02440\theta + 0.000740\theta^2$$
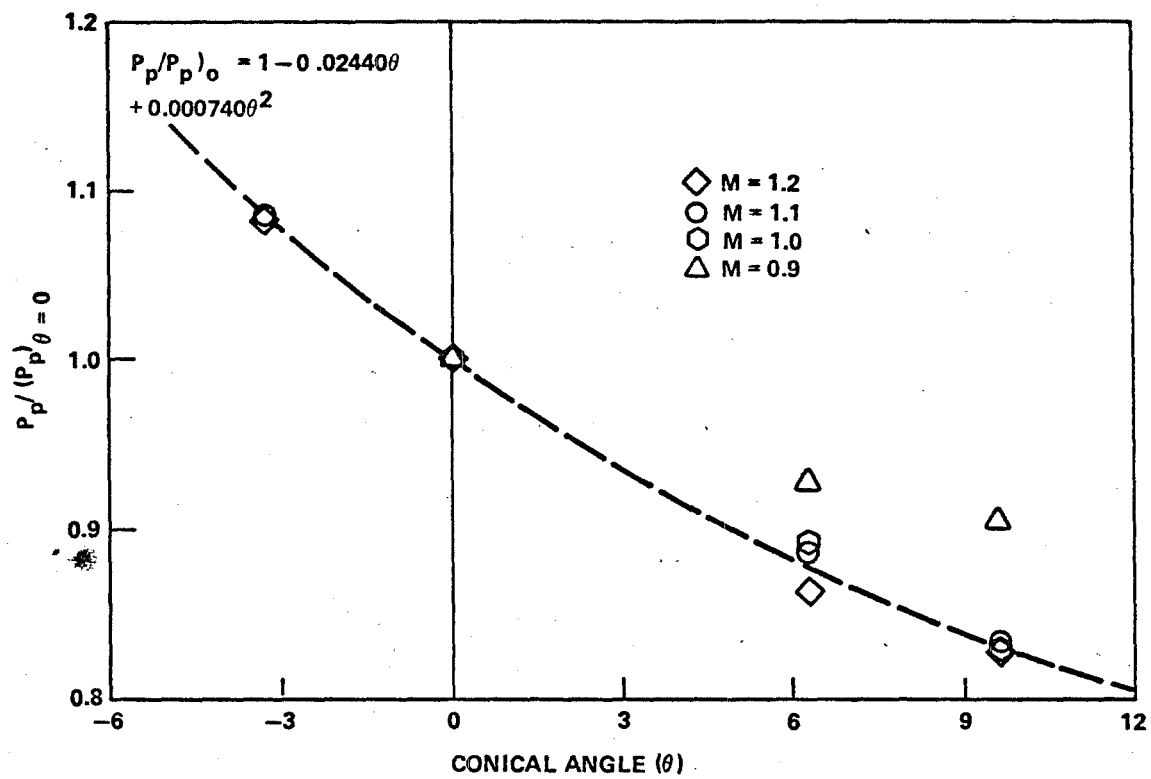
Figure 94.   Correlation of the limiting base
pressure for bodies with conical rear ends.
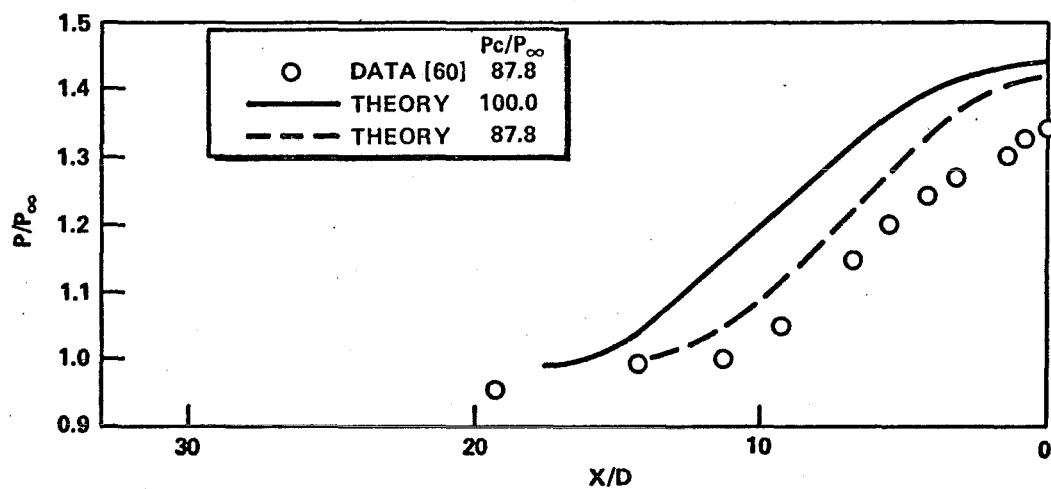
Figure 95. Predicted pressure rise on a parallel sided
body with M = 1.1:   body B1 with nozzle N1.

BOUNDARY LAYER
DEVELOPMENT,
SECTIONS III.A.1
AND III.A.3. $\triangle \theta$ Eqn. (55)
$\triangle H$ Eqn. (56)

FREE SHEAR
LAYER
SECTION III.A.5

EMPIRICAL PRESSURE
RISE EQN. (69)

PLUME BOUNDARY,
SECTION III.B

θ GIVEN

FREE SHEAR
LAYER,
SECTION III.A.5

$\triangle \theta$, EQN. (55)
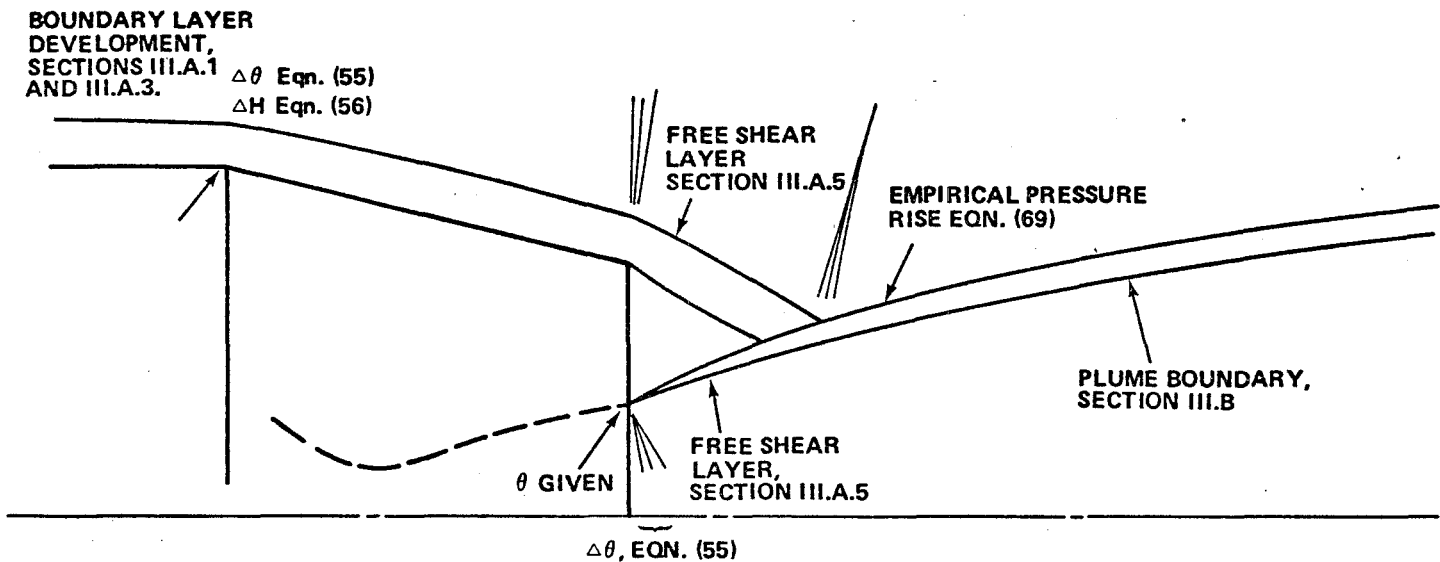
Figure 96. Itemized summary of the calculation components
when the base pressure is lower than ambient.
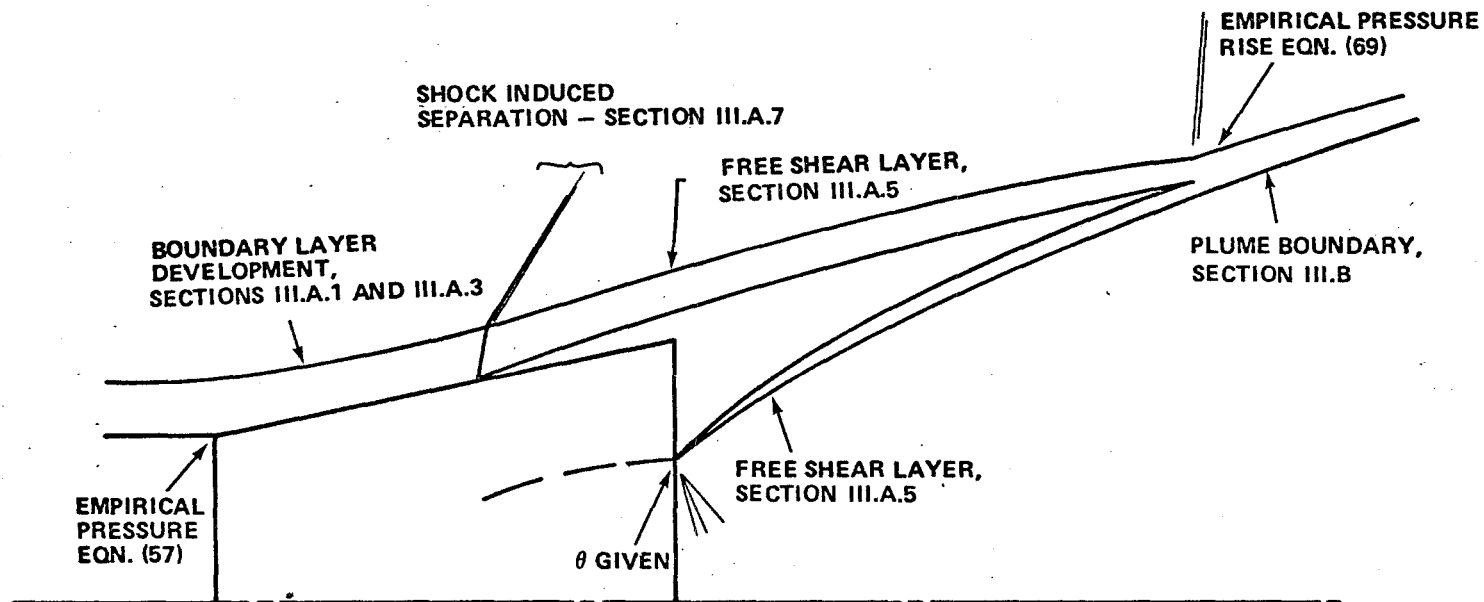
Figure 97. Summary of components used in interaction calculation
when the base pressure is greater than ambient.
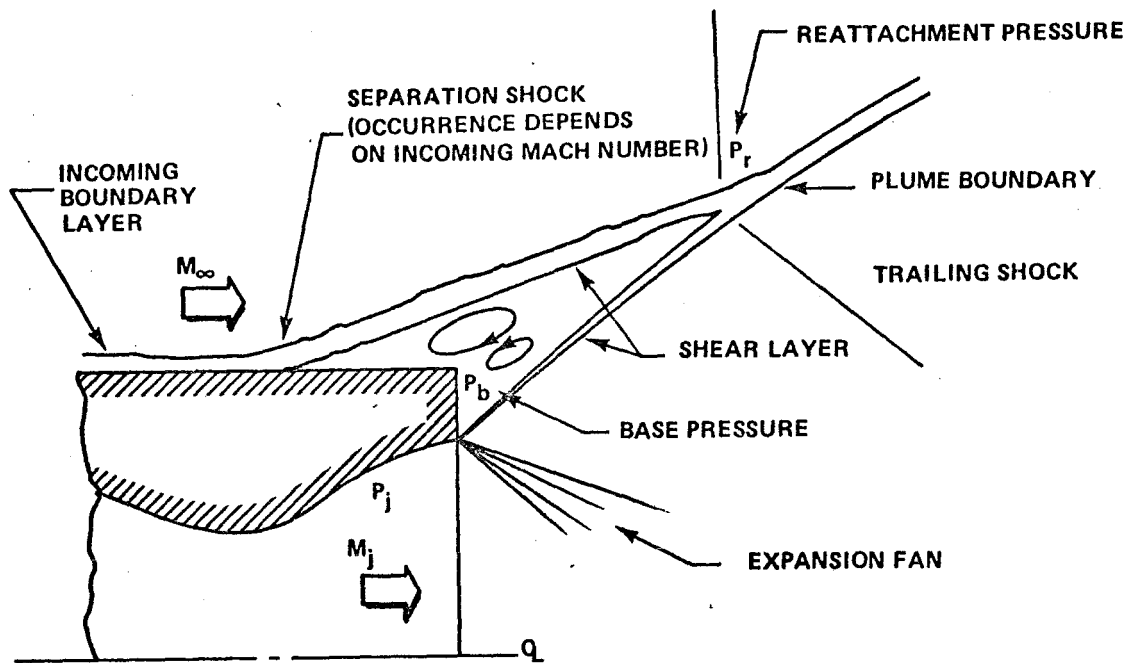
Figure 98. Schematic sketch of separation flow region.
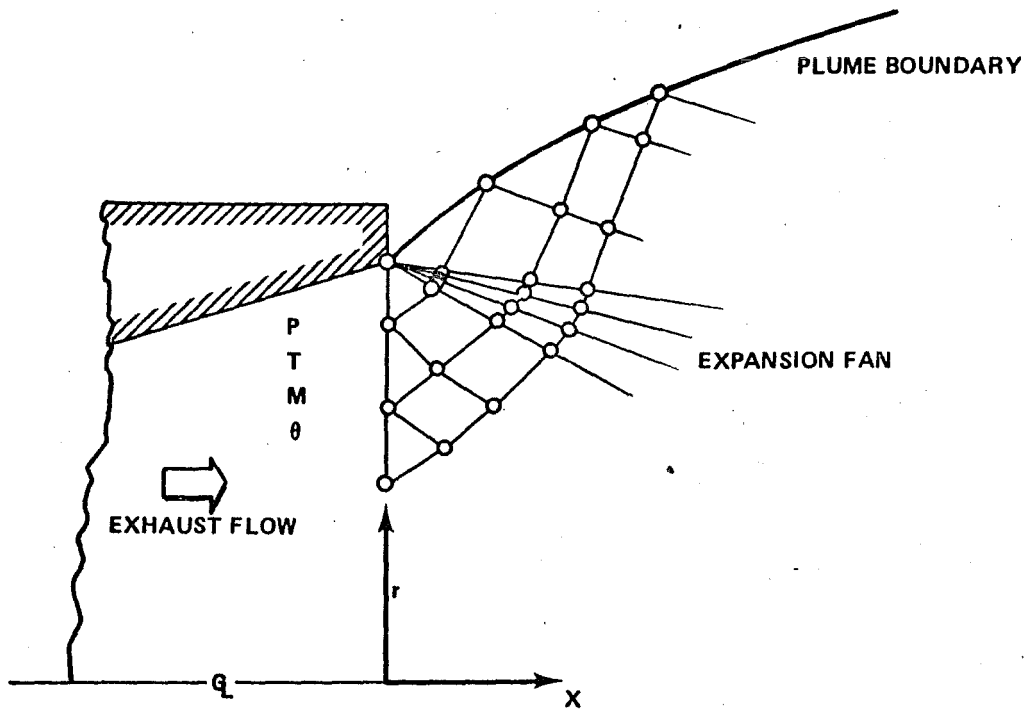
Figure 99. The characteristic mesh.

156
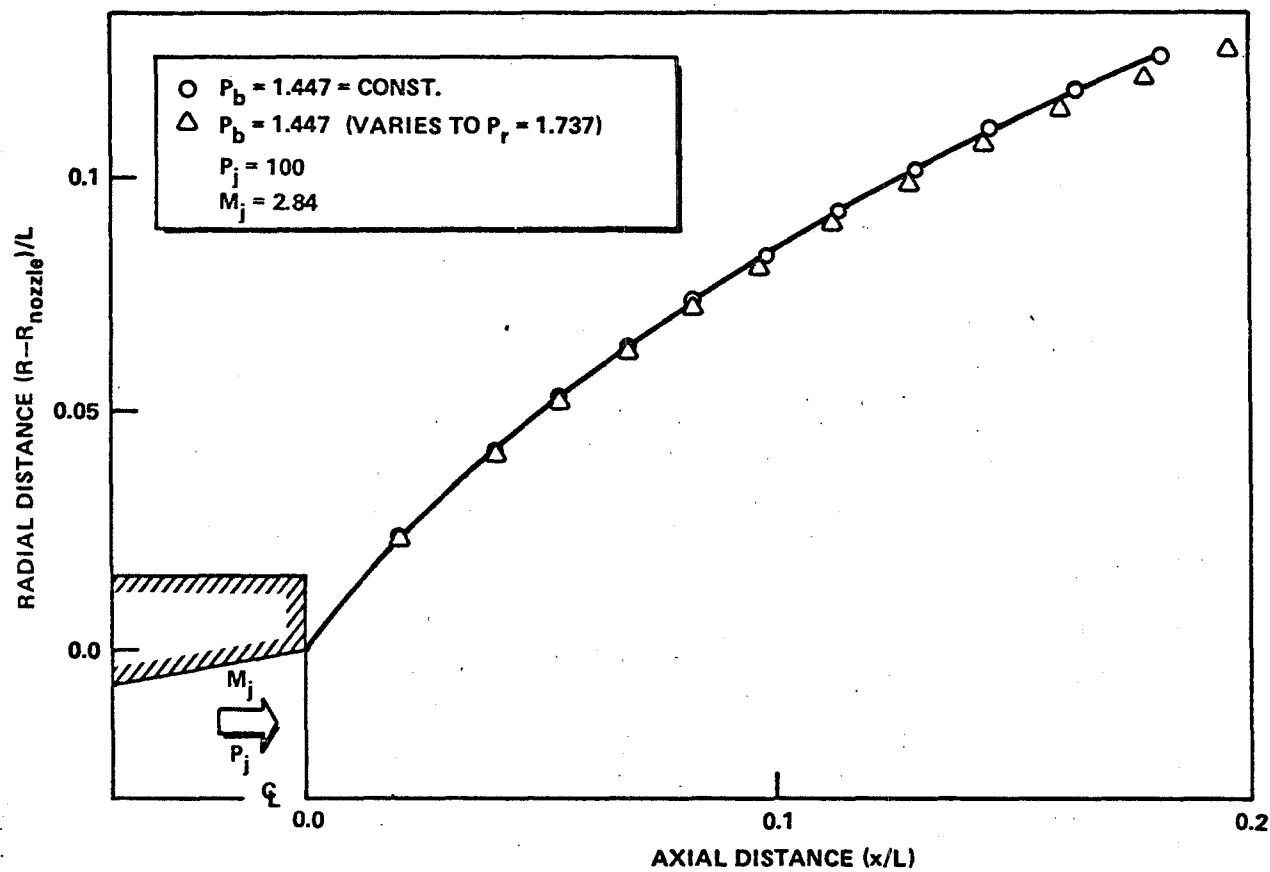
Figure 100. Effect of various external pressure distributions
    on plume boundary shape.
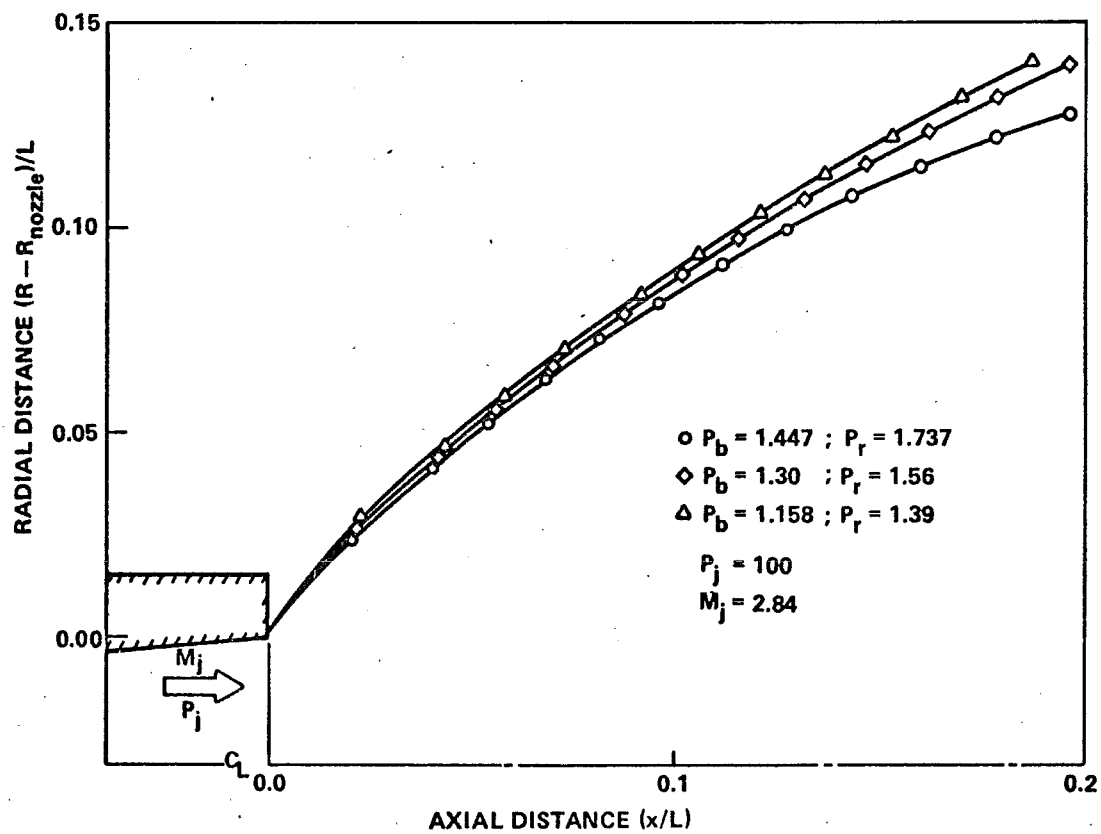
Figure 101. Effect of base pressure ratio on the plume shape.

158
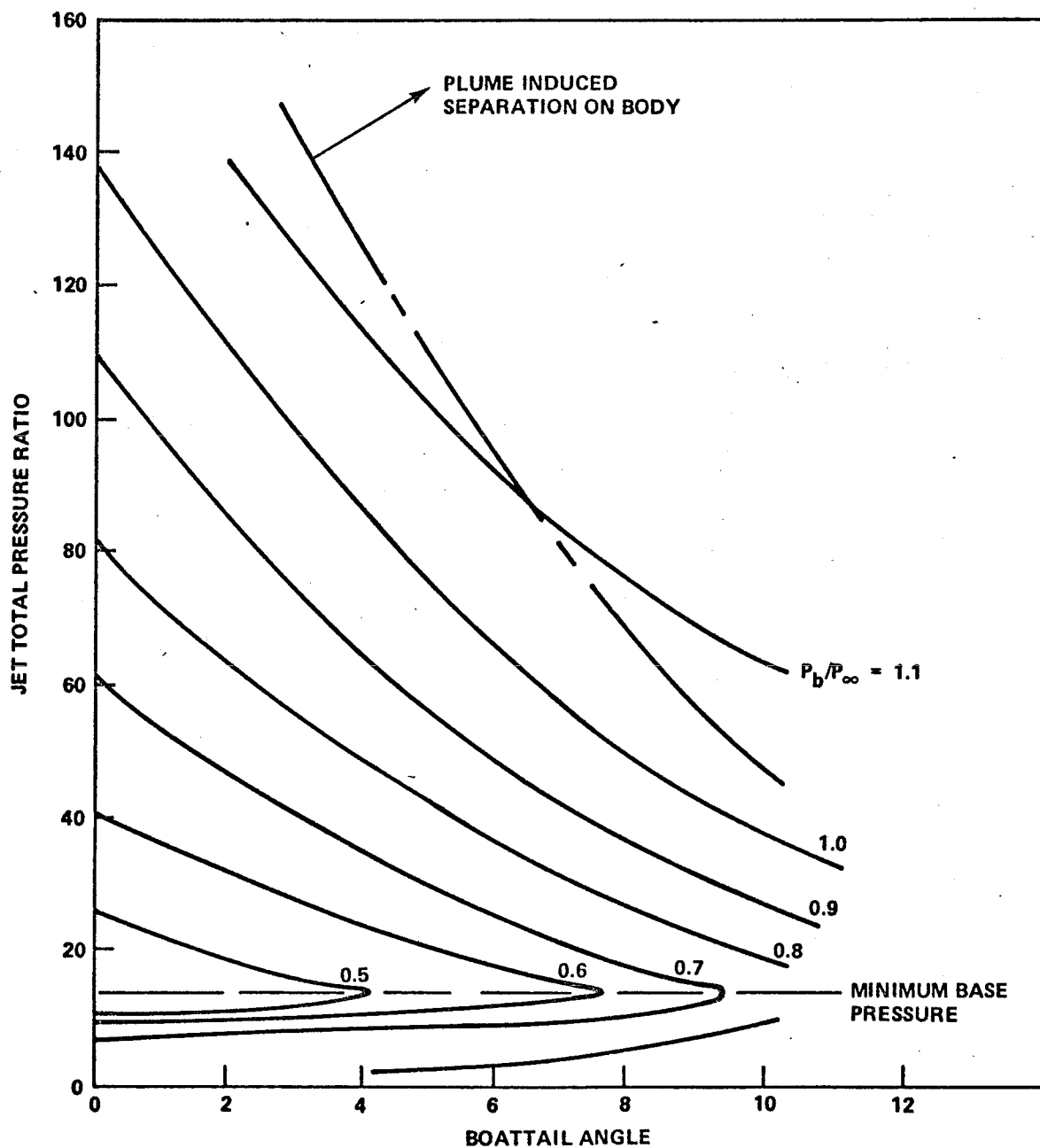
Figure 102. Contours of base pressure for various boattail
bodies: $M_\infty = 1.1$, bodies B3, B4, and B5 with nozzle N12.
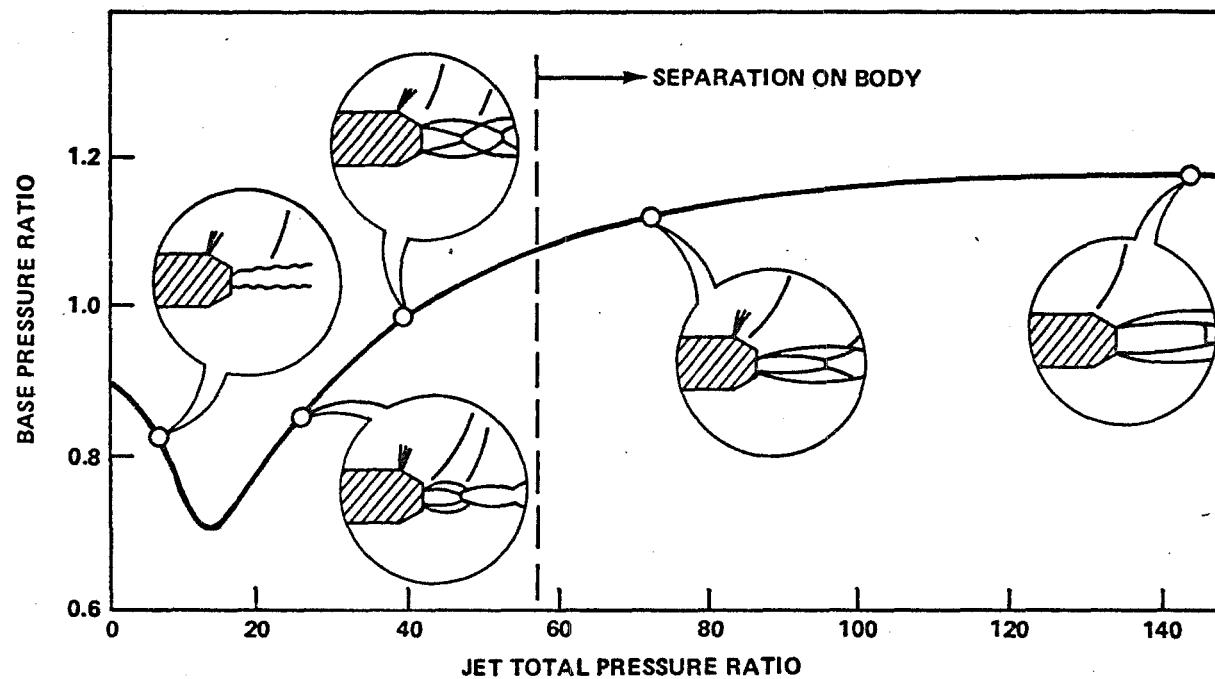
Figure 103. Overall effect of jet pressure ratio on base pressure
and flow structure: M_∞ = 1.1, body B3 with nozzle N12.
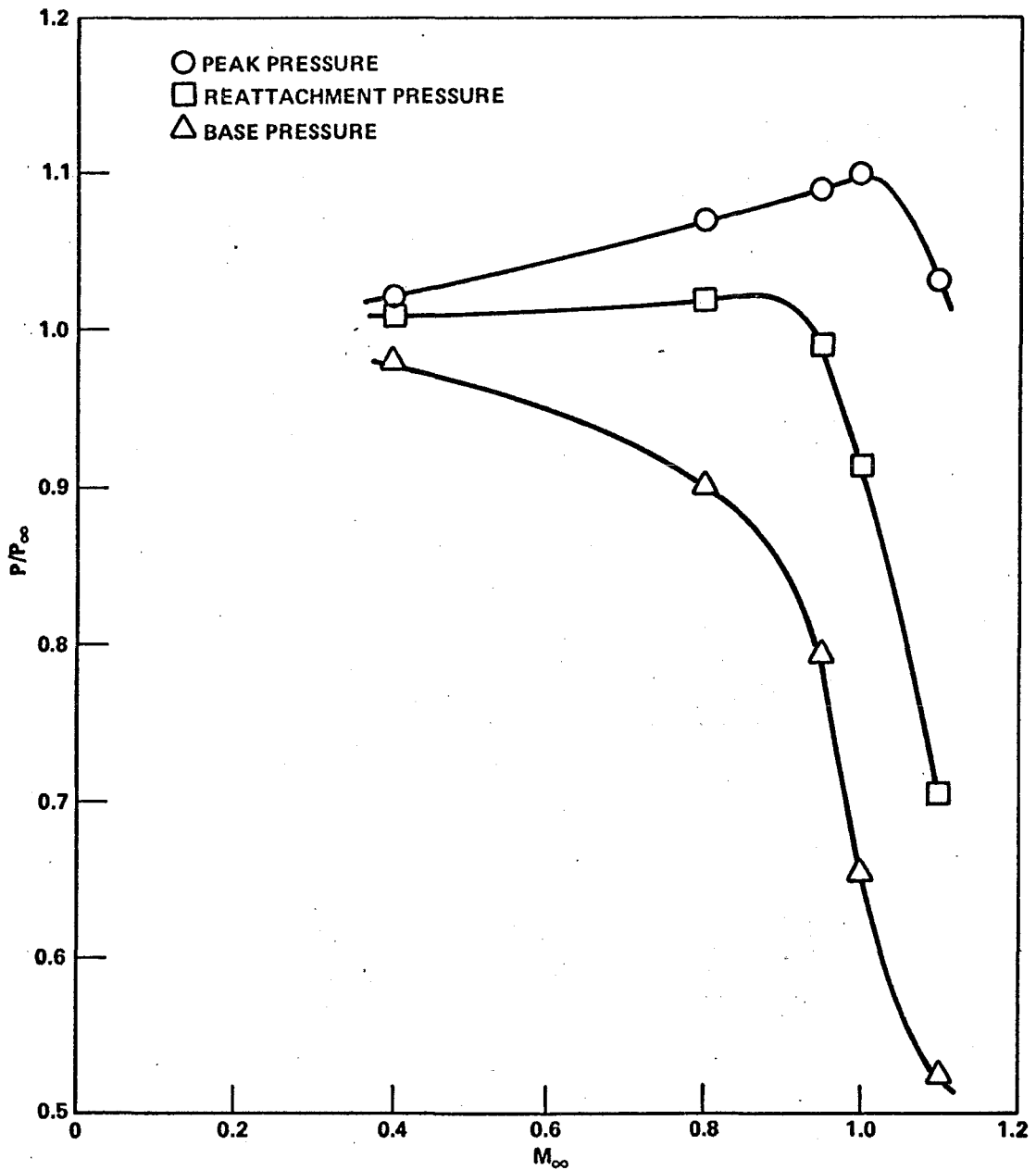
Figure 104. Variation of base pressure and reattachment pressure
for the flow over a rearward facing step [71].
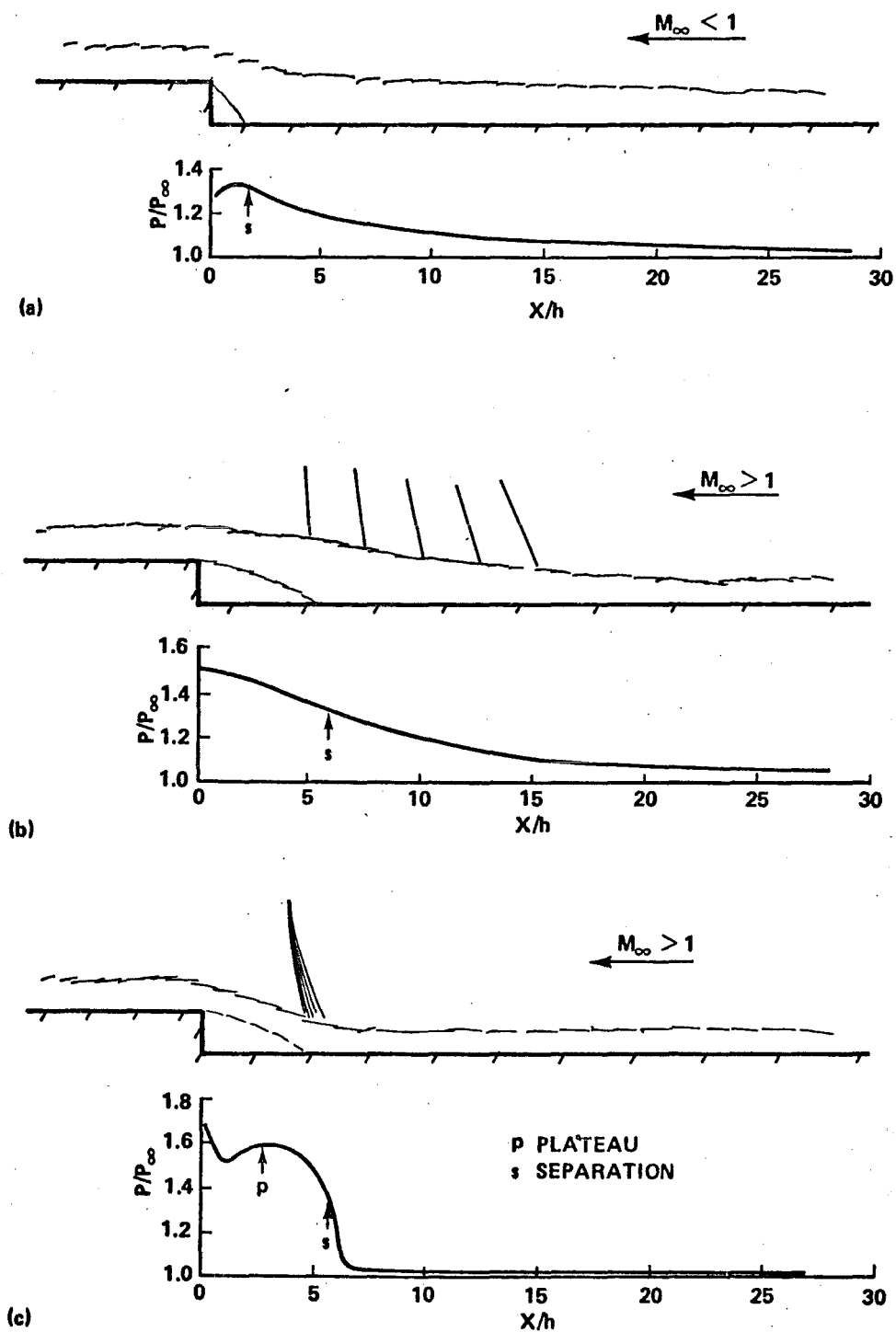
Figure 105. Flow over a forward facing step: (a) subsonic approach conditions, (b) supersonic isentropic flow, and (c) supersonic flow with shock separation.

162
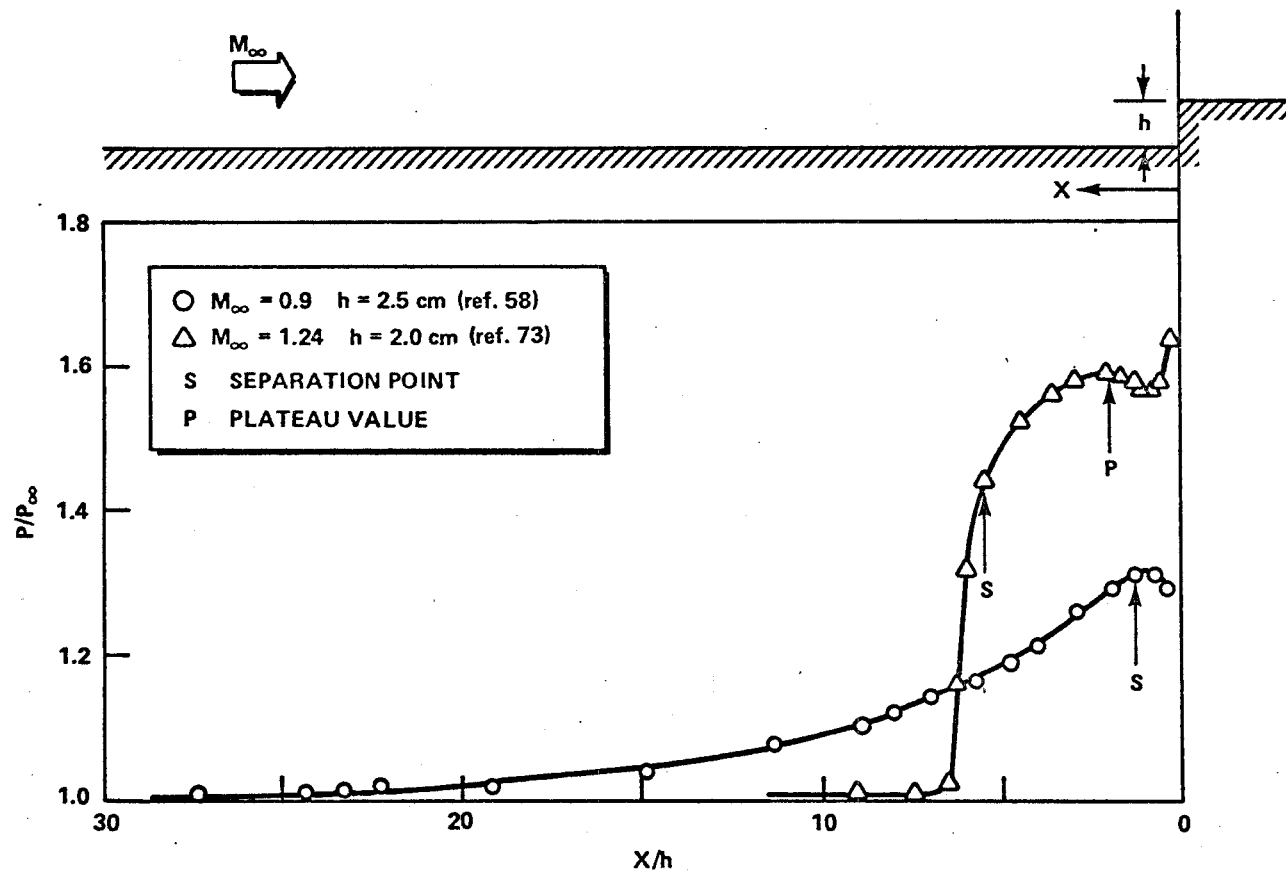
Figure 106(a). Flow over a forward facing step comparing the subsonic and supersonic flow configurations.

163
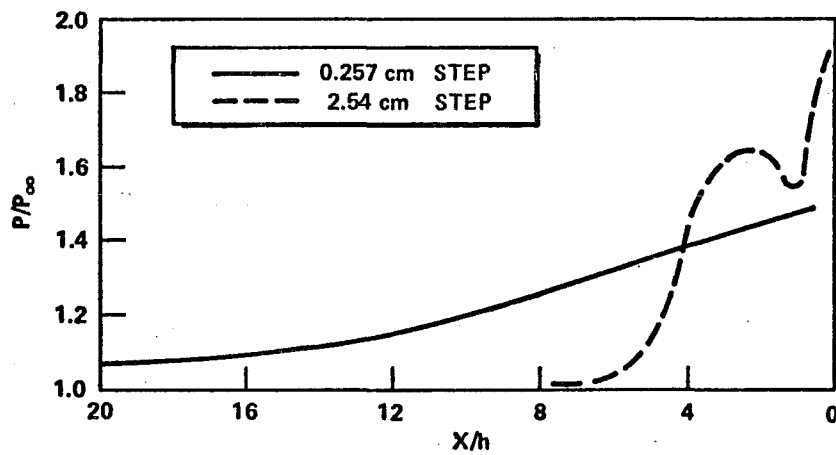
Figure 106(b). Flow over a forward facing step at $M_\infty = 1.61$.

164
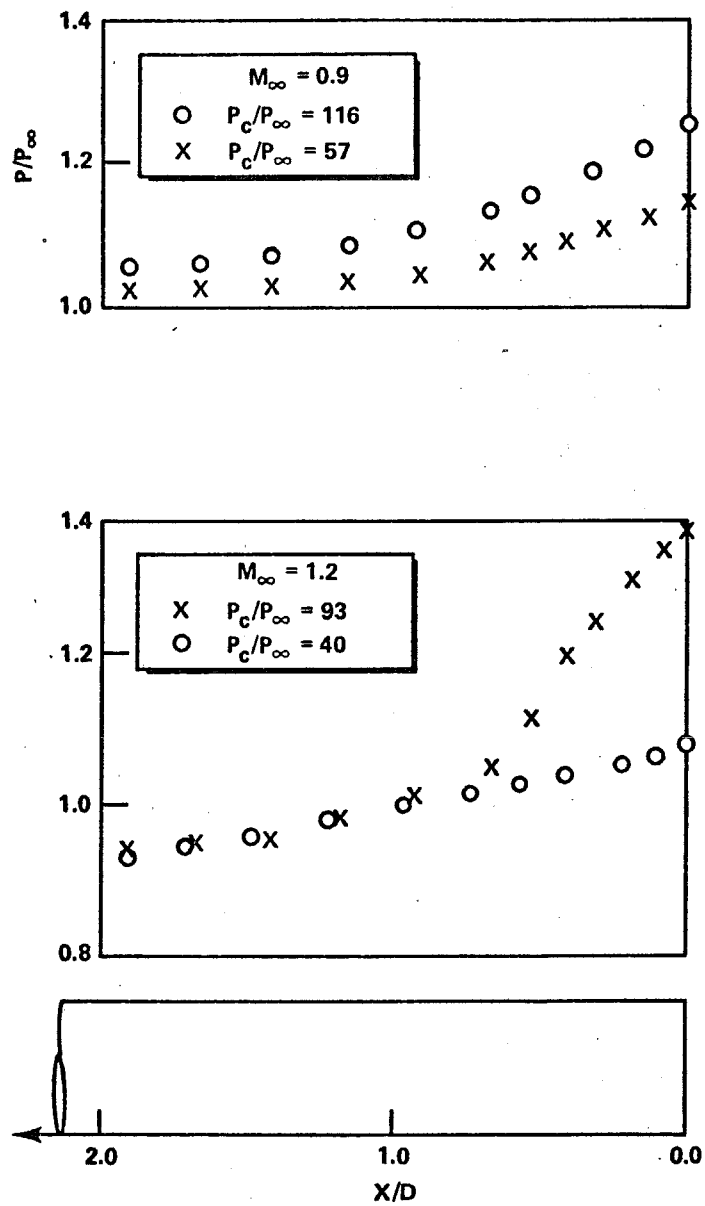
Figure 107. Measured surface pressure distribution on parallel sided body: body B1 with nozzle N1.
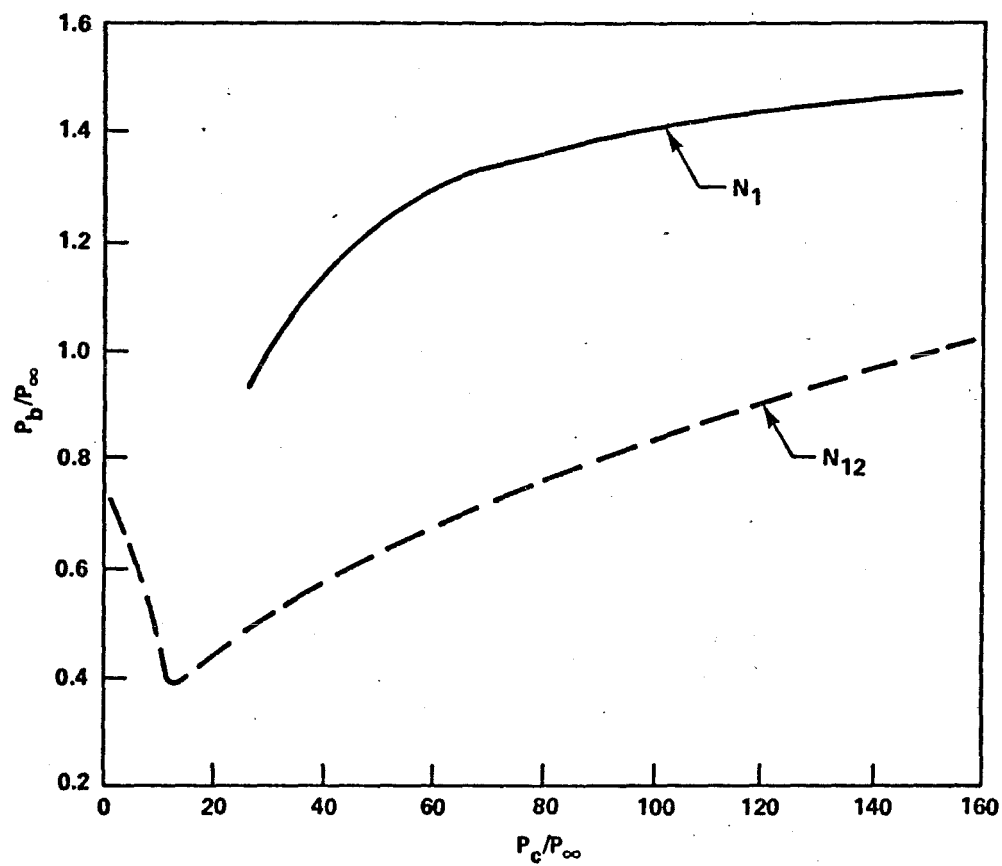
Figure 108. Effect of nozzle geometry on the base
pressure signature: M_∞ = 1.2, body B1.
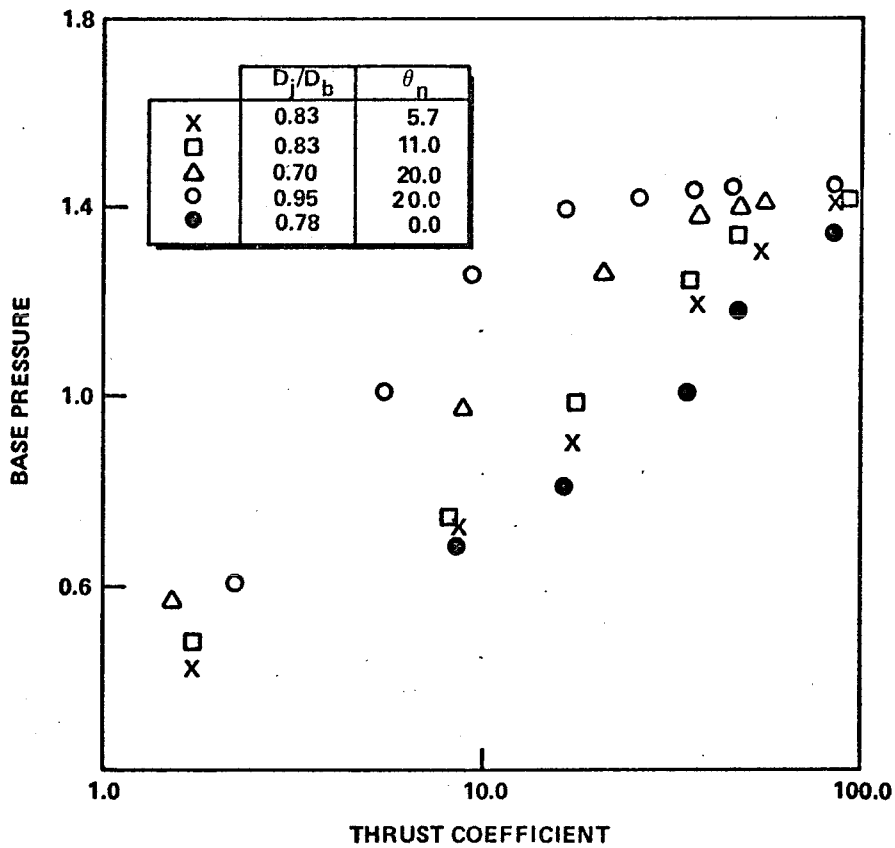
Figure 109.   The base pressure signatures corresponding
to various nozzle configurations.
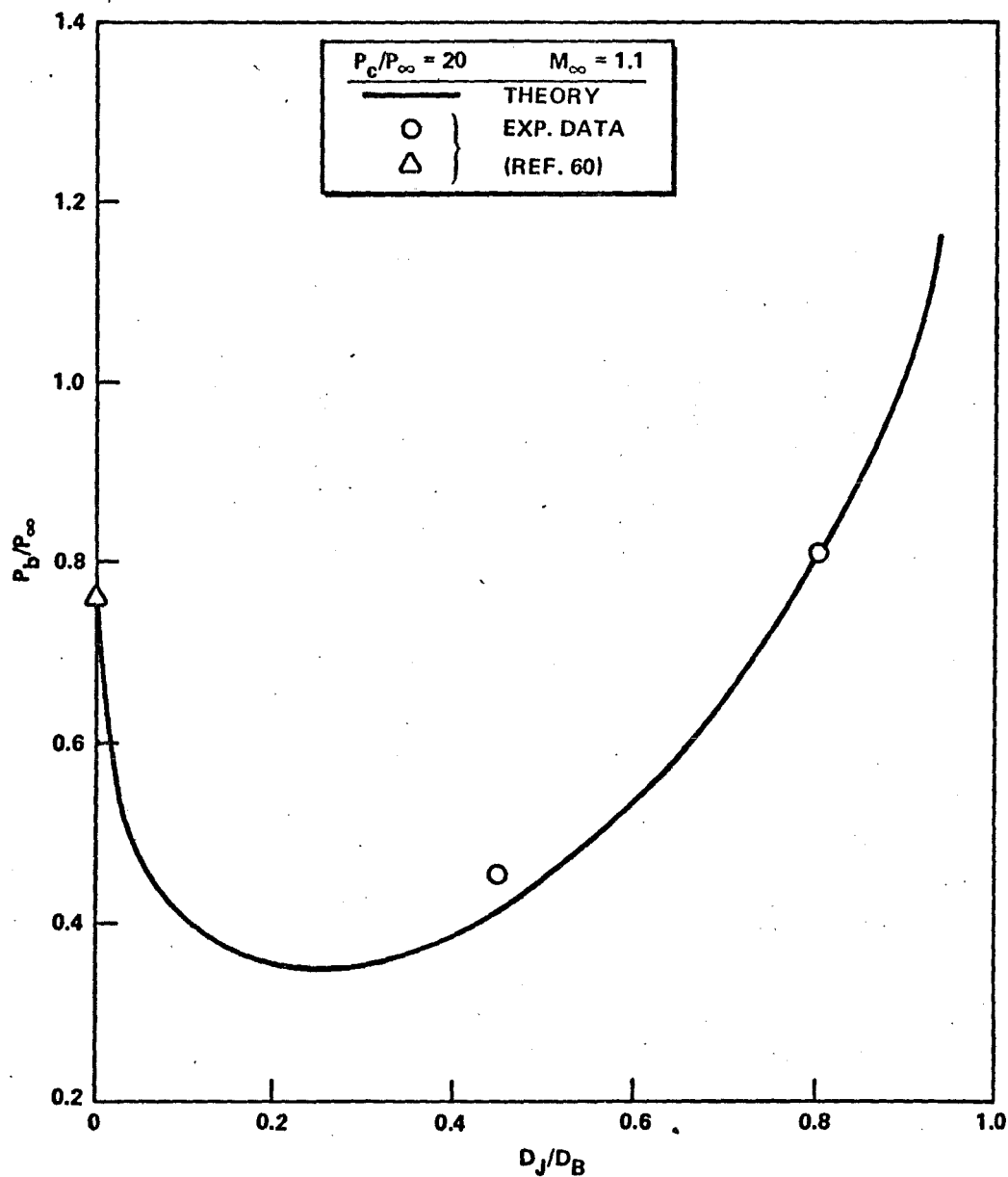
Figure 110.   Calculated results for nozzle diameter
   ratio effect on base pressure: body Bl.
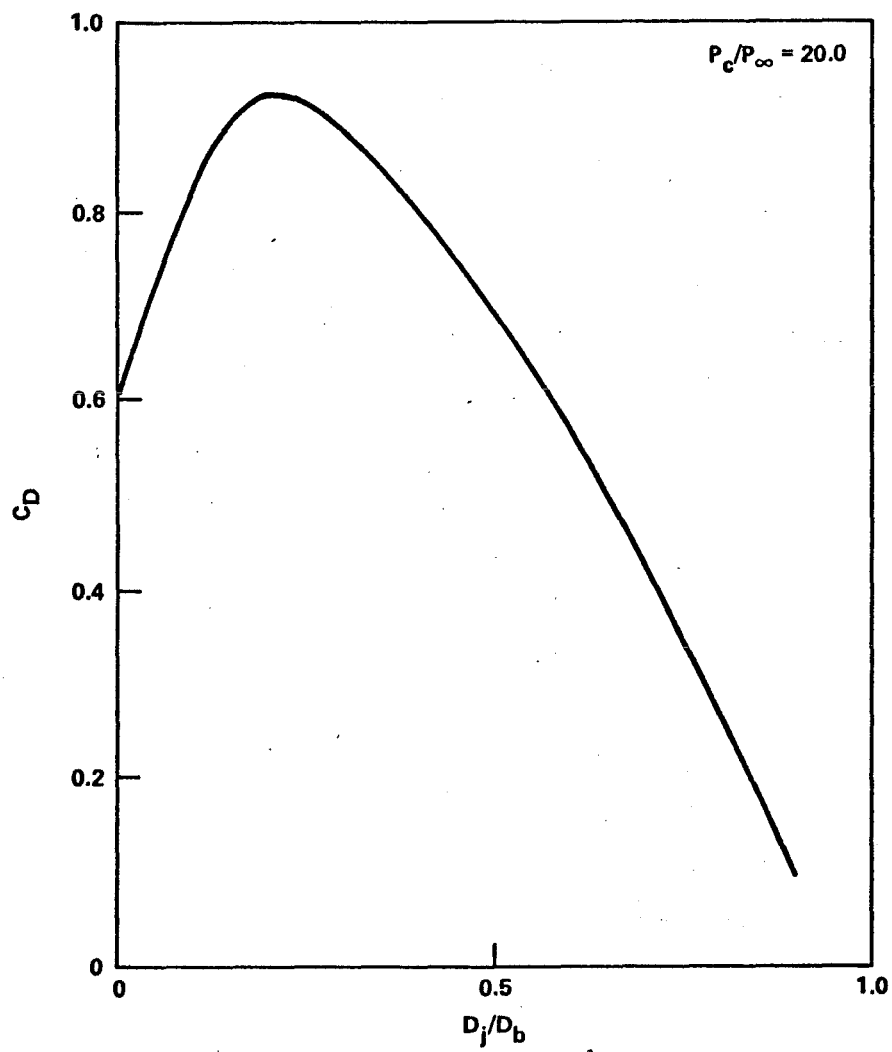
Figure 111. Drag coefficient variation corresponding
to the data in Figure 110.
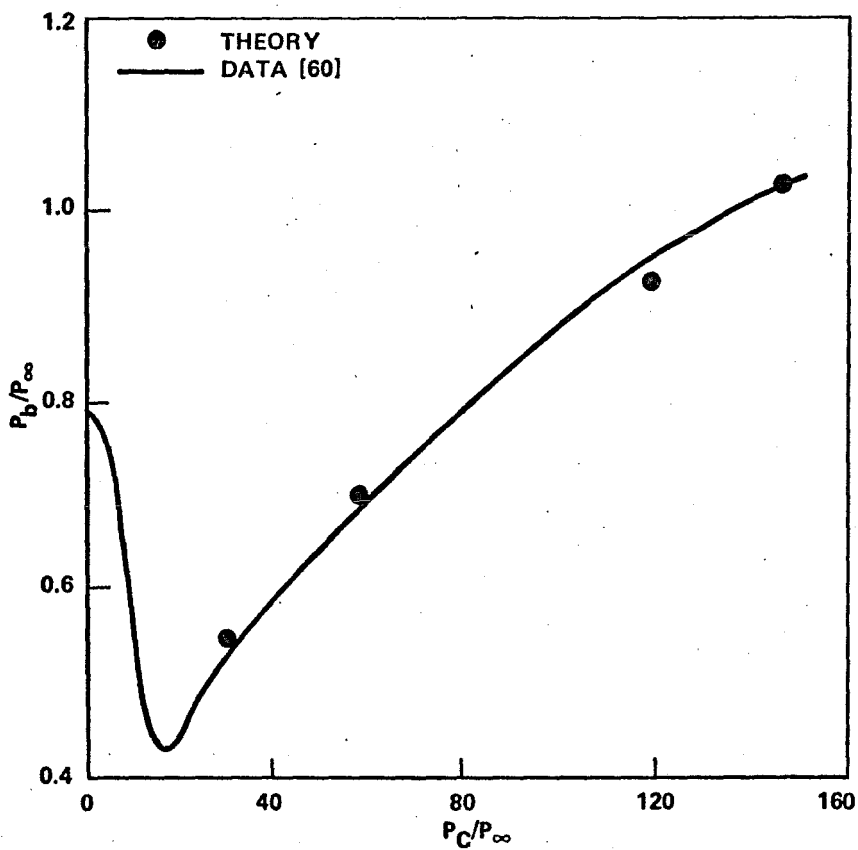
Figure 112.   Calculated base pressure for a parallel-sided body: $M_\infty = 1.1$, body B1 with nozzle N12.
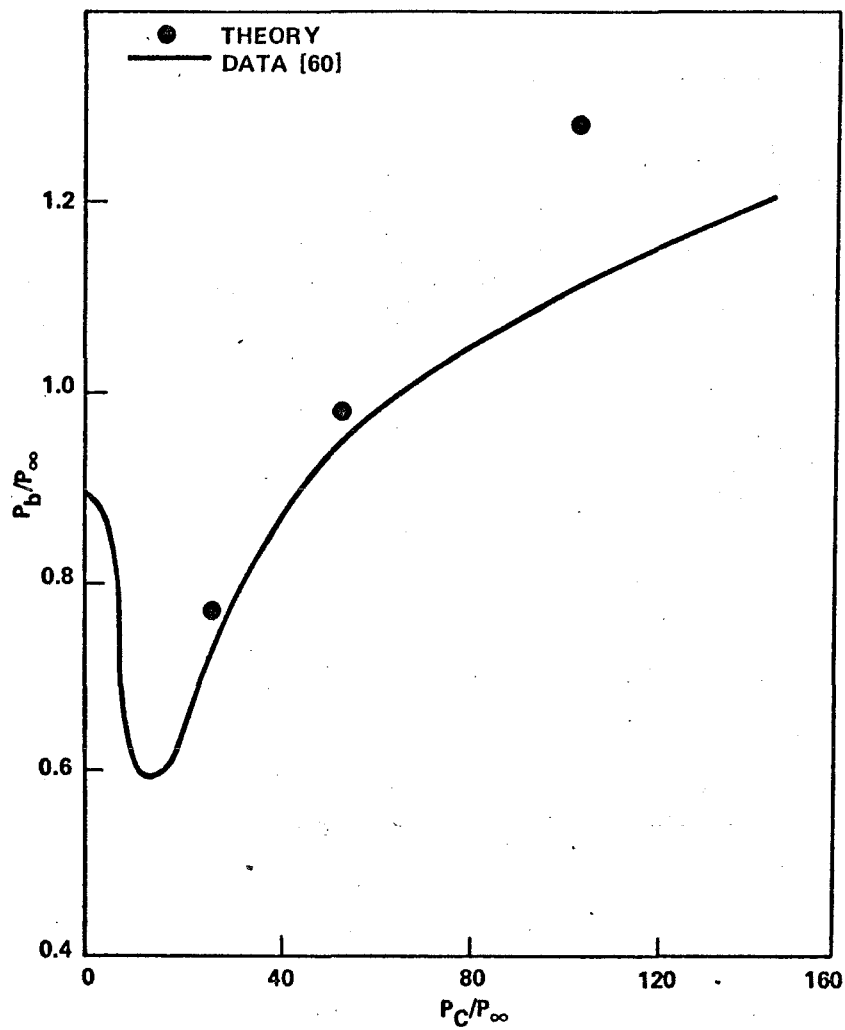
Figure 113. Calculated base pressure on body with a 6.5° boattail: $M_\infty = 1.1$, body B4 with nozzle N12.
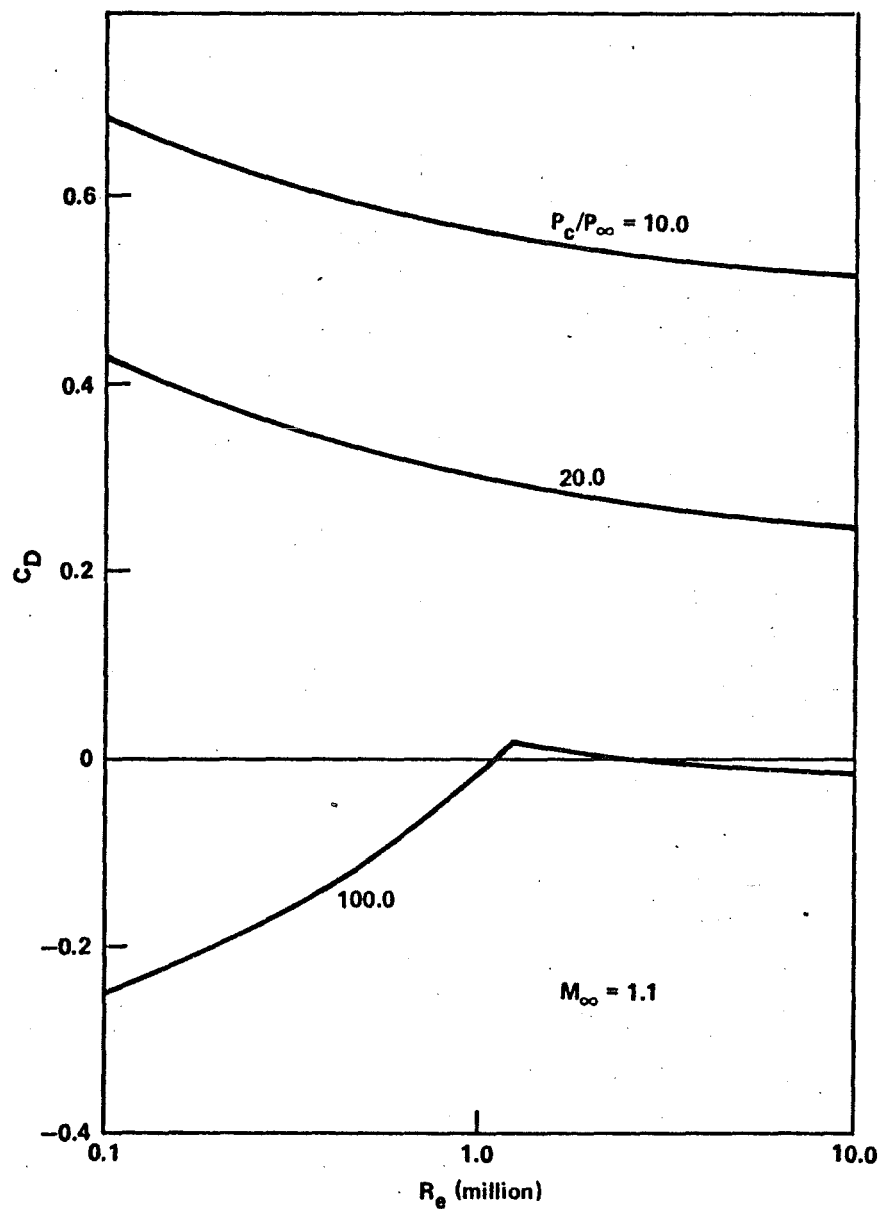
Figure 114. Influence of Reynolds number on drag coefficient
for different jet pressure ratios: $M_\infty = 1.1$, body B4
with nozzle N12.

172
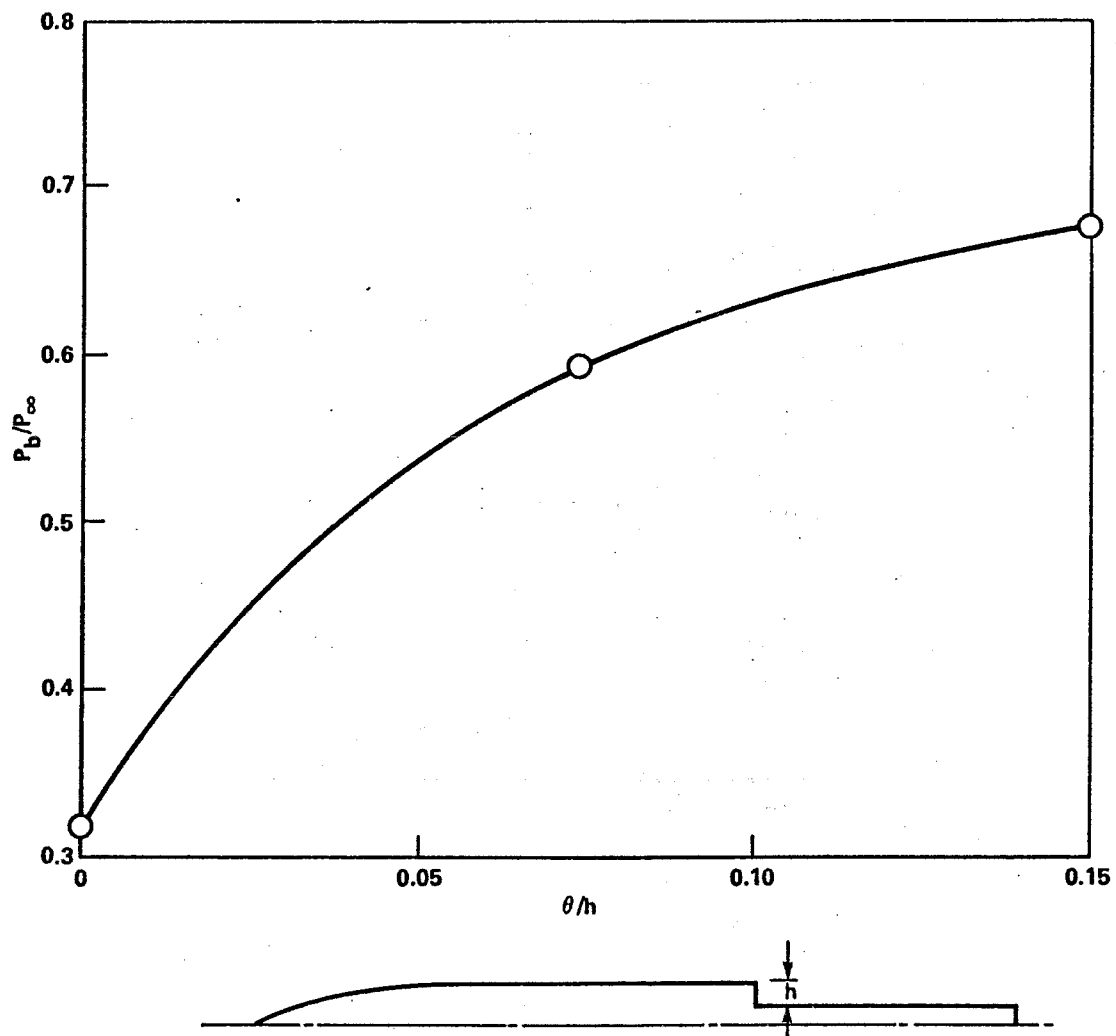
Figure 115. Effect of initial boundary layer thickness
on base pressure for flow over an axisymmetric back
step: $M_\infty = 1.1$.

173
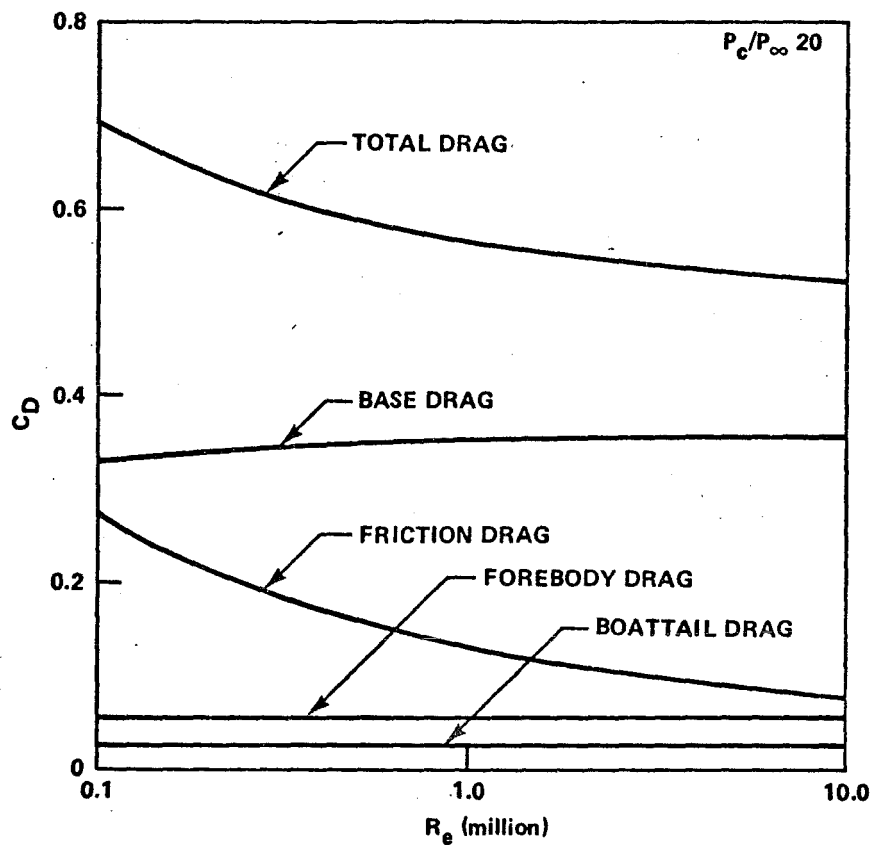
Figure 116. Variation of drag components with Reynolds
number: $M_\infty = 1.1$ and jet pressure ratio 20.

174
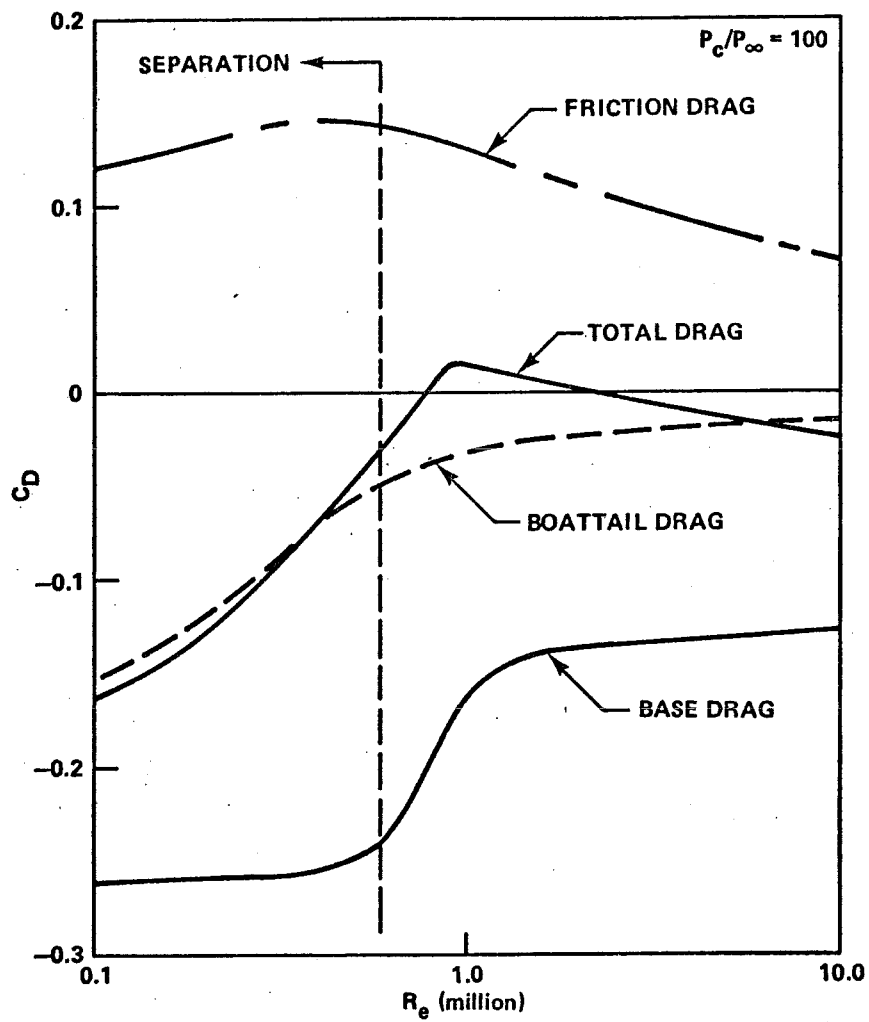
Figure 117. Effect of Reynolds number on drag
components: $M_\infty = 1.1$ and jet pressure
ratio 100.

175
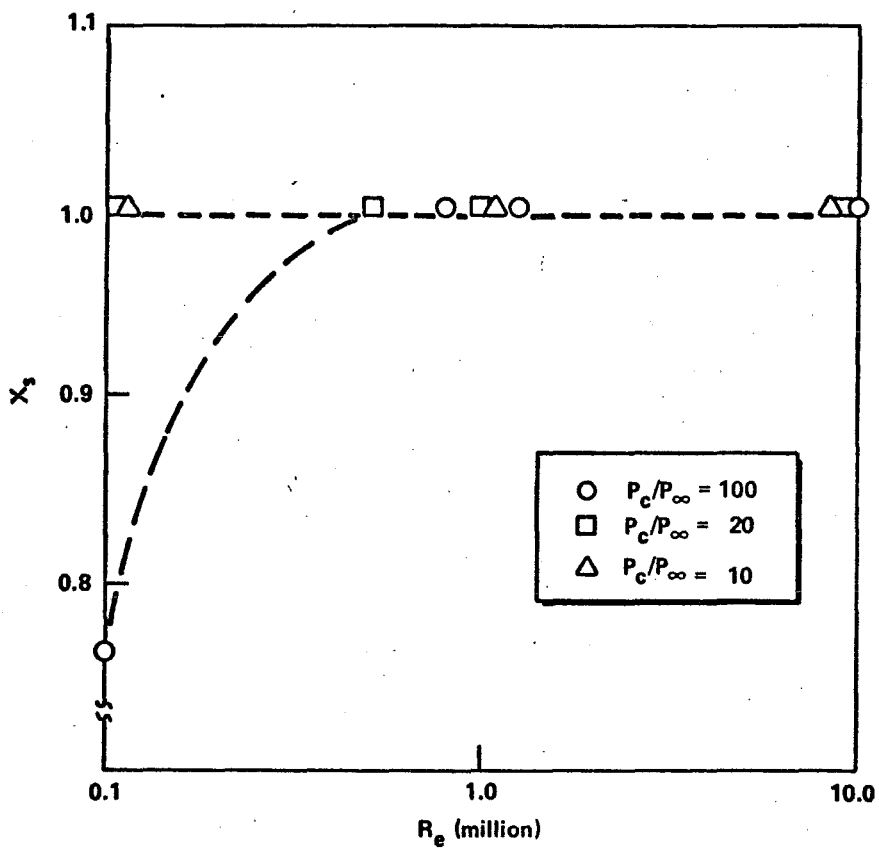
Figure 118. Predicted separation point for various jet pressure ratios as a function of Reynolds number: $M_\infty = 1.1$.

176
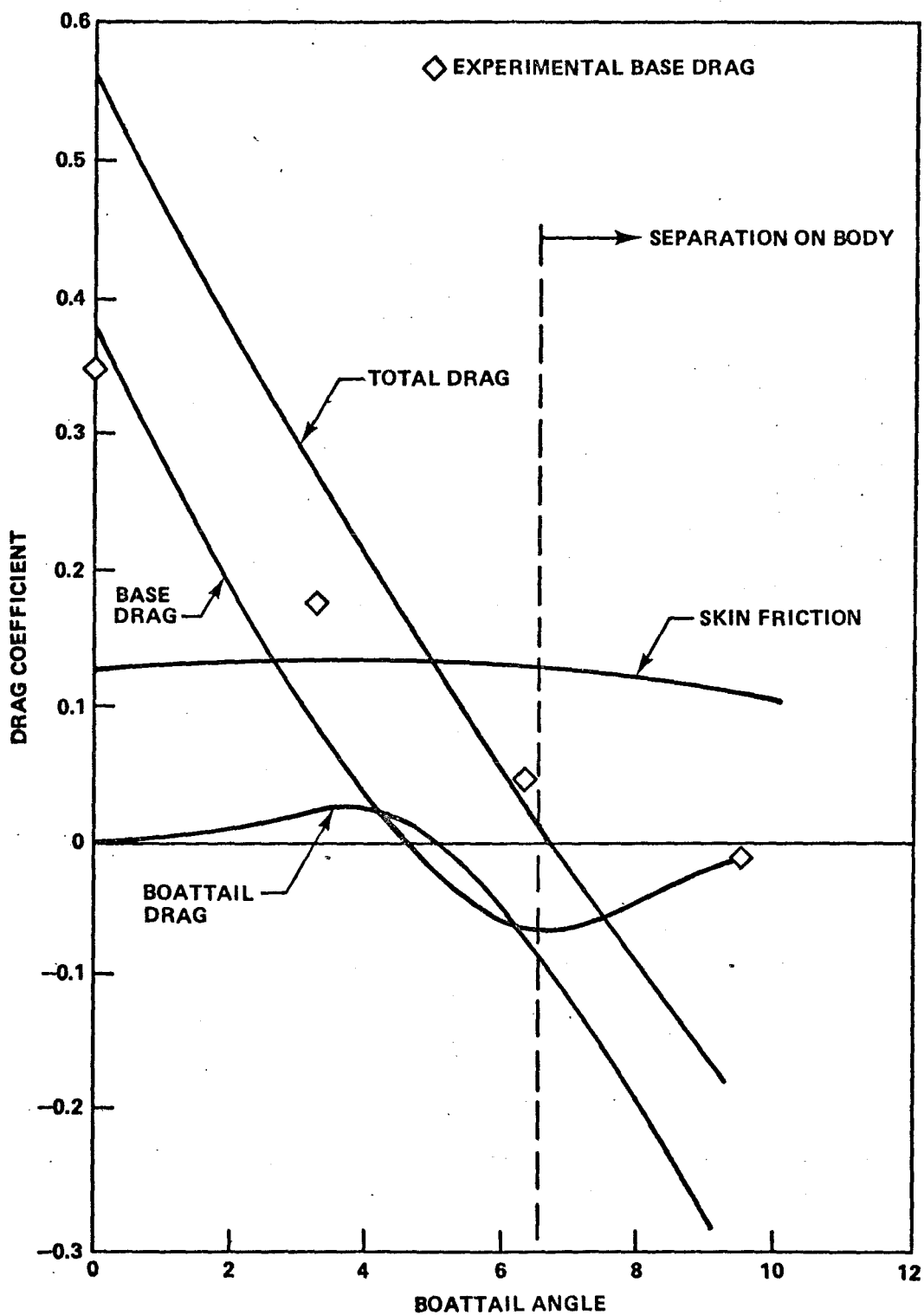
Figure 119. Theoretical drag predictions for boattailed
bodies at M_∞ = 1.1: jet total pressure ratio is
50.0; bodies B3, B4, and B5 with nozzle N12.

177
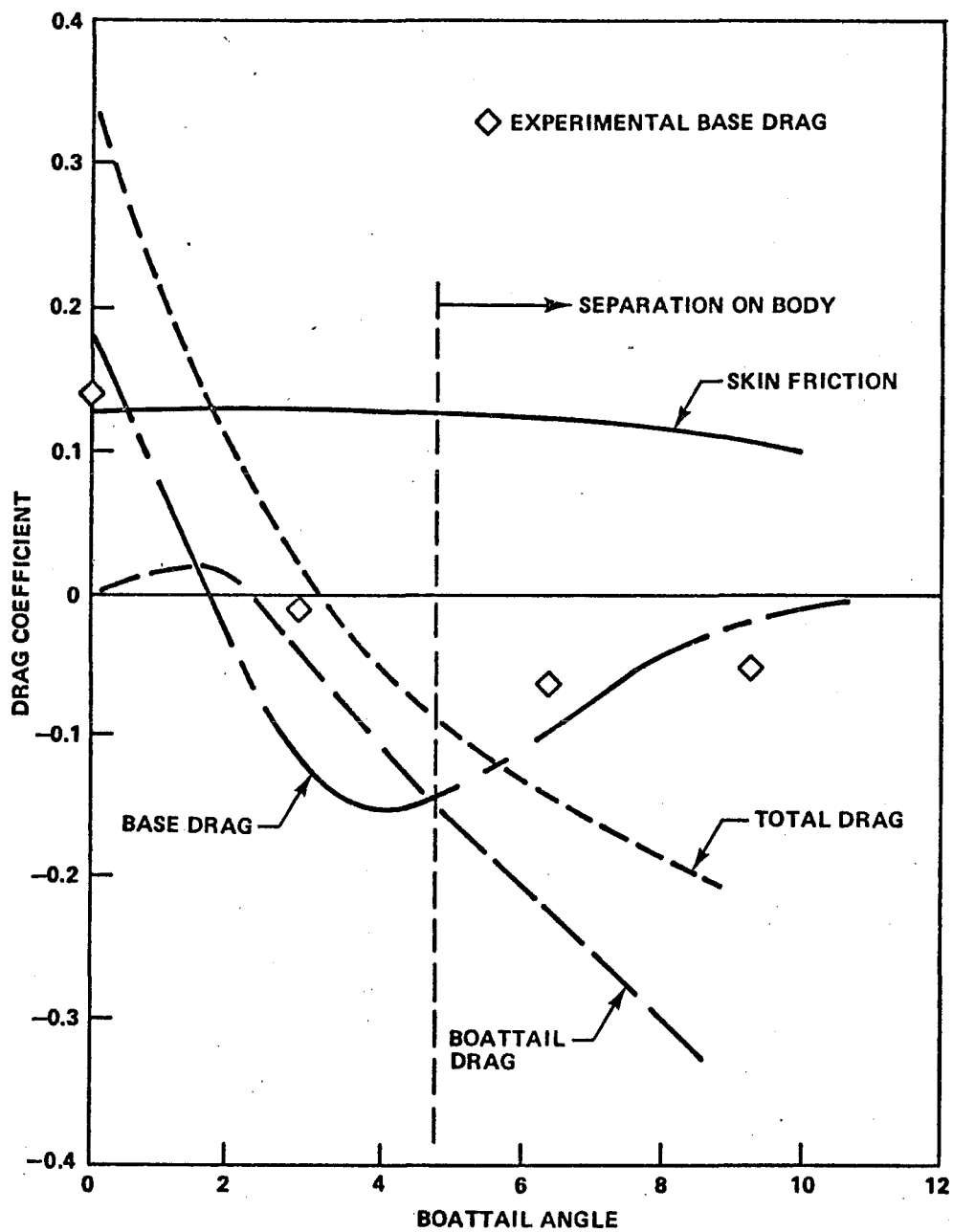
Figure 120. Theoretical drag predictions for boattailed bodies at $M_\infty = 1.1$: jet total pressure ratio is 100.0.
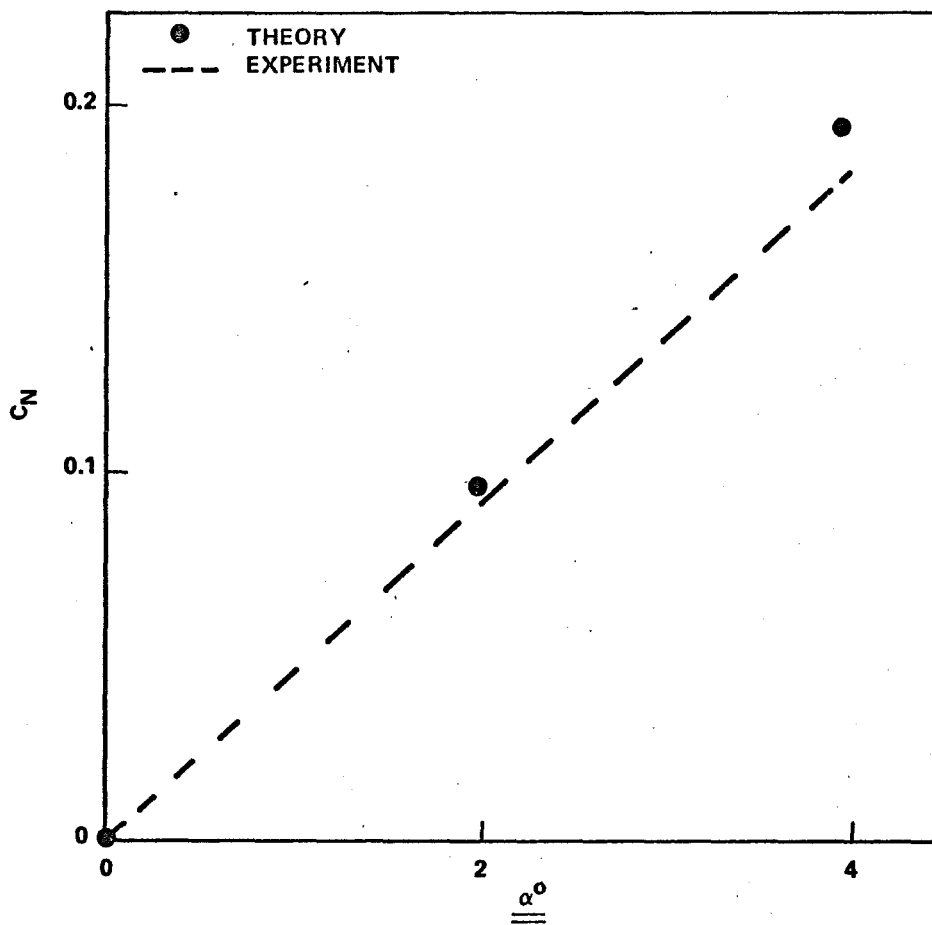
Figure 121. Predicted variation of lift with incidence for body MCDAC: $M_\infty = 1.0$ and jet off.
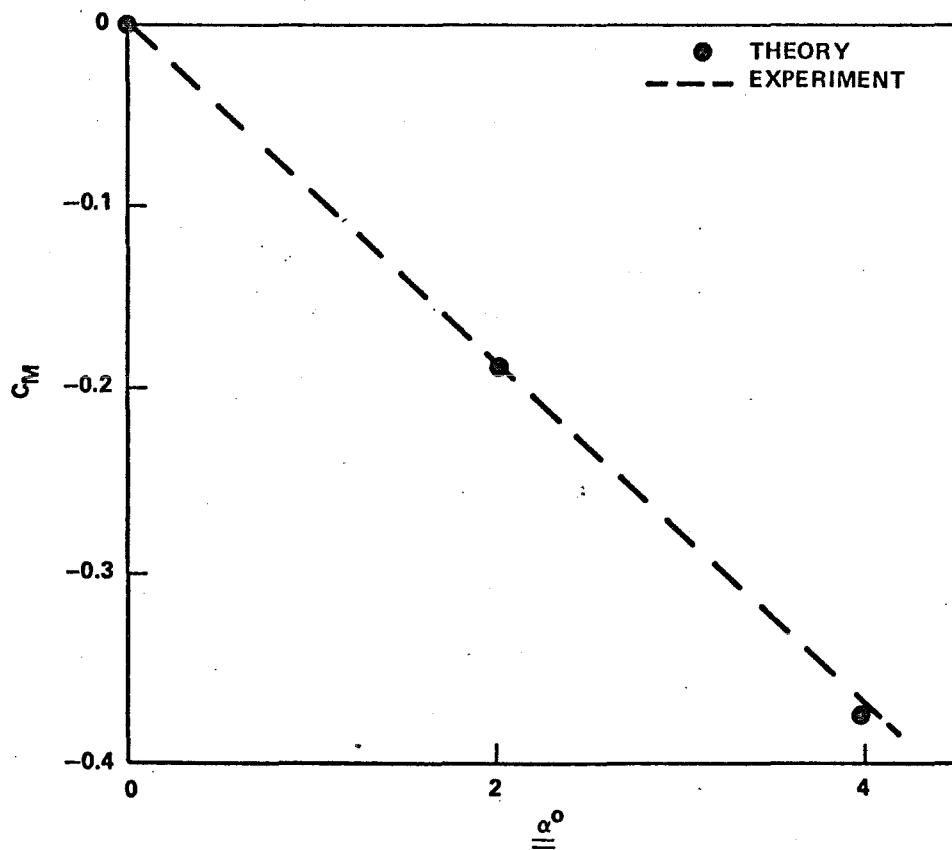
Figure 122. Predicted moment coefficient corresponding to the situation of Figure 121.
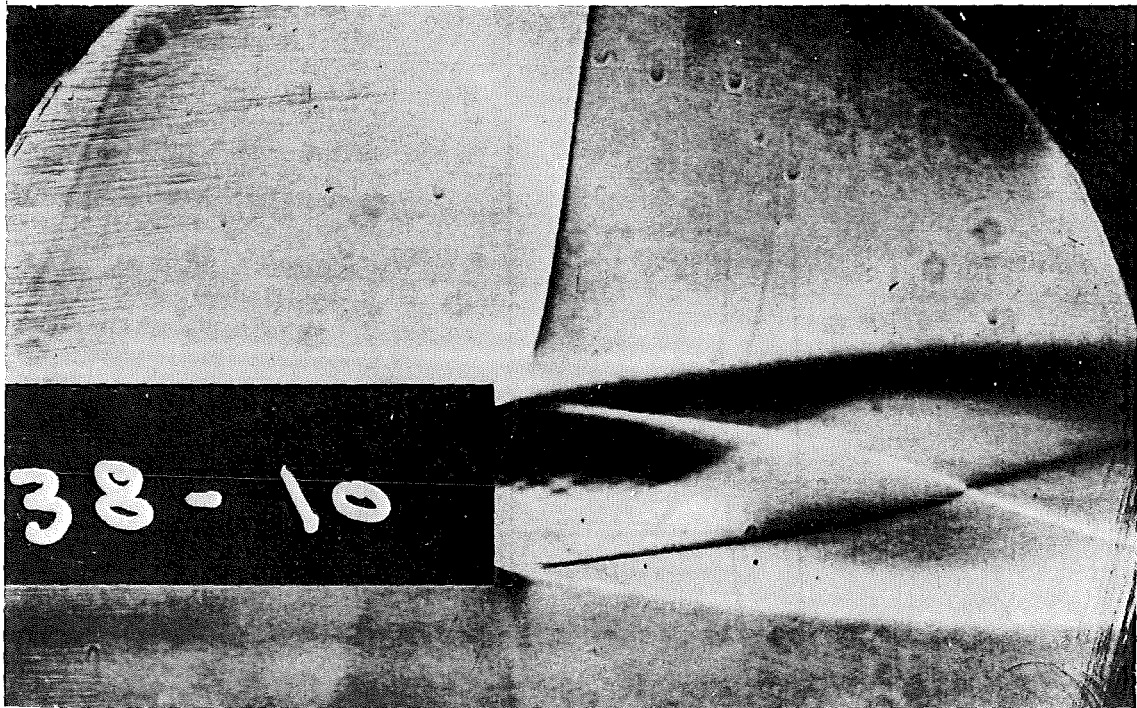
a. SCHLIEREN PHOTOGRAPH

b. CALCULATION

Figure 123.   Comparison of the interaction on body B1 with nozzle N4
   $M_\infty = 1.0$:   jet pressure ration = 50.1.

JET PRESSURE ⎱ ——— 50
RATIOS ⎰ ———— 100

X/L

182
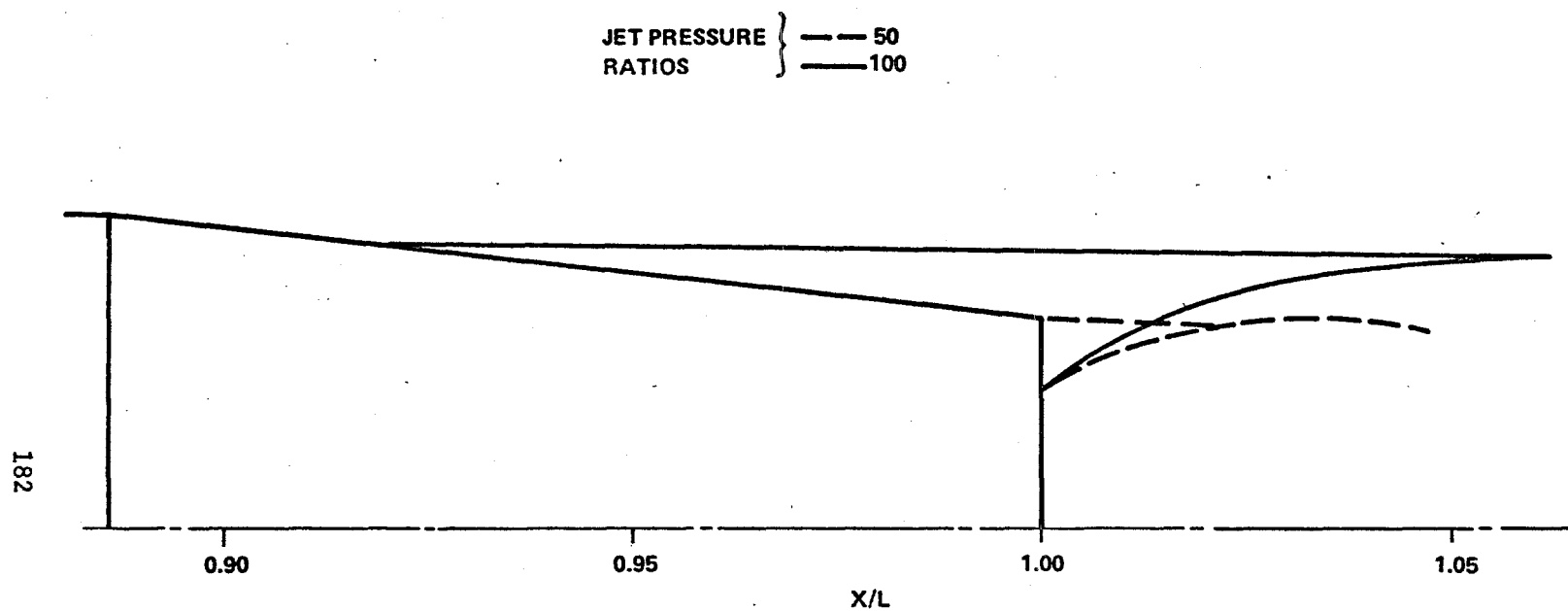
Figure 124. Effect of jet pressure ratio on the geometry of the
interaction: body B4 with nozzle N12, M_∞ = 1.1.
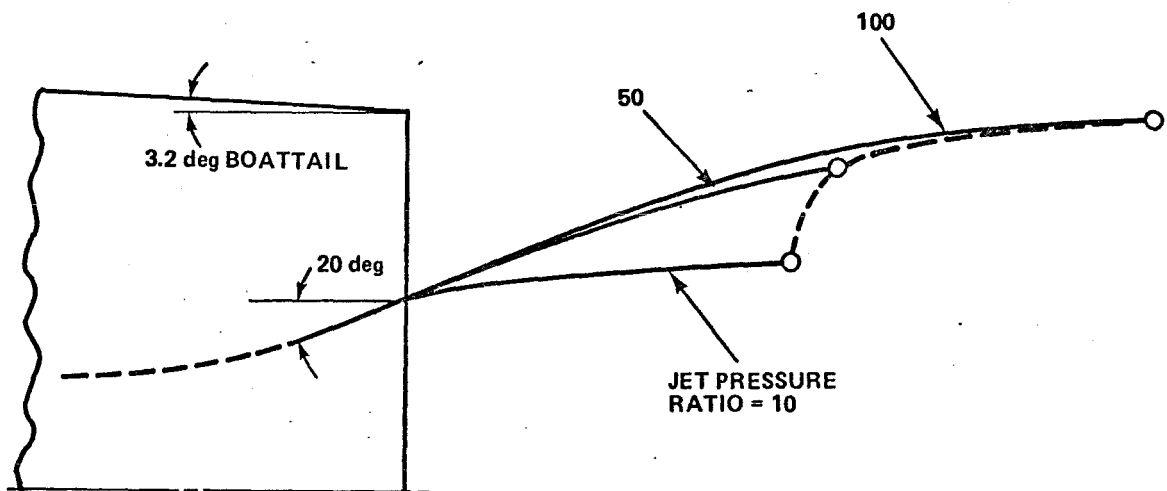
Figure 125. Locus of confluence points as the jet pressure ratio increases: body B5 with nozzle N12, $M_\infty = 1.1$.
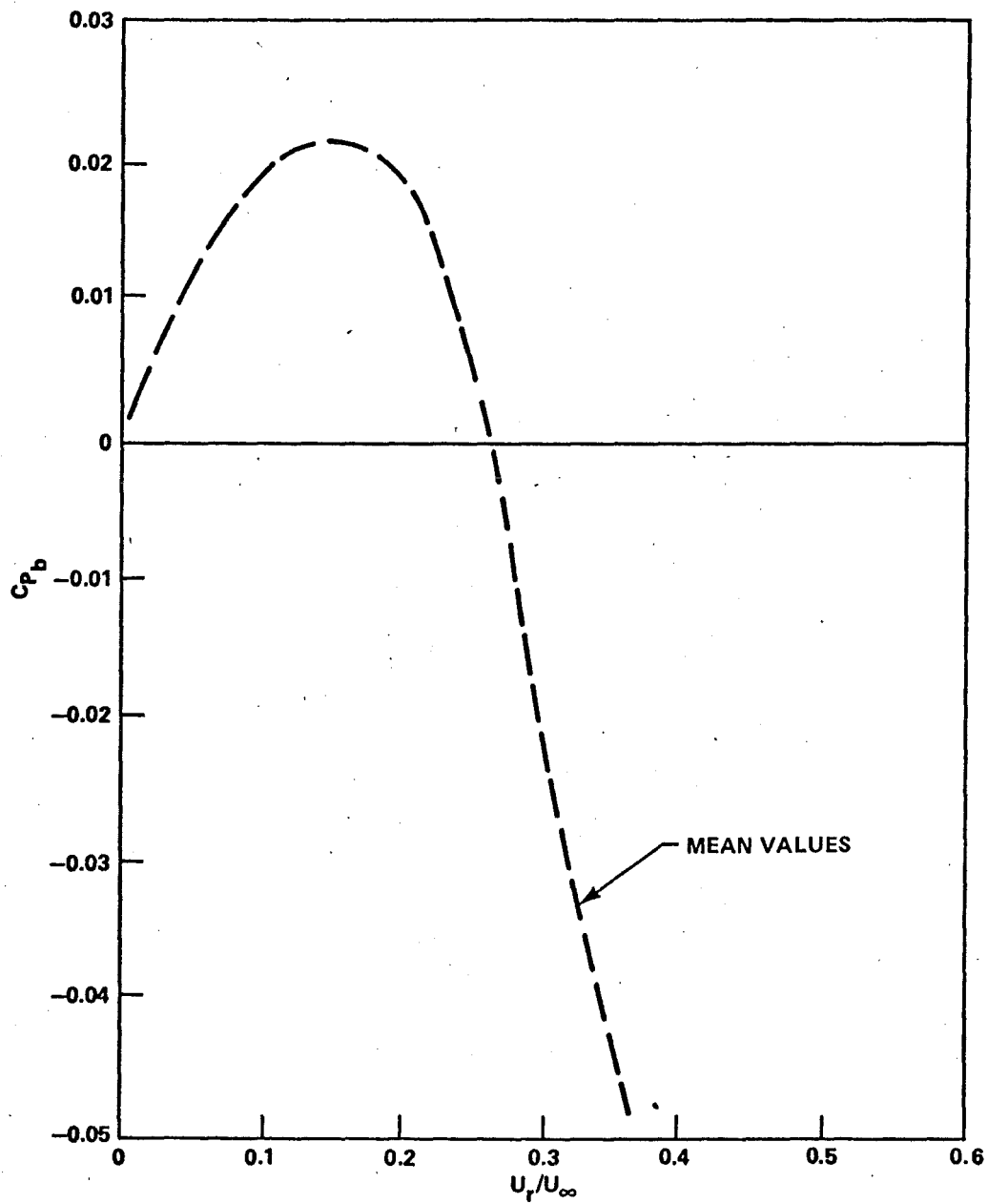
Figure 126. Effect of rotation on base pressure data [74].

184
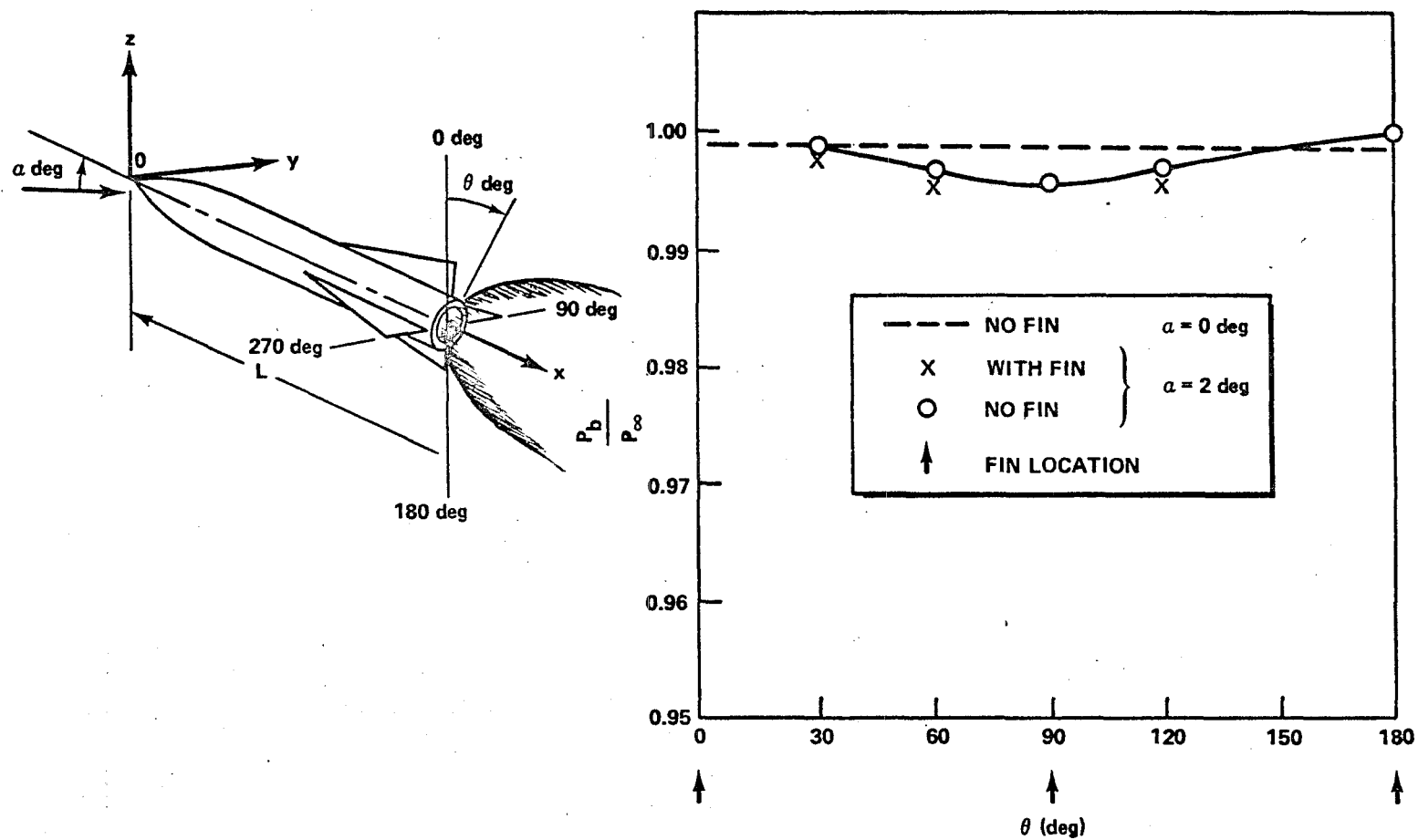
Figure 127. Potential flow pressure on the base plane: $M_\infty = 1.1$, body B1.
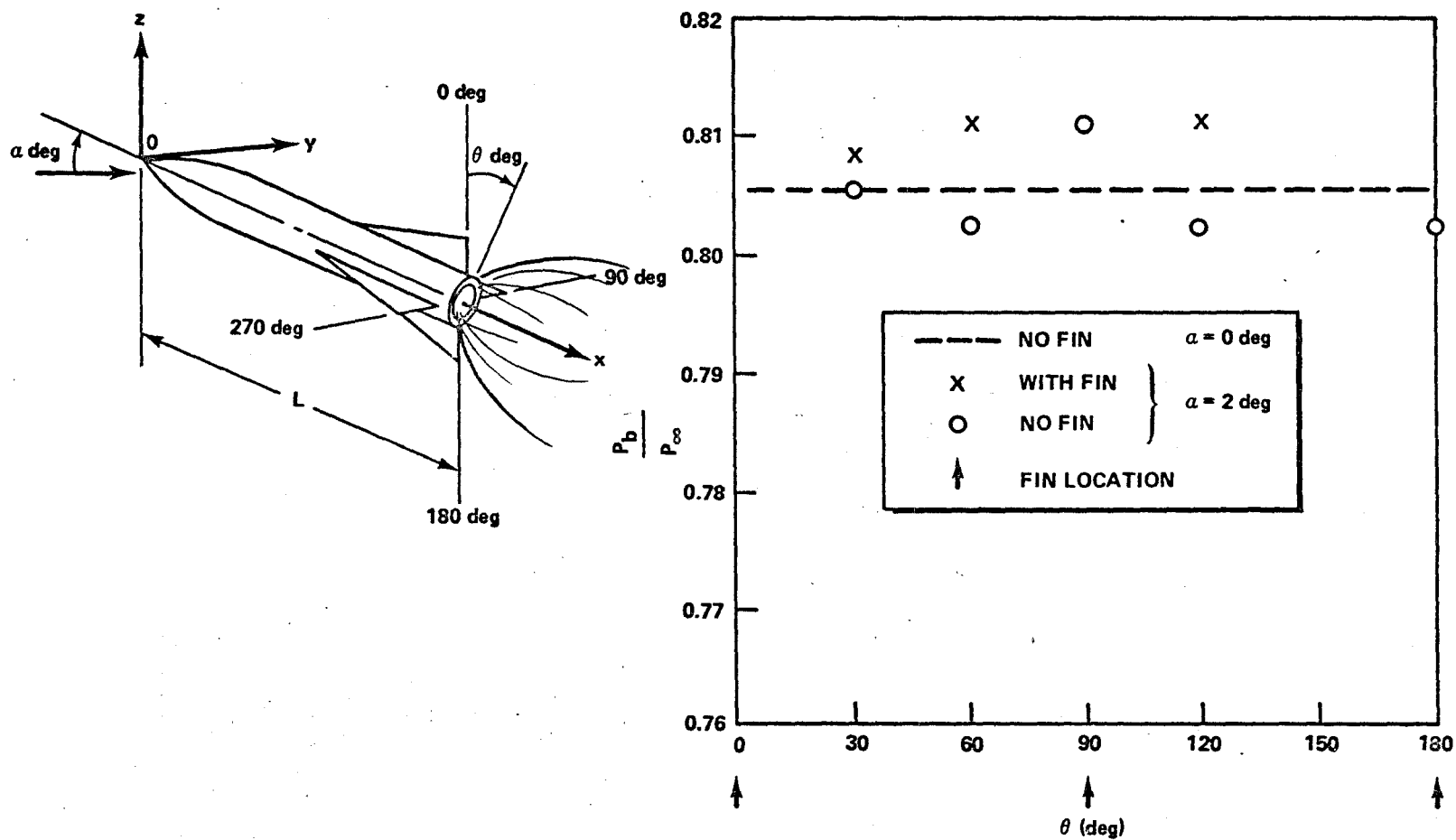
Figure 128.   Calculated base pressure with plume interaction:
M_∞ = 1.1 and jet pressure ratio = 100,   body B1

with nozzle N12.

LIST OF SYMBOLS

(Section II)

a   Body radius, location in x-direction of a fin corner (Figure 24).

$\cancel{R}$ Aspect ratio of a fin extended into a body.

b   Maximum spanwise length, location in y-direction of a fin corner (Figure 46).

c   Chordwise length at a fin root.

$C_{L\alpha}$ Lift coefficient.

$C_{N\alpha}$ Normal force coefficient.

C_p Surface pressure coefficient.

ΔC_p Difference of C_p, i.e., $\Delta C_p = (C_p)_{\text{lower part}} - (C_p)_{\text{upper part}}$ or $(C_p)_{\text{left part}} - (C_p)_{\text{right part}}$.

D   Body diameter.

D^m Derivative operator of order m.

d   Percentage of a location of a panel in x-direction.

e   Location of a local panel in y-direction.

g   Nonlinear correction term.

I_1, I_3 Complete elliptical integrals of the third kind (Reference 23).

I_2, I_4 Incomplete elliptical integrals of the third kind (Reference 23).

h   Half width of a local panel.

i $\sqrt{-1}$

K   Parabolic constant.

L   Body total length.

LPC	Local panel chard length.
ℓ	Nose length in II.9, chordwise length at y position in II.3.
M	Number of panels on half body.
M_∞	Mach number in free-stream.
n	Number of panels on half body.
P	Aerodynamic matrix [45].
$\Delta p/q$	Load distribution = ΔC_p
Q	Aerodynamic matrix [45].
q	Dynamic pressure = $\rho_o v_o^2/2$, source strength per unit body surface area.
R	Body radius in II.1, radius of circle in σ-plane corresponding to a surface of a fin-body combination in x-plane in II.2, Aerodynamic matrix [45] in II.3.
$\bar{R}$	Radius of secant body.
Re	Reynolds number.
r	Polar coordinate in x-plane, distance of two points.
ΔS	Panel area.
S_n^m	Sterling number.
s	Semi-spanwise length of a fin.
U_∞	Free-stream velocity.
u	Perturbation velocity component in x-direction.
V_o	Free-stream velocity.
v	Perturbation velocity component in y-direction.
$\vec{W}$	Velocity vector.
w	Perturbation velocity component in z-direction.
X	Physical plane (= y + iz).

188

x	Longitudinal coordinates.
$\underline{x},\underline{y},\underline{z}$ x,y,z x',y',z'	Body-fixed Cartesian coordinate systems (Figure 22).
z_o	Fin location mounted on a body in z-direction.
α	Angle of attack.
α_c	Angle of incidence.
β	Angle of yaw, or $\sqrt{1 - M^2}$
Γ	Circulation.
γ	Specific heat ratio = C_p/C_v, circulation strength per unit spanwise length, polar coordinate in σ-plane corresponding to a fin root in x-plane (Figure 28).
δ	Semi-apex angle of nose cone in II.1, cant angle of a fin in II.2, deflection angle of a flap or elevon in II.3.
μ	Polar coordinate in σ-plane corresponding to θ in x-plane (Figure 28).
θ	Polar coordinate in x-plane.
$\bar{\theta}$	$= 90° - \theta$
Φ	Nonlinear velocity potential.
ϕ	Linearized velocity potential in II.1 or small perturbation velocity potential in II.2.
$\tilde{\varphi}$	Transformed perturbation velocity.
φ	Angle of bank.
$\rho*$	Distance between two points.
ρ_o	Density in a free-stream.
σ	Mapping plane $(= \tau + iv)$.
τ	Cartesian coordinate in σ-plane.
v	Cartesian coordinate in σ-plane.

λ	Boattail angle in radians in II.1, slope of a local bound vortex, taper ratio.
Λ	Sweptback angle at a fixed chordwise position.
ω	Apparent angle of attack of a fin.

SUBSCRIPTS

b	Body.
f	Flap.
F	Fin.
e	Elevon.

i,j,k,l,υ,ʋ,μ, panel name.

n	normal to a surface.
t	Tangential to a surface.
d	Control point of a panel.
v	Bound vortes location.

(Sections III and IV)

a	Sound speed.
C_D	Drag coefficient.
C_f	Skin friction coefficient.
C_M	Pitching moment coefficient.
C_N	Normal force coefficient.
C_P	Pressure coefficient.
erf	Error function.
exp	Exponential function.
G	Modified trubulence production integral.

$\overline{G}$ Value of G for equilibrium flow.

G_α Modified stream function.

h   Step height.

H   Boundary layer shape factor.

$\overline{H}$ Incompressible laminar flow value of H.

K   Constant (Equation 73).

ℓ^* Length of free-shear layer.

R(x)   Local body radius.

Re   Reynolds number based on L.

s   Entropy.

T   Representation of turbulence stress (Equation 44).

T   Temperature.

u,v   Velocity components along coordinate directions x,r.

U   Velocity in stream direction.

u_τ Friction velocity.

u_β Wake component velocity.

x,r   Cylindrical coordinates.

x_p, y_p Coordinates of plume boundary.

L   Length of body.

M   Mach number.

P   Pressure gradient parameter.

p   Fluid pressure.

$\overline{q}$ Velocity vector.

y   Coordinate normal to shear layer.

z	Non-dimensional interaction length scale.
γ	Ration of specific heats.
δ	Boundary layer thickness.
$\delta*$	Displacement thickness of boundary layer.
$\delta**$	Density thichness.
Γ	Pressure rise coefficient (Equation 69).
ρ	Fluid density.
λ	Non-equilibrium parameter or characteristic angle.
θ	Boundary layer momentum thichness or turning angle.
$\theta*$	Boundary layer energy thickness.
θ_M	Angle for shock induced separation
μ	Mach angle.
ψ	Stream function.
υ	Kinematic viscosity of fluid.
τ	Reynolds shear stress.
κ	Von Karman constant.
π	3.14...
Δ	Modified shape factor.
η	Similarity parameter.
σ	Shear layer mixing cofficient.
χ	Pressure signature function.

SUBSCRIPTS

B	Base condition.
BL	Boundary layer.
C	Chamber condition or confluence point.

e   Conditon external to boundary layer.

f   Condition at flare juction.

J   Jet value.

m   Value on median streamline.

o   Stagnation or initial condtion.

P   Plateau or plume value.

ref Reference condition.

S   Separation condition.

SL or S Free shear layer.

t   Value at transition.

w   Value on wall.

∞   Free Stream Condition.

2   Value downstream of discontinuity.

REFERENCES

1. Wu, J. M., Aoyama, K., and Moulden, T. H., Transonic Flow Fields Around Various Bodies of Revolution Including Preliminary Studies on Viscous Effects With and Without Plume, US Army Missile Command, Redstone Arsenal, Alabama RD-TR-71-12, May 1971.

2. Aoyama, K., and Wu, J. M., On Transonic Flow Around Tangent Ogive Bodies, AIAA 8th Aerospace Sciences Meeting AIAA Paper No. 70-189, New York, January 1970.

3. Wu, J. M., and Aoyama, K., Studies of Flow Around Axisymmetric Bodies With and Without Plume Induced Separation at Transonic Speeds, US Army Missile Command, Redstone Arsenal, Alabama, RD-TR-70-3, March 1970.

4. Wu, J. M., and Aoyama, K., Transonic Flow Field Calculation Around Ogive Cylinders by Nonlinear-linear Stretching Method, US Army Missile Command, Redstone Arsenal, Alabama RD-TR-70-12, April 1970.

5. Wu, J. M., and Aoyama, K., Pressure Distributions for Axisymmetric Bodies with Discontinuous Curvature in Transonic Flow, US Army Missile Command, Redstone Arsenal, Alabama, RD-TR-70-25, November 1970.

6. Moulden, T. H., Spring, D. J., Saisi, R., K. Aoyama and Wu, J. M., "Bodies of Revolution at Transonic Speeds: The Estimation of Reynolds Number Effects," Facilities and Techniques for Aerodynamic Testing at Transonic Speeds and High Reynolds Number, NATO AGARD Meeting Proceedings, Goettingen, Germany, April 1971.

7. Moulden, T. M., and Wu, J. M., An Outline of Methods Applicable to Viscous Fluid Flow Problems, US Army Missile Command, Redstone Arsenal, Alabama, RD-TR-71-4, May 1971.

8. Aoyama, K., Analysis of Transonic Flow Field Around Bodies of Revolution Ph.D Thesis, The University of Tennessee Space Institute, Tullahoma, Tennessee, June 1971.

9. Wu, J. M., "Review on Transonic Flow Analytical Techniques: With Emphasis on Bodies of Revolution," Proceedings of the Ninth Technical Cooperation Program--Exterior Ballistic Meeting, Volume 2, Quebec City, Quebec, Canada, September 22-24, 1971.

10. Moulden, T. H., and Wu, J. M., "On the Conditions at the Separation Point of a Laminar Boundary--Layer," Zeitschrift fur Angewandte Mathematik and Mechanik, 1972 Volume 52, pp. 247-248.

11. Wu, J. M., and Aoyama, K., Analysis of Axisymmetric Bodies with Discontinuous Curvature in Transonic Flow, AIAA 10th Aerospace Sciences Meeting, Paper no. 72-137, San Diego, California, January 17-19 1972.

12. Wu, J. M., and Aoyama, K., Preliminary Review of Approximate Calculative Methods for Transonic Flow Around Bodies of Revolution, US Army Missile Command RD-TR-72-4, March 1972.

13. Wu, J. M., Moulden, T. H., Venghaus, H., Spring, D., and Henderson, J., "Plume Induced Separation from Single Nozzle Exhaust at Transonic Flight Speed," Proceedings of 7th JANNAF Meeting, on Jet Plume Technology, Redstone Arsenal, Alabama, April 1973.

14. Wu, J. M., Moulden, T. H., and Spring, D. J., "Flow Field Analysis for a Powered Rocket at Transonic Speeds," Proceedings of 10th International Symposium on Space Technology and Science, Tokyo, Japan, September 3-8, 1973.

15. Wu, J. M., and Lock, R., A Theory for Subsonic and Transonic Flow Over a Cone, With and Without Small Yawed Angle, US Army Missile Command Redstone Arsenal, Alabama, Technical Report RD-74-2 December 1973.

16. Venghaus, H. H., Study of Transonic Flow Over Various Bodies, Ph.D. Thesis, The University of Tennessee Space Institute, Tullahoma, Tennessee, June, 1974.

17. Venghaus, H. and Wu, J. M., An Approximate Transonic Calculative Method Applied to Various Smooth Shaped Nose-Cylindrical Bodies, US Army Missile Command, Redstone Arsenal, Alabama, RD-CR-74-2, May 10, 1974.

18. Wu, J. M. and Venghaus, H., A First Order Theory for Transonic Flow Over a Conical Flare, US Army Missile Command, Redstone Arsenal, Alabama, RD-CR-74-3, May 10, 1974.

19. Moulden, T. H., Wu, J. M., and Spring, D. J., "On Some Studies of Aft-End Design and its Influence on Plume Induced Separation in Transonic Flight," Proceedings of 8th JANNAF Meeting on Jet Plume Technology, Colorado Springs, Colorado, July 1974.

20. Wu, J. M., Moulden, T. H., and Spring, D. J., "On Some Problems Encountered in a Nozzle Configuration in Transonic Flight," Paper No. 14, Proceedings of AGARD Specialists Meeting on Airframe/Propulsion Interference, Rome, Italy, September, 1974.

21. Moulden, T. H., Wu, J. M., and Spring, D. J., "A Flow Field Model For, and Some Studies on the Drag of, an Engine Exhaust System at Transonic Flight Speeds," AIAA/SAE 10th Propulsion Conference, San Diego, California, October 1974, Journal of Spacecraft & Rockets, Volume 12, No. 7, July 1975, pp. 428-433.

22. Moulden, T. H., Wu, J. M., and Spring D. J., _A Discussion of Transonic Base Flows in the Presence of a Propulsive Jet_, (To appear in Progress in Aeronautics and Astronautics), 1976.

23. Uchiyama, N. and Wu, J.M., _Inviscid Flow Analysis on Body of Revolution with Slender Cruciform Canted Delta Fins at Small Angle of Incidence_, US Army Missile Command, Redstone Arsenal, Alabama, Technical Report RD-75-32 March 1975.

24. Wu, J.M., Moulden, T. H., Uchiyama, N., and Spring, D. J., "Transonic Flow Over a Powered Rocket with Fins," _Proceedings of the 11th International Symposium on Space Technology and Science_, Tokyo, Japan June 30-July 5, 1975.

25. Hosokawa, I., "A Comment on the Refinement of the Linearized Transonic Flow Theory," _J. Phys. Soc._ Japan, Volume 29, p. 252, 1970.

26. Moore, F. G., _Aerodynamics of Guided and Unguided Weapons, Parts I and II_, US Naval Weapons Laboratory, Virginia, TR-NWL-3018, December 1973.

27. Hosokawa, I., "A Simplified Analysis for Transonic Flow Around Thin Bodies," _Symposium Transonicum_ (Ed. by K. Oswatitsch), Springer-Verlag, Berlin, 1964, pp. 184-199.

28. Hosokawa, I., "A Refinement of the Linearized Transonic Flows Around Thin Bodies," _J. Phys. Soc._, Japan, Volume 15, 1960, pp. 149-157.

29. Spring, D. J., _Comparisons Between Experiments and An Approximate Transonic Calculative Method_, US Army Missile Command, Redstone Arsenal, Alabama, TR-RD-73-34, September 1973.

30. Loving, D. L., _Wind-Tunnel-Flight Correlation of Shock-Induced Separated Flow_, NASA, TN-D3580 1966.

31. Rubin, D. V., _Rocket Plume Effects on Boattail and Flare Bodies of Revolution at Transonic Speeds_, US Army Missile Command, TR-RD-71-12, May 1971.

32. Tani, T., "Local Two-Dimensional Approximation for Axisymmetric Transonic Flow," _Proceedings of the 16th Japan National Congress for Applied Mechanics_, 1966, pp. 224-228.

33. Spreiter, J.R., and Alksne, A. Y., _Slender-Body Theory Based on Approximate Solution of the Transonic Equation_, NASA, TR-2, 1959.

34. Mager, A., "On the Model of the Free-Shock-Separated Turbulent Boundary-Layer," _J. Aero. Sciences_, Volume 23, 1956, pp. 181-184.

35. Whitfield, D., _Private Communication_, ARO, Inc., Arnold Engineering Development Center, Tullahoma, Tennessee, May 1975.

36. Spreiter, J. R., _Aerodynamic Properties of Slender Wing Body Combination at Subsonic, Transonic and Supersonic Speeds_, NACA TN-1662, July 1948.

37. Spreiter, J. R., _The Aerodynamic Forces on Slender Plane-and Cruciform-Wing and Body Combinations_, NACA Report 962, March 1949.

38. Adams, G. J., and Dugan, D. W., _Theoretical Damping in Roll and Rolling Moment Due to Differential Wing Incidence for Slender Cruciform Wings and Wing-Body Combinations_, NACA Report 1088, September 1950.

39. Nielsen, J. N., _Missile Aerodynamics_, McGraw Hill Book Company, Inc., New York, 1960, p. 211.

40. Spreiter, J. R., and Stahara, S. S., "Aerodynamics of Slender Bodies Wing-Body Combinations at M_∞ =1 Theory and Experimental Evaluation", AIAA Paper, 1970.

41. Spreiter, J. R., and Stahara, S. S., _Calculative Techniques for Transonic Flows About Certain Classes of Airfoils and Slender Bodies_, NASA CR-1722, April 1971.

42. Lawrence, H. R., and Flax, A. H., "Body-Wing Interference at Subsonic and Supersonic Speeds — Survey and New Development," _Jr. Aero. Sci._, Volume 21, No. 5, May 1954.

43. Körner, H., _Berechnug der Potential Theoretischem Stromung um Flugel-Rumpf-Kombinationen und Vergleich mit Messungen_, Zeitschrift Fur Flugwissenschaften, 20 Jahrgang, Heft 9, September 1972.

44. Woodward, F. A., "Analysis and Design of Wing-Body Combinations at Subsonic and Supersonic Speeds," _J. Aircraft_ Volume 5, No. 6., November-December 1968.

45. Uchiyama, N. and Wu, J. M., _A Study on Various Slender and Non-Slender Fin-Body Combinations of Missile Configurations_, (in preparation for US Army Missile Command Technical Report), 1976.

46. Manro, M. E., Tinoco, E. N., Bobbitt, P. J., and Rogers, J. T., _Comparisons of Theoretical and Experimental Pressure Distributions on an Arrow-Wing Configuration at Transonic Speeds, Aerodynamic Analyses Requiring Advanced Computers, Part II_, Langley Research Center, Hampton, Virginia, NASA SP-347, March 1975.

47. South, J. C. and Jameson, A., "Relaxation Solutions for Inviscid Axisymmetric Transonic Flow over Blunt and Pointed Bodies," _AIAA Computational Fluid Dynamics Conference_, July 1973.

48. Whitcomb, R. T., "Review of NASA Supercritical Airfoils," 9th Congress of the International Council of the Aeronautical Sciences, Paper 74-10, August 1974.

49. Korst, H. H., "A Theory for Base Pressure in Transonic and Supersonic Flow," J. Applied Mechanics, Volume 23, 1956, p. 593.

50. Thwaites, B., "Approximate Calculation of the Laminar Boundary Layer," Aero Quarterly, Volume 1, 1949, p. 245.

51. Mangler, W., "Zusammenhang Zwischen Ebenen und Rotation Axynmetrischen Grenzschichter in Kompressiblen Medien," ZAMM, Volume 28, 1948, p. 97.

52. Stepanov, E. I., "On the Integration of the Laminar Boundary Layer Equations for a Motion with Axial Symmetry PMM Volume 11, 1947, p. 203.

53. Stewartson, K., "Correlated Incompressible and Compressible Boundary Layers," Proc. Roy. Soc., Volume A200, 1949, p. 84.

54. Illingworth, C. R., "Steady Flows in the Laminar Boundary Layer," Proc. Roy. Soc., Volume A199, 1949, p. 533.

55. Nash, J. F., "A Practical Calculation Method for Compressible Turbulent Boundary-Layers in Two-Dimensional Flows," Lockheed Georgia Research Memo, ER 9428, 1967.

56. Lumsdaine, E., and Fathy, A., "Effect of Normal Shock on Turbulent Boundary Layer Parameters," J. Basic Engineering, December 1971, p. 565.

57. Rose, W. C. and Johnson, D. A., "Turbulence in a Shock-Wave Boundary Layer Interaction," AIAA Journal, Volume 13, 1975, p. 584.

58. Wu, J. M., Moulden, T. H., Elfstrom, G. M., Reddy, K. C., Chen, C. W., Nygaard, R., Shen, L., Venghaus, H. H., and Anjaneyulu, K., Fundamental Studies on Subsonic and Transonic Flow Separation Summary Report, AEDC Tech. Report TR-75-95, 1974.

59. Nash, J. F., An Analysis of Two-Dimensional Turbulent Base Flow, Including the Effect of the Approaching Boundary Layer, ARC R&M 3344, 1963.

60. Rubin, D. V., A Transonic Investigation of Jet Plume Effects on Base and Afterbody Pressures of Boattail and Flare Bodies of Revolution, US Army Missile Command, Redstone Arsenel, Alabama, TR-RD-70-10, 1970.

61. Nash, J. F., "The Effect of an Initial Boundary Layer on the Development of a Turbulent Free Shear Layer," NPL Aero Report 1019, 1962.

62. Stratford, B. S., "The Prediction of Separation of the Turbulent Boundary Layer," JFM, Volume 5, 1959, p. 1.

63. McDonald, H., "A Study of the Turbulent Separated Flow Region Occurring at a Compression Corner in Supersonic Flow," JFM, Volume 22, 1965, p. 481.

64. Korst, H. H., and Tripp, W. "The Pressure on a Blunt Trailing-Edge Separating Two-Dimensional Supersonic Air Streams of Different Mach Numbers and Stagnation Pressures, but Identical Stagnation Temperatures," Proc. Midwest Conference on Solid and Fluid Mechanics, 1957.

65. Tetervin, N., "A Transformation Between Axisymmestric and Two-Dimensional Turbulent Boundary Layers," AIAA Journal, Volume 8, 1970, p. 985.

66. Zukoski, E. E., Turbulent Boundary-Layer Separation in Front of a Forward Facing Step," AIAA Journal, Volume 5, 1967, p. 1746.

67. Reubush, D. E., "The Effect of Reynolds Number on Boattail Drag," Paper presented to AIAA 13th Aerospace Sciences Meeting, Pasadena, January 1975.

68. Chamberlin, R., and Blaha, B. J., "Flight and Wind Tunnel Investigation of the Effects of Reynolds Number on Installed Boattail Drag at Supersonic Speeds," AIAA Paper 73-139, Washington, D. C., 1973.

69. Czarnecki, K. R., and Jackson, M. W., "Turbulent Boundary Layer Separation due to a Forward Facing Step," AIAA Paper 74-581, Palo Alto, California, 1974.

70. Deep, R. A., Henderson, J. H., and Brazzel, C. E., Thrust Effects on Missile Aerodynamics, US Army Missile Command, Redstone Arsenal, Alabama, TR-RD-71-9, May 1971.

71. Nash, J. F., Quincey, V. G., and Callinan, J., Experiments on Two-Dimensional Base Flow at Subsonic and Transonic Speeds, ARC R&M 3427, 1966.

72. Henderson, J. H., Results of Transonic Wind Tunnel Investigations to Determine the Effects of Nozzle Geometry and Jet Plume on the Aerodynamics of a Body of Revolution, US Army Missile Command, Redstone Arsenal, Alabama, TR-RD-72-17, 1972.

73. Wilson, R., and Maurer, F., _An Experimental Investigation of Turbulent Separated Boundary Layers at Low Supersonic Mach Numbers_, German DLR FB 70-30, 1970.

74. Badrinarayanan, M. A., and Kangovi, S., _Base Flow Behind Rotating Axisymmetric Body_, Report 71-FM5, Indian Institute of Science, Bangalore, 1971.

BIBLIOGRAPHY

Hedman, S. G., Vortex Lattice Method for Calculating of Quasi Steady State Loadings on Thin Elastic Wings in Subsonic Flow, FFA Rep. 105, 1966.

Körner, H., Theoretische Parameteruntersuchungen an Flugel-Rumpf-Kombinationen, DLR-FB 72-63, 1972.

Sears, W. R., General Theory of High Speed Aerodynamics, Volume VI, Princeton University Press, 1954.

Viswanath, P. R., and Narasimha, R., "Two-Dimensional Boattailed Bases in Supersonic Flow," Aero Quarterly, Volume 25, 1974, p. 210.

Weeks, T. M., "Base Flow Studies in and Calibration of the New 15" AFFDL Transonic Facility," Proc. 37th Semiannual Meeting of the Supersonic Tunnel Association, May 1972.

Appendix A. COMPUTER PROGRAM UTILIZATION

A subsequent document will give greater details of the computer program, along with a full listing and documentation of its capabilities. The objective here is to simply outline the input to the program and to present a sample output. Table A-1 gives the symbol and format inputs for calculation of the potential flow and the viscous interaction. Table A-2 presents the same information for the calculations when the surface Mach number distribution is given. In this latter case, there are again two options [with IOPT being redefined (see Table (A-2)] so that either a boundary layer calculation or a combined boundary layer calculation/plume interaction can be determined. This option allows experimental pressure distributions along the body to be used in place of a potential flow calculation. The input surface pressure distribution can be in the form of a pressure coefficient, when the parameter IM = 1, or as a local Mach number distribution (then IM = 0). All internal calculations in the program use the local Mach number and all required interchanges between Mach number and pressure, or velocity are done to the basis of isentropic flow.

The basic flow diagram through the program is shown in Figure A-1, while Table A-3 explains the notation used in Table A-1 and A-2 and in the computer program. Reference should also be made to Figure A-2.

All geometric lengths associated with the body configuration are input in the same units and non-dimensionalized (with respect to BDLN) within the program. Non-dimensional input is admissible provided BDLN is specified to be unit length. Angles are input in degrees.

The potential flow calculation requires the specification of two parameters CS and A. Appropriate values for these are given in Table A-4. During the process of the calculation, there is an iteration on these values to determine the final solution. The final values for CS and A are displaced (Figure A-3a) where CS identifies with the sonic point and A retains its symbol. As experience is gained in the use of the program for various body shapes, better first estimates for CS and A than those provided in Table A-4 can be established for faster convergence.

Sample data cards are shown in Table A-5 and the corresponding computer output is given on Figure A-3. In this example there are four figures of output giving the potential flow, the boundary layer development and the interaction with the plume (Figure A-3b-A-3e). The body selected for this example had a 4-calibre tangent ogive nose and a parallel sided aft-end. There were no fins. It should be noted that the geometric data of the body are returned to the output in non-dimensional form. The body length (BDLN) is, however, recorded in the output. Notation used with the output display is presented on Table A-6.

The option IC = 0 or 1 determines whether the potential flow is calculated or not. The potential flow is not calculated when a surface pressure distribution is input data (IØPT = 3). The main value of the IC = 0 option is that it allows several (ICASE) different viscous flow calculations (with various Reynolds number or jet pressure ratio) for only one potential flow calculation. Thus, put IC = 1 for the first data set and the specification IC = 0 would be made for all subsequent data sets in the sequence. The potential flow solution is stored in the program until overwritten by a subsequent calculation or input data in the IØPT = 3 mode.

The program is normally run with the calculation being performed along a single azimuthal strip at the specified angle BE. In this mode IL = 0. Placing IL = 1 in the input data will initiate a sequence of calculations for BE = 0, 30, 60, ..., 180 and an integration for the normal force coefficient.

TABLE A-1. INPUT CARDS FOR POTENTIAL FLOW AND VISCOUS INTERACTION CALCULATIONS (IØPT = 0, 1 OR 2)

Card	Symbol Sequence	Format (Fortran IV)
1	ICASE	I3
2	TITLE CARD FOR EACH RUN*	18A4
3	IØPT, IC, IF, IND, NST, IL	6I5
4	MINF, CS, A, PINF, REN	5F 10.6
5	BDLN, XSHLD, XBT, XN, XS	5F 10.6
6	RENØZ, PJ, THJ, XMJ, THJ1, TØ	6F 10.6
7	THBL, THC, RB, RC	4F 10.6
8	AL, BE, THPS, RCN	4F 10.6
9	ANG, CRD, FSPN, XF, PH	5F 10.6

*Cards 2-9 are repeated "ICASE" times

TABLE A-2. INPUT CARDS FOR BOUNDARY LAYER AND VISCOUS INTERACTION CALCULATIONS (IØPT = 3)

Card	Symbol Sequence	Format (Fortran IV)
1.	ICASE*	I3
2-9	As in Table A-1	As in Table A-1
10	IN, IM, IØPT**	3I3
11	XST	F 10.6
12	X(I) (I = 1, IN)	7F 10.6
13	R(I) (I = 1, IN)	7F 10.6
14	M(I) (I = 1, IN)	7F 10.6

*Cards 2-14 are repeated "ICASE" times
** Only values IØPT = 0 or 2 are sensible

TABLE A-3. NOTATION*

Symbol	Definition	Units
ICASE	Number of runs in given data set.	-
IØPT	Selects calculation options (See Figure A-1).	-
IC	IC = 0 omits the potential flow calculation.	-
IF	IF = 0 omits the fin calculation.	-
IND	IND = 1 for potential flow calculations on the body.	-
	IND = 2 is for calculations off the body (done at radius RCN) but within a mixed subsonic/supersonic region.	-
	IND = 3 does off body calculations in cases where the flow character does not change.	-
NST	NST = 0 for base flows with a plume.	-
	NST = 1 for base flow in the absence of a plume.	-
IL	IL = 0 calculates flow at one azimuthal angle only.	-
	IL = 1 determines flow at seven azimuthal angles and determines the lift coefficient ($\alpha \neq 0$ only).	-
MINF	Free-stream Mach number.	-
CS, A	Constants for potential flow calculation (See Table A-4).	-
PINF	Free-stream pressure.	psi
REN	Reynolds number in millions.	-
BDLN	Reference length of body.	Length (units L say)

* See also Figure A-2.

205

Symbol	Definition	Units
XBT	Distance from nose to boattail (or flare) corner.	L
XN	Nozzle length.	L
XS	Transition point for boundary layer calculation.	L
RENØZ	Nozzle exit radius.	L
PJ	Jet total pressure ratio.	-
THJ	Nozzle exit angle.	Degrees
XMJ	Nozzle exit Mach number.	-
THJ1	Boundary layer momentum thickness at nozzle exit.	L
TØ	Jet total temperature.	°R
THBL	Boattail conical angle (< 0 for flare).	Degrees
THC	Nose conical angle (conical nose only).	Degrees
RB	Base radius.	L
RC	Main body radius.	L
AL	Body incidence.	Degrees
BE	Azimuthal angle (see Figure 4).	Degrees
THPS	Initial shear layer angle.	Radians
RCN	Off-body radius.	L
ANG	Fin cant angle.	Degrees
CRD	Fin root chord.	L
FSPN	Fin span.	L
XF	Location of fin.	L
PH	Azimuthal location of fin (see Figure 22).	Degrees
IN	Array size for input pressure distribution.	-
IM	IM = 0 if Mach number distribution input.	-
	IM = 1 if pressure coefficient distribution input.	-

Symbol	Definition	Units
XST	Location of discontinuity in input pressure distribution.	L
X(I)	Distance array for input pressure distribution.	L (I = 1, IN)
R(I)	Body radius array for input pressure distribution.	(I = 1, IN)
M(I)	Input pressure distribution (see definition for IM)	(I = 1, IN)

TABLE A-4. VALUES FOR CONSTANTS CS AND A

MINF	CS	A
MINF < 1.0	0.67	-17.5
MINF = 1.0	0.5	- 2.0
MINF > 1.0	0.5	-10.0

TABLE A-5. INPUT CARDS USED FOR SAMPLE PROBLEM

STATEMENT NUMBER (1–5)	Cont. (6)	FORTRAN STATEMENT (7–60)
1		
		SAMPLE CALCULATION
0		1 0 1 0 0
1.1		0..5 -5..5206 14.7 1..2
32.5		10..0 32..5 0..0 10..0
1.	0	02 87..7 20..0 2.7 0..001 500..0
0.	0	0..0 1..25 1.25
0.	0	0..0 0..3 0.0
0.	0	0..0 0..0 0.0 0..0

TABLE A-6. SYMBOLS USED ON COMPUTER OUTPUT

| Symbol	Definition
X	Non-dimensional distance along body.
X (page 4 only)	Non-dimensional distance along plume (origin at nozzle exit plane).
R	Non-dimensional local body radius.
R (page 4 only)	Non-dimensional plume radius.
M	Local Mach number.
DR/DX	Body slope.
CP	Local pressure coefficient.
D	Body reference parameter (= 2 RC).
P	Local pressure (psi).
PINF	Free-stream pressure.
H	Boundary layer form factor.
THETA	Boundary layer momentum thickness (non-dimensional).
DEL	Boundary layer displacement thickness (non-dimensional).
CF	Local skin friction coefficient.
BLTH	Boundary layer thickness (non-dimensional).
S	Non-dimensional distance along plume boundary.
XP, YP	Coordinates of confluence point (non-dimensional) with origin at nozzle exit plane.
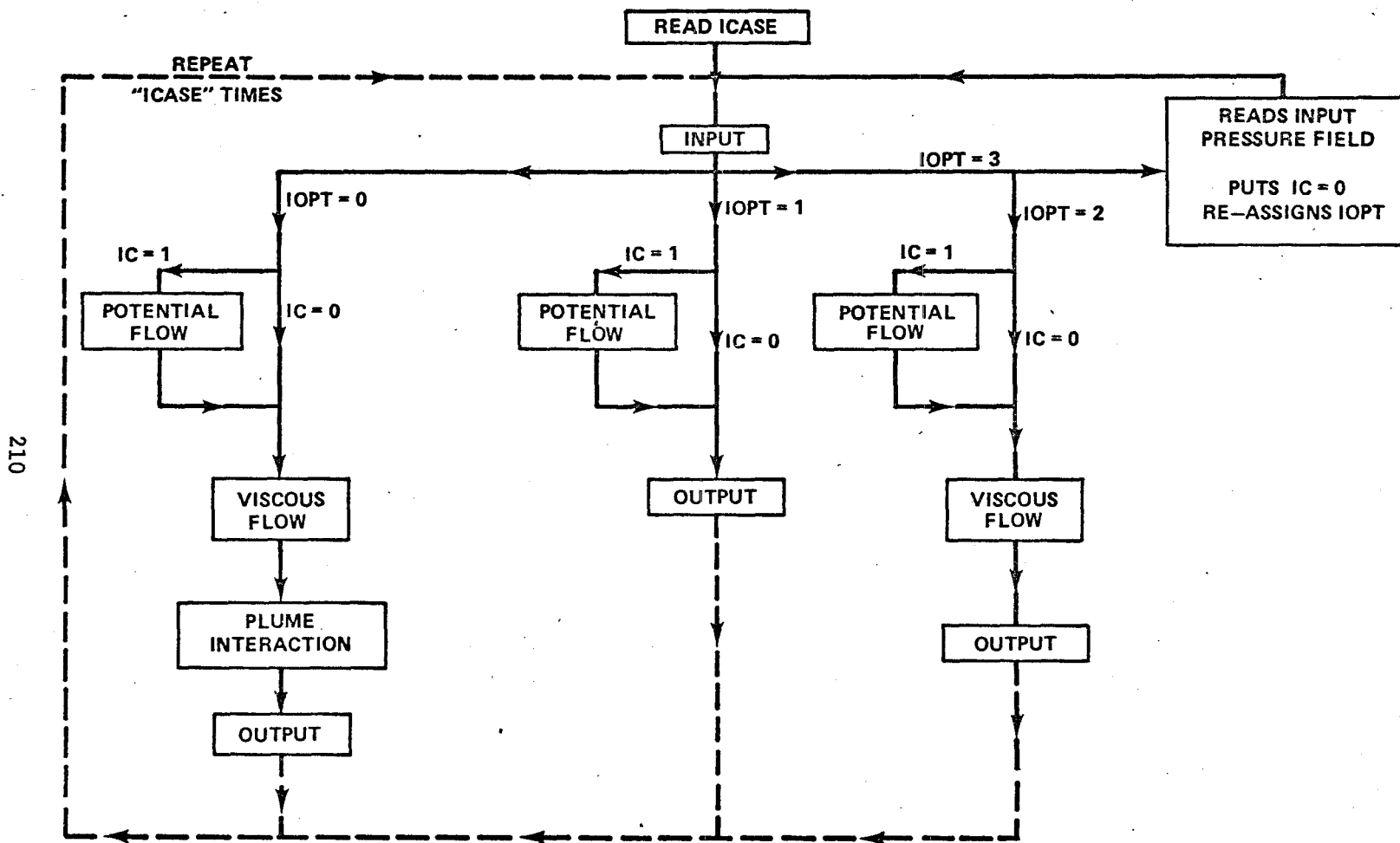
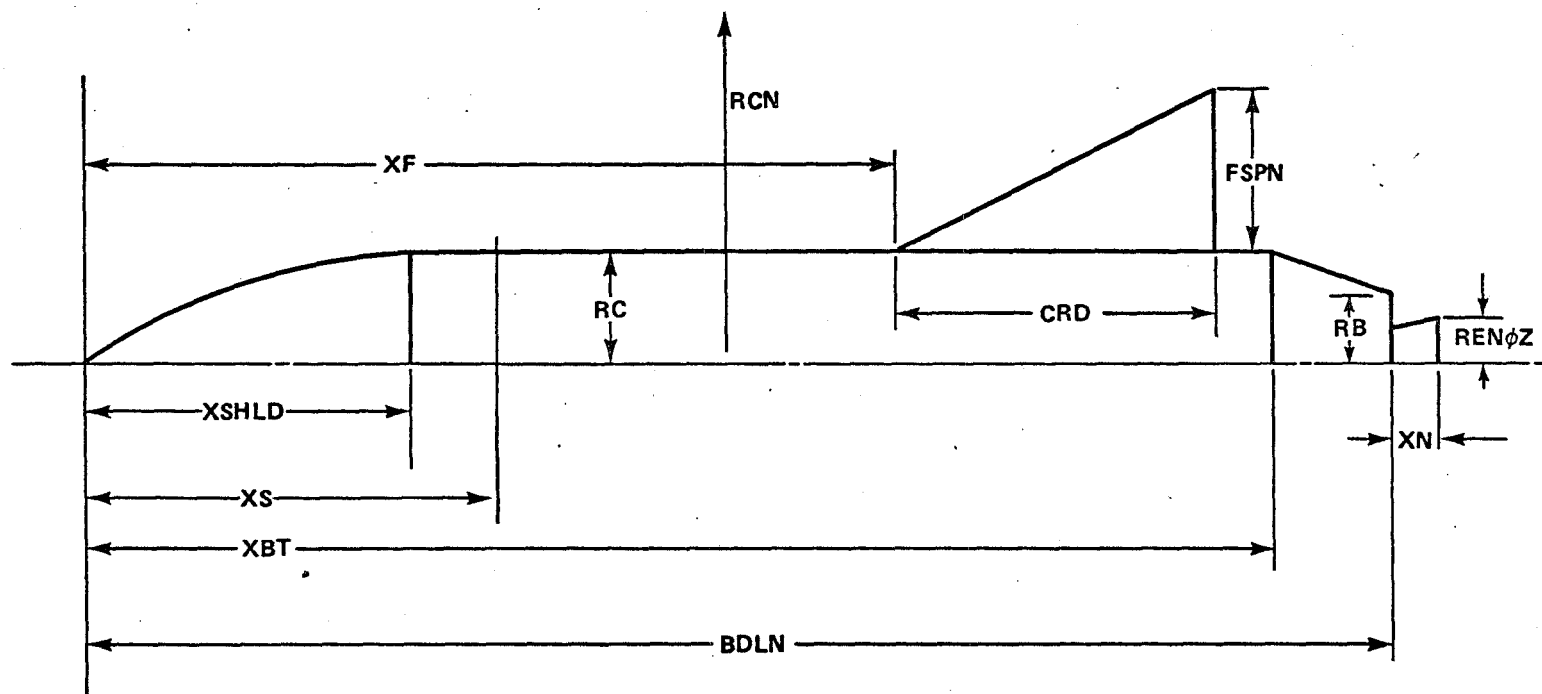Figure A-1. Basic flow diagram for computer program.

Figure A-2. Notation for input to computer program.

SAMPLE CALCULATION

POTENTIAL FLOW SOLUTION

FREE STREAM MACH NUMBER = 1.1000   INCIDENCE = 0.0000   ASIMUTH ANGLE = 0.0000

X	R	M	DR/DX	CP	X/D	P/PINF
0.000000	0.000000	0.000000	.250000	1.000000	0.000000	2.135136
.025000	.005996	.907633	.229688	.297502	.325000	1.251984
.050000	.011484	.966566	.209375	.203428	.650000	1.172303
.075000	.016465	1.004459	.189063	.144147	.975000	1.122093
.100000	.020938	1.030680	.168750	.103778	1.300000	1.087900
.125000	.024902	1.054798	.148438	.067166	1.625000	1.056890
.150000	.028359	1.078057	.128125	.032361	1.950000	1.027410
.175000	.031309	1.097325	.107813	.003920	2.275000	1.003320
.200000	.033750	1.115509	.087500	-.022582	2.600000	.980873
.225000	.035684	1.133017	.067188	-.047777	2.925000	.959533
.250000	.037109	1.150051	.046875	-.072021	3.250000	.938998
.275000	.038027	1.166867	.026563	-.095478	3.575000	.919130
.300000	.038438	1.183200	.006250	-.118168	3.900000	.899912
.325000	.038462	1.198899	0.000000	-.139415	4.225000	.881746
.350000	.038462	1.137304	0.000000	-.053497	4.550000	.954349
.375000	.038462	1.123354	0.000000	-.033412	4.875000	.971277
.400000	.038462	1.116283	0.000000	-.023702	5.200000	.979924
.425000	.038462	1.112070	0.000000	-.017596	5.525000	.985096
.450000	.038462	1.109333	0.000000	-.013618	5.850000	.988465
.475000	.038462	1.107449	0.000000	-.010877	6.175000	.990787
.500000	.038462	1.106097	0.000000	-.008907	6.500000	.992455
.525000	.038462	1.105094	0.000000	-.007444	6.825000	.993695
.550000	.038462	1.104329	0.000000	-.006328	7.150000	.994640
.575000	.038462	1.103732	0.000000	-.005456	7.475000	.995379
.600000	.038462	1.103256	0.000000	-.004761	7.800000	.995968
.625000	.038462	1.102870	0.000000	-.004198	8.125000	.996445
.650000	.038462	1.102553	0.000000	-.003734	8.450000	.996837
.675000	.038462	1.102288	0.000000	-.003347	8.775000	.997165
.700000	.038462	1.102065	0.000000	-.003021	9.100000	.997441
.725000	.038462	1.101875	0.000000	-.002743	9.425000	.997677
.750000	.038462	1.101711	0.000000	-.002503	9.750000	.997880
.775000	.038462	1.101568	0.000000	-.002295	10.075000	.998057
.800000	.038462	1.101444	0.000000	-.002112	10.400000	.998211
.825000	.038462	1.101334	0.000000	-.001952	10.725000	.998347
.850000	.038462	1.101237	0.000000	-.001809	11.050000	.998467
.875000	.038462	1.101150	0.000000	-.001683	11.375000	.998575
.900000	.038462	1.101072	0.000000	-.001569	11.700000	.998671
.925000	.038462	1.101002	0.000000	-.001467	12.025000	.998757
.950000	.038462	1.100939	0.000000	-.001375	12.350000	.998836
.975000	.038462	1.100882	0.000000	-.001291	12.675000	.998906
1.000000	.038462	1.100825	0.000000	-.001207	13.000000	.998977

SONIC POINT = .0933   SHOCK LOCATION = 1.0000   A = -5.5206

Figure A-3a.   Sample output, potential flow.

SAMPLE CALCULATION

BOUNDARY-LAYER DEVELOPMENT

BODY LENGTH = 32.50000

X	R	M	H	THETA	DEL	CF	BLTH
0.000000	0.000000	0.000000	2.500000	0.000000	0.000000	0.000000	0.000000
.025000	.005996	.907633	2.880175	.000046	.000131	.005738	.000656
.050000	.011484	.966566	3.223654	.000076	.000244	.002833	.001219
.075000	.016465	1.004459	3.276579	.000095	.000311	.002334	.001555
.100000	.020938	1.030680	3.316132	.000111	.000368	.002037	.001842
.125000	.024902	1.054798	3.343049	.000126	.000420	.001863	.002098
.150000	.028359	1.078057	3.369895	.000139	.000468	.001738	.002338
.175000	.031309	1.097325	3.398990	.000152	.000516	.001617	.002581
.200000	.033750	1.115509	3.419217	.000165	.000563	.001533	.002815
.225000	.035684	1.133017	3.438153	.000178	.000611	.001459	.003055
.250000	.037109	1.150081	3.455039	.000191	.000660	.001398	.003299
.275000	.038027	1.166807	3.470341	.000205	.000710	.001345	.003551
.300000	.038438	1.183200	3.484051	.000219	.000763	.001296	.003816
.325000	.038462	1.198899	2.180744	.000249	.000544	.004495	.001959
.350000	.038462	1.137304	2.123398	.000332	.000705	.004049	.002577
.375000	.038462	1.123354	2.107373	.000395	.000832	.003800	.003053
.400000	.038462	1.116283	2.100196	.000448	.000940	.003629	.003459
.425000	.038462	1.112070	2.096041	.000497	.001041	.003497	.003833
.450000	.038462	1.109333	2.093331	.000543	.001136	.003388	.004187
.475000	.038462	1.107449	2.091443	.000587	.001228	.003296	.004526
.500000	.038462	1.106097	2.090159	.000629	.001316	.003217	.004852
.525000	.038462	1.105094	2.089165	.000671	.001401	.003147	.005169
.550000	.038462	1.104329	2.088417	.000711	.001484	.003085	.005477
.575000	.038462	1.103732	2.087842	.000750	.001566	.003030	.005778
.600000	.038462	1.103256	2.087380	.000788	.001645	.002979	.006073
.625000	.038462	1.102870	2.087003	.000826	.001724	.002933	.006363
.650000	.038462	1.102553	2.086702	.000863	.001801	.002891	.006647
.675000	.038462	1.102288	2.086447	.000899	.001876	.002852	.006927
.700000	.038462	1.102065	2.086228	.000935	.001951	.002816	.007203
.725000	.038462	1.101875	2.086045	.000971	.002025	.002782	.007475
.750000	.038462	1.101711	2.085886	.001005	.002097	.002750	.007744
.775000	.038462	1.101568	2.085748	.001040	.002169	.002721	.008010
.800000	.038462	1.101444	2.085628	.001074	.002240	.002693	.008272
.825000	.038462	1.101334	2.085522	.001108	.002310	.002666	.008532
.850000	.038462	1.101237	2.085427	.001141	.002380	.002641	.008789
.875000	.038462	1.101150	2.085344	.001174	.002449	.002618	.009044
.900000	.038462	1.101072	2.085269	.001207	.002517	.002595	.009296
.925000	.038462	1.101002	2.085202	.001240	.002585	.002573	.009546
.950000	.038462	1.100939	2.085140	.001272	.002652	.002553	.009794
.975000	.038462	1.100882	2.085085	.001304	.002718	.002533	.010040
1.000000	.038462	1.100825	2.085030	.001356	.002826	.002503	.010439

TRANSITION AT X = .3154
SEPARATION AT X = .9999
SHOCK LOCATION = 1.0000

Figure A-3b. Boundary layer calculation.

FREE-STREAM MACH NUMBER = 1.1000   REYNOLDS NUMBER = 1.2000
SEPARATION AT X = 1.0000   BOATTAIL AT X = 1.0000

(CONE AT X = 0.0000)

MODIFIED PRESSURE DISTRIBUTION

X	R	M	P/PTNF	X/D
0.000000	0.000000	0.000000	2.135136	0.000000
.025000	.005996	.907633	1.251984	.325000
.050000	.011484	.966566	1.172303	.650000
.075000	.016465	1.004459	1.122093	.975000
.100000	.020938	1.030680	1.087900	1.300000
.125000	.024902	1.054798	1.055890	1.625000
.150000	.028359	1.078057	1.027410	1.950000
.175000	.031309	1.097325	1.003320	2.275000
.200000	.033750	1.115509	.980873	2.600000
.225000	.035684	1.133017	.959533	2.925000
.250000	.037109	1.150081	.934998	3.250000
.275000	.038027	1.166807	.919130	3.575000
.300000	.038438	1.183200	.899912	3.900000
.325000	.038462	1.198899	.881746	4.225000
.350000	.038462	1.137304	.956349	4.550000
.375000	.038462	1.123354	.971277	4.875000
.400000	.038462	1.116283	.979924	5.200000
.425000	.038462	1.112070	.985096	5.525000
.450000	.038462	1.109333	.988465	5.850000
.475000	.038462	1.107449	.990787	6.175000
.500000	.038462	1.106097	.992455	6.500000
.525000	.038462	1.105094	.993695	6.825000
.550000	.038462	1.104329	.994640	7.150000
.575000	.038462	1.103732	.995379	7.475000
.600000	.038462	1.103256	.995968	7.800000
.625000	.038462	1.102870	.996445	8.125000
.650000	.038462	1.102553	.996837	8.450000
.675000	.038462	1.102288	.997165	8.775000
.700000	.038462	1.102065	.997441	9.100000
.725000	.038462	1.101875	.997677	9.425000
.750000	.038462	1.101711	.997880	9.750000
.775000	.038462	1.101568	.998057	10.075000
.800000	.038462	1.101444	.998211	10.400000
.825000	.038462	1.101334	.998347	10.725000
.850000	.038462	1.101237	.998467	11.050000
.875000	.038462	1.101150	.998575	11.375000
.900000	.038462	1.101072	.998671	11.700000
.925000	.038462	1.091585	1.010465	12.025000
.950000	.038462	1.005990	1.120082	12.350000
.975000	.038462	.908227	1.251173	12.675000
1.000000	.038462	.831940	1.356314	13.000000

DRAG BREAK-DOWN	I	FRICTION	I	BOATTAIL	I	BASE	I	FOREBODY	II	TOTAL	I
I VALUES	I	.1272	I	0.0000	I	-.1504	I	.0562	II	.0330	I
I PERCENT VALUES	I	385.7625	I	0.0000	I	-456.1944	I	170.4320	II	100.0000	I

Figure A-3c. Pressure distribution with plume interaction.

SAMPLE CALCULATION

FREE STREAM MACH NUMBER = 1.1000   REYNOLDS NUMBER =   1.2000

JET PRESSURE RATIO = 5.7667   FREE STREAM PRESSURE = 14.7000

JET TOTAL PRESSURE =   87.7000   JET TOTAL TEMPERATURE =   500.00

THRUST COEFFICIENT = 31.26.310   BASE PRESSURE = 1.2774

SEPARATION POINT AT 1.0000   JET EXIT MACH NUMBER = 2.7000

PLUME GEOMETRY

X	R	S
0.000000	.035831	0.000000
.003946	.034464	.004744
.012295	.034496	.014492
.016458	.040573	.019144
.020724	.042507	.023828
.025111	.044315	.028573
.029621	.045999	.033387
.034254	.047559	.038276
.039010	.048992	.043243
.043887	.050295	.048291
.048884	.051465	.053423
.053998	.052496	.058640
.059225	.053334	.063943
.064563	.054121	.069330
.070005	.054700	.074803
.075546	.055115	.080360
.081180	.055356	.085999
.086899	.055414	.091719
.092696	.055281	.097517
.098562	.054946	.103392

NOZZLE HALF ANGLE =20.0000
NOZZLE RADIUS = .0308
BASE RADIUS = .0385   DIAMETER RATIO = .8016

PLUME INTERSECTION POINT   XP = 1.0158   YP = .0402
REATTACHMENT PRESSURE = 1.353
PLATEAU PRESSURE = 1.4493
SEPARATION PRESSURE = 1.3045
SHEAR LAYER INCLINATION =   4.3120

Figure A-3d. Details of the interaction.

215

SAMPLE CALCULATION

SUMMARY OF BODY GEOMETRY

BODY LENGTH -L =32.5000
BODY RADIUS/L = .0385
SHOULDER LOCATION/L = .3077
NOZZLE EXIT PLANF/L = 1.0000

FREE STREAM CONDITIONS

INCIDENCE = 0.0000 DEGREES
FREE STREAM MACH NUMBER = 1.1000
REYNOLDS NUMBER = 1.2000 MILLION
JET EXIT MACH NUMBER = 2.7000
JET TOTAL PRESSURE RATIO =24.5000

SUMMARY OF FORCE COEFFICIENTS

NORMAL FORCE COEFFICIENT = 0.0000
PITCHING MOMENT COEFFICIENT ABOUT NOSE = 0.0000
TOTAL DRAG COEFFICIENT = .2781

DRAG COMPONENTS

	PRESSURE	FRICTION	BOATTAIL	BASE
END OF CALCULATION	.0562	.1272	0.0000	.0947

Figure A-3e. Summary of the flow.

216

Appendix B. SUMMARY OF BODY GEOMETRIES
USED IN STUDY

All bodies "B" are fitted with a 4-caliber tangent ogive nose and have a 2.5-in. diameter cylindrical main body. The entire length of the bodies was 32.5 in. MCDAC is a 3-caliber tangent ogive nose body which is 37.5-in. long and 3.75 in. in diameter. A summary of bodies are presented in Table B-1, and a summary of nozzles are presented in Table B-2.

TABLE B-1. BODIES

Symbol	Boattail Angle* (deg)	Boattail Length (in.)
B1	0.0	-
B3	9.5	2.05
B4	6.3	2.05
B5	3.2	2.05
B7	-3.3	7.50
B8	-6.5	3.75
B9	-3.3	3.75
MCDAC	0.0	-

*Flared bodies are donated by a negative angle.

TABLE B-2. NOZZLES

Symbol	Diameter Ratio*	Exit Angle, (deg)	Exit Mach Number
N1	0.800	20	2.7
N4	0.78	0	2.7
N12	0.450	20	2.7
N14	0.600	0	2.7

*Based on 2.5 in. cylinder body diameter

DISTRIBUTION

No. of Copies

Defense Documentation Center
Cameron Station
Alexandria, Virginia 22314 — 12

Commander
US Army Materiel Development and Readiness Command
ATTN: DRCRD — 1
     .DRCDL — 1
5001 Eisenhower Avenue
Alexandria, Virginia 22333

The University of Tennessee
Space Institute
ATTN: Dr. Wu — 30
Tullahoma, Tennessee 37388

Neilsen Engineering and Research, Inc.
ATTN: Dr. Neilsen — 1
      John Fidler — 1
510 Clyde Ave
Mt. View, CA 94043

Dr. H. G. Knoche — 1
Messerschmitt-Bolkow-Blohm
Postfach 80 11 49
8000 Munchen 80
West Germany

DRSMI-FR, Mr. Strickland — 1
   -LP, Mr. Voigt — 1
   -R, Dr. McDaniel — 1
     Dr. Kobler — 1
   -RBD — 3
   -RD — 1
   -RBL — 3
   -RDK, Dr. Spring — 20
   -RPR (Record Set) — 1
     (Reference Copy) — 1

218